HYDROTHERMAL SYNTHESIS METHODS TO INFLUENCE ACTIVE SITE AND CRYSTALLITE PROPERTIES OF ZEOLITES AND CONSEQUENCES FOR CATALYTIC ALKANE ACTIVATION

A Dissertation
Submitted to the Faculty
of
Purdue University
by
Philip M. Kester

In Partial Fulfillment of the
Requirements for the Degree
of
Doctor of Philosophy

May 2020
Purdue University
West Lafayette, Indiana

THE PURDUE UNIVERSITY GRADUATE SCHOOL
STATEMENT OF DISSERTATION APPROVAL

Prof. Rajamani Gounder, Chair
Davidson School of Chemical Engineering
Prof. Jeffrey T. Miller
Davidson School of Chemical Engineering
Prof. Fabio H. Ribeiro
Davidson School of Chemical Engineering
Prof. Corey M. Thompson
Department of Chemistry

Approved by:
Prof. John Morgan
Head of the Graduate Program

To my wife, parents, family, and friends, who all sacrificed to make what follows possible.

ACKNOWLEDGMENTS

To Professor Raj Gounder, who first recruited me to Purdue as a new faculty member in 2013 and pushed me to become a better researcher, mentor, and teacher. Your encouragement over the years has guided my professional and personal development, and taught me how to effectively conduct and communicate scientific research at the highest level.

To Professors Fabio Ribeiro and Jeff Miller for providing rigorous technical feedback and guidance during my time at Purdue, and broadening my worldview on catalysis through unique viewpoints on fundamental heterogeneous kinetics and new approaches to zeolite synthesis.

To Prof. Nick Delgass, whose mentorship in the laboratory and on the golf course helped me through technical and personal challenges during my Ph.D. I aspire to be as passionate about life and my career as you.

I acknowledge the mentorship provided by Dr. Jamie Harris, Dr. Ravi Joshi, Dr. John Di Iorio, and Dr. Michael Cordon, who collectively established the Gounder research group and guided my work as a new graduate student. I would also like to thank Dr. Jason Bates and Dr. Juan Carlos Vega-Vila for the many years of camaraderie in the Gounder group, and all other current members of the group for their friendship and assistance. I would also like to acknowledge Dr. Yury Zvinevich for continuous laboratory assistance and troubleshooting. Other technical contributors to this work through direct discussions and those with their students include Prof. Enrique Iglesia (UC Berkeley), Prof. Bill Schneider (Notre Dame), Prof. Aditya Bhan (U Minnesota), Prof. David Hibbitts (U Florida), and Prof. Jeffery Rimer (U Houston).

To my friends from Purdue, I am grateful for the time we spent playing music, eating pizza, and celebrating accomplishments every Tuesday night. These endeavors were pursued with Dr. Jason Bates, Dr. Scott McClary, Dr. Rob Warburton, and Adam Wingate, who was last spotted heading west.

Finally, I would like to thank my wife Amy for reminding me to focus on what matters most and be the best person I can be. I also thank my parents, family, and friends for their support over the last several years that made my endeavors possible.

TABLE OF CONTENTS

LIST OF TABLES

LIST OF FIGURES

Figure Page

ABSTRACT

Kester, Philip M. Ph.D., Purdue University, May 2020. Hydrothermal Synthesis Methods to Influence Active Site and Crystallite Properties of Zeolites and Consequences for Catalytic Alkane Activation. Major Professor: Rajamani Gounder.

Zeolites are crystalline microporous solid acids composed of silica-rich frameworks with aliovalent Al heteroatoms substituted in crystallographically-distinct locations and arrangements, which generate anionic lattice charges that can be compensated by protons and extraframework metal cations or complexes that behave as catalytic active sites. Protons that charge-compensate Al are similar in Brønsted acid strength, yet differ in reactivity because their bound intermediates and transition states are stabilized by van der Waals interactions with confining microporous cavities, and by electrostatic interactions with proximal heteroatoms and adjacent protons. A diverse array of framework Al and extraframework H^+ site ensembles are ubiquitous in low-silica and low-symmetry zeolite frameworks (e.g., MFI, MOR), which cause measured turnover rates to reflect the reactivity-weighted average of contributions from each distinct site ensemble. The reactivity of distinct sites can be further masked by diffusion barriers often imparted by microporous domains and secondary reactions of primary products, which become increasingly prevalent as products encounter higher numbers of active sites during diffusion prior to egress from zeolite crystallites. Consequently, catalytic behavior often depends on zeolite material properties at orders-of-magnitude different length scales, which depend on the specific protocols used in their synthesis and crystallization.

In this work, CHA zeolites that contain only one symmetrically-distinct lattice site for Al substitution are used as model materials to decouple the effects of proton location and proximity in vibrational spectra and turnover rates for acid catalysis.

Interactions between proximal protons influence their equilibrium distribution among anionic lattice O atoms in $AlO_{4/2}^{-}$ tetrahedra, and result in temperature-dependent changes to vibrational frequencies and intensities of the asymmetric OH stretching region in infrared spectra measured experimentally and computed by density functional theory (DFT). Protolytic propane cracking and dehydrogenation, a catalytic probe reaction of the intrinsic reactivity of Brønsted acid protons, occur with turnover rates (748 K, per H^+) that are an order-of-magnitude higher on paired protons than isolated protons, resulting from entropic benefits provided to late carbonium ion-pair transition states by proximal protons. These results indicate that cationic transition states can be stabilized entropically through multi-ion interactions with lattice anion and cation sites. Precise interpretation and quantification of the reactivity of different types and ensembles of Brønsted acid protons in zeolites requires that protolytic chemistry prevails in the absence of secondary active sites or other kinetically-relevant processes, a requirement generally met for alkane cracking but not dehydrogenation on H-form zeolites. Propane dehydrogenation activation energies vary widely (by $>$100 kJ mol^{-1}) among H-form zeolites of different structure (MFI, MOR, CHA) and composition (Si/Al = 10 – 140) because reactant-derived carbonaceous deposits form *in situ* and catalyze alkane dehydrogenation under non-oxidative conditions through hydride transfer pathways. Contributions of reactant-derived active sites to propane dehydrogenation rates are quantified through a series of transient and steady-state kinetic experiments with co-fed alkene and dihydrogen products, and are found to depend on gradients in product pressures that are present in integral reactors under non-ideal plug-flow hydrodynamics. Propane dehydrogenation rates collected at initial time-on-stream and in the presence of co-fed H_2 solely reflect protolytic reaction events and can be used to interpret differences in the reactivity of distinct proton sites and ensembles for alkane activation catalysis. The reaction conditions identified here can be used to remove or suppress thee reactivity of carbonaceous active sites during catalysis, or to engineer the formation of organocatalysts on zeolite surfaces for selective dehydrogenation or hydride transfer reactions.

Synthetic strategies to decouple bulk and active site properties at disparate length scales, which are typically correlated in MFI zeolites crystallized hydrothermally, are developed by adding a second heteroatom and organic structure directing agent (SDA) to synthesis media. Crystallite size and morphology are independently varied from Al content by incorporating B heteroatoms into zeolitic frameworks, which generate protons that are catalytically irrelevant compared to those compensating Al, and NH_3 temperature-programmed desorption methods are developed to differentiate between these two types of proton sites. The siting of Al heteroatoms in distinct locations and ensembles is influenced by the decrease in cationic charge density among occluded SDAs, in cases where ethylenediamine is co-occluded with tetra-*n*-propylammonium cations. The co-occlusion of organic SDAs enables crystallizing MFI zeolites with different bulk properties but similar Al distributions, or with similar bulk properties and different Al distributions. MFI zeolites crystallized with these methods provide model materials that can be interrogated to decouple the effects of bulk and atomic-scale properties on acid catalysis, and open opportunities to exploit these material properties by designing active site ensembles and crystallite diffusion properties for catalytic chemistries that depend on coupled reaction-transport phenomena.

1. INTRODUCTION

Zeolites are a class of crystalline microporous tectosilicates comprised of tetrahedrally-coordinated Si atoms linked by O atoms in arrangements that create pores and cavities ranging from 3-15 Å in diameter interconnected in one, two, or three-dimensional networks [1]. While purely siliceous molecular sieves are used in gas adsorption and separation applications (e.g., CO_2 [2], light hydrocarbons [3]), additional functionality is introduced via isomorphous substitution of Si^{4+} atoms by Al^{3+} that imparts a local charge disparity in the lattice requiring compensation by extraframework cations (e.g., H^+, Na^+, Ca^{2+}), present either as vestiges of hydrothermal synthesis or introduced by post-synthetic ion-exchange procedures. Extraframework protons that compensate Al heteroatoms serve as Brønsted acid sites that catalyze a variety of industrially-relevant chemical reactions, including fluid catalytic cracking (FCC) of heavy hydrocarbons [4], alkene oligomerization [5], and aromatic alkylation and disproportionation [6]. Framework Al heteroatoms can also compensate extraframework metal cations relevant for NO_x selective catalytic reduction (SCR) on Cu-CHA zeolies [7], methane dehydroaromatization on Mo-MFI [8], and ethane ammoxiation on Co-MFI zeolites [9].

The first scientific classification of zeolites is attributed to the Swedish mineralogist Cronstedt [10], who in 1756 observed water vapor being evolved from a naturally-occurring mineral (later identified as stilbite [11]) upon rapid heating in a flame and coined the name "zeolite", derived from the Greek words zéō (to boil) and líthos (stone). Such naturally-occurring zeolites crystallize under basic conditions in the presence of alkali metal (e.g., Na^+, K^+) or alkaline earth metal (e.g., Ca^{2+}, Ba^{2+}) cations that compensate anionic charges associated with Al tetrahedra. By emulating these conditions, the laboratory of St. Claire Deville performed the first known hydrothermal zeolite synthesis by crystallizing levynite in 1862 [12]. Only naturally-occurring zeolite topologies were known until 1948, when Barrer reported the hydrothermal synthesis of zeolite types P and Q, which had no natural analog, from synthetic solutions containing Na^+ and Ba^{2+} cations and natural minerals as precursors [13]. Following this discovery, many new synthetic zeolites were crystallized in the 1950s using similar synthetic approaches, including LTA [14] and FAU [15]. By the end of the decade, Union Carbide was synthesizing FAU zeolites for use in isomerization reactions [16], and soon thereafter Mobil was using FAU as an FCC catalyst [4,16].

Up to this point in the history of zeolite synthesis, high quantities of alkali cations in synthesis solutions (e.g., $Na^+/Si > 2$ for LTA [14] and FAU [15]) led to crystalline solids with Si/Al ratios generally less than 2. By supplying alkylammonium cations of lower cationic charge density per unit volume, LTA and FAU zeolites were crystallized with higher Si/Al ratios than those attainable with only alkali cations due to the lower packing densities of larger cations within extracrystalline voids [17]. Many new synthetic zeolites were discovered with the addition of alkylammonium cations in synthesis solutions, most notably beta (*BEA) zeolites crystallized with teatraethylammonium (TEA^+) [18] and MFI zeolites with tetra-n-propylammonium (TPA^+) [19,20]. High-silica beta zeolites have found use in alkylation catalysis for their ability to host bulky aromatic intermediates and products [21,22], and MFI zeolites have been used for alkene oligomerization in the Mobil Olefins to Gasoline and Distillate process (MOGD, [23–25]) and alkane isomerization catalysis [26]. Since the introduction of TEA^+ and TPA^+ to zeolite syntheses, many other organic SDAs have been added to the zeolite synthesis repertoire to crystallize new frameworks [27] and efforts continue to design and predict organic SDAs for new zeolite topologies [28,29]. In parallel, additional heteroatoms have been substituted into silica-rich zeotypes during hydrothermal synthesis, including other trivalent heteroatoms (B [30], Ga [31], Fe [32]) that are compensated by extraframework protons of varying acid strength [33], and tetravalent metals (e.g., Sn, Ti, Zr [34]) that act as Lewis acids for a variety of Meerwein–Ponndorf–Verley oxidation (MPVO) reactions [35, 36].

The diversity in zeolite composition, structure, and functionality afforded by hydrothermal synthesis methods provide means to perform a variety of catalytic reactions in shape- and size-selective containers that confine active sites and organic guest molecules. Early applications of zeolites often relied on their shape-selective properties, by which access of reactant molecules to intracrystalline active sites and diffusion of products from microporous domains is controlled by the size and connectivity of zeolite pores [37, 38]. These principles are responsible for higher selectivity of toluene alkylation and disproportionation reactions to *para*-xylene over *ortho*- and *meta*- isomers on MFI zeolites than on mesoporous solid acids, because *para*-xylene diffuses $>10^3$ times faster than isomers with larger kinetic diameters in MFI [39]. In certain cases, only a subset of active sites is accessible to reactant molecules in zeolites that contain distinct pore environments. Such is the case for xylene isomerization on FER zeolites, where reactants can only access protons confined in 10-membered ring (10-MR) channels and not smaller 8-MR voids [40]. Carbon deposition is also slower on H-form zeolites with smaller pore environments that cannot accommodate polyaromatic coke deposits during n-hexane and 3-methylpentane reactions at 700 K [41].

The shape-selective properties of zeolites, however, extend beyond size exclusion and diffusion limitation principles. Derouane and co-workers first identified the role of van der Waals interactions supplied by the inorganic lattice in stabilizing organic adsorbates in microporous oxides (the "nest effect") as the basis for different n-pentane cracking rates among H-form zeolites [42, 43], previously interpreted as differences in intrinsic acid strength of Brønsted acid protons between frameworks of varying electronegativity [44]. Subsequent publications outlined the first methods to compute van der Waals interactions between adsorbates and curved zeolite pores by treating the adsorbate as an isotropic polarizable molecule and the lattice as a uniform dielectric [45], which were then applied to predict chemical shifts in ^{13}C NMR with tetramethylammonium (TMA^+) cations and ^{129}Xe NMR with guests occluded in a diverse set of zeolite frameworks [46]. Simultaneous calorimetric and gravimetric experiments performed by Eder and co-workers quantified enthalpic and entropic components of *n*-alkane adsorption free energies in zeolites [47], where adsorbates whose size more closely matched that of the microporous void benefited most from favorable van der Waals contacts with lattice O atoms at the expense of entropic penalties from confinement. These enthalpy-entropy tradeoffs are also responsible for the site-specific reactivity of Brønsted acid protons in 8-MR side pockets of MOR zeolites over the larger 12-MR channels for dimethyl ether (DME) carbonylation to methyl acetate, even though all active sites are accessible to reactants, because enthalpic stabilization of carbonylation transition states relative to surface-abundant DME-derived intermediates overcomes entropic losses from confinement at relatively low temperatures (438 K) used for this chemistry [48]. Similar conclusions were reached for propane cracking and dehydrogenation in 8-MR pockets of MOR zeolites at higher temperatures (748 K), although because partial confinement of carbonium ion transition states incurred less severe entropic losses that outweighed the potential for enthalpic gains [49]. More recent work from the Iglesia group has used density functional theory (DFT) methods to quantify van der Waals interactions between the lattice and guests for hydrogen transfer [50], alkene oligomerization [51], and acetone condensation [52] catalysis. Collectively, these principles prescribe that the "right fit" between the inorganic oxide and organic guest that minimizes free energy differences between transition states and relevant intermediates will maximize the rate of a chemical transformation in microporous solid acids [53], provided that reactants can access the active site and products can diffuse to extracrystalline spaces. Therefore, siting Al heteroatoms and their associated extraframework cations among distinct T-sites and microporous voids provide strategies to influence adsorption and catalytic phenomena even among microporous solid acids of a given framework structure and composition, motivating development of zeolite synthesis methods to exploit these phenomena and purposefully direct the placement of Al atoms to specific T-sites and voids.

Hydrothermal zeolite synthesis proceeds though a series of nucleation, growth, and dissolution processes to crystallize solid products with occluded templates [54]. Pure-silica molecular sieves are metastable solids with energies of 6.8-14.4 kJ (mol SiO_2)$^{-1}$ relative to quartz [55, 56], and framework-template interactions generally stabilize frameworks by 1-6 kJ (mol SiO_2)$^{-1}$ [57]. These small energetic differences between silica structures and framework-SDA combinations highlight the importance of kinetics in zeolite nucleation and growth [58]. Silica dissolution rates in basic conditions relevant for hydroxide-mediated synthesis depend on the precursor structure [59], and liberation of monomeric silicates makes them available to SDAs found in zeolite synthesis solutions. Foundational studies of template-silicate interactions during silicalite-1 (Si-MFI) synthesis have been reported by Chang and Bell [60] and Burkett and Davis [61]. The former proposed that silica precursors isomorphously substitute water in clathrated TPA^+ cations ($Si/TPA^+ \sim 24$) before organizing into crystalline networks, and the latter used ^1H–^{29}Si CP MAS NMR to provide evidence for cross-polarization from ^1H nuclei in TPA^+ to ^{29}Si nuclei in clathrates prior to crystallization, while these nuclei did not cross-polarize in mixtures containing TMA^+ cations under the same conditions. These results are consistent with the presence of “magic number clusters” of 21 or 23 water molecules in TPA^+ clathrates observed via electrospray mass spectrometry, while water clusters of varying size form indiscriminately around TMA^+ cations [62].

These conclusions regarding template-silicate interactions during zeolite synthesis consider only pure-silica zeolites, however, and the presence of anionic Al heteroatoms introduces additional ion-pair interactions with cationic structure directing agents [63] that can influence Al siting in crystallographically-distinct locations and ensembles [64]. For instance, when mixtures of TMA^+ and pyrrolidine were used to crystallize FER zeolites, Rietveld refinement of X-ray diffraction data showed that TMA^+ cations preferentially occupied 8-MR cavities while pyrrolidine was found in both 10-MR channels and 8-MR cavities in FER zeolites crystallized in the presence or absence of TMA^+, influencing the abundance of Al heteroatoms in 8- and 10-MR voids sited by the cationic SDAs [65]. Similar FER syntheses used mixtures of TMA^+ and substituted pyrrolidines as SDAs, and the fraction of Brønsted acid protons in 10-MR voids accessible to pyridine titrants depended on the structure and packing density of occluded SDAs [40]. Román-Leshkov and co-workers later used synthetic mixtures with cyclic amines to show parallel methods to crystallize FER zeolites of similar bulk compositions (Si/Al = 13 - 17) but with different abundances of protons in 8-MR and 10-MR voids, as evidenced by site-specific DME carbonylation kinetics [66]. Mixtures of SDAs have also been used to influence Al siting in MFI zeolites [67], including cationic SDA mixtures (TPA^+-Na^+ [68]) and neutral-cationic SDA mixtures (pentaerythritol-Na^+ [69]). Evidence for biased Al siting in 10-MR channel environments (∼0.55 nm) or larger intersections (∼0.7 nm) in these works was found in relative ratios of *n*-hexane and 3-methylpentane cracking rates in the constraint index test [70], wherein bulkier transition states for 3-methylpentane cracking than *n*-hexane cracking are preferentially stabilized in larger microporous domains. Normalized catalytic turnover rates and selectivities can therefore report on the distribution of Al among distinct T-sites and voids when activation free energies depend on confinement.

Considerations of diverse Al distributions in zeolites must also include proximal Al ensembles ("paired Al"). These configurations have been implicated to influence Brønsted acid-catalyzed reactions in MFI zeolites (e.g., alkene oligomerization [71,72], alkane cracking [73]), and are also required to charge-compensate divalent metal cations or clusters in extraframework positions (e.g., MoO_x^{2+} [74], Co^{2+} [75]). Considerable efforts have been made by the Dědeček group to site proximal Al atoms in MFI zeolites [64], and the number of Al pairs counted by Co^{2+} ion-exchange procedures has been found to depend on the Si and Al precursors (e.g., tetraethylorthosilicate, sodium silicate) and counter-anions (e.g., Cl^-, OH^-) used in synthesis [76,77], though differences in Al proximity did not trend systematically or predictably with any given synthetic parameter over a range of compositions (Si/Al = 10 - 60). More recently, Di Iorio and Gounder [78] have reported on Al isolation and pairing in CHA zeolites of fixed bulk composition (Si/Al $\sim$ 15), where the abundance of Al pairs was influenced by the cationic charge density of synthesis solutions, controlled by the ratio of *N,N,N*-trimethyl-1-admantylammonium ($TMAda^+$) and Na^+ cations as SDAs. Bimolecular methanol dehydration catalysis that proceeded through associative routes with co-adsorbed methanol molecules on CHA zeolites containing predominantly isolated protons was $>10\times$ faster (415 K, per H^+) at paired sites, and is proposed to proceed through dissociative routes mediated by methoxy intermediates on these sites based on *in situ* IR spectra showing methoxy deformation modes at 1457 cm^{-1} [79]. In general, methodologies to influence Al distributions in zeolites rely on mixtures of organic and/or inorganic SDAs of different structure, charge, or propensity for incorporation into crystalline solids, and the stability of organic intermediates and transition states during catalysis depend on these local Al arrangements.

Many alkylammonium cation SDAs tend to crystalize certain frameworks during hydrothermal synthesis and occlude in well-defined stoichiometries, such as the incorporation of one TPA^+ per intersection in MFI [60] or one $TMAda^+$ per cage in CHA [80]. Secondary non-specific structure directing agents can serve a pore-filling role in place of a fraction of structure-specific SDAs, as demonstrated by Zones and coworkers for adamantyl SDAs and non-specific amines (e.g., methylamine, butylamine) in MWW zeolites, where the adamantyl templates are responsible for MWW nucleation followed by growth of crystalline products with non-specific amines [81,82]. Elemental analysis of crystalline products showed that structure-specific SDAs are preferentially incorporated from mixtures containing insufficient quantities of adamantyl cations (per Si) for maximum inclusion in MWW (SDA/Si < 0.08), decreasing the amount of structure-specific SDA required for crystallization of the desired phase. While motivations to replace bulky organic SDAs in zeolite synthesis are often derived from their cost and adverse environmental consequences [83], these methods may also introduce the ability to bias Al location and proximity in zeolites. Other strategies to occlude different SDAs into zeolite frameworks include seeding synthesis solutions with small amounts (~10 wt%) of the desired crystal phase to overcome primary nucleation barriers present when structure-specific SDAs are absent [54], providing flexibility in the composition of the synthesis solution and crystalline products. These methods have been used to grow beta [84] and MFI [85] zeolites with Na^+ in the absence of organic cations, albeit in the presence of crystalline seeds made with TEA^+ and TPA^+ cations, respectively. In other cases, mixtures containing SDAs that, on their own, crystallize specific frameworks are instead able to structure-direct a third phase when present together in synthesis, as reported by Kumar and co-workers for MOR [86]. Mixtures of $TMAda^+$ and 1,2-hexanediol that independently crystallized CHA and MFI, respectively, instead crystallized MOR under similar synthetic conditions, and Rietveld refinement of X-ray diffraction data showed that bulky amine occludes in the larger 12-MR channels while the alcohol resides in 8-MR side pockets. These strategies collectively provide parallel routes to crystallize zeolite frameworks with diverse organic and inorganic occluded SDAs, which may bias the siting of Al heteroatoms and reactivity of their charge-compensating protons for acid catalysis.

Rates, product selectivities, and deactivation during catalysis by zeolites are influenced not only by populations of distinct active site structures, but also on bulk properties (e.g., crystallite size, morphology, composition) that influence intracrystalline residence times of bulky intermediates and products that can unavoidably undergo sequential reactions when diffusion limitations are imposed by the microporous host. These material properties contribute to a characteristic diffusion parameter, representing a measure of the number of active sites a molecule encounters per unit length in microporous domains, and is found in Thiele modulus expressions for coupled reaction and diffusion in porous catalyst particles. In the case of propene oligomerization on H-form zeolites, C_2-C_{12} alkene product selectivities more closely resembled binomial distributions expected from prevalent secondary reactions of primary C_6 products in zeolites with longer diffusion parameters at fixed conversion (~ 1%), consistent with the preferential increase in intracrystalline residence times of bulky intermediates [87]. Similar findings have been reported by the Bhan group in methanol-to-hydrocarbons (MTH) catalysis on MFI zeolites, where the role of crystallite size and morphology [88] and active site density [89] have been separately quantified to show that bulky aromatics that propagate ethene formation prevail over olefinic intermediates that make propene with increasing diffusion parameters. However, zeolite crystallite size and composition are typically correlated in conventional hydrothermal synthesis, where more Al-dense compositions generally form smaller crystallites [90–92], thereby attenuating differences in characteristic diffusion parameters while having unknown general implications for the siting of heteroatoms in distinct T-sites or ensembles. Efforts to engineer zeolite crystal size and morphology include the use of diammonium surfactants as organic SDAs to crystallize MFI sheets that are only ∼2 nm thick [93], alcohol and amine additives that bind selectively to certain crystal facets during growth phases and influence diffusion paths in distinct intrapore networks [94, 95], and through introduction of boron heteroatoms that also influence resulting crystallite size [96] but generate Brønsted sites that are much weaker acids (by ∼70 kJ mol^{-1} [33]) than those at Al heteroatoms and thus essentially unreactive in the contexts of most acid-catalyzed reactions. These methods aim to decrease diffusion path resistances while retaining microporous containers required for shape-selective properties. However, little work has been done to simultaneously influence macroscopic crystallite properties and Al siting within distinct locations and ensembles. By independently controlling zeolite properties at these length scales ($10^{-10} - 10^{-5}$ m), site-weighted reactivity of protons at distinct Al sites and the role of elementary steps in complex reaction networks during coupled reaction-diffusion can be quantified in microporous solids for Brønsted acid catalysis and for metal-derived active sites of varying valency.

In Chapter 2, we use single T-site CHA zeolites as model materials to decouple the roles of site location and proximity, using infrared spectroscopy and high-temperature acid catalysis as probes of proximal Al heteroatoms and their charge-compensating cations. CHA zeolites of similar bulk composition (Si/Al $\sim$ 15) but with different amounts of isolated and paired Al are synthesized according to previously reported methods [78]. Conventionally, divalent Co^{2+} titrants are used in aqueous ion-exchange procedures and probe proximal Al heteroatoms that serve as structural surrogates of proton active sites. However, IR spectra in the asymmetric OH stretching region of CHA zeolites provide more direct quantification of active sites distributed among the four crystallographically-distinct O atoms in $AlO_{4/2}^{-}$ tetrahedra. Integrated areas of OH stretching features for CHA zeolites containing predominantly isolated protons are temperature-insensitive, while those for CHA containing paired Al reversibly decrease with increasing temperature (448 - 748 K). DFT calculations suggest that isolated proton configurations are nearly isoenergetic, while higher-energy paired proton configurations have lower dipole moment first-derivatives on average, leading to temperature-sensitive IR spectra for CHA zeolites containing nonzero fractions of paired Al atoms. These findings rationalize previous observations of temperature-sensitive IR spectra in lower-symmetry frameworks (e.g., MOR, MFI [97, 98]), previously attributed incorrectly to the delocalization of protons from the lattice to greater extents with increasing temperature [99]. Monomolecular propane cracking first-order apparent rate constants (748 K, per H^+) are an order-of-magnitude higher on paired protons than isolated protons, driven by entropic stabilization of late carbonium ion-pair transition states. The distribution of isolated and paired protons is perturbed by partial ion-exchange with Na^+ cations that selectively replace paired protons, decreasing propane cracking rates (per residual H^+) on CHA zeolites that contain paired Al sites. The number of residual paired protons estimated with IR spectroscopy is fewer than the number of paired Al heteroatoms, corroborating DFT and kinetic interpretations that Na^+ cations preferentially exchange paired protons. Similar catalytic consequences of site pairing for protolytic alkane reactions with entropic benefits have been previously reported with in MFI zeolites [73], although these interpretations are convoluted with the presence of protons in different pore environments that have also been interpreted to influence protolytic alkane reaction rates in MFI [100]. This highlights the need to quantify diverse active site arrangements dictated by Al location and proximity, and the role of the latter for IR spectroscopy and acid catalysis.

Protolytic alkane cracking and dehydrogenation serve as high-temperature reactive probes in zeolites and have been used demonstrate varied reactivity of Brønsted acid protons through interpretations of enthalpic and entropic contributions to carbonium ion free energies in distinct void environments [49, 100], similar to the methods used in Chapter 2 for propane cracking on paired protons in CHA. However, significant variation in reported propane dehydrogenation activation energies and entropies have precluded unambiguous interpretations of carbonium ion free energies on H-form zeolites. For instance, apparent protolytic propane cracking barriers were similar among independent reports (147 – 165 kJ mol^{-1}) on a variety of H-form zeolites (MFI, MOR, FAU, MWW, FER, and *BEA [49, 101–105]), while apparent dehydrogenation activation energies varied from 65 - 202 kJ mol^{-1} under the same conditions, incorrectly attributed to different kinetically-relevant processes for protolytic reactions (e.g., product desorption [102, 103]) or to other intrinsic active sites present in zeolites (e.g., extraframework Al [101]). In Chapter 3, we use a combination of steady-state and transient kinetic experiments in the presence and absence of co-fed alkane dehydrogenation products to quantify the contributions of intrinsic Brønsted acid sites and reactant-derived carbonaceous active sites to measured propane dehydrogenation rates on H-form zeolites. Propane cracking and dehydrogenation kinetics extrapolated to zero catalytic turnovers in the presence of co-fed H_2 solely reflect protolytic reaction events, as evidenced by the absence of product inhibition and apparent activation energies that differ by gas-phase proton affinities of C-C and C-H bonds in propane reactants. Hydride transfer events on reactant-derived intermediates that form propene are characterized by product inhibition and apparent activation energies that are ~100 kJ mol^{-1} lower than those expected for protolytic pathways, and depend on reactant partial pressure and residence time, and on hydrodynamic properties in Péclet number expressions when axial diffusion and convective flux are of commensurate magnitudes. Protolytic dehydrogenation rates are thermodynamically consistent with propene hydrogenation kinetics collected under conditions where the number and reactivity of carbonaceous deposits is negligible. This work provides methods to quantify protolytic dehydrogenation rates and activation free energies in zeolites through hydrogenation of secondary reactive species, and informs protocols to deposit carbonaceous intermediates in zeolites that are relevant for dehydrogenation [106] and electrochemical [107] applications.

In general, rate, product selectivity, and deactivation during catalysis by zeolites can depend on macroscopic zeolite properties (e.g., crystallite size, morphology, composition) and on distinct active site structures that influence adsorbate and transition state free energies. Certain zeolite properties tend to be correlated in hydrothermal synthesis methods, as methods to vary bulk and microscopic properties rely on the specific combination of SDAs, precursors, and other additives in synthesis mixtures. Therefore, we set out to independently vary MFI zeolite properties at different length scales (10^{-10} – 10^{-5} m) by adding additional heteroatoms and SDAs to circumvent typically observed trends. In Chapter 4, we crystallize MFI zeolites with TPA^+ and ethylenediamine as co-organic SDAs in the presence of B and Al heteroatoms. B-Al-MFI zeolite crystallite size and morphology can be controlled by the quantity of B heteroatoms, independent of Al content, under conditions where synthesis solutions contain significantly more B than Al (Si/B = 2.6 - 13, Si/Al = 88 - 176). Brønsted acid protons originating from B heteroatoms are weaker acids than those from Al (by $\sim$70 kJ mol^{-1} [33]), and new titration protocols are developed using NH_3 to differentiate between these sites for normalization of catalytic turnover rates. Typical NH_3 temperature-programmed desorption methods used for aluminosilicates overestimate the number of protons relevant for acid catalysis in boroaluminosilicates, because NH_3 is adsorbed at B and Al heteroatoms following aqueous-phase ion-exchange procedures. NH_3 molecules can be selectively removed from B-Al-MFI zeolites at 433 K following saturation in aqueous-phase NH_4NO_3 solution, or selectively adsorbed during gas-phase titration at the same temperature, and thus subsequent temperature-programmed desorption quantifies only those protons relevant for acid catalysis. This result is corroborated by zero-order methanol dehydration rate constants (415 K) that predominantly depend on acid strength [33] that are similar among Al-MFI and B-Al-MFI zeolites when normalized by the number of protons associated with Al heteroatoms quantified by selective titrations, while first-order methanol dehydration rate constants that depend on both acid strength and confinement suggest that Al heteroatoms and their protons preferentially reside in MFI channel intersections. This work provides methods to crystallize MFI zeolites with different crystallite sizes and compositions, but with similar distributions of Al heteroatoms in crystallographically-distinct locations, which can be used as model materials to decouple the roles of reaction and diffusion in catalysis by MFI zeolites. We expect these titration protocols can be extended to other frameworks, including small-pore zeolites (e.g., CHA, LTA) where other common bulky titrants (e.g., pyridine) are excluded from microporous domains.

In Chapter 5, we extend synthesis methods from Chapter 4 to more Al-dense compositions (Si/Al $\sim$ 50) and prepare MFI zeolites from mixtures containing only TPA^+ or TPA^+/ethylenediamine mixtures as organic SDAs to study their role in siting proximal Al heteroatoms. Co^{2+} ion-exchange protocols were validated to ensure that all Al pairs were saturated, using NH_3 temperature-programmed desorption methods to quantify the 2:1 stoichiometry expected for replacement of each monovalent cation with a divalent Co^{2+} cation and UV-visible spectroscopy to verify that Co-oxides were absent. Using these ion-exchange protocols, the number of paired Al ensembles is quantified on this suite of MFI zeolites. Al-MFI and B-Al-MFI zeolites prepared only with TPA^+ contain a nonzero number of paired Al ensembles (20 – 40 % Al in pairs), consistent with previous reports for MFI zeolites of similar composition [77], and contain one TPA^+ per channel intersection, the maximum amount that MFI can accommodate [60]. MFI zeolites made with TPA^+ and ethylenediamine contain predominantly isolated Al ($<$ 5% Al in pairs), and TPA^+ in approximately half of the channel intersections, consistent with the TPA^+/Si ratio of 0.02 supplied to synthesis solutions. Ethylenediamine fills the remaining void spaces, reminiscent of other non-specific amines in zeolite synthesis [81, 82], and does so in increasing amounts with the addition of B heteroatoms in a 1:2 ratio observed previously in B-MFI synthesis with ethylenediamine [108, 109]. The structural isolation of Al is therefore related to decreases in effective cationic charge density supplied by occluded TPA^+ cations because of dilution by occluded ethylenediamine in crystalline solids. Addition of B heteroatoms decreases resulting crystallite sizes, as discussed in Chapter 4, but does not influence the distribution of Al pairs counted by Co^{2+} ion-exchange procedures. These methods provide synthetic control over bulk MFI properties, and the siting of Al heteroatoms in distinct ensembles that are relevant for Brønsted acid catalysis [72, 73] and for charge-compensating extraframework cations that serve or precursors to active sites for methane dehydroaromatization on Mo-MFI zeolites [8] and partial methane oxidation on Cu-MFI zeolites [110].

2. EFFECTS OF BRØNSTED ACID SITE PROXIMITY IN CHA ZEOLITES ON INFRARED SPECTRA AND KINETICS OF MONOMOLECULAR PROPANE ACTIVATION

2.1 Abstract

The arrangement of framework Al heteroatoms in isolated and paired configurations in CHA zeolites introduces diversity in the distribution of their charge-compensating Brønsted acid protons among crystallographically-distinct oxygen atoms and void environments. The normalized molar absorptivities of Brønsted acidic OH stretches in infrared spectra of H-CHA zeolites containing non-zero fractions of 6-MR Al pairs, quantified by Co^{2+} titration, decrease reversibly with increasing temperature, while those for H-CHA zeolites with predominantly 6-MR isolated Al sites are invariant with temperature. Periodic density functional theory (DFT) calculations show that paired proton configurations differ in energy by $\sim$40 kJ mol^{-1}, and higher-energy configurations have lower dipole-moment first derivatives that result in lower absorptivity of OH groups with increasing temperature. In contrast, isolated protons are nearly isoenergetic (within 10 kJ mol^{-1}), rendering their IR spectra insensitive to temperature even though different proton configurations give rise to distinct OH stretching features. Protolytic propane cracking rates (748 K, per H^+) are $\sim$10× higher on paired protons than isolated protons, reflecting less negative apparent activation entropies that suggest paired proton sites entropically stabilize late carbonium ion-like transition states. Apparent rate constants (per H^+) decrease with partial titration of H^+ with Na^+ in CHA zeolites containing non-zero fractions of paired Al sites, consistent with DFT calculations suggesting that Na^+ cations preferentially titrate paired Al heteroatoms. These conclusions clarify previous reports of the temperature sensitivity of asymmetric OH IR stretches in H-zeolites attributed incorrectly

to delocalization of protons from the lattice, and provide additional insight into prior reports of protolytic *n*-alkane cracking and dehydrogenation rates that have been attributed to differences in both the location and proximity of acid sites in H-MFI zeolites.

2.2 Introduction

The distribution of Brønsted acid protons among distinct void environments in zeolites is dictated by the siting of aliovalent Al heteroatoms in crystallographically-distinct tetrahedral sites (T-sites) within a given framework, because protons are localized to the four lattice O atoms in $AlO_{4/2}^{-}$ tetrahedra [111, 112]. Confining environments that surround Brønsted acid protons influence the stability of adsorbed intermediates and transition states through van der Waals contacts supplied by lattice O atoms that provide enthalpic benefits at the expense of entropic losses [47], and the "right fit" between the organic guests and inorganic host balances these trade-offs in order to minimize their Gibbs free energy [53]. Catalytic turnover rates are therefore sensitive to confinement when transition states and relevant intermediates are not equally sensitive to confinement, as demonstrated for methanol dehydration on MFI [33], and for dimethyl ether carbonylation [48] and protolytic propane reactions [49] on MOR zeolites.

In general, the siting of Al heteroatoms among distinct T-sites in zeolites is not random, but depends on synthetic variables including the identity and number of structure directing agents (SDAs) and precursors in synthesis solutions [64], providing a strategy to influence reactivity among zeolites of a given framework structure and composition by selectively positioning active sites within different voids. This has been demonstrated by Román-Leshkov and co-workers, who used tetramethylammonium cations and cyclic amines as organic SDAs to crystallize FER zeolites (Si/Al = 13-17) with different fractions of protons in smaller 8-membered ring (8-MR) voids that more effectively stabilize DME carbonylation transition states than larger 10-MR voids [66]. Interpretations of catalytic phenomena at distinct proton sites in zeolites must also consider proximal active site arrangements, as these have also been implicated to influence monomolecular alkane reactions [73] and propene oligomerization [71, 72] on MFI zeolites. Monomolecular *n*-alkane (C_3-C_5) cracking and dehydrogenation rates (783-863 K, per H^+) were reportedly higher due to less negative activation entropies on H-MFI zeolites with lower Si/Al ratios that were able to compensate increasing amounts of Co^{2+} cations, suggesting that the carbonium ion-like transition states occurred later along reaction coordinates and thus more closely resembled alkene and alkane products at paired sites [73]. Different consequences of proton proximity have been reported for alkene oligomerization catalysis on zeolites, as Mlinar and co-workers observed lower steady-state oligomerization rates (500-550 K, 2 kPa C_3H_6) on more Al-dense MFI zeolites with higher fractions of Al pairs and used DFT to show that barriers for hexene desorption decreased relative to trimerization when adsorbates are present on nearby acid sites [71]. In contrast, Bernauer and co-workers observed higher steady-state propene oligomerization rates (473-533 K, 22 kPa) on MFI zeolites with higher fractions of paired sites, quantified by Co^{2+} ion-exchange, and argued that cationic repulsion of nearby acid sites was responsible for faster product desorption [72]. Fundamental studies on the role of site proximity in acid catalysis motivate synthetic methods to systematically influence the fraction of Al pairs in zeolite frameworks, because a diverse set of Al pairs may exist in zeolites containing multiple distinct T-sites. Mixtures of tetrapropylammonium (TPA^+) and Na^+ cations, and different Si and Al precursors, have been used to crystallize MFI zeolites over a variety of compositions ($Si/Al = 12$-61) and Co^{2+} ion-exchange capacities ($Co^{2+}/Al = 0.02$-0.36), although the number of paired Al sites titrated by Co^{2+} did not systematically or predictably depend on any of these synthetic variables [77]. CHA zeolites with $Si/Al \sim 15$, but with 0-44% of Al in paired configurations have been synthesized from mixtures of *N,N,N*-trimethyl-1-admantylammonium ($TMAda^+$) and Na^+ cations, and $Al(OH)_3$ or $Al(i\text{-}o\text{-}Pr)_3$ precursors, and the number of paired Al sites correlated with the number of Na^+ cations retained in crystalline products [78, 79]. Turnover rates of bimolecular methanol dehydration to dimethyl ether were ~10× higher (415 K, per H^+) on paired protons than isolated protons in CHA, proposed to result from a change in mechanism from a concerted pathway mediated by protonated methanol dimers to a sequential mechanism mediated by methoxy intermediates [78]. Therefore, the distribution of Al heteroatoms among crystallographically-distinct T-sites and local ensembles can dictate the reactivity of their charge-compensating protons, and methods to quantify these active site types are required to determine their consequences for acid catalysis.

CHA zeolites serve as a model to quantify the role of acid site proximity in zeolites, because they contain only one crystallographically-distinct T-site for Al substitution. Bare Cu^{2+} and Co^{2+} cations are stabilized at Al pairs within the same 6-MR and separated by one or two Si atoms, as evidenced by density functional theory (DFT) calculations [78, 113]. Many more Al-Al pair combinations exist in lower-symmetry frameworks (e.g., MOR, MFI), however, resulting in a variety of divalent cation exchange sites associated with different Al pairs [114,115], and reactivity measurements conflate the effects of proton location and proximity. Ultimately, divalent cations are functional probes of Al arrangements and not of the distribution of Brønsted acid protons, as Al heteroatoms are structural surrogates for H^+ stes [116] and the quantity of divalent cation exchange sites depends on the identity and ionic radius of the cation [117]. ^{29}Si MAS NMR can be used to quantify the number of Al heteroatoms separated by one Si atom from the Q_2 feature at -101 ppm [118] although these features also include contributions from silanol groups [119], and lattice Al pairs identified by NMR may be adjacent to different voids and thus stabilize Brønsted acid protons in different channels or cavities [76]. Therefore, functional definitions of Al pairing in zeolites are incomplete descriptors of the number of proximal Brønsted acid protons, motivating the use of other spectroscopic or catalytic methods to quantify these active sites.

Asymmetric OH stretches of unperturbed Brønsted acid protons in zeolites appear at ~3600 cm^{-1} in infrared (IR) spectra and serve as a more direct probe of these active sites than cation exchange and NMR methods. The density of protons in zeolites has been quantified with molar extinction coefficients, measured by perturbing Brønsted acidic OH stretches with known quantities of base titrants, although a range of these coefficients have been reported (2-20 cm μmol^{-1}) on H-form zeolites (e.g., MFI, FAU MOR) under a variety of conditions (87-423 K) [120–124]. Wavenumbers are generally lower for Brønsted acid protons within smaller confining voids due to hydrogen bonding with nearby lattice O atoms [125]. In certain frameworks, base titrants of appropriate size can quantify the number of protons in different voids, such as pyridine [126] and *n*-hexane [48] titrants that perturb protons in 12-MR channels (3610 cm^{-1}) but not in 8-MR side pockets (3590 cm^{-1}) of MOR zeolites. Protons in more confined voids generally have higher molar extinction coefficients due to charge transfer through H-bonds that increase dipole moment first-derivatives [127, 128]. However, the presence of Brønsted acid sites in close proximity has unknown consequences for asymmetric OH stretching features in H-form zeolites, and may be masked by the ubiquitous presence of isolated protons among crystallographically-distinct Al atoms and void environments.

Here, we use IR spectroscopy and DFT methods to probe the arrangement of protons among the four bridging O atoms in framework Al tetrahedra in isolated and paired configurations in single T-site CHA zeolites. The molar absorptivity of Brønsted acidic OH stretches associated with 6-MR paired Al configurations is larger than those at 6-MR isolated Al sites, giving rise to higher normalized vibrational features at ~3600 cm^{-1} in IR spectra. Experimental IR spectra and Boltzmann-weighted DFT-simulated spectra show that vibrational intensities of bridging OH groups at 6-MR paired Al sites decrease with increasing temperature (448-748 K) as higher energy proton configurations are selectively populated, while protons at isolated Al are isoenergetic and thus their corresponding IR spectra are insensitive to temperature. We use monomolecular propane cracking as a probe reaction under conditions where Brønsted acid active sites are uncovered during catalytic turnover to show that apparent rate constants (per total H^{+}, 748 K) are an order of magnitude larger at paired protons than isolated protons, providing evidence that the proximity of Brønsted acid sites in zeolites can entropically stabilize carbonium ion transition states. Sodium cations preferentially exchange at paired Al sites, leaving residual isolated protons as the predominant active site in Na-H-CHA zeolites for monomolecular alkane activation, as evidenced by apparent rate constants (per residual H^+, 748 K) that decrease with Na^+/H^+ ratios in CHA containing 6-MR paired Al sites but not for CHA with predominantly 6-MR isolated Al sites. These results reflect the heterogeneities in Brønsted acid proton siting and reactivity that are regulated by the arrangement of framework Al atoms, even within single T-site CHA zeolites of fixed composition.

2.3 Experimental Methods

2.3.1 Synthesis and post-synthetic treatments of CHA zeolites

CHA zeolites were synthesized according to hydrothermal methods reported by Di Iorio and Gounder [78] from synthesis media comprised of molar ratios of 1 SiO_2/ 0.0333 Al_2O_3/ 0.5-x TMAdaOH/ x NaOH/ 44 H_2O, where x ranged from 0–0.25. In a typical synthesis, a 1 M TMAdaOH solution (25 wt%, Sachem) was diluted with deionized water (18.2 MΩ) in a perfluoroalkoxy alkane (PFA) container (Savillex Corp.) and stirred for 15 min under ambient conditions. Then, $Al(OH)_3$ (98 wt%, SPI Pharma) or $Al(i\text{-}o\text{-}Pr)_3$ (98 wt%, Sigma-Aldrich) was added to the solution and stirred for 15 min under ambient conditions. NaOH (98 wt%, Alfa Aesar) was then added to the mixture, which was homogenized for an additional 15 min. Finally, colloidal silica (Ludox HS 40, 40 wt%, Sigma-Aldrich) was added and the contents of the PFA jar were stirred for 2 h under ambient conditions until the solution was homogeneous. The solution was then placed in a 45 mL Teflon-lined stainless-steel autoclave (Parr Instruments) and heated in a forced convection oven (Yamato DKN-402C) at 433 K and rotated at 40 rpm for 144 h. Recovered solids were washed with deionized water and mixtures of deionized water and acetone (99.999%, Sigma-Aldrich) (1:1 by mass) in alternating steps (70 g solvent (g solid)$^{-1}$ per wash) and separated by centrifugation until the pH of the supernatant liquid was constant, then dried for 24 h at 373 K in stagnant ambient air. Organic SDAs were removed by treatment under flowing dry air (1.67 cm^3 s^{-1} g$_{cat}^{-1}$, 99.999% UHP, Indiana Oxygen) at 853 K (0.0167 K s^{-1}) for 10 h.

2.3.2 Preparation of monovalent and divalent cation-exchanged CHA zeolites

Aqueous-phase ion-exchange procedures were performed as reported by Di Iorio and Gounder [78]. Following removal of occluded organic SDAs, residual Na$^+$ cations were removed by aqueous-phase ion-exchange in a 1.0 M NH_4NO_3 solution (8.0 wt% in deionized H_2O, 100 cm^3 (g solid)$^{-1}$; 99.9 wt%, Sigma-Aldrich) for 24 h at ambient conditions. Solids were recovered via centrifugation and washed with deionized water four times (70 cm^3 (g solid)$^{-1}$), then dried at 373 K for 24 h under stagnant ambient air. NH$_4$-form samples were converted to their H-form by treatment in flowing dry air (1.67 cm^3 s^{-1} g$_{cat}^{-1}$, 99.999% UHP, Indiana Oxygen) at 773 K (0.0167 K s^{-1}) for 4 h to obtain H-form samples.

H-CHA zeolites were converted to their Co^{2+}-form by ion-exchange in aqueous $Co(NO_3)_2$ solutions (0.25 M $Co(NO_3)_2$ in deionized water, 100 cm^3 (g solid)$^{-1}$; 99 wt%, Sigma-Aldrich) for 4 h at ambient conditions under 300 rpm stirring. Samples were then washed with deionized water four times (70 cm^3 (g solid)$^{-1}$), then dried at 373 K for 24 h under stagnant ambient air. Co^{2+}-form samples were then treated in flowing dry air (1.67 cm^3 s^{-1} g$_{cat}^{-1}$, 99.999% UHP, Indiana Oxygen) at 773 K (0.0167 K s^{-1}) for 4 h.

NH$_4$-CHA zeolites were partially exchanged with Na$^+$ cations in aqueous NaCl solutions (0.01-0.15 M, 100 cm^3 (g solid)$^{-1}$; 98 wt%, Macron) for 24 h under ambient conditions. Na$^+$-exchanged samples were then washed four times in deionized water (70 cm^3 (g solid)$^{-1}$), then dried at 373 K for 24 h under stagnant ambient air. Na-H-form samples were then treated in flowing dry air (1.67 cm^3 s^{-1} g$_{cat}^{-1}$, 99.999% UHP, Indiana Oxygen) at 773 K (0.0167 K s^{-1}) for 4 h.

2.3.3 Physiochemical characterization of CHA zeolites

Crystal structures of CHA zeolites were verified after removal of organic SDAs with powder X-ray diffraction (XRD) patterns using a Rigaku SmartLab X-ray diffractometer with a Cu Kα radiation source operating at 1.76 kW. In a typical experiment, 0.01 g of CHA were loaded into a zero-background, low-dead-volume sample holder (Rigaku) and diffraction patterns were collected at a scan rate of 0.0167° s^{-1} and a step size of 0.01°.

Micropore volumes were calculated from Ar adsorption isotherms measured at 87 K with a Micromeritics ASAP 2020 surface area and porosity analyzer. CHA zeolites (0.03–0.05 g, sieved to 180–250 μm) were degassed under vacuum (5 μmHg) at 393 K for 2 h, followed by further heating to 623 K (0.167 K s^{-1}) under vacuum (<5 μmHg) for 9 h. The volumetric uptake of Ar (from 0.05–0.35 P/P_0) was used to estimate micropore volumes (cm^3 (g solid)$^{-1}$). These micropore volumes were quantitatively similar (± 10%) to those calculated from the first minimum in a semilogarthmic derivative plot of the isotherm, given by $\partial(V_{ads})/\partial(\ln(P/P_0))$ vs. $\ln(P/P_0)$.

Elemental compositions of CHA zeolites were determined with atomic absorption spectroscopy (AAS) with a PerkinElmer Model AAnalyst 300 atomic absorption spectrometer. Aqueous samples were prepared by dissolving ~0.03 g of solid in 2 g of hydrofluoric acid (48 wt%, Alfa Aesar) and allowed to sit for 24 h, then diluted in 50 g of deionized water (18.2 MΩ). ***[Caution: when working with HF acid, use appropriate personal protective equipment, ventilation, and other safety precautions].*** Absorbances were measured with radiation sources at wavelengths of 309.3 nm in a reducing acetylene/nitrous oxide flame for Al, and wavelengths of 589.0 nm and 240.7 nm for Na^+ and Co^{2+}, respectively, in an oxidizing air/acetylene flame. Elemental compositions were calculated from calibration curves obtained from absorbances measured from known standards.

The total number of Brønsted acid sites in H-CHA and Na-H-CHA zeolites was estimated with temperature-programmed desorption (TPD) after aqueous-phase ion-exchange with NH_4^+ cations. NH_4-form (or Na-NH_4-form) samples (0.02–0.05 g, sieved to 180–250 μm) were loaded into a U-shaped quartz reactor and supported with quartz wool, then placed in a clam-shell furnace in a Micromeritics AutoChem II 2920 Chemisorption analyzer equipped with an Agilent 5973N mass-selective detector. Samples were heated to 873 K (0.167 K s^{-1}) under flowing He (15 cm^3 s^{-1} (g solid)$^{-1}$), and effluent mixtures were sent to the mass-selective detector for quantification. Calibration and deconvolution methods were performed according to previous methods [129] to quantify the number of NH_3 molecules desorbed from zeolite samples.

2.3.4 Infrared spectra of OH stretching features in H-CHA and Na-H-CHA zeolites

H-CHA and Na-H-CHA zeolites were pressed into self-supporting wafers (0.02–0.04 g cm^{-1}) and sealed within a custom-built quartz IR cell with CaF_2 windows. Details on the construction of the IR cell can be found in [130]. Zeolite wafers were treated in flowing dry air (10 cm^3 s^{-1} (g solid)$^{-1}$) purified by an FTIR purge gas generator (Parker Balston, <1 ppm CO_2) to 803 K (0.0167 K s^{-1}) for 2 h, then cooled to 748 K under flowing He (10 cm^3 s^{-1} (g solid)$^{-1}$). IR spectra were collected with a Nicolet 4700 spectrometer with a Hg-Cd-Te detector (MCT, 77 K), and 64 scans at 2 cm^{-1} resolution were averaged in the 4000-400 cm^{-1} range at temperatures of 448-748 K. Backgrounds were subtracted with IR spectra collected with an empty IR cell under flowing He.

2.3.5 Density functional theory methods

All DFT calculations were performed using the Perdew-Burke-Ernzerhof (PBE) functional [131] within the Vienna Ab-Initio Simulation Package (VASP) [132]. Core-valence interactions were modeled using the projector augmented wave method [133, 134]. Plane wave energy cutoffs were set to 800 eV for lattice constant optimizations, and 400 eV for all other calculations. The self-consistent field electronic calculations were considered converged when the energy change between iterations was less than 1×10^{-6} eV, and geometry optimizations continued until the maximum force on any atom was less than 0.01 eV/Å. A 36 T-site CHA supercell was obtained from the Database of Zeolite Structures [135]. The purely siliceous lattice constants were optimized by allowing ions, lattice shape, and lattice size to update. All subsequent calculations were done using the optimized lattice constants. Harmonic vibrational frequencies were computing using density functional perturbation theory [136]. Structure input files and modifications were made within the Atomic Simulation Environment [137].

2.3.6 Monomolecular propane cracking kinetic measurements

H-CHA or Na-H-CHA zeolites (0.02–0.10 g, sieved to 180–250 μm) were loaded into a quartz reactor (7 mm inner diameter) and supported between two plugs of quartz wool (Acros Orgnaics). Reactor temperatures were controlled with a resistively-heated three-zone furnace (Applied Test Systems Series 3210) and Watlow controllers (EZ-Zone series), and catalyst temperatures were measured with a Type K thermocouple at the external surface of the quartz reactor tube placed at the middle of the catalyst bed. Samples were treated in a stream of flowing O_2 (5 kPa O_2 with balance He, 99.999% UHP, Indiana Oxygen) or H_2 (99.999% UHP, Indiana Oxygen) at 803 K for 2 h (0.0167 K s^{-1}), then cooled to 748 K in flowing He (99.999% UHP, Indiana Oxygen) and held for 0.5 h to remove O_2 or H_2 from transfer lines. Propane (10 kPa, 5 kPa Ar, balance He, Indiana Oxygen) was diluted in He to pressures of 0.6–2.2 kPa and sent to the reactor at site-times of 10-300 s (mol H^+) (mol C_3H_8)$^{-1}$. Reactant and product gas-phase concentrations were measured with a gas chromatograph (HP 6890 Series) equipped with a flame ionization detector and a GS-Alumina KCl capillary column (0.53 mm inner diameter, Agilent). Propane conversions were held below 1% to mitigate secondary bimolecular reactions of product alkenes. Ethene and methane were formed in equimolar quantities (1.0 ± 0.1), as expected for protolytic propane cracking on Brønsted acid protons. Apparent activation enegies and entropies were calculated from normalized propane cracking rates (per H^+) at 718–778 K.

2.4 Results and Discussion

2.4.1 Synthesis and characterization of model CHA zeolites with varying Al and proton proximity

CHA zeolites of similar bulk composition (Si/Al $\sim$ 15), but varying framework Al arrangements, were synthesized according to procedures reported by Di Iorio and Gounder [78]. Physiochemical properties of the zeolite samples studied here are summarized in Table 2.1, and XRD patterns (Figure 2.16, Section 2.6.1) and micropore volumes (0.16-0.22 cm^3 g^{-1}) measured from Ar adsorption isotherms (87 K, Figure 2.17) were consistent with the CHA topology. Al heteroatoms were predominantly incorporated into tetrahedral lattice positions, evidenced by Brønsted acid sites quantified by NH_4^+ titration and subsequent NH_3 temperature programmed desorption (TPD) that are present in near unity ratios to the total Al content measured by atomic absorbance spectroscopy (H^+/Al = 0.75-1.02, Table 2.1). Titration of proximal framework Al heteroatoms by Co^{2+} cations was evidenced by Langmuirian Co^{2+} ion-exchange isotherms, the exchange of two protons per Co^{2+} as quantified by the selective titration of residual H^+ sites on Co-zeolites by NH_3 using titration and TPD procedures, and the absence of Co-oxides in UV-Visible spectra of dehydrated Co-CHA samples [78]. In CHA zeolites, bare divalent Co^{2+} and Cu^{2+} cations charge-compensate similar numbers of proximal Al sites [78], and most effectively stabilize anionic $AlO_{4/2}^-$ pairs in configurations that allow these cations to adopt four-fold coordination with lattice O atoms in a 6-MR while being less stable at other Al configurations by at least 0.5 eV [117]. Therefore, Co^{2+} titration in CHA zeolites reflects energetically-favorable Al-Al configurations that do not violate Lowenstein's rule, corresponding to two Al heteroatoms in the same 6-MR separated by one or two Si atoms (i.e., 6-MR paired Al) [78].

Table 2.1.: Physiochemical properties of H-zeolites.

Zeolite	Si/Al[a]	H^+/Al[b]	2×Co/Al[c]	Micropore volume[d] (/ $cm^3 g^{-1}$)
CHA (14.5, 0%)	14.5	0.75	0.00	0.19
CHA (16.0, 0%)	16.0	0.98	0.00	0.20
CHA (17.5, 0%)	17.5	0.99	0.00	0.21
CHA (15.5, 8%)	15.5	0.96	0.08	0.19
CHA (15.5, 13%)	15.5	0.90	0.13	0.17
CHA (14.8, 18%)	14.8	0.99	0.18	0.22
CHA (13.8, 20%)	13.8	1.02	0.20	0.20
CHA (16.2, 24%)	16.2	0.76	0.24	0.17
CHA (15.0, 44%)	15.0	0.81	0.44	0.16
CHA (26.1, 0%)	26.1	0.97	0.00	0.22

[a] Determined by atomic absorption spectroscopy. Errors are ±10%.
[b] Determined by NH_3 temperature-programmed desorption. Errors are ±10%.
[c] Determined by atomic absorption spectroscopy. Errors are ±10%.
[d] Calculated from Ar adsorption isotherms (87 K). Errors are ±0.02 cm^3 g^{-1}.

CHA zeolites crystallized from solutions containing $TMAda^+$ as the sole SDA contained predominantly isolated Al and are unable to charge-compensate divalent Co^{2+} cations (Table 2.1). When a fraction of $TMAda^+$ cations in synthesis solutions were replaced with Na^+ as an inorganic co-SDA, the percentage of Al in paired configurations increased from 0% to 18%, as the Na^+/$TMAda^+$ ratio in synthesis solutions increased from zero to unity, consistent with previous experimental results that proposed the occlusion of Na^+ nearby quarternary N^+ centers in $TMAda^+$ cations so as to retain enthalpically favorable contacts between the hydrophobic adamantly group and siloxane portions of the framework [78]. Substitution of $Al(OH)_3$ with Al(*O*-*i*-*Pr*)$_3$ as the Al precursor in mixtures containing $Na^+/TMAda^+ = 1$ crystallized a CHA sample with a higher percentage of Al in paired configurations to 44% (Table 2.1), in agreement to previous reports of CHA synthesis [79]. While the cause of this difference remains a topic of ongoing investigation, it is reminiscent of differences in Al proximity among MFI zeolites synthesized from various Si and Al precursors [77].

These CHA zeolites, of fixed Al content but systematically varying Al arrangement, constitute a suite of model catalysts to decouple the effects of Al substitution in crystallographically-distinct positions and of the relative proximity of these Al substitutions, because the CHA topology contains only one unique T-site. Co^{2+} titration methods provide information about isolated and paired arrangements of framework Al, which are only structural surrogates for Brønsted acid active sites [116]. Therefore, we measure and analyze IR spectra of the OH stretching region to directly probe the arrangement of proton active sites that are relevant for Brønsted acid catalysis.

2.4.2 Experimental IR spectroscopic characterization of isolated and proximal protons in CHA zeolites

IR spectra of asymmetric OH stretching vibrations in H-CHA zeolites show two main features at 3575 and 3600 cm^{-1} (Figure 2.1), which have previously been assigned to protons occupying two different lattice O atoms that orient OH groups towards the 6-MR and 8-MR windows of CHA, respectively, as identified from Rietveld refinement of neutron diffraction data collected at 5 K [138]. The relative ratios of these two components are not the same among CHA samples of similar bulk composition (Si/Al $\sim$ 15) but varying Al arrangement, evident by the feature at 3600 cm^{-1} that becomes more prominent with increasing 6-MR paired Al content (Figure 2.1). Furthermore, these IR spectra are normalized to the integrated area of lattice Si-O-Si overtone and combination modes and by the number of protons counted by NH_3 TPD, and thus reflect a similar number of OH oscillators, yet the integrated area for bridging OH stretches increases systematically with the fraction of paired Al (Figure 2.1 inset).

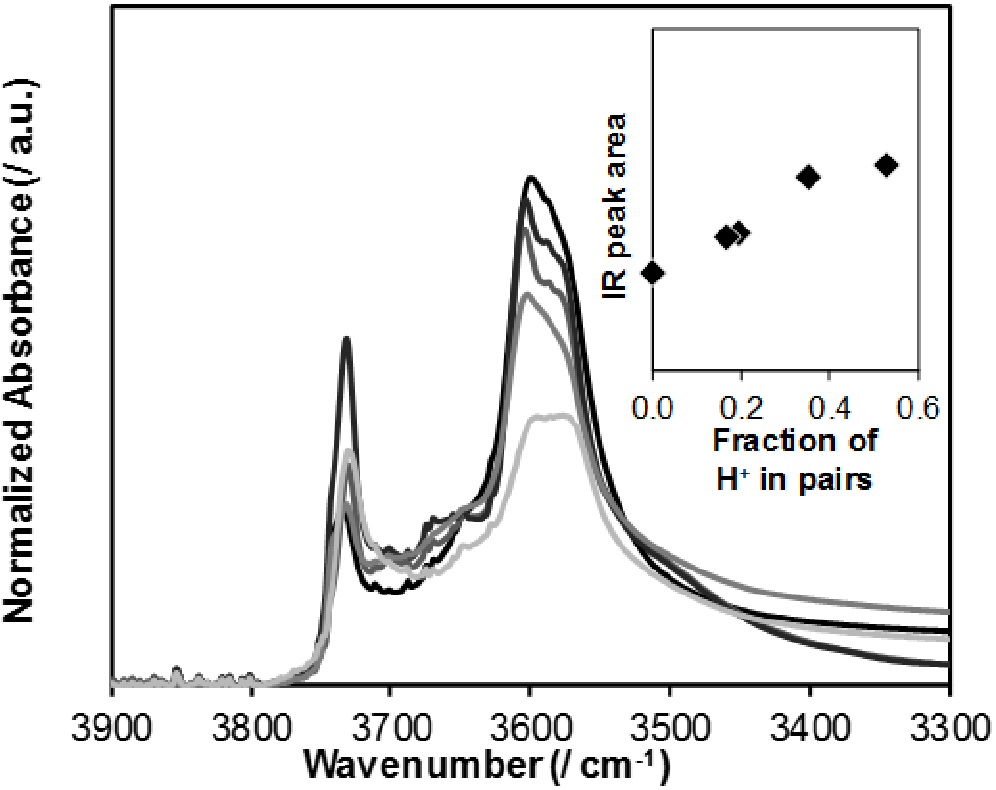

Figure 2.1.: Normalized IR spectra (415 K, He) of H-CHA zeolites of fixed Al content (Si/Al = 15) with different percentages of Al in pairs (0%, 18%, 24%, 30%, and 44%, from light to dark). Inset shows normalized OH stretching region peak area as a function of H$^+$ in pairs.

Among H-CHA zeolites containing predominantly isolated Al atoms, IR features and intensities in the OH stretching region are essentially invariant with temperature (448-748 K, Figure 2.2a), and integrated OH peak areas are also independent of temperature (Figure 2.3). In contrast, among H-CHA zeolites containing finite fractions of 6-MR paired Al (18% paired Al in Figure 2.2b; 44% paired Al in Figure 2.2c), IR features and intensities vary reversibly with temperature (448-748 K), and integrated OH peak areas decrease systematically with increasing temperature (Figure 2.3). Such reversible changes with temperature in integrated OH absorbance have been reported in prior work for FAU, MFI, MOR, and CHA zeolites [97–99,139], and interpreted to reflect the delocalization of protons from anionic lattice oxygens near framework Al that would result in the disappearance of O-H vibrations. Yet, this interpretation contradicts the temperature insensitivity of OH stretching vibrations in H-CHA zeolites containing predominantly 6-MR isolated Al (Figure 2.2a).

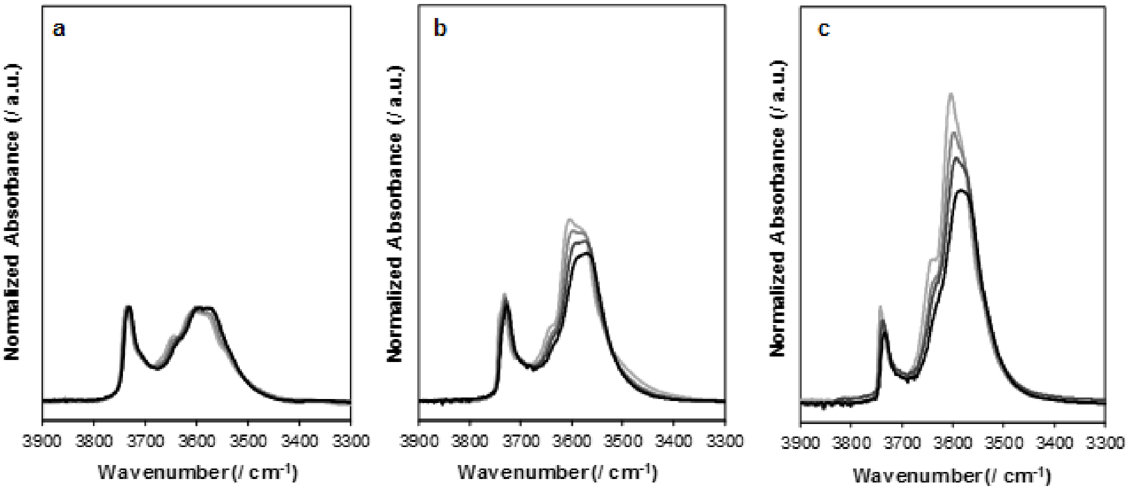

Figure 2.2.: IR spectra of (a) H-CHA (16.0, 0%), (b) H-CHA (14.8, 18%), and (c) H-CHA (15.0, 44%) as a function of temperature (448 K, 548 K, 648 K, 748 K; light-to-dark).

Experimentally-measured IR spectra reflect ensemble-averaged configurations of protons distributed among the four lattice O atoms associated with each $AlO_{4/2}^{-}$ tetrahedra, as hopping of protons among these O atoms is equilibrated even at ambient temperatures [112, 116]. Thus, the OH structures identified from neutron diffraction experiments performed at 5 K [138] are likely different than the distribution of OH structures detected in IR spectra at ambient temperatures and above, and perhaps different still from the OH distributions that prevail under catalytically-relevant conditions. As a result, the experimental observations in Figures 2.1-2.3 motivate new questions regarding the influence of framework Al proximity on proton configurations in CHA zeolites. First, why does the integrated absorbance (per H^+ group) in the Brønsted acidic OH stretching regions increase with Al proximity? Second, why do the two features in Brønsted acidic OH stretching regions change in relative intensity with Al proximity? Third, why are OH stretching features for protons compensating

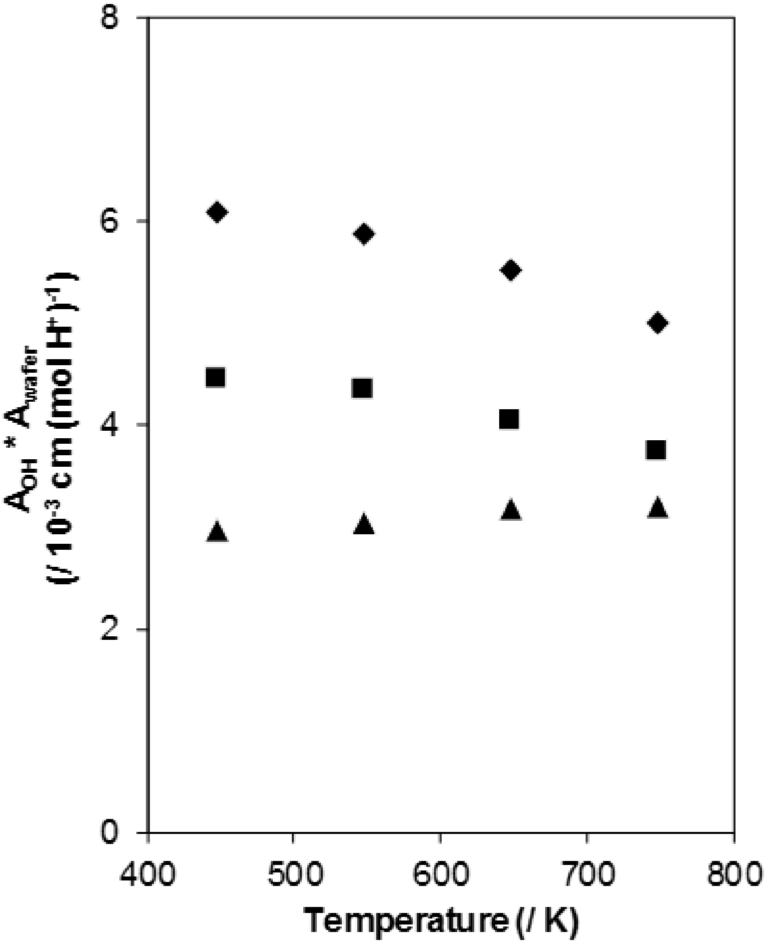

Figure 2.3.: Normalized OH stretching region absorbances on H-CHA (16.0, 0%) (▲), (b) H-CHA (14.8, 18%) (■), and (c) H-CHA (15.0, 44%) (◆) as a function of temperature.

isolated Al invariant with temperature, while those for protons compensating paired Al observed to decrease with increasing temperature? In order to answer these questions, we next use DFT methods to enumerate the different proton configurations that charge-compensate isolated and paired Al in CHA and predict their IR spectra.

2.4.3 Theoretical assessment of IR spectral features of isolated and proximal protons in CHA

Full details of the CHA structural models can be found in Table 2.6 (Section 2.6.2). Although CHA contains only one crystallographically-unique T-site, charge-compensating Brønsted acid protons can be located at four distinct lattice O atoms vicinal to each Al heteroatom. Each O atoms is associated with three different rings, which are comprised of 4, 6, or 8 T-atoms. The nomenclature used to refer to each unique OH configuration is a three-number code reflecting the number of T-atoms in these three rings (644, 844, 864, 884). Isolated proton structures previously reported by our group [117] were relaxed with optimized lattice constants, and Figure 2.4 shows the most stable configurations for protons at each of these O atoms. These four minimum energy configurations are nearly isoenergetic (within 0.1 eV, Table 2.2), in quantitative agreement with previous reports for protons at isolated Al atoms in CHA [117,140,141]. Minimum energy configurations for each O atom reflect positioning of the proton within the largest available ring (either a 6- or 8-MR), and rotation of the proton between different void environments at a given O atom results in energetic penalties resulting from additional lattice strain. Therefore, we conclude that the four proton structures in Figure 2.4 represent the most sampled configurations for isolated protons in CHA zeolites.

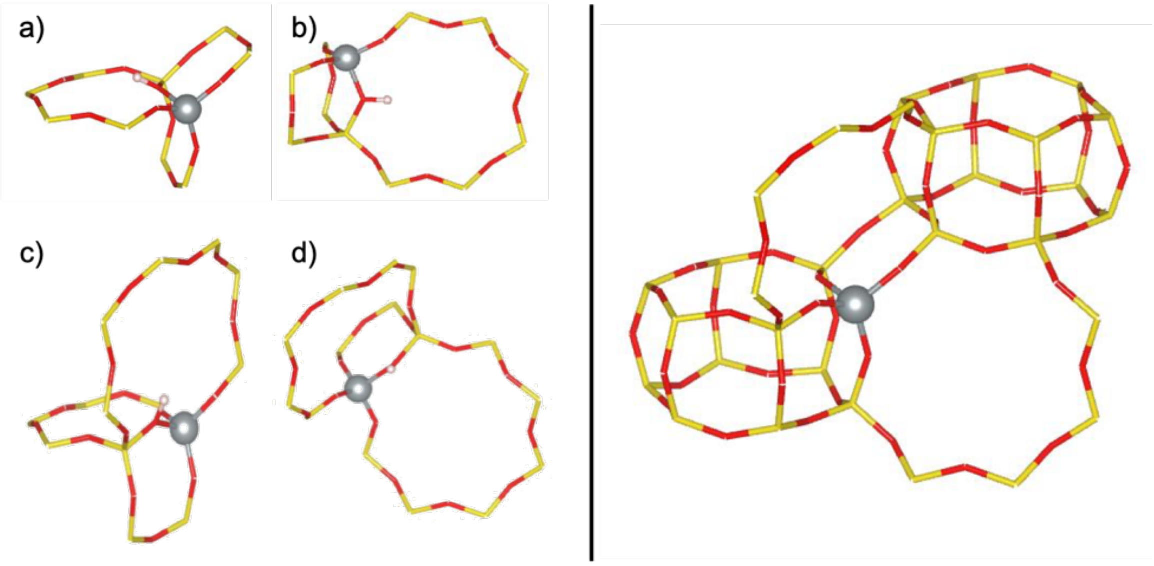

Figure 2.4.: Energy-minimized structures of protons charge-compensating isolated Al in CHA at the four crystallographically-unique O atoms; (a) 644; (b) 844; (c) 864; (d) 884 (left). Placement of the isolated Al in the CHA framework (right).

Table 2.2.: Energies, vibrational frequencies, and infrared intensities of OH sites at isolated Al atoms.

Proton Location	Relative Energy (/ eV)	O-H IR Frequency (/ cm^{-1})	O-H IR Intensity (/ a.u.)
644	0.030	3581	0.192
844	0.000	3606	0.217
864	0.023	3583	0.230
884	0.065	3589	0.189

Using these energies, the Boltzmann-weighted occupancy of the proton at each of these four O atoms is calculated as a function of temperature, assuming proton hopping is equilibrated [112, 116]. These relative occupancies are plotted in Figure 2.5 (calculation details in Section 2.6.3). The total number of protons in any 8-MR environment is also shown as a function of temperature in Figure 2.5, calculated from the sum of the relative occupancy of protons at 844, 864, and 884 sites. Given that that each OH group preferentially occupies the largest available ring among the three rings it is contained within, macroscopically observed differences in proton siting among 6-MR and 8-MR locations reflect the identity of the O atom associated with the proton, and not the occupation of different rings by a proton at a given O atom.

Each of the four proton configurations do not change in relative population by more than 10% across the temperature range studied (448-748 K). Moreover, the total number of protons in an 8-MR is also similar with increasing temperature in this range, because the decrease in the population of 844 sites is compensated for by an increase in the population of 884 sites. Other computational measurements of proton energies among distinct O atoms in CHA showed quantitatively similar differences in relative energies (<10 kJ mol^{-1}) and proton occupancies that vary by ~20% over a similar temperature range (300-800 K) [142]. Therefore, we conclude that the sampling of protons among the four lattice O atoms is insensitive to temperature because of the nearly isoenergetic energies of proton siting at these distinct configurations.

IR spectra were simulated for minimum-energy structures of isolated protons by calculating their vibrational frequencies and dipole moment derivatives to determine IR peak centers and intensity, respectively (computational details in Section 2.6.3). There are two distinct computational IR features that differ by 24 cm^{-1}, in agreement with previously simulated IR for CHA [142], and the experimental results for H-CHA zeolites (Figure 2.2) [138]. Calculated and adjusted vibrational modes are listed in Table 2.7 (Section 2.6.3). Figure 2.6 shows the simulated IR spectra for protons at each of the four O sites, and their Boltzmann-weighted average at 448 K. The vibrational feature at ~3600 cm^{-1} in the simulated spectrum predominantly

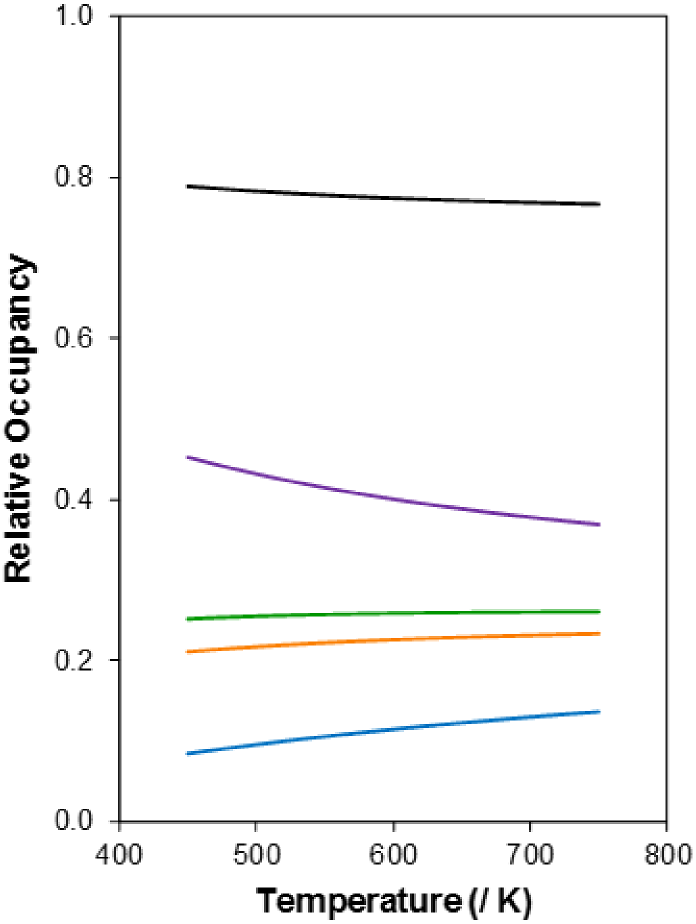

Figure 2.5.: Relative occupancy of protons at crystallographically-distinct O atoms at isolated Al atoms in CHA. 644 (orange), 844 (purple), 864 (green), 884 (light blue), and sum of 844, 864, and 884 configurations (black).

reflects protons at the 844 O site, while the feature at ~3580 cm^{-1} reflects contributions from protons at the other three O sites (644, 864, 884) that correspond to proton location in both 6-MR and 8-MR environments. This observation contradicts previous assignments for features at 3600 cm^{-1} and 3575 cm^{-1} to reflect protons occupying 8-MR and 6-MR environments of CHA, respectively, from neutron diffraction data collected at 5 K that may constrain protons to occupy a different distribution than at ambient temperatures. The composite spectrum generated from adding the four principal component features for each O site results in two IR peak centers at

$\sim$3600 and 3580 cm^{-1} with approximately equal intensity, similar to that observed in experimental IR spectra of protons in H-CHA zeolites containing isolated Al sites (Figure 2.2a). Additionally, because the population of protons among the four O sites only changes by less than 10% from 448-748 K (Figure 2.5), simulated IR spectra do not vary significantly with temperature (Figure 2.18, Section 2.6.3), even though the principal components for each O site has a distinct vibrational frequency and dipole moment derivative. Therefore, we conclude that experimental IR spectra of protons compensating isolated Al in H-CHA zeolites (Figure 2.2a) are insensitive to temperature because the equilibrium distribution of protons does not vary significantly with temperature.

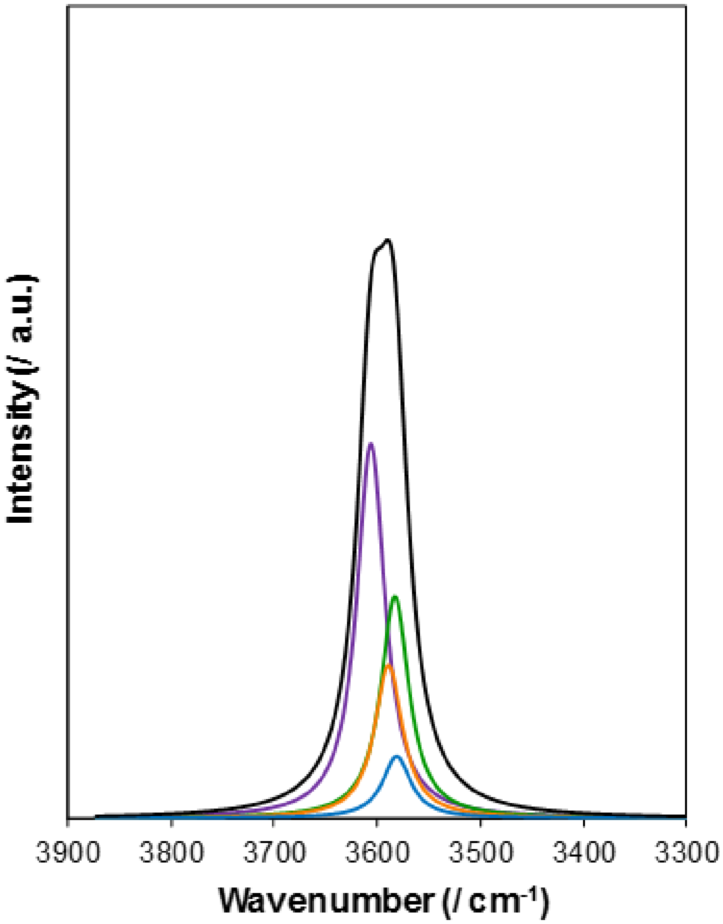

Figure 2.6.: Simulated IR spectra for protons at O atoms in CHA at 448 K. 644 (orange), 844 (purple), 864 (green), 884 (light blue), and summation of these contributions (black).

We next compute the energies of protons that charge-compensate paired Al arrangements. While divalent Co^{2+} cations selectively titrate Al ensembles within the same 6-MR separated by one or two Si atoms [117], ^{29}Si MAS NMR data have previously suggested that the latter is the predominant configuration of paired Al in CHA zeolites (Si/Al $\sim$ 15) synthesized with mixtures of $TMAda^+$ and Na^+ [78]. Therefore, we use a model with two Al heteroatoms in the same 6-MR separated by two Si atoms as a prototype for a 6-MR paired Al arrangement. Within this arrangement, there are sixteen possible configurations for proton occupancy, and ten of these configurations are unique due to symmetry across the 6-MR. The energies of these configurations are given in Figure 2.7.

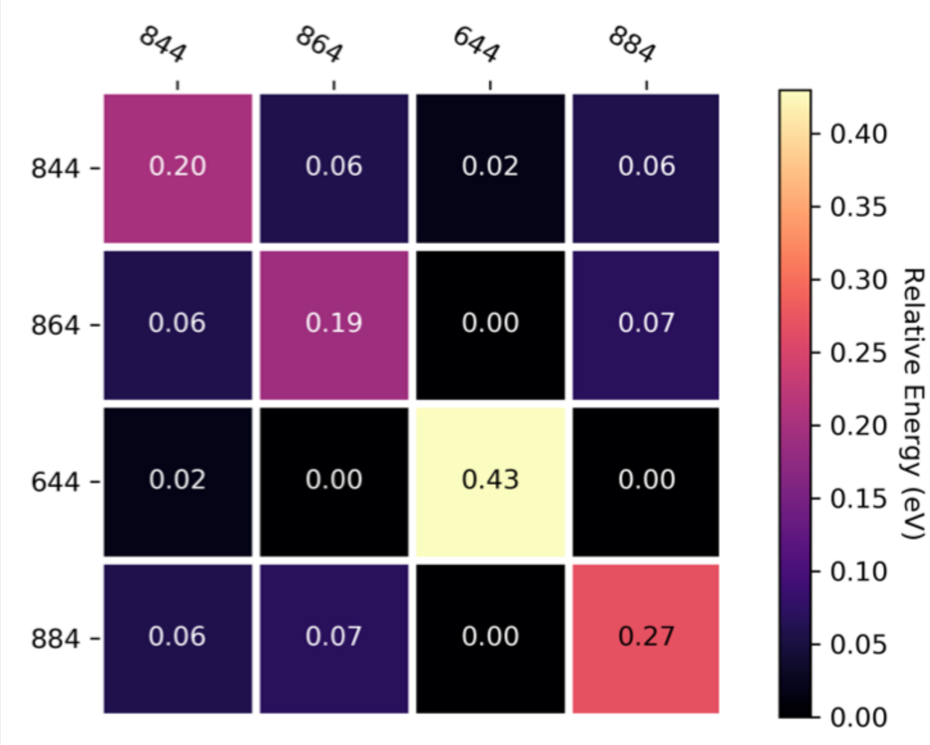

	844	864	644	884
844	0.20	0.06	0.02	0.06
864	0.06	0.19	0.00	0.07
644	0.02	0.00	0.43	0.00
884	0.06	0.07	0.00	0.27

Figure 2.7.: Matrix of proton configuration energies for paired Al in CHA. Rows represent position of one proton and columns represent position of the second proton.

In contrast to the four distinct configurations for isolated protons, these ten distinct configurations for proximal protons differ in energy by 0.4 eV, resembling results reported by Li and co-workers for protons charge-compensating different paired Al configurations [117]. Protons serve to screen electrostatic repulsion between anionic framework Al centers, resulting in a net electrostatic attraction between $AlO_{4/2}^{-}$-H^{+} pairs that are formally neutral. Therefore, the energy of each configuration reflects the ability of the two protons to electrostatically stabilize anionic Al-Al pairs. The most favorable proton configurations for this paired Al arrangement contain one proton at the 644 O site, and the second proton at one of the O sites containing an 8-MR (844, 864, 884). Higher-energy configurations reflect situations in which both protons are located in 8-MR environments, particularly at crystallographically-identical O atoms, and the least stable configuration is the only one that places both protons in the same ring, reflecting the most severe electrostatic repulsion experienced when protons occupy the same void. Energetic differences among paired proton configurations become less severe at longer Al-Al distances, and only differ by ∼15 kJ mol^{-1} at Al-Al pairs separated by three Si atoms in 8-MR (Figure 2.19, Section 2.6.4), similar to the relative energies of isolated proton configurations (Table 2.2). Using the energies in Figure 2.7, the relative occupancy of protons at the four O atoms at this paired Al configuration can be calculated as a function of temperature by a Boltzmann-weighted average and is shown in Figure 2.8. A larger fraction of protons occupy the 644 O site at paired configurations than in isolated configurations (∼40% and ∼20%, respectively) as a consequence of the stability conferred by proximal Al heteroatoms when one proton points across the 6-MR. The relative occupancy of protons among each 8-MR void is ∼20% and insensitive to temperature due to tradeoffs between lower and higher-energy states that populate at different temperatures.

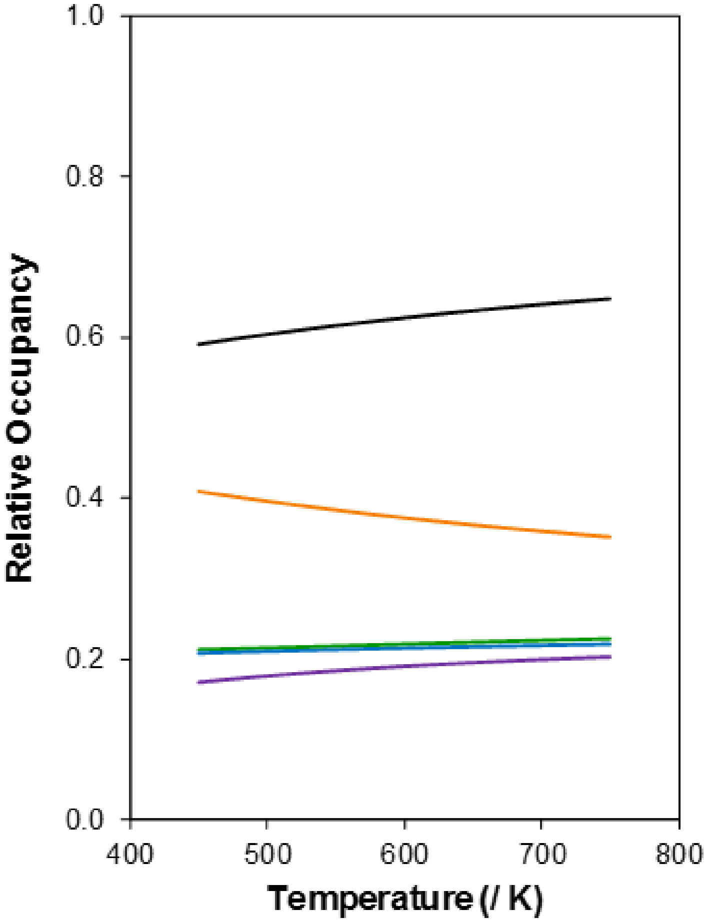

Figure 2.8.: Relative occupancy of protons at crystallographically-distinct O atoms at isolated Al atoms in CHA. 644 (orange), 844 (purple), 864 (green), 884 (light blue), and sum of 844, 864, and 884 configurations (black).

Simulated IR spectra for paired proton configurations as a function of temperature (448-748 K) are shown in Figure 2.9. Proton configurations that are higher in energy have lower dipole moment first derivatives, on average (Figure 2.20, Section 2.6.4). Therefore, the intensity of asymmetric OH stretching features in IR spectra decrease systematically with increasing temperature as these configurations are increasingly sampled and are recovered at lower temperatures when protons relax to lower-energy configurations, consistent with experimental spectra shown in Figures 2.2b and 2.2c for H-CHA zeolites with 18% and 44% of Al in pairs, respectively. Simulated IR spectra for protons at Al-Al pairs in the same 8-MR are less sensitive to temperature (Figure 2.21, 2.6.4), because of the more similar energy landscape of their proton-proton configurations. We conclude that proton distributions among the four O atoms in $AlO_{4/2}^{-}$ tetrahedra depends on the local arrangement of framework Al heteroatoms, because the energies of two proton and two Al site configurations depend on the ability of protons to screen electrostatic repulsion between proximal anionic Al centers without incurring proton-proton electrostatic repulsion. The energetic biasing of certain proton configurations imparted by paired framework Al arrangements in CHA results in experimentally observed OH IR spectra that are sensitive to temperature, because the principal components for each proton configurations differ in their dipole moment derivatives and have different intrinsic peak intensities.

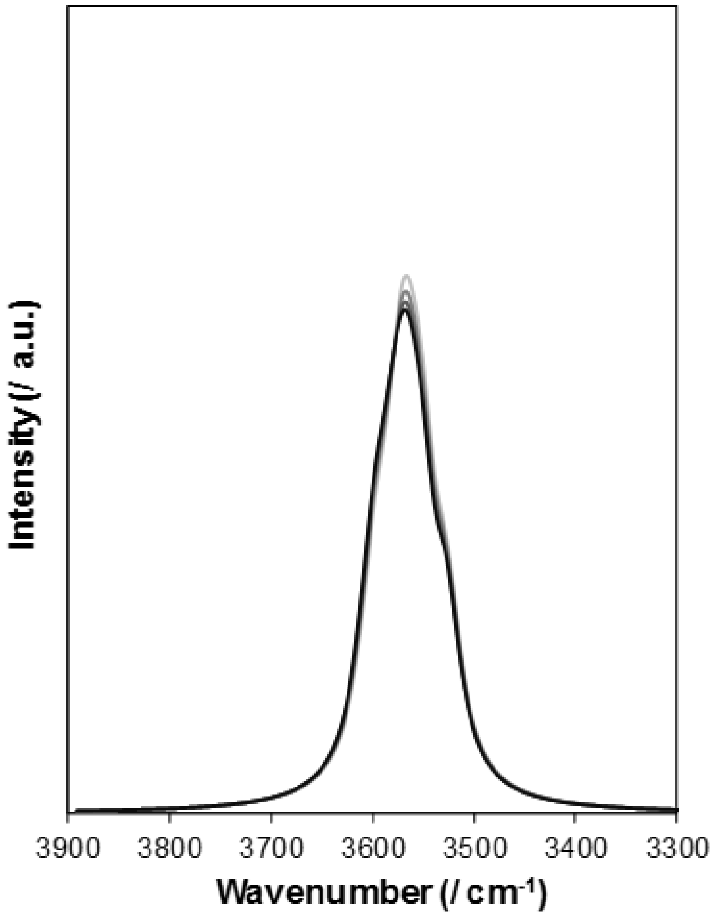

Figure 2.9.: Simulated IR spectra of paired protons in CHA as a function of temperature (448, 548, 648, 748 K; light-to-dark).

Reversible decreases in molar absorptivity in the OH stretching region have been observed on FAU, MOR, MFI and CHA zeolites with increasing temperature [97–99], and collectively attributed to the delocalization of Brønsted acid protons from the lattice under these conditions (373-773 K). However, these observations contradict those here for isolated protons in CHA, whose IR spectra are insensitive to temperature (Figure 2.2a), which is likely a result of the similar energies of protons occupying the four lattice O atoms in isolated $AlO_{4/2}^-$ tetrahedra. However, we note that not all isolated protons in different frameworks meet this criterion. Jones and Iglesia [140] have reported deprotonation energies (DPE) for isolated protons at crystallographically-distinct Al and O atoms in several zeolite frameworks (MFI, beta, MOR, FER, CHA, and FAU), which reflect the difference in gaseous protons and deprotonated lattice O sites, relative to the protonated lattice. Differences in DPE among different OH groups at a given Al T-site thus reflect differences in OH stability, given rigorous cancellation of energies of gaseous protons and of the deprotonated lattice, for which anionic charges delocalized among lattice Si and O atoms in the second and third coordination shell around the Al site [33]. Protons at isolated Al sites in CHA and FAU zeolites, which share a common double 6-MR building unit with one crystallographically-unique T-site are nearly isoenergetic (within 10 kJ mol^{-1}) (Figure 2.10), while protons at isolated Al in other topologies (e.g., MFI, MOR, FER, and beta) differ in energy by up to 42, 42, 24, and 32 kJ mol^{-1}, respectively, depending on the location of the Al site (Figure 2.10) [140]. Thus, energetic differences among configurations of isolated protons in these other zeolite frameworks may be responsible for observed temperature dependences in OH stretching regions in IR spectra [97–99], because the principal component spectra for each OH site need not be identical.

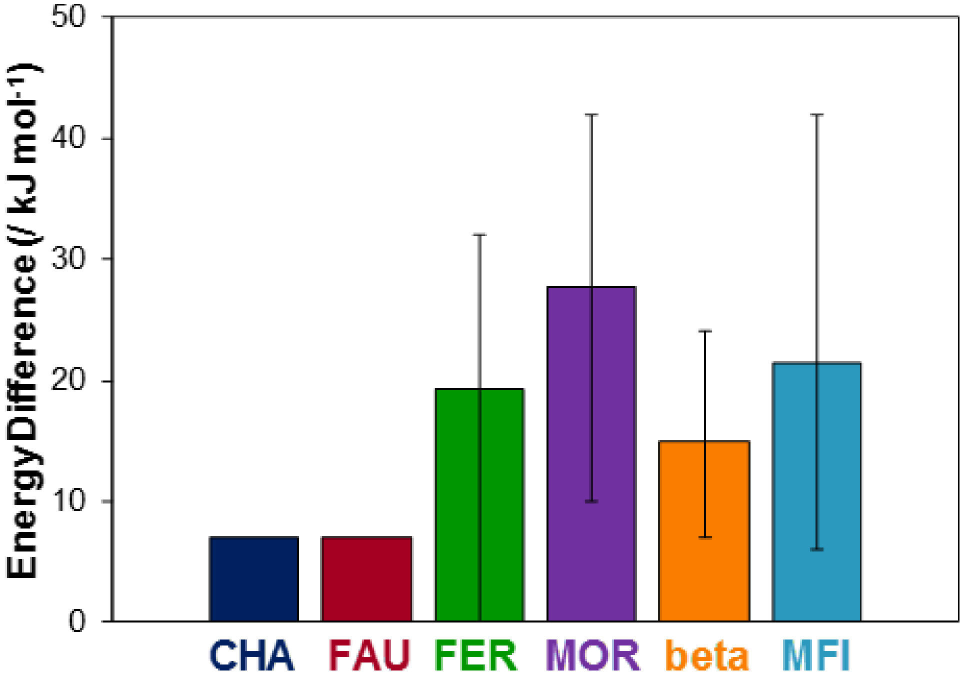

Figure 2.10.: Relative energies of Brønsted acid protons among crystallographically-distinct O atoms in isolated $AlO_{4/2}^{-}$ tetrahedra in H-form zeolites. Bars represent the arithmetic mean energy difference between protons occupying different lattice O atoms in isolated Al tetrahedra, and error bars represent the minimum and maximum energy difference among crystallographically-distinct T-sites. Adapted from [140].

2.4.4 Distribution of protons in Na-H-CHA zeolites

Protons in H-CHA zeolites were partially replaced with Na^+ cations through ion-exchange protocols, and the number of residual protons counted by NH_3 TPD are shown in Table 2.3. Figures 2.11a and 2.11b show IR spectra for CHA zeolites with 18% and 44% Al in 6-MR pairs, respectively, and ~50% of their protons exchanged with Na^+ cations. Normalized absorptivity in the asymmetric OH stretching region decreased reversibly with increasing temperature (448-748 K), as observed in H-CHA zeolites containing a finite fraction of Al pairs (Figures 2.2b and 2.2c).

Table 2.3.: Fraction of Brønsted acid protons in Na-H-CHA zeolites relative to H-form samples.

Zeolite	H^+/H^+_{parent}
$Na_{47}H_{53}CHA$ (14.5, 0%)	0.53
$Na_{59}H_{41}CHA$ (14.5, 0%)	0.41
$Na_{49}H_{51}CHA$ (14.8, 18%)	0.51
$Na_{36}H_{64}CHA$ (15.0, 44%)	0.64
$Na_{55}H_{45}CHA$ (15.0, 44%)	0.45
$Na_{69}H_{31}CHA$ (15.0, 44%)	0.31

[a] Measured by NH_3 TPD. Errors are ±10%.

These observations suggest that the set of Na^+-H^+ cation ensembles that compensate paired Al sites show similar energetic and dipole moment derivative differences as observed among H^+-H^+ pairs. Twelve stable Na^+-H^+ configurations were identified with periodic DFT methods, and the Na^+ cation occupies one of three locations within these site pairs: the 6-MR (Figure 2.12a), or two different 8-MR voids (Figures 2.12b and 2.12c). Of these twelve configurations, the Na^+ cation is in the 6-MR in the two most stable configurations, leaving the proton to reside in an 8-MR (Figure 2.22, Section 2.6.5), suggesting that larger Na^+ cations preferentially occupy smaller voids in Na-H-CHA zeolites. Energies of these twelve configurations differed by ~0.5 eV, quantitatively consistent with those observed for H^+-H^+ pairs. Finally, simulated

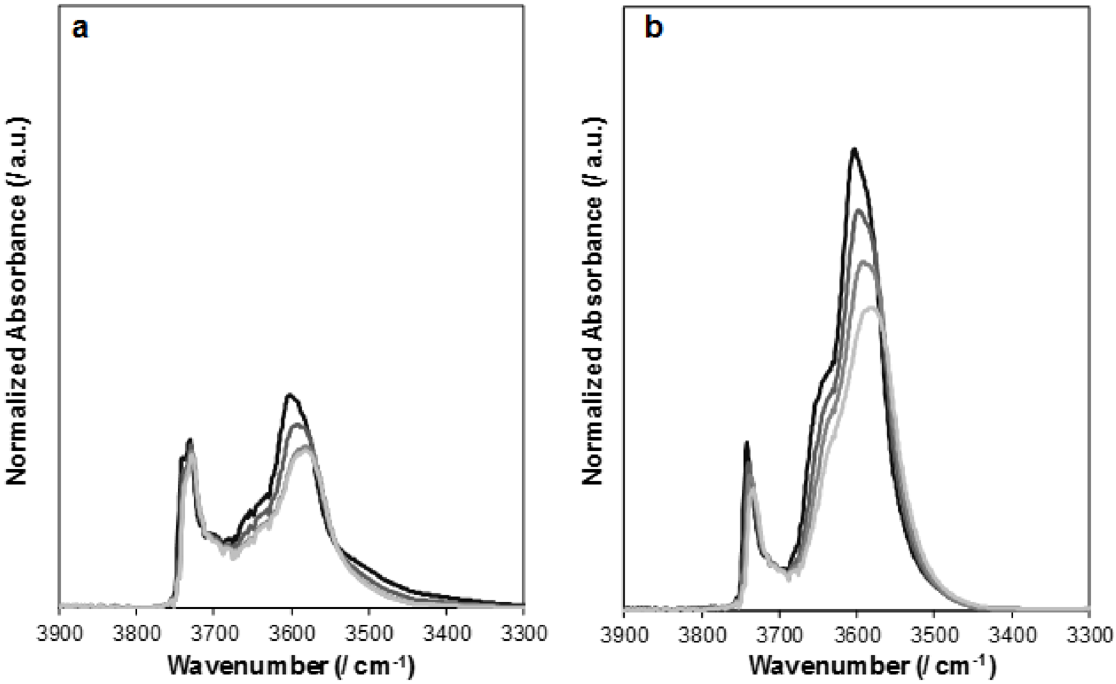

Figure 2.11.: Normalized IR spectra of Na-H-CHA zeolites at 448-748 K in 100 K intervals from dark to light. (a) 18% Al in pairs, $H^+/H^+_{parent} = 0.51$; (b) 44% Al in pairs, $H^+/H^+_{parent} = 0.45$.

IR spectra decrease in molar absorptivity with increasing temperature (Figure 2.13), because configurations with lower dipole moment first derivates have higher energies and are increasingly sampled.

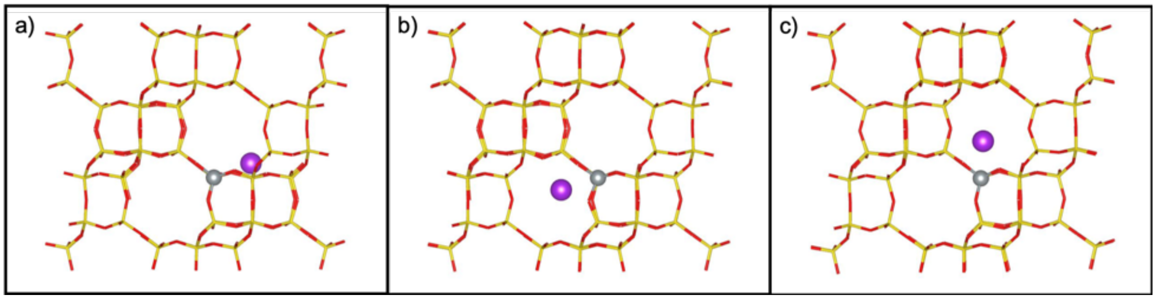

Figure 2.12.: Na^+-H^+ cations charge-compensating paired Al sites with the Na^+ cation in the (a) 6-MR, (b) 8-MR, (c) and 8-MR voids.

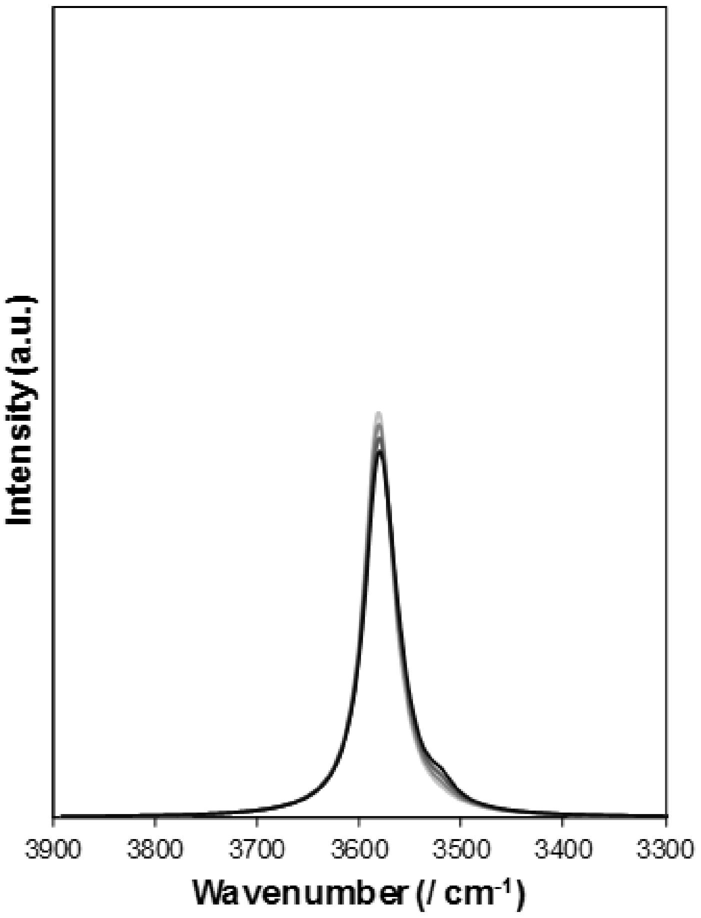

Figure 2.13.: Simulated IR spectra of Na$^+$-H$^+$ sites at Al pairs in CHA zeolites at 448, 548, 648, and 748 K, from light-to-dark.

Similar IR experiments were performed by Schoonheydt and Uytterhoeven, who measured IR spectra on H-FAU, and on Na-H-FAU zeolites with approximately equimolar ratios of H$^+$ and Na$^+$ cations [97]. Asymmetric OH stretching features at $\sim$3550 cm^{-1} and $\sim$3650 cm^{-1}, corresponding to protons occupying sodalite cages and supercages, respectively, decreased reversibly in H-FAU with increasing temperature, similar to observations here on H-CHA zeolites containing 6-MR Al pairs (Figures 2.2b and 2.2c). With replacement of $\sim$50% of H$^+$ for Na$^+$, the 3550 cm^{-1} feature was no longer observed, and the 3650 cm^{-1} feature became insensitive to temperature in Na-H-FAU [97]. This observation suggests that Na$^+$ cations preferentially occupied the smaller available voids in FAU zeolites, and similar conclusions have been made in MOR zeolites by Bhan and co-workers who used IR spectroscopy of MOR zeolites with adsorbed n-hexane to show that Na^+ cations preferentially exchange with protons in 8-MR voids over larger 12-MR channels [48]. Here, we estimate a $\sim$10 kJ mol^{-1} preference for Na^+ cations residing in 6-MR of CHA (Section 2.6.5), consistent with these previous conclusions that larger Na^+ cations are preferentially stabilized by van der Waals interactions with lattice O atoms over smaller H^+ cations. We conclude that asymmetric OH stretching vibrations of Na-H-CHA zeolites have similar temperature sensitivity to H-CHA zeolites due to systematically lower dipole moment first-derivatives of higher-energy configurations, and that the siting of Na^+-H^+ pairs in CHA zeolites is influenced by the preference of larger Na^+ cations to reside in smaller voids. Next, we use monomolecular propane cracking as a probe reaction that renders Brønsted acid protons predominantly uncovered during catalysis, reflecting conditions used for IR spectroscopy and DFT experiments.

2.4.5 Kinetic assessments of isolated and paired protons in CHA zeolites using monomolecular propane cracking

Table 2.4 shows apparent first-order rate constants (per H^+, 748 K) for monomolecular propane cracking on H-CHA zeolites (Si/Al $\sim$ 15), along with apparent activation energies and entropies calculated from the temperature dependence of these rates. Propane cracking rates (per H^+, 718-778 K) increased linearly with reactant propane pressure (Figure 2.23, Section 2.6.6), consistent with H^+ sites that are unoccupied during catalysis. Propane cracking rate constants were insensitive to reactant site-time (Figure 2.24, Section 2.6.6), ethene and methane were formed in equimolar quantities (1.0 ± 0.10), and no products larger than C_3 were observed. Therefore, monomolecular alkane activation pathways at Brønsted acid protons in CHA zeolites prevail under the conditions studied here, and the transition state formalisms described here can be used to interpret rate data [143].

Table 2.4.: Monomolecular propane cracking rate constants (748 K, per H^+), apparent activation energies, and apparent activation entropies on H-CHA zeolites.

Zeolite	k^a_{app}	E^b_{app}	ΔS^c_{app}
H-CHA (14.5, 0%)	0.4	164	-99
H-CHA (16.0, 0%)	0.3	159	-106
H-CHA (17.5, 0%)	0.4	156	-110
H-CHA (15.5, 8%)	1.0	167	-86
H-CHA (15.5, 13%)	0.8	153	-107
H-CHA (14.8, 18%)	1.1	159	-97
H-CHA (13.8, 20%)	1.7	171	-77
H-CHA (16.2, 24%)	1.2	169	-82
H-CHA (15.0, 44%)	2.5	166	-80
H-CHA (26.1, 0%)	0.3	154	-114

[a] Units are 10^{-3} mol (mol H^+)$^{-1}$ s^{-1} (bar C_3H_8)$^{-1}$. Error is ±15%.
[b] Units are kJ mol^{-1}. Error is ±8 kJ mol^{-1}.
[c] Units are J mol^{-1} K^{-1}. Error is ±9 J mol^{-1} K^{-1}.

Monomolecular propane cracking rates differ by a factor of ~8 among H-CHA zeolites of similar bulk Al (and H^+) densities, suggesting that not all Brønsted acid protons are equally reactive. Normalized rate constants and turnover frequencies reflect Gibbs free energy differences between the ion pair transition state relative to a vacant proton and the gas-phase alkane (derivations in Section 2.6.6). Apparent activation energies and entropies are therefore given by:

$$E_{app} = E_{int} + \Delta H_{ads} \tag{2.1}$$

$$\Delta S_{app} = \Delta S_{int} + \Delta S_{ads} \tag{2.2}$$

Apparent activation entropies are calculated from pre-exponential factors, calculated from apparent rate constants (per H^+):

$$k_{app} = A_{app} exp(-\frac{E_{app}}{k_b T}) \tag{2.3}$$

$$\Delta S_{app} = R(ln(A_{app}) - ln(\frac{k_bT}{h})) \tag{2.4}$$

Propane cracking rates (per H^+, 748 K) increased systematically with the fraction of Al in 6-MR pairs quantified by Co^{2+} ion-exchange on CHA zeolites of similar composition (Si/Al ∼ 15, Figure 2.14). Four independent samples that contain predominantly 6-MR isolated Al sites had similar apparent rate constants ($k_{app,iso}$ = 0.4×10^{-3} mol (mol H^+)$^{-1}$ s^{-1} (bar C_3H_8)$^{-1}$, Table 2.4), providing evidence that a similar distribution of active sites exist between these samples and that internal mass transfer limitations did not influence propane cracking rates. Assuming observed rates can be described by a linear combination of reactions at isolated and paired sites, an apparent rate constant for propane cracking at paired protons can be estimated by:

$$r = k_{app,iso}X_{iso} + k_{app,pair}X_{pair} \tag{2.5}$$

In Eq. 2.5, X_{iso} and X_{pair} are the fraction of protons in isolated and paired configurations, respectively. This model is represented by the solid line in Figure 2.14, and the estimated apparent rate constant for monomolecular propane cracking at paired protons is 5.1×10^{-3} mol (mol H^+)$^{-1}$ s^{-1} (bar C_3H_8)$^{-1}$, approximately 12 times higher than that for isolated protons. The influence of Al proximity on catalysis could be to compensate protons that are biased to more reactive configurations (e.g., 6- or 8-MR), but not to directly influence the free energy of the transition state, or to provide a proton that directly stabilizes the carbonium ion or the conjugate base. At 748 K, the relative occupancy of protons at any of the four crystallographically-distinct O atoms in CHA differ by only ∼2× between 6-MR isolated and paired Al configurations (Figs. 2.5 and 2.8, Section 2.4.3), which does not account for the order-of-magnitude difference in monomolecular propane cracking. Therefore, we surmise that the proximal proton serves to stabilize the carbonium ion transition state because the ∼12× increase in propane cracking rate at paired Al ensembles is larger than the ∼2× difference in proton occupancy.

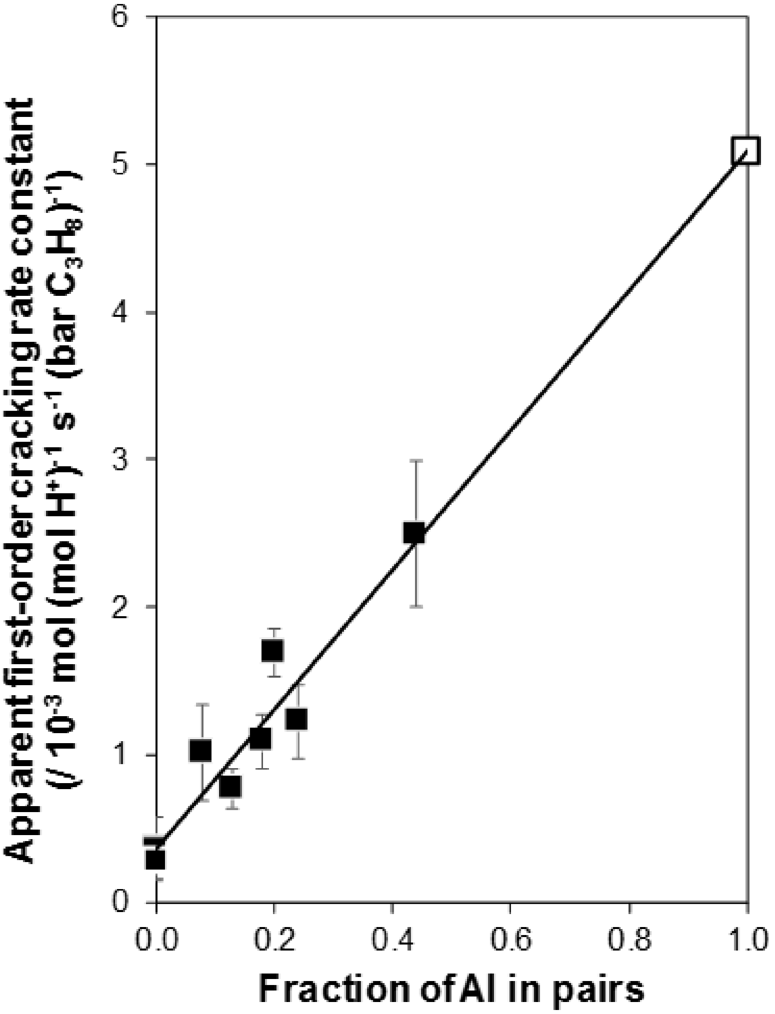

Figure 2.14.: Monomolecular propane cracking rates (748 K, per H^+) on H-CHA zeolites as a function of the fraction of Al in 6-MR pairs quantified by Co^{2+} ion-exchange. Open symbol represents estimated first-order rate constant for propane cracking at paired protons.

Several other adsorption and catalytic phenomena have been reported to be sensitive to proton proximity (e.g., propene oligomerization in MFI [71,72], water adsorption in MFI [144], acetone adsorption in MFI [73]), although MFI zeolites contain a distribution of Al in distinct T-sites that may also influence rate measurements. In CHA zeolites, similar analyses to those used here showed that methanol dehydration to DME was faster in first-order and zero-order kinetic regimes on paired protons in

CHA zeolites (per H^+, 415 K, 0.1-22 kPa CH_3OH). Surface methoxy intermediates were proposed to be stabilized under these conditions by paired Al ensembles, as evidenced by surface methoxy deformation modes present in in situ IR spectra of H-CHA zeolites containing 6-MR Al pairs but not for those with predominantly 6-MR isolated Al sites, potentially providing a lower free energy path for methanol dehydration with a ~10× increase in rate [79]. The low coverage of Brønsted acid sites by reactants and intermediates during monomolecular propane cracking precludes the use of spectroscopic probes of surface intermediates here, so we next consider the enthalpic and entropic contributions to carbonium ion free energies at these sites in CHA and relate these to hypothetical pathways in Born-Haber thermochemical cycles for monomolecular alkane activation.

Propane cracking apparent activation energies did not vary systematically with the fraction of Al in 6-MR pairs and have an arithmetic mean value of 162 kJ mol^{-1} (Figure 2.25a, Section 2.6.6), consistent with previous reports of monomolecular propane cracking on FAU [101], MFI [49, 101], and beta zeolites [102]. Born-Haber thermochemical cycles have been used to interpret apparent activation energies of acid catalyzed-reactions in zeolites [145] including monomolecular alkane activation [49], where measured energetic barriers are related to a series of hypothetical steps required to reach the transition state. One such hypothetical path involves deprotonation of the zeolite lattice and separation of the proton to non-interacting distances, followed by protonation of the gas-phase alkane to form the carbonium ion, and finally solvation of the transition state in the zeolite near the anionic $AlO_{4/2}^-$ tetrahedron. Energies associated with these three steps appear in the right-hand side of Eq. 2.6.

$$E_{app} = DPE + PA + E_{stab} \tag{2.6}$$

The proton affinity (PA) of a C-C bond in propane is a gas-phase property and thus does not depend on the siting of Al heteroatoms or charge-compensating protons. Ensemble-averaged deprotonation energies (DPE) calculated for isolated protons in zeolites (e.g., CHA, FAU, MFI, MOR, FER, and beta) using periodic DFT methods are similar, despite differences in Al-O-Si bond angles and OH vibrational frequencies within and between zeolite topologies that are commonly used to infer differences in acid strength in zeolites [140]. Sierka and co-workers found using embedded cluster models that DPEs of protons at Al heteroatoms in FAU separated by one Si atom are greater than those separated by two or more Si atoms [146]. More recently, Nystrom and co-workers showed that a proton charge-compensating an Al heteroatom stabilizes a deprotonated $AlO_{4/2}^{-}$ tetrahedron across a 6-MR or 8-MR of CHA, leading to ensemble-averaged DPEs that are lower at these proximal Al ensembles than for isolated Al [141]. Because protons are predominantly unoccupied during monomolecular propane cracking, we surmise that this ionic stabilization may influence the stability of the transition state when the lattice is deprotonated at paired Al sites. Ionic interactions between the carbonium ion and anionic lattice contribute to E_{stab}, and a fraction of the energy required for deprotonation is recovered in this interaction, attenuating differences in DPE that are manifested in apparent activation energies [147]. Due to the cationic nature of the transition state (+0.9e [148]), differences in DPE that may exist from the ability of a proximal proton to stabilize the conjugate base may be experimentally indistinguishable. Therefore, we cannot assess differences in DPE between isolated and paired protons from these data, because the energy penalty of deprotonation is partially recovered by the conjugate base via ion-pair interactions with the localized charge in the carbonium ion.

Apparent activation entropies were similar for propane cracking on H-CHA zeolites with predominantly 6-MR isolated Al (-114 – -99 J mol^{-1} K^{-1}) and became systematically less negative with increasing fractions of 6-MR paired Al (Table 2.4; Figure 2.25b, Section 2.6.6). Using the estimated rate constant for propane cracking at paired protons (5.1×10^{-3} mol (mol H^+)$^{-1}$ s^{-1} (bar C_3H_8)$^{-1}$) and the mean activation energy (162 kJ mol^{-1}), an apparent activation entropy of -79 J mol^{-1} K^{-1} was calculated for propane cracking at paired protons, which is ~25 J mol^{-1} K^{-1} less negative than that for isolated protons. These differences in measured activation entropies, and similarities in activation energies, are similar to those reported for

n-butane cracking on MFI zeolites with increasing bulk Al density [73], which was surmised to arise from a carbonium ion that was more product-like in the presence of a nearby proton.

Differences in monomolecular alkane activation rates on MOR [49] and MFI [100] zeolites have been interpreted on the basis of siting of Al heteroatoms and protons in microporous voids of varying size and geometry, because the van der Waals contacts between organic guests and lattice O atoms mediate enthalpy-entropy tradeoffs in transition state free energies [53]. In the case of MOR, carbonium ions that are partially confined in 8-MR side pockets suffer from weaker dispersive stabilization from lattice O atoms than those in 12-MR channels but benefit from entropic gains from increased retention of gas-phase entropy for the late transition state. As a result, monomolecular propane and n-butane cracking and dehydrogenation occur predominantly at protons in smaller 8-MR side pockets of MOR. Several studies have reported that n-butane cracking and dehydrogenation rates (per H^+, 753 K [73], 773 K [100]) increase systematically with bulk Al density in MFI zeolites, containing 10-MR straight and sinusoidal channels that are ~0.55 nm in diameter that intersect to form larger ~0.70 nm voids. Janda and Bell [100] attributed this to the preferential siting of Al in MFI intersections at higher Al densities, as inferred from deconvolution of d-d charge transfer bands in UV-visible spectra of Co^{2+}-form MFI zeolites collected following dehydration protocols [149]. Activation energies were similar on samples with increasing Al densities while apparent activation entropies were systematically less negative, consistent with the siting of carbonium ions in less-confined voids.

These arguments regarding isolated Al and proton siting in crystallographically-distinct environments cannot be extrapolated to CHA zeolites, because CHA contains only one unique T-site for Al substitution. While isolated Al heteroatoms are crystallographically identical in CHA zeolites, paired Al heteroatoms are structurally distinct from isolated Al sites. DFT calculations have shown that charge-compensating protons in paired Al ensembles in CHA serve to screen electrostatic repulsion of nearby $AlO_{4/2}^-$ tetrahedra, an in certain cases stabilize paired Al ensembles relative to isolated Al [117]. We have also presented evidence that local Al configurations in CHA influence the equilibrium distribution of Brønsted acid protons among the four O atoms vicinal to Al (Sections 2.4.2 and 2.4.3), but by a factor of ~2 that is less than the ten-fold increase in propane cracking rates at paired Al sites. Therefore, we conclude that proximal proton sites stabilize later carbonium ion-like transition states relevant for monomolecular propane cracking, as previously inferred from data on lower-symmetry MFI frameworks [73]. Next, we measure propane cracking rates on Na-H-CHA zeolites to show that the identity of the cation adjacent to Brønsted acid protons influences the stability of these carbonium ion transition states.

2.4.6 Kinetics of monomolecular propane cracking on Na-H-CHA zeolites

Heterogeneities in Brønsted acid site reactivity have been identified by titrating a fraction of protons with non-reactive Na^+ cations in cases where Na^+ preferentially titrates H^+ sites of varying reactivity. For instance, stronger dispersive interactions preferentially stabilize Na^+ in the 8-MR side pockets of MOR zeolites that confine the most reactive protons for DME carbonylation [48]. NH_4-CHA zeolites containing 0% or 44% of Al in pairs were partially-exchanged with Na^+ cations, and the number of residual protons was quantified by NH_3 TPD. Propane cracking rate constants (748 K, per H^+), and apparent activation energies and entropies, are given in Table 2.5 for Na-H-CHA zeolites.

Propane cracking rate constants on Na-H-CHA zeolites are shown in Figure 2.15 and were similar on Na-H-CHA (14.5, 0%) as protons were replaced with Na^+ (0.3–0.4 $\times 10^{-3}$ mol (mol $H^+)^{-1}$ s^{-1} (bar $C_3H_8)^{-1}$). Apparent activation energies and entropies also did not vary systematically with decreasing H^+ densities (Table 2.5), suggesting that the distribution of active sites in Na-H-CHA zeolites containing predominantly 6-MR isolated Al was unaffected by the presence of Na^+. This provides evidence that isolated protons in CHA are similarly reactive for monomolecular propane cracking, or that Na^+ cations are non-selective titrants of acid sites that differ in reactivity but cannot compensate Co^{2+} cations. Propane cracking rates decreased systematically

Table 2.5.: Monomolecular propane cracking rate constants (748 K, per H^+), activation energies, and activation entropies on Na-H-CHA zeolites.

Zeolite	H^+/H^+_{parent}	k^a_{app}	E^b_{app}	ΔS^c_{app}
$Na_0H_{100}CHA$ (14.5, 0%)	1.00	0.4	164	-99
$Na_{47}H_{53}CHA$ (14.5, 0%)	0.53	0.3	159	-108
$Na_{59}H_{41}CHA$ (14.5, 0%)	0.41	0.3	162	-105
$Na_0H_{100}CHA$ (15.0, 44%)	1.00	2.5	166	-80
$Na_{36}H_{64}CHA$ (15.0, 44%)	0.64	0.5	166	-94
$Na_{55}H_{45}CHA$ (15.0, 44%)	0.45	0.5	162	-99
$Na_{69}H_{31}CHA$ (15.0, 44%)	0.31	0.3	166	-97

[a] Units are 10^{-3} mol (mol H^+)$^{-1}$ s^{-1} (bar C_3H_8)$^{-1}$. Error is ±15%.

[b] Units are kJ mol^{-1}. Error is ±8 kJ mol^{-1}.

[c] Units are J mol^{-1} K^{-1}. Error is ±9 J mol^{-1} K^{-1}.

from 2.5×10^{-3} mol (mol H^+)$^{-1}$ s^{-1} (bar C_3H_8)$^{-1}$ to 0.3×10^{-3} mol (mol H^+)$^{-1}$ s^{-1} (bar C_3H_8)$^{-1}$ on Na-H-CHA (15.0, 44%) with increasing replacement of H^+ with Na^+. Apparent activation energies were similar on this series of Na-H-CHA zeolites (162–166 kJ mol^{-1}, Table 2.5), while apparent activation entropies became ~20 J mol^{-1} K^{-1} more negative with increasing Na^+ titration. Propane cracking rates, activation energies, and activation entropies measured on $Na_{69}H_{31}CHA$ were similar to those on H-CHA zeolites containing predominantly isolated Al, providing evidence that a similar distribution of active sites exist on these samples. This finding suggests that Na^+ cations preferentially titrate paired Al ensembles in CHA zeolites, and that the stability of the carbonium ion transition state at paired Al sites is influenced by the presence of a nearby proton.

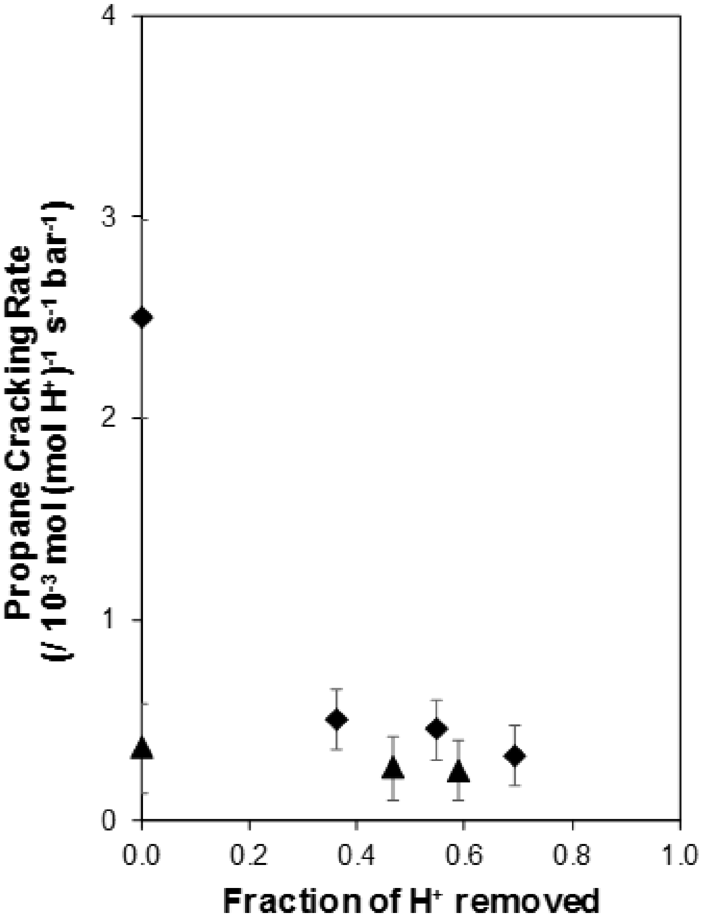

Figure 2.15.: Monomolecular propane cracking rate constants (748 K) on Na-H-CHA zeolites containing 0% Al in pairs (▲) and 44% Al in pairs (◆).

2.5 Conclusions

The equilibrium distribution of Brønsted acid protons among crystallographically-distinct O atoms in CHA zeolites depends on the local arrangement of $AlO_{4/2}^{-}$ tetrahedra. While protons that compensate isolated Al heteroatoms show similar probabilities to occupy any of the four O atoms in isolated Al tetrahedra, paired proton distributions are influenced by the energetic benefits of a Brønsted acid proton sitting in a 6-MR that contains two Al heteroatoms. These energetic consequences are observable with IR spectroscopy, because higher-energy paired proton configurations tend to have lower dipole moment first-derivates, resulting in lower molar absorptivity at higher temperatures. In contrast, the nearly isoenergetic landscape of proton configurations at isolated Al render their IR spectra insensitive to temperature, clarifying previous interpretations of decreasing intensities of OH stretching vibrations in lower-symmetry zeolite frameworks where energetic biasing is found between O atoms within a given T-site. Protolytic propane cracking rate constants (748 K, per H^+) are $\sim$10× higher on paired protons than isolated protons and likely stabilize carbonium ion-like transition states that occur later along the reaction coordinate, providing entropic benefits of $\sim$25 J mol^{-1} K^{-1} that lower activation Gibbs free energies at paired sites. These observations are consistent with previous reports on H-MFI zeolites of different bulk composition, which have been independently attributed to reflect the location [100] or proximity [73] of active sites in these lower-symmetry frameworks. Here, partial removal of H^+ sites with Na^+ cations shows that protolytic cracking rate constants decrease (per H^+) on Na-H-CHA zeolites that contain 6-MR Al pairs, suggesting that these cations preferentially titrate these more reactive sites and confirming that proximal protons to stabilize carbonium ion-like transition states. DFT calculations confirm the preferential titration of 6-MR paired Al sites by Na^+, and that residual H^+ sites at Na^+-H^+ pairs tend to reside in larger 8-MR voids. This work highlights the heterogeneities and distributions of Brønsted acid protons among crystallographically-distinct environments in zeolites, which persist even in single T-site CHA zeolites, and the role of acid site pairs in stabilizing carbonium ion-like transition states relevant for protolytic alkane activation.

2.6 Supporting Information

2.6.1 Powder X-ray diffraction patterns and adsorption isotherms of CHA zeolites

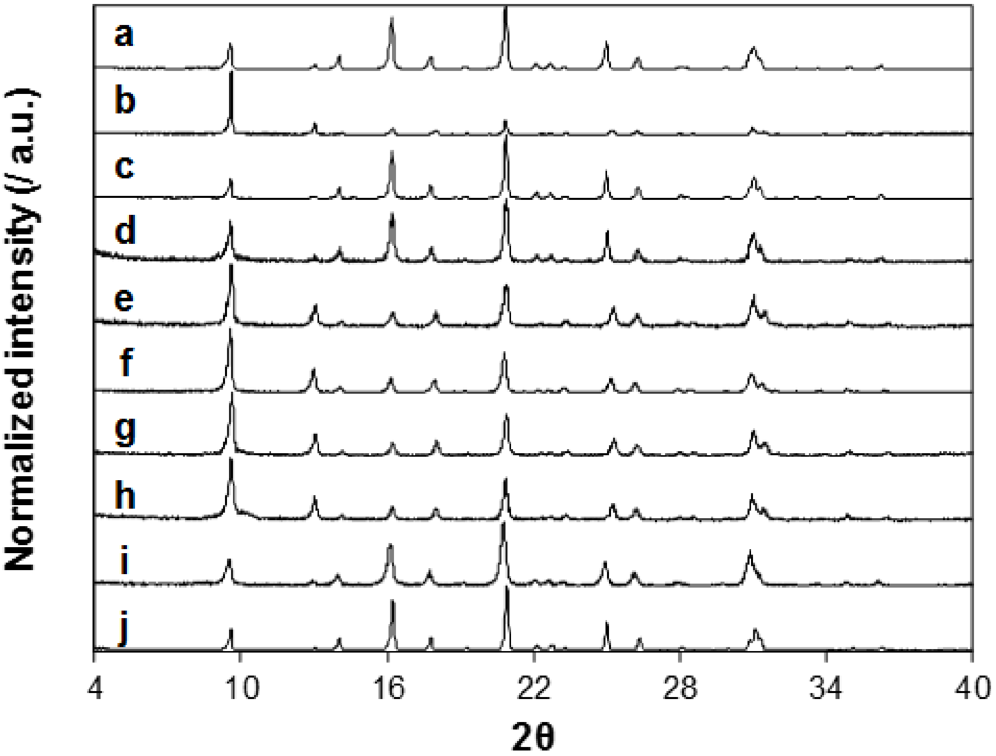

Figure 2.16.: XRD patterns of (a) CHA (14.5, 0%), (b) CHA (16.0, 0%), (c) CHA (17.5, 0%), CHA (15.5, 8%), CHA (15.5, 13%), CHA (14.8, 18%), CHA (13.8, 20%), CHA (16.2, 20%), CHA (15.0, 44%), and CHA (26.1, 0%).

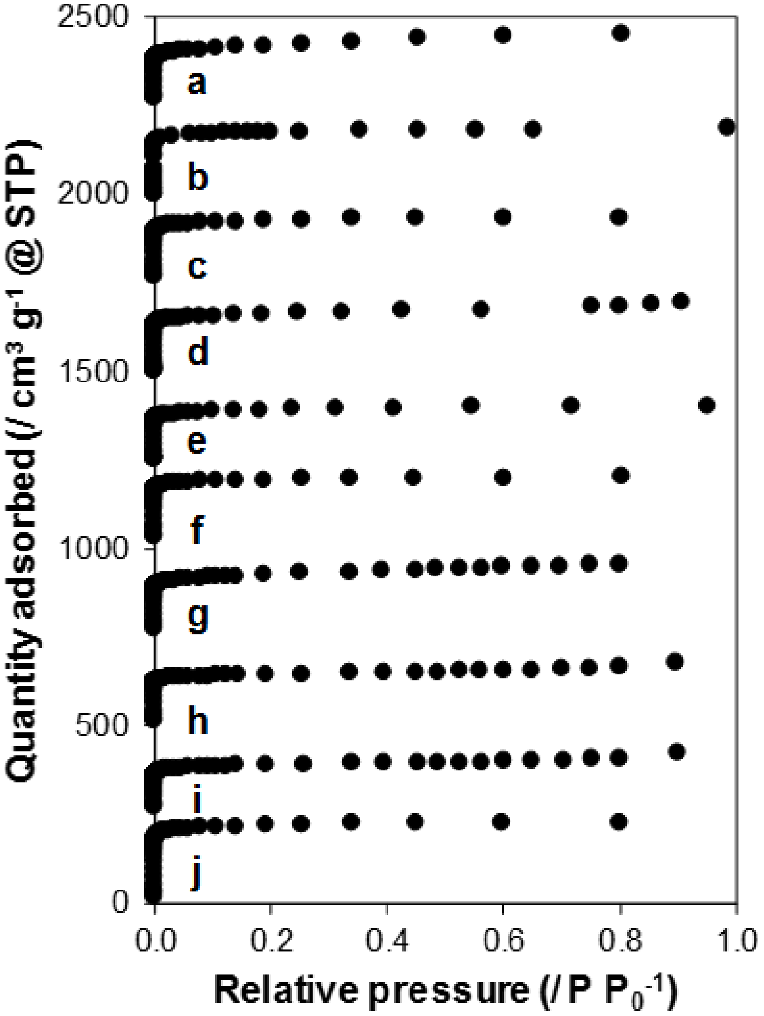

Figure 2.17.: Ar adsorption isotherms (87 K) of (a) CHA (14.5, 0%), (b) CHA (16.0, 0%), (c) CHA (17.5, 0%), CHA (15.5, 8%), CHA (15.5, 13%), CHA (14.8, 18%), CHA (13.8, 20%), CHA (16.2, 20%), CHA (15.0, 44%), and CHA (26.1, 0%). Isotherms are offset by 250 cm^3 g^{-1} for clarity.

2.6.2 DFT optimziation of CHA supercell

The purely siliceous hexagonal 36 T-site CHA unit cell was optimized using VASPs built-in optimizer, while allowing ion positions, lattice shape, and lattice volume to adjust with each iteration. This was continued until the energy change between iterations was less than 1 × 10^{-6} eV. The optimized volume was found to be 2432 Å^3. Optimized lattice constants and angles are shown in Table 2.6. These lattice constants were used for all subsequent calculations.

Table 2.6.: Optimized lattice constants and angles for the CHA supercell.

	Lattice Constant (/ Å)		Lattice Angle (/ degrees)
a	13.71	α	90
b	13.71	β	90
c	13.71	γ	120

2.6.3 Computed isolated proton energies and vibrational spectra

To generate the isolated proton structures, one Si atom was converted to an Al atom within the CHA supercell. A proton was placed at each of the four oxygens surrounding the Al, and those four structures were relaxed until the maximum force on any atom was less than 0.01 eV/Å. The Boltzmann-weighted occupancy of for the proton at each of the four O atoms was calculated with equation 2.7.

$$P_i = \frac{exp(-\frac{E_i}{k_b T})}{\sum_i exp(-\frac{E_i}{k_b T})} \tag{2.7}$$

In this expression, P_i is the probability that the proton occupies the ith O atom, E_i is the energy of the relaxed structure, and k_b is the Boltzmann constant. Vibrational analysis was performed on the optimized structures while freezing every atom in place, except for the proton and the oxygen with which it is bound, in order to reduce computational cost. Calculated vibrational frequencies are overestimated compared to experimental results in this work. In order to make quantitative comparisons, all calculated vibrational frequencies are scaled by a factor of 0.973. Intensities were calculated using equation 2.8 [150] where l is the index for a particular atom, M is the number of atoms in the simulation, e_β is the eigenvector of the vibrational mode, α,β are the Cartesian polarizations, and $Z^*_{\alpha,\beta}$ is the Born effective charge tensor. The energies, vibrational frequencies, and vibrational intensities are shown in Table 2.7.

$$I(\omega) = \sum_{\alpha=1}^{3} |\sum_{l=1}^{M} \sum_{\beta=1}^{3} Z^*_{\alpha,\beta}(l) e_\beta(l)|^2 \tag{2.8}$$

Table 2.7.: Energies, vibrational frequencies, and infrared intensities for protons at an isolated Al in the CHA framework.

Proton position	Relative Energy[a]	Vibrational Frequency[b]	Adjusted Vibrational Frequency[b]	Vibrational Intensity[c]
844	0.000	3707	3606	0.217
864	0.021	3683	3583	0.230
644	0.024	3689	3589	0.192
884	0.064	3681	3581	0.189

[a] Units are eV.
[b] Units are cm^{-1}.
[c] Arbitrary units.

Vibrational intensities were adjusted by their Boltzmann probability at a given temperature and spreading was induced with a Lorentzian distribution using a half-width of 17 cm^{-1}. The adjustments to the intensities follow Equation 2.9. This half-width value was selected arbitrarily to visually align the simulated and experimental IR spectra, and was used for all future spectra presented. This is done for each of the four isolated structures over a range of 3300-3900 cm^{-1}. Those four spectra are summed together to simulate the IR spectra for isolated protons in CHA, and are shown at different temperatures (448-748 K) in Figure 2.18.

$$I(\omega) = I_{DFT}exp(\frac{-\Delta E}{k_bT})(\frac{1}{\gamma\pi})(\frac{\gamma^2}{(w-w_0^2)^2+\gamma^2}) \tag{2.9}$$

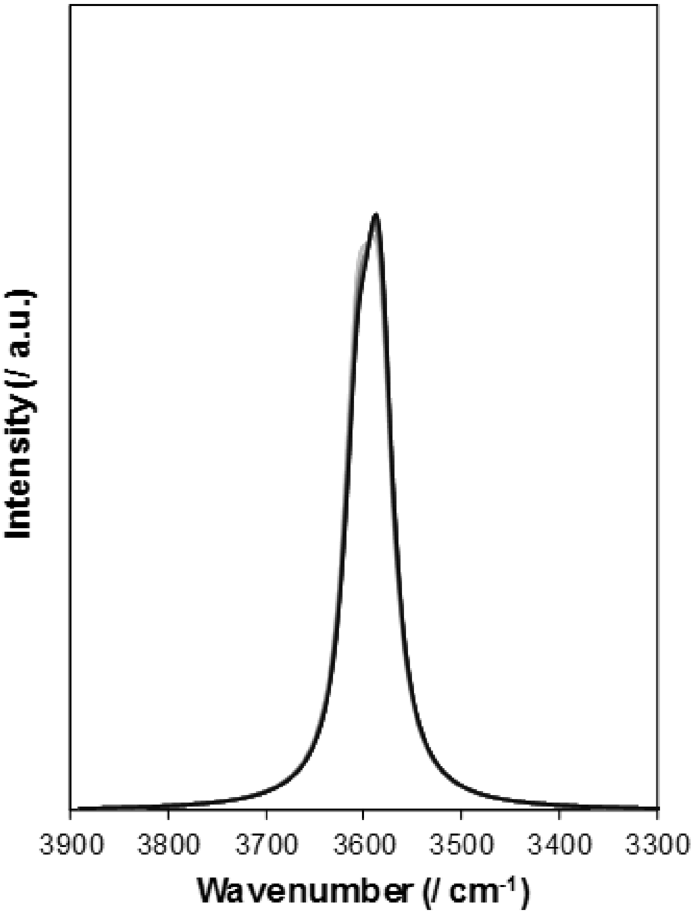

Figure 2.18.: Simulated IR spectra for isolated Al in the CHA framework at 448 K, 548 K, 648 K, and 748 K, from light-to-dark.

2.6.4 Computed proton energies and IR spectra for various Al-Al pairs in H-CHA

We considered three different types of Al-Al pairs in the CHA framework: 3NN in the 6-MR, 3NN in an 8-MR, and 4NN in an 8-MR. For each of these pairs, the proton geometry is largely unchanged from the isolated case. Protons point into the largest available ring associated with the oxygen that they are bound to. Least favorable configurations are found when the two protons point in to the same ring and repel each other to point slightly out of the plane of the ring. The relative energies for each pair type are available in Figure 2.19. The 3NN in the 6-MR is a symmetric pair, visible from the energy matrix, while the other two pairs are not. Relative energy differences decrease as the Al atoms are in larger rings and separated by more Si atoms.

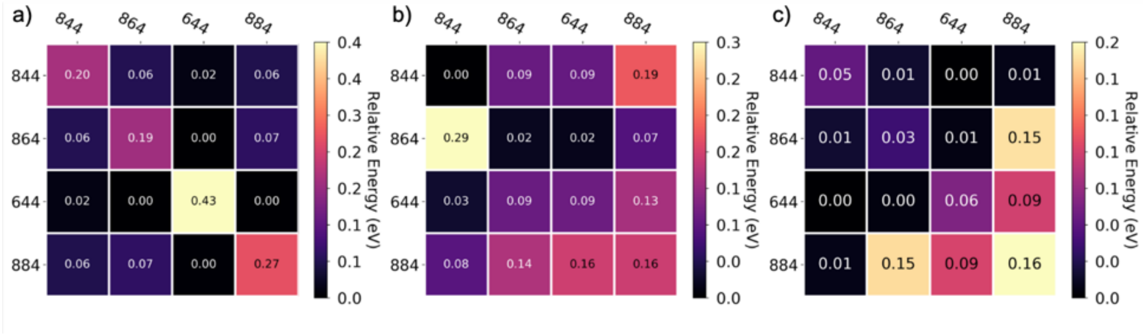

Figure 2.19.: Proton configuration relative energy for a) 3NN in the 6-MR, b) 3NN in an 8-MR, and c) 4NN in an 8-MR.

We simulated the IR spectra for the same 3 Al-Al pairs as listed in the previous section, available in Figure 2.21. These spectra are generated in the same way as the isolated case, by considering the contribution from each of the available proton configurations, and Boltzmann weighting those configurations with the relative energies listed in the previous section. In order to make quantitative comparisons, all IR spectra are normalized by the number of Al atoms in the simulation. We see that the 3NN pair in the 6-MR is the only one that has two distinct features, and is

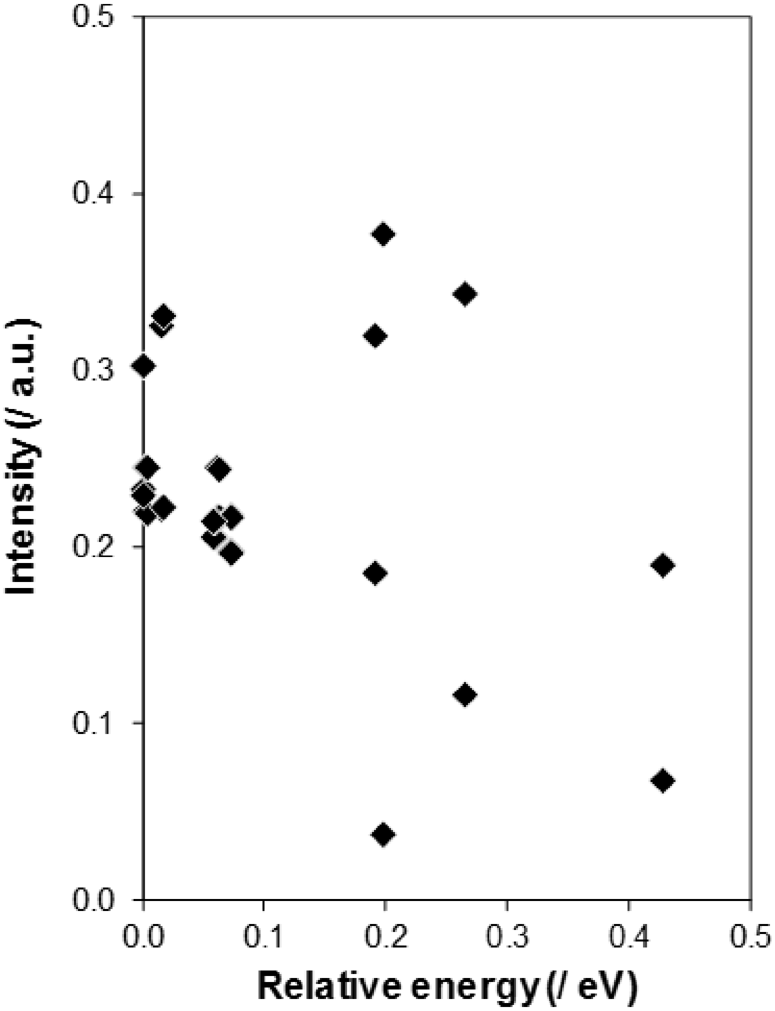

Figure 2.20.: Relative intensities of OH stretching vibrations of paired proton configurations (3NN in the 6-MR) as a function of their energy.

dependent on temperature, while Al-Al pairs found in the same 8-MR have smaller energetic differences in proton configurations and similar IR spectra at 448-748 K.

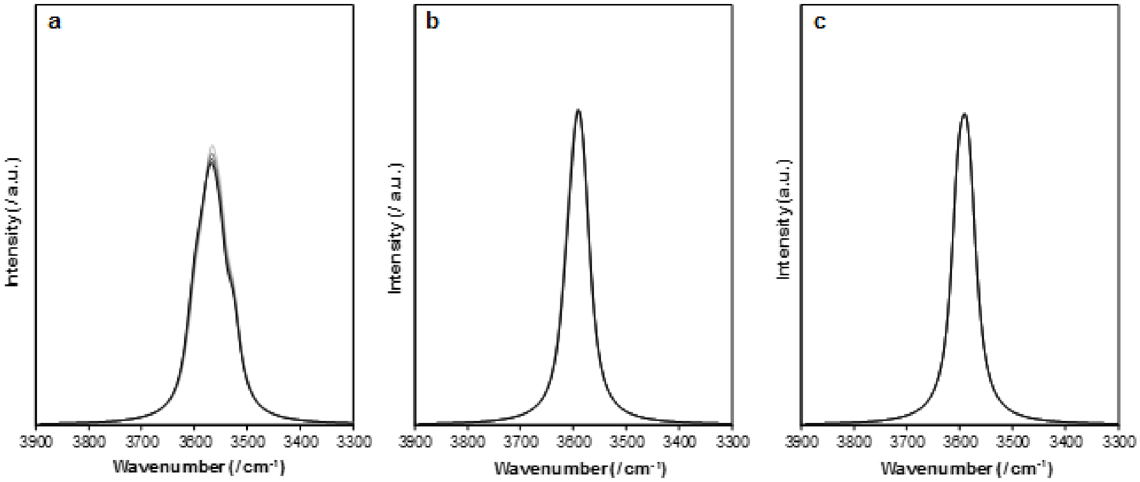

Figure 2.21.: Simulated IR spectra for a) 3NN 6-MR, b) 3NN 8-MR, and c) 4NN 8-MR at 448, 548, 648, and 748 K from light-to-dark.

2.6.5 Computed proton energies and IR spectra for Na-H-CHA

Each Al heteroatom in CHA neighbors two 8-MRs, a 6-MR, and three 4-MRs. The Na^+ cation can sit in the 6-MR (Figure 2.12a), 8-MR1 (Figure 2.12b), or 8-MR2 (Figure 2.12c), each providing three possible configurations. For an isolated Al, the Na^+ has a preference of 0.088 eV to sit in the 6-MR over the 8-MR. When modeling the Na-exchanged pairs, we found strong periodic image interactions between neighboring charges. To remedy this, the supercell was doubled in the Y direction. For the 3NN Al pair in the 6-MR, the energies are provided in Figure 2.22, the lowest energy configurations contain the Na atom is in the 6-MR, and the H atom points into an 8-MR. The highest energy configuration is when both the Na^+ and H^+ point into the 6-MR. The energies for the Na atom sitting in either of the 8-MRs in the paired case are similar.

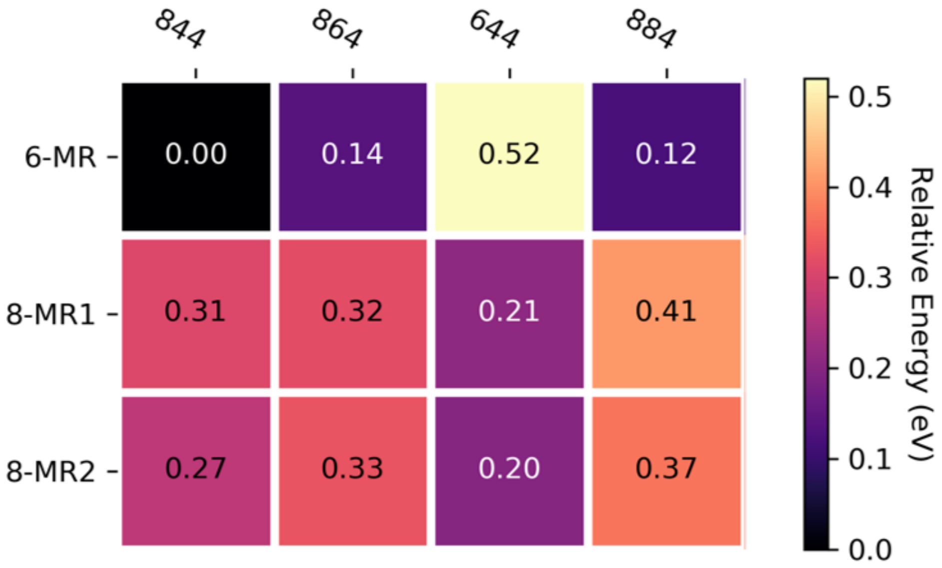

Figure 2.22.: Relative energies for the 12 unique Na^+-H^+ configurations at paired Al sites. Location specifies environment around Na^+ cation.

The ion exchange energy preference for Na^+ siting is found using the model reaction shown in Equation 2.10. For each species in the reaction, the lowest energy configuration was used. Since the paired Na calculations use supercells that have been doubled in the Y direction, the supercell for each of the other species in the reaction was also doubled in the Y direction. We find that there is a 10 kJ mol^{-1} preference for Na^{+} ions to site at a 3NN Al pair in the 6-MR compared to an isolated Al.

$$ZNa + Z_2H_2 \rightarrow ZH + Z_2HNa \tag{2.10}$$

2.6.6 Interpretations of monomolecular propane cracking on H-CHA zeolites

Monomolecular alkane cracking proceeds via a protolytic mechanism first described by Haag and Dessau [151] through protonation of a carbon-carbon bond in an alkane adsorbed at a Brønsted acid proton [47] to form a three-center, two-electron carbonium ion transition state that decomposes to a smaller alkene and corresponding alkane in equimolar amounts. Transition state treatments for monomolecular alkane activation in zeolites that depend on thermodynamic activities of reactants and transition states [49] are given by:

$$r = \frac{k_bT}{h} exp(\frac{-\Delta G^{\circ\ddagger}}{RT})\frac{\gamma_{H^+Z}C_{H^+Z}\gamma_{a_z}C_{a_z}}{\gamma_{\ddagger}} \tag{2.11}$$

The fraction of Brønsted acid sites covered by reactant alkanes during catalysis (C_{a_z}) is related to gas-phase (P_a) and hypothetical transition state pressures ($P_{\ddagger}$) by Langmuirian-type expressions, because adsorption of C_3-C_6 n-alkanes is specific to Brønsted acid protons up to saturation coverages [47], as given by:

$$C_{a_z} = \frac{K_{ads}P_a}{1 + K_aP_a + K_{\ddagger}P_{\ddagger}} \tag{2.12}$$

In Equation 2.12, K_a and $K_{\ddagger}$ are equilibrium constants for reactant alkane adsorption at a Brønsted acid proton and formation of the carbonium ion transition state from the adsorbed alkane, respectively. Thermodynamic activity coefficients, γ_i, of a given species is given by Equation 2.13:

$$\gamma_i = a_i^\circ(1 + K_a P_a + K_\ddagger P_\ddagger) \tag{2.13}$$

where a_i° is the thermodynamic activity at the reference state and is related to the configurational entropy of adsorbates on active sites. In the case of monomolecular alkane cracking, because both adsorbed alkanes and transition states occupy the same active site, γ_{a_z} and $\gamma_\ddagger$ are identical and rigorously cancel in Eq. 2.11. Additionally, in low coverage regimes C_{H^+Z} and γ_{H^+Z} approach unity, allowing for the simplification of equation 2.11.

$$r = \frac{k_b T}{h} exp(\frac{\Delta S^\ddagger}{R}) exp(\frac{-\Delta H^\ddagger}{RT}) C_{a_z} \tag{2.14}$$

When protons are predominantly uncovered by reactant alkanes, equation 2.14 can be rewritten in terms apparent first-order kinetics with respect to alkane pressure.

$$r = k_{int} K_a P_a = k_{app} P_a \tag{2.15}$$

In Equation 2.15, k_{int} is the intrinsic rate constant for protonation of an adsorbed alkane and k_{app} is the apparent rate constant and includes free energy contributions from the adsorption of propane at a proton and alkane protonation.

The absence of intracrystalline mass transfer limitations was confirmed by measuring monomolecular propane cracking rates on a H-CHA sample with a lower volumetric density of active sites (Si/Al = 26.1), but with a similar distribution of sites in predominantly isolated configurations. Propane cracking rates were similar between this sample and others of higher active site density but similar distributions of Al heteroatoms (Table 2.4, Figure 2.14), providing evidence that rates were not influenced by internal concentration gradients of reactant propane.

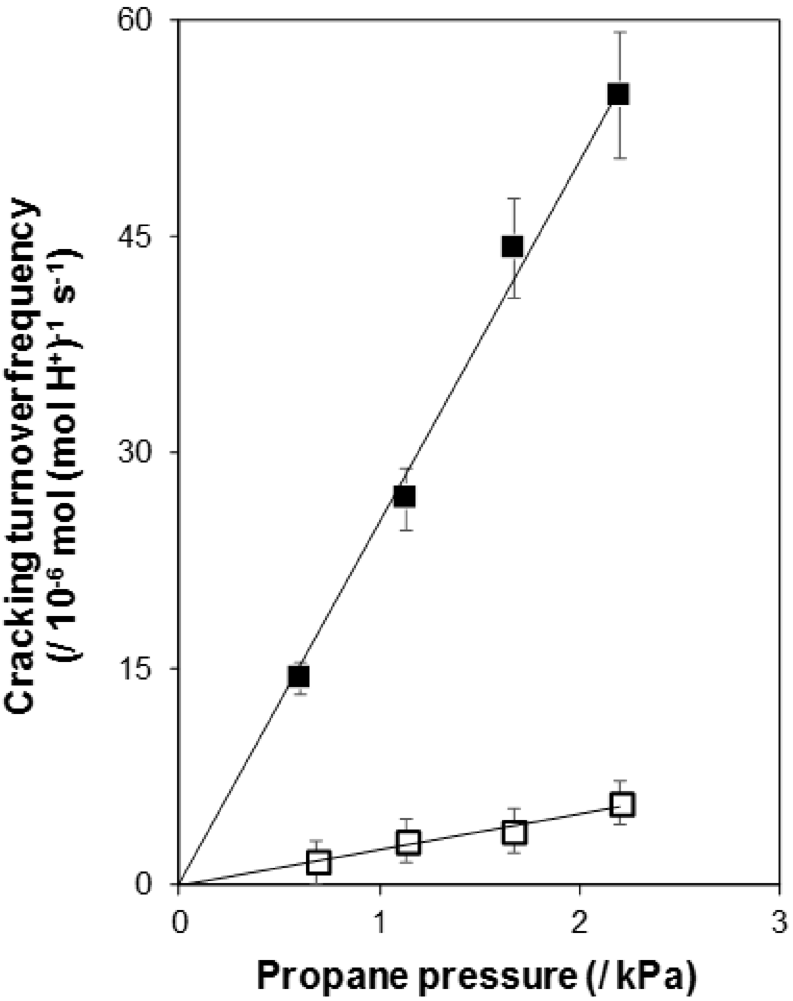

Figure 2.23.: Propane cracking turnover frequencies (748 K, per H^+) on H-CHA (16.0, 0%) (□) and H-CHA (15.0, 44%) (■) as a function of propane pressure.

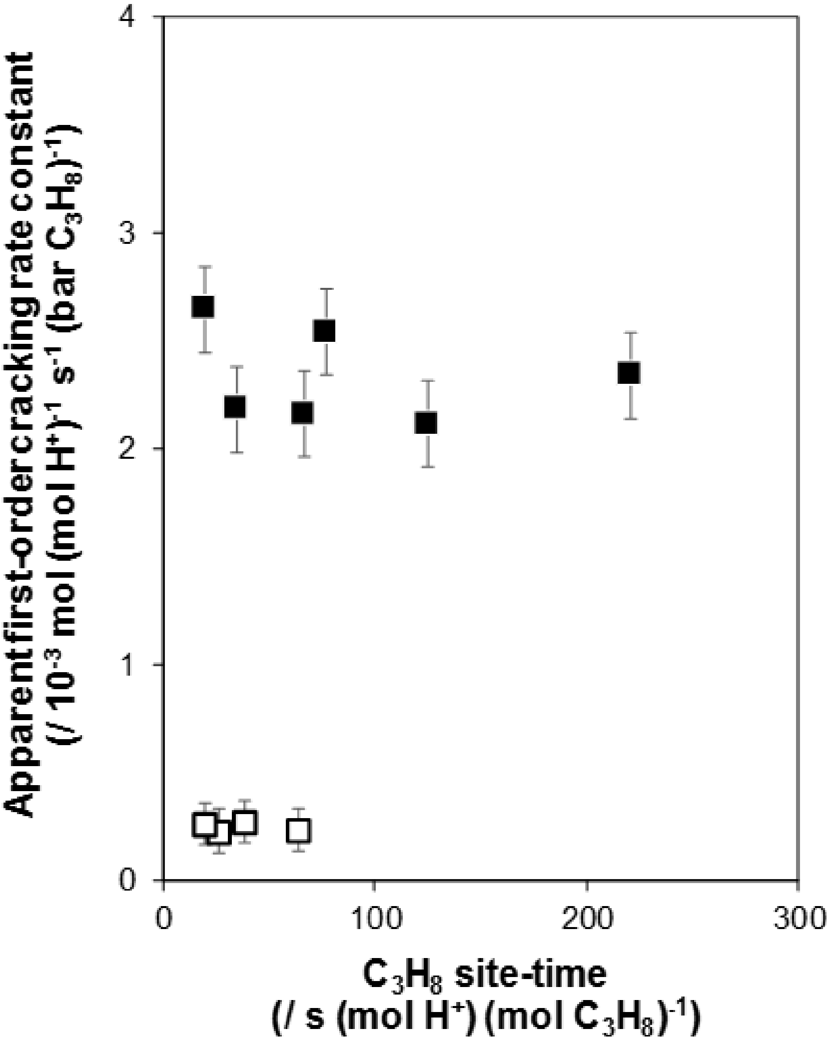

Figure 2.24.: First-order apparent propane cracking rate constants (748 K, per H^+) on H-CHA (16.0, 0%) (□) and H-CHA (15.0, 44%) (■) as a function of propane site-time.

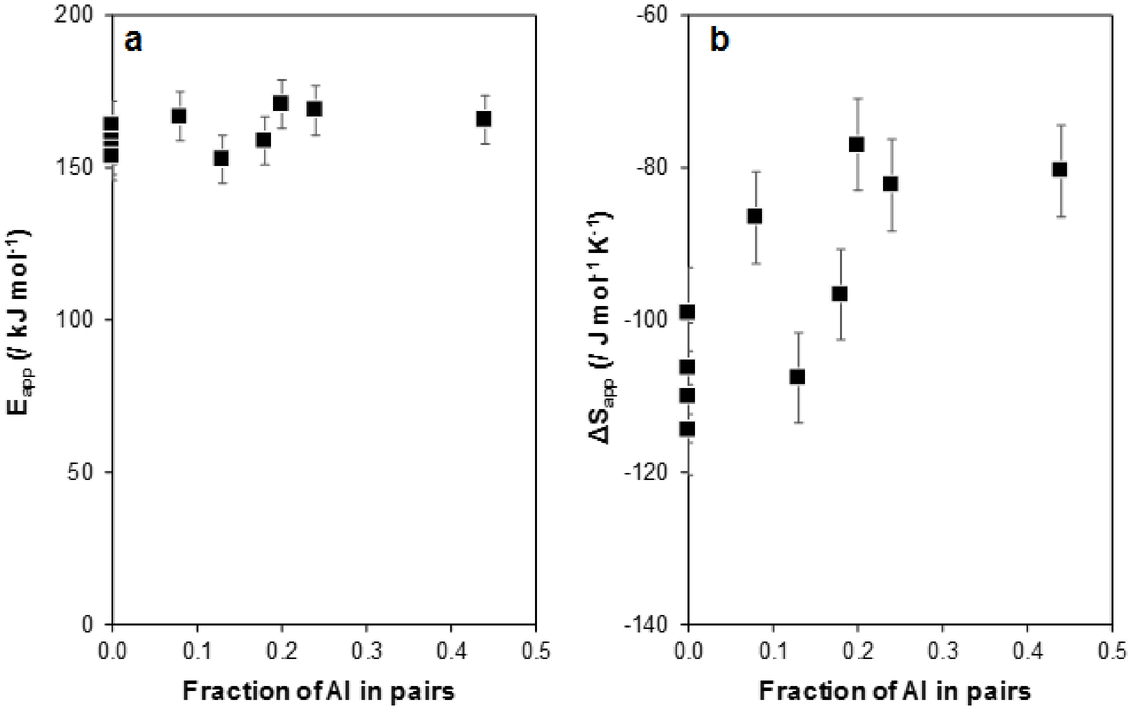

Figure 2.25.: (a) Apparent activation energies (718-778 K) and (b) apparent activation entropies (748 K) of monomolecular propane cracking on H-CHA zeolites as a function of the fraction of Al in pairs.

2.7 Acknowledgements

We acknowledge co-authors Jerry Crum (Notre Dame) and Prof. Bill Schneider (Notre Dame) for DFT calculations and assistance in writing this manuscript. We acknowledge financial support from the National Science Foundation under Cooperative Agreement No. EEC-1647722, an Engineering Research Center for the Innovative and Strategic Transformation of Alkane Resources (CISTAR). We thank Dr. John Di Iorio (Purdue University) and Claire Nimlos (Purdue University) for helpful technical discussions during the preparation of this manuscript.

3. ALKANE DEHYDROGENATION CATALYZED BY BRØNSTED ACIDIC AND REACTION-DERIVED CARBONACEOUS ACTIVE SITES IN ZEOLITES

3.1 Abstract

Alkane dehydrogenation rates on acidic zeolites measured in the presence of co-fed H_2 during initial contact with reactants solely reflect protolytic reactions at Brønsted acid sites, while rates measured without co-fed H_2 and at later reaction times reflect additional contributions from an extrinsic dehydrogenation function derived from reactants and products. This extrinsic function consists of unsaturated organic residues that catalyze dehydrogenation turnovers by accepting H-atoms from alkanes and recombining them as H_2. Such hydrogen transfer routes are inhibited by alkenes and H_2 products and proceed with activation barriers much lower than for protolytic dehydrogenation at H^+ sites, causing them to become more prevalent at lower temperatures and for zeolites with lower H^+ densities. The number, composition, and reactivity of these extrinsic carbonaceous active sites depend on the local concentrations of reactants and products, which vary with alkane and H_2 pressure, bed residence time, and axial mixing. These extrinsic catalytic moieties form within H_2-deficient regions of catalyst beds, but can be removed by thermal treatments in H_2, which fully restore zeolite catalysts to their initial state. Carbonaceous deposits do not catalyze alkane cracking reactions; thus, cracking rate constants serve as a reporter of the state of proton sites and their invariance with product pressure, residence time and axial mixing confirm that protons remain unoccupied and undisturbed as extrinsic organic residues change in number, composition, and reactivity. The rates of the reverse reaction (alkene hydrogenation) under H_2-rich conditions inhibit the formation and the reactivity of these organic residues, and taken together with formalisms based on non-equilibrium thermodynamics, confirm that alkane dehydrogenation occurs solely

via protolytic routes only at the earliest stages of reaction in the presence of added H_2. These findings provide a coherent retrospective view of the root causes of the literature discord about alkane dehydrogenation turnover rates and activation barriers on acidic zeolites, variously attributed to extraframework Al or radical active sites and to turnovers limited by alkene desorption instead of protolytic steps. Importantly, these findings also prescribe experimental protocols that isolate the kinetic contributions of protolytic dehydrogenation routes, thus ensuring their replication, while suggesting strategies to deposit or remove extrinsic organocatalytic functions that mediate hydrogen transfer reactions.

3.2 Introduction

Zeolites and microporous solid acids are ubiquitous in the catalytic conversion of light alkanes to alkenes via dehydrogenation and cracking reactions [152] and in the subsequent conversion of alkenes to larger hydrocarbons via oligomerization [23,153], alkylation [22] and aromatization [154] reactions. Brønsted acid sites are present in aluminosilicate zeolites in their proton forms as hydroxyl groups that bridge framework Si and Al atoms, where the proton balances the negative charge created by substituting Al for Si. These protons react with C-C or C-H bonds in alkanes to form penta-coordinated $(\text{C-C-H})^+$ or $(\text{C-H-H})^+$ carbonium ion-like transition states in monomolecular (i.e., protolytic) cracking and dehydrogenation pathways, respectively [151]. Protolytic alkane reactions tend to prevail at high temperatures (>623 K) and low conversions ($<2\%$) because carbonium ion transition states are less stable than their carbenium ion analogs, formed using alkenes as "initiators", which mediate bimolecular cracking routes [155,156]; such bimolecular routes prevail at higher alkene pressures and lower temperatures. The kinetic signatures of protolytic alkane activation are evident in measured barriers for first-order cracking and dehydrogenation rate constants that differ by the ensemble-averaged proton affinity among the different C-C and C-H bonds in gaseous alkane reactants, according to Born-Haber thermochemical cycle analyses [49,157,158]; in the case of propane, measured activation barriers are 25-40 kJ mol^{-1} higher for dehydrogenation (185-200 kJ mol^{-1}) than for cracking (160 kJ mol^{-1}) [49]. Protolyic alkane dehydrogenation routes also prevail on zeolites that do not contain other active site functions, such as metals [159–164] and cations [165,166] that are purposely introduced or present as adventitious impurities [167,168]. When such functions are also present, the carbonium-ion-like transition states that form at proton sites cause them to behave as a less competent function for activating C-H bonds in alkane dehydrogenation reactions.

Previous studies of propane reactions on H-form zeolites at conditions that tend to favor protolytic pathways (675-875 K, 2-10 kPa C_3H_8) [49,101–105] have reported activation barriers that vary widely for dehydrogenation (65-202 kJ mol^{-1}) but which are quite similar in all studies for cracking (147-165 kJ mol^{-1}), suggesting that dehydrogenation at non-protonic sites may also occur at certain conditions or on a subset of these nominally similar catalysts. Narbeshuber et al. measured an H/D kinetic isotope effect (KIE) of 1.7 (at 773 K) for n-butane cracking (the ratio of rates for n-C_4H_{10} and n-C_4D_{10} reactants) on H-MFI (Si/Al = 35) that would be consistent with kinetically-relevant proton insertion into alkane C-C bonds, but a KIE value of only 1.1 for n-butane dehydrogenation [101]. Such low KIE values for nC_4 dehydrogenation, together with measured activation barriers for C_3-C_6 n-alkane dehydrogenation that increased systematically with carbon chain length (95-160 kJ mol^{-1}), suggested that steps other than proton insertion into alkane C-H bonds were relevant for dehydrogenation events [101]. These observations were interpreted in terms of alkene desorption from bound alkoxides as the sole kinetically-relevant dehydrogenation step [169], as also invoked by van Bokhoven and co-workers to rationalize propane dehydrogenation barriers of 123-178 kJ mol^{-1} measured on H-form zeolites with different framework topology (*BEA, MOR, MFI, FAU; 675-875 K) [102,103]. The kinetic relevance of alkene desorption, however, requires relevant coverages of alkoxides and thus rate inhibition by alkene products, which were not reported in these studies. At first glance, such a proposal would appear consistent with observations by Janda and Bell that n-butane dehydrogenation rates (773 K) on H-MFI

(Si/Al = 12) were lower when butenes were added to the reactant stream [100]; yet, product inhibition of acid sites should have also inhibited cracking rates and caused dehydrogenation rates to become less than first-order in alkane pressure, in contradiction with their reported first-order dependence of rates on alkane pressure. These proposals were shown to be incorrect by Li and co-workers; their *in operando* infrared spectra collected during n-butane reactions on H-MFI (Si/Al = 29) at 618-710 K did not detect any changes in the intensity or frequency of the acidic OH stretches ($\sim$3600 cm^{-1}) with changes in bed residence time, which led to concomitant changes in dehydrogenation rates, presumably as a result of changes in the prevalent product concentrations [105]. These observations indicate that products must inhibit dehydrogenation reactions at another active function that is distinct from protons, and that non-protonic functions lead to measured activation energies (90 kJ mol^{-1}) and entropies (-190 J mol^{-1} K^{-1}) for propane dehydrogenation [105] that differ significantly from those expected for protolytic pathways from Born-Haber thermochemical cycle analyses (200 kJ mol^{-1} and -60 J mol^{-1} K^{-1}, respectively [49]).

The identity of non-protonic alkane dehydrogenation active sites on zeolites has been the subject of broad speculation, leading to proposals that extraframework Al species can act as Lewis acid centers that mediate such reactions [170] and that homolytic O-H cleavage at high temperatures ($\sim$1073 K) in inert environments form radical species at lattice O atoms that mediate such reactions [171], all without compelling theoretical or experimental evidence. These alternate active site proposals were invoked in studies that reported activation barriers for propane dehydrogenation that varied widely (84-187 kJ mol^{-1}) and were much lower than expected for protolytic pathways (200 kJ mol^{-1}). These studies collectively suggest that non-protonic active sites contribute to dehydrogenation events, but the identity and genesis of such active sites remain unclear. Non-protolytic alkane dehydrogenation pathways are typically attributed to active functions derived from structures inherent to aluminosilicate zeolites, and not from structures derived from reactants as extrinsic components that reside within (but are not an intrinsic part of) zeolite voids.

This study reports evidence that propane dehydrogenation rates (718-778 K) during initial contact with reactants on H-form zeolites pretreated in H_2 and measured in differential reactors (i.e., with alkene and H_2 products co-fed) solely reflect protolytic alkane activation at Brønsted acid sites. In sharp contrast, steady-state propane dehydrogenation rates measured in the absence of co-fed products are inhibited by propene and H_2 and occur via pathways with measured barriers that are significantly lower (by 100-150 kJ mol^{-1}) than those for protolytic dehydrogenation ($\sim$200 kJ mol^{-1}); propane cracking rates measured simultaneously and arising only from protolytic pathways at H^+ sites are not inhibited by products. Propane reactants and/or their propene products form unsaturated organic residues within zeolite voids when H_2 pressures are low, and such residues can transfer hydrogen atoms with propane to form propene and then can desorb H_2 to restore their unsaturation, thus behaving as catalytic sites for alkane dehydrogenation. The kinetic behavior of reaction-derived carbonaceous deposits extrinsic to zeolite surfaces provides a unifying explanation for the origin of non-protolytic alkane dehydrogenation observed on acidic zeolites among discordant literature reports over the past few decades. This work also establishes experimental protocols to avoid corruptions caused by carbonaceous deposits in studies of the intrinsic catalytic properties of acidic zeolites.

3.3 Experimental Methods

3.3.1 Synthesis and treatments of zeolites

MFI (CBV3024E, CBV8014, CBV28014) and MOR (CBV21A) zeolites were obtained from Zeolyst International in NH_4-form and converted to their H-form via treatment in flowing dry air (1.67 cm^3 s^{-1} (g solid)$^{-1}$, UHP, 99.999%, Indiana Oxygen) to 773 K (0.0167 K s^{-1}) for 4 h. CHA zeolites were synthesized according to the procedures reported by Di Iorio and Gounder [78] from a solution with a molar composition of 1 SiO_2/ 0.067 $Al(OH)_3$/ 0.5 TMAdaOH/ 44 H_2O, where TMAdaOH refers to *N,N,N*-trimethyl-1-adamantylammonium hydroxide (1 M TMAdaOH solution; 25 wt%, Sachem). This solution was subjected to a crystallization procedure at 433 K (under rotation at 30 rpm) for 144 h. The solids formed were washed with deionized water and acetone (>99.5 wt%, Sigma-Aldrich) in alternate washes (30 cm^3 (g solid)$^{-1}$ per wash) until the pH of the supernatant solution was constant (~7.5). The washed solids were then separated by centrifugation, treated in ambient air at 373 K for 24 h, and then in flowing dry air (1.67 cm^3 s^{-1} (g solid)$^{-1}$, UHP, 99.999%, Indiana Oxygen) to 853 K (0.0167 K s^{-1}) and held for 10 h in order to remove the organic species occluded during hydrothermal synthesis protocols. CHA samples were subsequently converted to their NH_4-form by aqueous-phase ion exchange (100 cm^3 (g solid)$^{-1}$) in a 1 M NH_4NO_3 solution (8.0 wt% in deionized H_2O; 99.9 wt%, Sigma-Aldrich) for 24 h under ambient conditions, then washed 4 times in deionized water (30 cm^3 (g solid)$^{-1}$ per wash) and recovered via centrifugation. NH_4-CHA was converted to H-CHA via the same method as used for converting NH_4-form MFI and MOR zeolites to their H-form.

3.3.2 Structural and textural properties of zeolite samples

Crystal structures were confirmed from X-ray powder diffractograms (XRD) collected using a Rigaku Smartlab X-ray diffractometer equipped with a Cu Kα radiation source operating at 1.76 kW. In typical experiments, samples (0.01 g) were loaded into a zero-background low-dead-volume sample holder (Rigaku) and diffractograms were collected over a 4–40° 2θ range with a step size of 0.01° and a scan rate of 0.0167° s^{-1}.

Micropore volumes of MFI and MOR zeolites were determined from N_2 uptakes (77 K; Micromeritics ASAP 2020 surface area and porosity analyzer). H-MFI and H-MOR samples (0.03–0.05 g, pelleted and sieved to 180–250 μm) were evacuated by heating to 393 K (0.167 K s^{-1}) in dynamic vacuum (6.7 mbar) for 2 h, and then heating to 623 K (0.167 K s^{-1}) and holding for 9 h. Volumetric uptakes of N_2 at relative pressures of 0.05–0.35 P/P_0 were linearly extrapolated to zero relative pressure to estimate micropore volumes (cm^3 (STP) g^{-1}). Micropore volumes of H-

CHA zeolites were determined from Ar adsorption isotherms (87 K) measured using procedures similar to those used for N_2 adsorption isotherms, and were similar to those estimated from the semi-logarithmic derivative plot of the adsorption isotherm given by $\partial(V_{ads})/\partial(\ln(P/P_0))$ vs. $\ln(P/P_0)$. All reported micropore volumes were similar (within 10%) between these two methods.

The Al content in MFI, MOR, and CHA zeolites was measured by atomic absorption spectroscopy (AAS) using a PerkinElmer Model AAnalyst 300 atomic absorption spectrometer, and the Si/Al ratio for each sample was calculated from the unit cell formula. Samples were prepared for analysis by adding ∼0.02 g of solid to 2 g HF (48 wt%, Alfa Aesar) and allowing the sample to dissolve for 3 days at ambient temperatures. The HF acid solution was then diluted with 50 g of deionized water. ***[Caution: when working with HF acid, use appropriate personal protective equipment, ventilation, and other safety precautions]***. Absorbances were measured using a wavelength of 309.3 nm in a reducing acetylene/nitrous oxide flame. Elemental compositions were calculated from calibration curves generated from standard solutions.

The number of acidic protons was determined from the amount of NH_3 evolved during thermal treatment of samples in their NH_4-form (NH_3 TPD) using a Micromeritics AutoChem II 2920 Chemisorption analyzer and an Agilent 5973N mass-selective detection system to identify gaseous products evolved from zeolite samples. NH_4-form zeolites (0.02–0.05 g) were loaded into a U-shaped quartz reactor and supported with quartz wool and placed in a clam-shell furnace. Calibration and deconvolution methods were performed according to previous reports [129].

3.3.3 Catalytic rate and selectivity measurements

Zeolites in their H-form (0.005-0.20 g, sieved to 180-250 μm) were placed within a quartz tube (7 mm I.D.) and supported between quartz wool plugs. The reactor temperature was controlled using a resistively-heated three-zone furnace (Applied Test Systems Series 3210) and Watlow controllers (EZ-Zone series). Temperatures were measured with a Type K thermocouple placed at the external surface of the quartz reactor tube at the midpoint of the catalyst bed. Samples were treated in a flowing stream of O_2 (5 kPa) in He (UHP, 99.999%, Indiana Oxygen) or in pure H_2 (UHP, 99.999%, Indiana Oxygen) at 803 K for 2 h (0.0167 K s^{-1}), and then cooled to reaction temperature (718-778 K) in flowing He or H_2, and held for 0.5 h. Propane (10 kPa, 5 kPa Ar, balance He, Indiana Oxygen) and H_2 were diluted in He to pressures of 0.6-2.2 kPa and 0-20 kPa, respectively, at volumetric flow rates of 0.4-2.9 cm^3 s^{-1} (at STP) and fed to the reactor. Propane conversions were kept below 2% at all conditions to minimize secondary reactions, which become prevalent as alkene pressures increase with increasing alkane conversions. Reactant and product concentrations in the inlet and outlet streams were measured by gas chromatography (HP 6890 Series) using flame ionization detection and a GS-Alumina KCl capillary column for molecular speciation (0.53 mm I.D., Agilent).

Alkene and H_2 co-products were introduced along with alkane reactants by converting a fraction of the propane in the reactant mixture (<1%) on a catalyst bed of H-MFI-17. This pre-bed was placed in a separate reactor and resistively-heated furnace (National Element Inc. Model FA120, held at temperatures between 718-748 K) located upstream of the reactor described above, which contained the zeolite sample (held at 748 K) intended for measurement of propane cracking and dehydrogenation rates. The composition of the effluent stream from the first reactor was quantified by bypassing the second reactor and instead delivering it to the GC. After the effluent from the first reactor containing propane and products (0.5-16 Pa) became invariant in composition, it was delivered to the inlet of the second reactor. Product formation rates on H-MFI-17 or H-MFI-140 in the second reactor were determined by differences in composition of its influent and effluent streams.

Propene hydrogenation rates were measured by treating H-form zeolites in 101 kPa H_2 at 803 K for 2 h (0.0167 K s^{-1}) and cooling under H_2 to 748 K. Propene (1 kPa, 5 kPa Ar, balance He, Indiana Oxygen) and H_2 were diluted in He to 0.03-0.06 kPa and 30-100 kPa, respectively, and molar flow rates were varied to achieve site contact times between 200-2000 s (mol H^+) (mol C_3H_6)$^{-1}$. Reactant and product concentrations were quantified using the GC methods reported above for propane dehydrogenation reactions.

3.4 Results and Discussion

In light of the disparate propane dehydrogenation activation barriers on H-form zeolites reported in the literature, we start in Section 3.4.1 by describing zeolite pre-treatments and reaction conditions that result in the sole involvement of proton sites in propane dehydrogenation turnovers. The kinetic signatures of protolytic alkane pathways become evident from the relative barriers measured for dehydrogenation and cracking and from the strict first-order dependence of turnover rates on propane pressure and the absence of any kinetic inhibition by dehydrogenation products (propene, H_2). Section 3.4.2 then shows that H-form zeolites can acquire an extrinsic dehydrogenation site that forms during exposure to propane reactants and/or its alkene products when H_2 is essentially absent. Such extrinsic active sites catalyze propane dehydrogenation at rates with lower barriers than protons, but they are strongly inhibited by dehydrogenation products (propene, H_2). These extrinsic sites do not catalyze propane cracking, which occurs solely at protons at all reaction conditions.

Section 3.4.3 provides evidence that these extrinsic sites consist of unsaturated organic residues that can extract H-atoms from reactant alkanes and then recombine them to desorb H_2, thus restoring their unsaturation and enabling catalytic turnovers. The formation and reactivity of these carbonaceous deposits can be suppressed by treating H-form zeolites in H_2 instead of oxidizing environments, and by introducing high H_2 pressures in inlet streams in order to avoid forming H_2-deficient regions within catalyst beds. In Section 3.4.4, rate measurements without co-fed products are reported on zeolites of different framework topology and H^+ site density. These data reveal both the general nature of these phenomena for microporous solid acids and the increasing prevalence of extrinsic active sites as the density of proton-free voids increases in zeolite samples. Adequate precautions taken to avoid H_2-deficient regions within catalyst beds allow measurements of proton-catalyzed monomolecular alkane dehydrogenation uncorrupted by contributions from extrinsic sites, as confirmed in Section 3.4.5 by measurements of the reverse propene hydrogenation reaction in excess H_2 and by treatments based on De Donder relations between chemical affinities for elementary steps and their equilibrium and rate constants. We conclude in Section 3.4.6 by summarizing the precautions required in order to isolate the contributions from proton-catalyzed alkane dehydrogenation and by examining the role of extrinsic carbonaceous active sites in causing discrepancies among previous literature reports of alkane dehydrogenation.

Table 3.1 summarizes the proton site and structural properties of the zeolites used in this study. Three MFI zeolites and one MOR zeolite were obtained commercially and one CHA zeolite was prepared using reported protocols [78]. X-Ray diffraction (XRD) patterns (Figure 3.8, Section 3.6.1) and micropore volumes calculated from N_2 (77 K; MFI, MOR, Figure 3.9, Section 3.6.1) and Ar (87 K; CHA, 3.10, Section 3.6.1) adsorption isotherms confirmed the structure and crystallinity of each topology based on comparisons to the International Zeolite Association (IZA) database [135]. The number of acidic protons from NH_3 evolution during temperature-programmed desorption (TPD) was similar to the number of Al atoms in each sample ($H^+/Al =$ 0.72-0.98, Table 3.1), consistent with the predominant presence of Al heteroatoms within the silicate frameworks.

Table 3.1.: Proton site and structural properties of H-form zeolites.

Sample[a]	Origin	Si/Al[b]	Number of H^+ sites			Micropore volume[e] (/ $cm^3 g^{-1}$)
			(/10^{-3} mol g^{-1})[c]	(/ Al)	(/ unit cell)[d]	
MFI-17	Zeolyst CBV3024E	17	0.66	0.72[f]	3.8	0.15
MFI-43	Zeolyst CBV8014	43	0.32	0.85	1.8	0.14
MFI-140	Zeolyst CBV28014	140	0.12	0.92	0.7	0.14
MOR-10	Zeolyst CBV21A	10	1.51	0.94	4.4	0.19
CHA-16	Ref. [78]	16	0.96	0.98	2.1	0.21

[a] Sample nomenclature is X-Y. X = Framework type. Y = Si/Al ratio.

[b] Determined by AAS. Uncertainty is ±10%.

[c] Determined by NH_3 TPD. Uncertainty is ±10%.

[d] Based on unit cells containing 96 (MFI), 48 (MOR), and 36 (CHA) T-atoms.

[e] Calculated from N_2 (MFI, MOR) and Ar (CHA) adsorption isotherms.

[f] H^+/Al values less than 1 on H-MFI-17 have been measured independently using *in situ* pyridine ($H^+/Al = 0.65$) and *ex situ* NH_3 ($H^+/Al = 0.52$) titrations [33].

3.4.1 Transient and steady-state rates of propane reactions on acidic zeolites

Zeolites in their H-form were treated in flowing H_2 (101 kPa, 803 K, 2 h) and then exposed to propane at different pressures and molar flow rates in order to vary site contact times (s (mol H^+) (mol C_3H_8)$^{-1}$) with H_2 (20 kPa) also present in the inlet stream. Rates of formation of ethene and propene products (per H^+, 748 K) were measured as a function of time-on-stream. Forward rates of propene formation were determined by rigorously correcting measured rates of propene formation by the approach-to-equilibrium (η) term; values of η were less than 0.03 at the low propane conversions used here (<1%), even at high inlet H_2 pressures (additional details in Section 3.6.3).

Figure 3.1 shows that on H-MFI-17 (data on all MFI, MOR, and CHA samples in Figures 3.11-3.15, Section 3.6.2), first-order rate constants (mol (mol H^+)$^{-1}$ s^{-1} bar(C_3H_8)$^{-1}$) measured for ethene formation were independent of propane pressure and site contact time at all times-on-stream (Figure 3.1a), while those for propene formation were so only at the very early stages of reaction (Figure 3.1b). Measured first-order rate constants for propene formation systematically increased with time-on-stream over a period corresponding to less than one turnover (C_3H_6 formed per H^+), and approached a nearly constant value that depended on both the propane pressure and site contact time (Figure 3.1b).

For all zeolites studied, ethene and propene site-time yields (STY; product formation rate per H^+) extrapolated to zero cumulative product turnovers (i.e., initial time-on-stream) were proportional to propane pressure (Figures 3.1c and 3.1d) and independent of site contact time. These data indicate that reaction products do not inhibit cracking or dehydrogenation rates on H-form zeolite samples at these conditions (Figure 3.16, Section 3.6.2). These initial ethene and propene STY extrapolate to zero values at zero propane pressure, consistent with cracking and dehydrogenation rates that are strictly proportional to the propane pressure and independent of the concentration of products during the early stages of reaction:

$$r_{0,i} = k_{meas,i} P_{C_3H_8} \tag{3.1}$$

Here, $r_{0,i}$ is the propane cracking (i = C) or dehydrogenation (i = D) rate extrapolated to zero turnovers, $k_{meas,i}$ is the corresponding first-order rate constant, and $P_{C_3H_8}$ is the propane pressure. The molar ratios of ethene to methane in products were near unity on all samples (1.0 ± 0.1, Figure 3.17, Section 3.6.2). Propene and H_2 were the only other products detected, indicating the absence of bimolecular alkene-initiated reactions mediated by carbenium ions [155]. These observations are consistent with the prevalence of monomolecular protolytic cracking and dehydrogenation reactions catalyzed by acidic protons, during the early stages of use in catalysis.

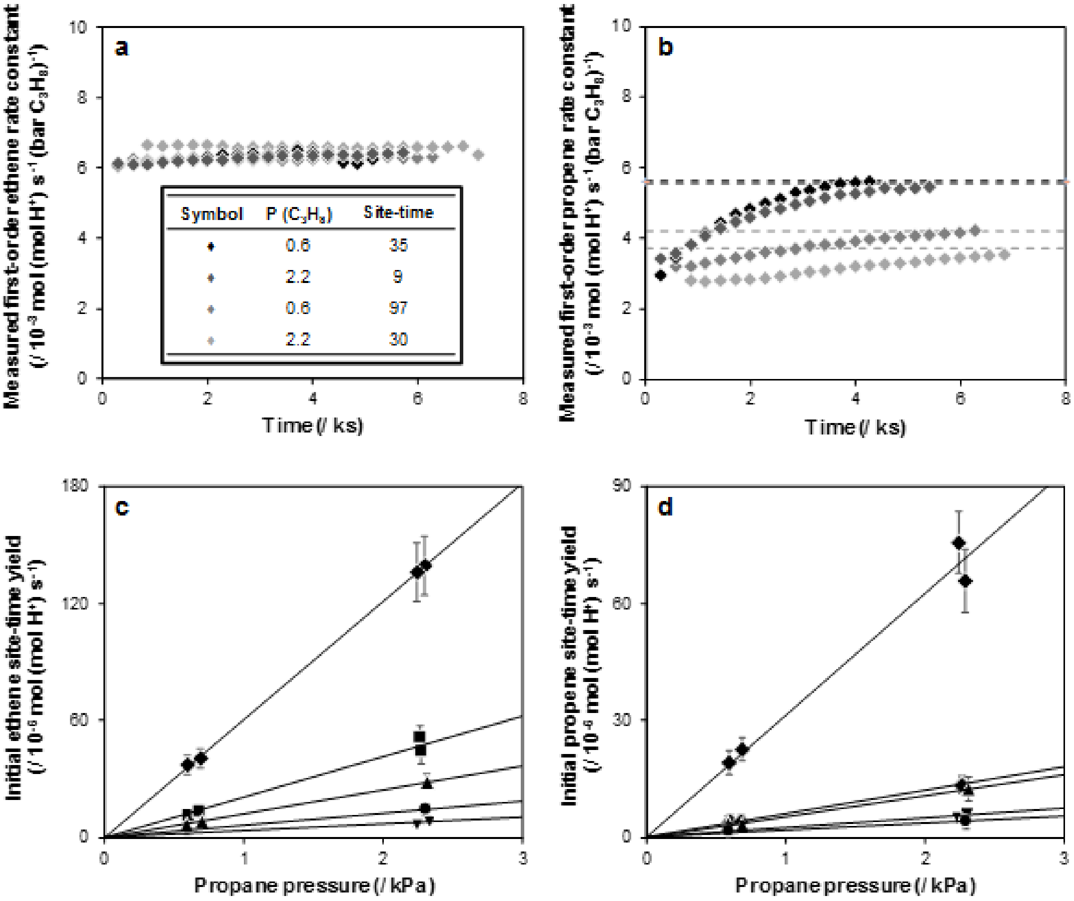

Figure 3.1.: Rate data (748 K) for propane reactions with co-fed H_2 (20 kPa) on H-form zeolites after treatment in H_2 (101 kPa, 803 K, 2 h). Transient changes in first-order rate constants (per H^+) measured for (a) ethene and (b) propene formation on H-MFI-17 at varying conditions (C_3H_8 pressures (kPa), site contact times (s (mol H^+) (mol C_3H_8)$^{-1}$, see legend in (a)), with dashed lines of different shades of gray to represent steady-state values at each condition in (b). Initial (c) ethene and (d) propene site-time yields (per H^+) on H-MFI-17 (◆), H-MFI-43 (■), H-MFI-140 (●), H-MOR-10 (▲), and H-CHA-16 (▼); solid lines are regressions of the data to Eq. 3.1.

First-order rate constants for protolytic propane cracking and dehydrogenation on H-zeolites were determined by regressing the data in Figures 3.1c and 3.1d to the functional form of Equation 3.1. Their values are listed in Table 3.2 together with those reported on the same samples by Gounder and Iglesia [49] at similar conditions (748 K, per H^+, 0-4 kPa C_3H_8) from rates measured at steady-state but without H_2 added to inlet streams. Protolytic propane cracking rate constants are similar to those previously reported (±20%) on H-MFI-17, H-MFI-43, and H-MOR-10. Protolytic propane dehydrogenation rate constants were also similar on H-MFI-17 and H-MFI-43 in both studies, but were about four-fold lower on H-MOR-10 in this study (Table 3.2) than in the previous study [49].

Table 3.2.: Kinetic parameters for protolytic propane cracking and dehydrogenation on H-form zeolites measured here (20 kPa co-fed H_2) and reported in [49] (no co-fed H_2).

		H-MFI-17	H-MFI-43	H-MFI-140	H-MOR-10	H-CHA-16
			Cracking			
$k_{meas,C}$ (748 K)^a	This work	6.2	1.6	0.6	1.2	0.4
	Ref [49]	6.3	1.5	n.m.*	1.4	n.m.*
$E^b_{meas,C}$	This work	150	150	164	150	154
	Ref [49]	155	150	n.m.*	160	n.m.*
$\Delta S^c_{meas,C}$	This work	-94	-104	-95	-109	-112
	Ref [49]	-88	-106	n.m.*	-99	n.m.*
			Dehydrogenation			
$k_{meas,D}$ (748 K)^a	This work	3.3	0.7	0.2	0.5	0.3
	Ref [49]	3.9	0.8	n.m.*	2.2	n.m.*
$E^b_{meas,D}$	This work	189	193	200	210	189
	Ref [49]	204	194	n.m.*	198	n.m.*
$\Delta S^c_{meas,D}$	This work	-47	-56	-56	-34	-69
	Ref [49]	-26	-52	n.m.*	-56	n.m.*

[a] Units of 10^{-3} mol (mol H^+)$^{-1}$ s^{-1} (bar C_3H_8)$^{-1}$; Uncertainty is ±15%.
[b] Units of kJ mol^{-1}; Uncertainty is ± 8 kJ mol^{-1}.
[c] Units of J mol^{-1} K^{-1}; Uncertainty is ± 10 J mol^{-1} K^{-1}.
*n.m.; not measured.

Measured activation energies and entropies for propane cracking and dehydrogenation were calculated from initial propane cracking and dehydrogenation rates on all zeolites between 718–778 K, after treatment in H_2 (101 kPa, 803 K, 2 h) and with 20 kPa H_2 present in the inlet stream (Figures 3.18-3.22, Section 3.6.2). As for the rate data at 748 K, ethene and propene STY at 718 K and 778 K were first-order in propane pressure (Figure 3.23, Section 3.6.2) and thus not inhibited by products (Figure 3.24, Section 3.6.2), because inhibition would have caused STY to increase sub-linearly with propane pressure from the concomitant increase in pressures of its dehydrogenation products. These rate data and those reported by Gounder and Iglesia [49] were used to determine activation energies (Figure 3.25, Section 3.6.2), which are summarized in Table 3.2. Activation energies measured here for protolytic cracking (150-164 kJ mol^{-1}; Table 3.2) are similar to those reported previously on H-zeolites (145-167 kJ mol^{-1} [101–105]), and measured dehydrogenation activation energies of 189-210 kJ mol^{-1} (Table 3.2) are about 40 kJ mol^{-1} higher than those for protolytic propane cracking.

Measured activation energies for protolytic cracking and dehydrogenation in the first-order kinetic regime reflect the formation energies of their respective carbonium ion-like transition states from a gaseous reactant molecule and an uncovered proton [49]. The higher barriers for propane dehydrogenation than for cracking (by 25-40 kJ mol^{-1}), as measured here and in previous work [49], reflect the less exothermic proton affinity of C-H than C-C bonds in propane (by 25–40 kJ mol^{-1} [172,173]) according to Born-Haber thermochemical cycle analyses [49,158] (additional details in Section 3.6.4). These activation energies for propane dehydrogenation are consistent with the earlier report by Gounder and Iglesia [49]; they are among the highest values reported on H-form zeolites from rate measurements at steady-state using propane as the reactant without added H_2 to inlet streams (67–202 kJ mol^{-1} [49, 101–105]). Activation energies for propane cracking measured here are essentially identical to those reported in earlier studies (145–167 kJ mol^{-1}). Propane cracking rates remained invariant with time-on-stream (Figure 3.1a; Figures 3.11-3.15, Section 3.6.2), confirming that proton active sites remain predominantly uncovered and undisturbed during conditions typical of protolytic alkane activation catalysis. Taken together, these observations implicate a distinct non-protonic active site as the genesis of the additional propene observed with increasing time-on-stream during the approach to the catalytic steady-state. This second dehydrogenation active site appears to form *in situ*, as it is not present at zero turnovers on H-zeolite samples pretreated in H_2. It selectively reacts propane to form propene without concurrent cracking events, via pathways that proceed with much lower barriers and different kinetic behavior than protons, as discussed in the next section.

3.4.2 Product inhibition by dihydrogen and propene at reaction-derived active sites

Propene formation rates (748 K, per H^+) on H-form zeolites measured with 20 kPa H_2 in the inlet stream increased with time-on-stream and approached constant values (Figure 3.1b; Figures 3.11-3.15, Section 3.6.2). These constant values depend on the specific propane pressure and site contact time (or residence time) of each experiment. These asymptotic rates are lower for experiments at longer bed residence times and higher propane pressures, both of which lead to higher propane conversion and thus to higher product pressures (Figure 3.27, Section 3.6.5). The number of dehydrogenation turnovers (C_3H_6 formed per H^+) required to attain steady-state propene formation rates at each condition was below unity (0–0.6 per H^+; Figures 3.11-3.15, Section 3.6.2), suggesting that the transient approach to steady-state is unrelated to dehydrogenation turnovers at H^+ sites.

The inhibition of propane dehydrogenation rates by H_2 and alkene products was confirmed by co-feeding reaction products. These products were formed on a bed of H-form zeolite (H-MFI-17) that was placed before a subsequent reactor that contained the zeolite sample (either H-MFI-17 or H-MFI-140) used for measurement of reaction rates. This pre-reactor was used to convert a small percentage ($\sim$1%) of the inlet molar rate of propane to its cracking and dehydrogenation products before its effluent stream entered the second bed. As the pre-bed temperature was increased (718–748

K) to increase the propene and H_2 pressures entering the second bed (kept at 748 K), propene formation rates measured on the sample in the second bed decreased and ultimately became insensitive to H_2 and C_3H_6 product pressures above ~2 Pa of each product; in contrast, ethene formation rates were unaffected by the presence or pressure of dehydrogenation products (Figure 3.28, 3.6.6). At H_2 and C_3H_6 pressures above 2 Pa, propane cracking and dehydrogenation rates were similar to those extrapolated to zero turnovers when samples were pre-treated in H_2 and when H_2 was present in the inlet stream (Figure 3.28). These results indicate that propene and H_2 inhibit dehydrogenation rates on the extrinsic active site, even at the very low product pressures of purportedly differential conditions. These observations serve as a useful reminder that reaction rates, and thus the concentrations of any species that determine such rates, must remain essentially invariant (i.e., gradientless) throughout a catalytic packed bed in order to ensure differential conditions, which are not guaranteed solely by low reactant conversions.

The transient evolution of propane cracking and dehydrogenation rates was also monitored in the absence of dehydrogenation products in the inlet stream after treating H-form zeolites in O_2-containing streams (5 kPa O_2 in balance He, 803 K) instead of pure H_2 streams (803 K). Treatments with O_2-containing streams are commonly used in attempts to remove adventitious organic residues from zeolites before rate measurements [49,101–105]. Ethene and propene formation rates (per H^+) are shown in Figure 3.2a on H-MFI-43 as a function of time-on-stream (data on all samples in Figure 3.29, Section 3.6.7). Ethene formation rates (per H^+) remained constant with time-on-stream and were similar to those measured in the presence of co-fed H_2 (Figure 3.2a, dotted line). In contrast, propene formation rates (per H^+) decreased about two-fold before reaching constant values (Figure 3.2a). Both initial and steady-state propene formation rates (per H^+) were higher than the protolytic dehydrogenation rate (Figure 3.2a, dashed line) determined from measured rates extrapolated to zero turnovers with H_2-containing inlet streams (Figure 3.1b; Figures 3.11-3.15).

After attaining constant propene formation rates on each sample, increasing or decreasing the residence time led to additional transients that decreased or increased steady-state propene formation rates, respectively (Figure 3.30, Section 3.6.7). Ethene formation rates, however, remained unchanged throughout these experiments (Figure 3.30). In the absence of co-fed products, these constant ethene formation rates were proportional to propane pressure and unaffected by residence time (Figure 3.2b), but those for propene formation increased sub-linearly with propane pressure and decreased as the residence time and the prevalent product pressures increased (Figure 3.2c). As a result, first-order propene formation rate constants on H-form zeolites measured in the absence of co-fed products systematically decreased when propene pressures increased as a result of higher propane reactant pressures and longer residence times (Figure 3.31, Section 3.6.7). These data are consistent with inhibition of the extrinsic active site by dehydrogenation products, as also observed during deliberate co-feeding of dehydrogenation products (Figure 3.28).

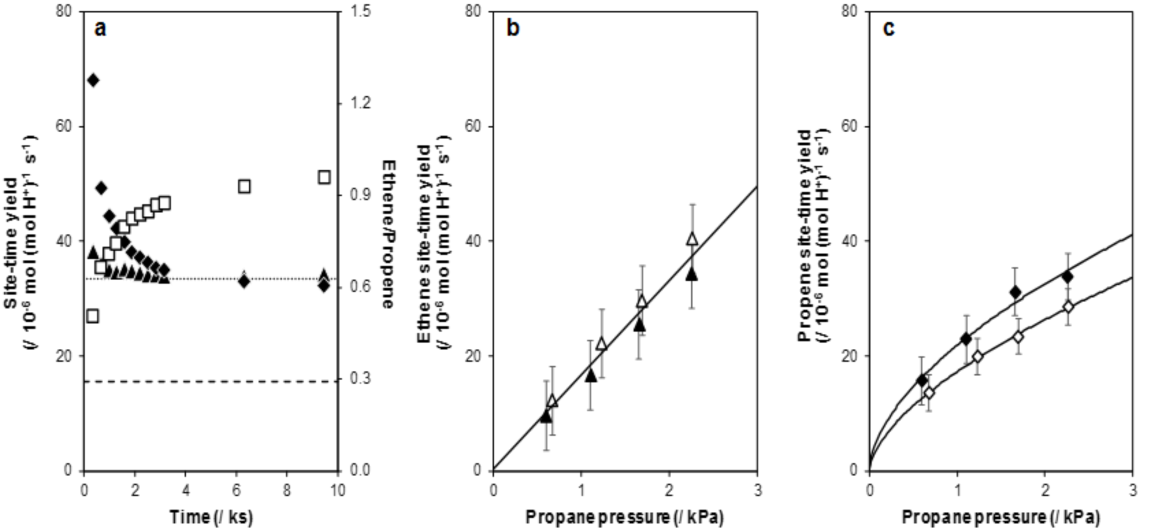

Figure 3.2.: (a) Transient ethene (▲) and propene (◆) site-time-yields (748 K, per H^+) and ethene/propene ratios (□) on H-MFI-43 measured at 2.2 kPa C_3H_8 and a residence time of 2 s (mol H^+) m^{-3} following pretreatment in 5 kPa O_2 (803 K, 2 h); expected protolytic cracking (dotted line) and dehydrogenation (dashed line) rates calculated from rate constants in Table 3.2. Steady-state (b) ethene and (c) propene site-time yields (748 K, per H^+) measured at different residence times (7 s (mol H^+) m^{-3} (open symbols); 2 s (mol H^+) m^{-3} (closed symbols)). Solid line in (b) represents regression of data to Eq. 3.1, while solid curves in (c) represent regression of data to a power-law model solely intended to guide the eye.

The monotonic decrease in measured first-order propene formation rate constants with increasing propene and H_2 pressure was not evident on all samples (Figure 3.31, Section 3.6.7), suggesting that back-mixing of partially converted reactant streams led to higher propene pressures at the beginning of catalyst beds in certain cases. The relatively short beds (ratio of bed length to aggregate diameter <20) used in these experiments led to significant axial mixing. The relative rates of convection and axial dispersion were similar in these cases, leading to Péclet numbers of order one [174] (Section 3.6.8). Smaller Péclet numbers cause inhibiting products to disperse more readily to earlier axial positions along the bed, thus enhancing their inhibitory effects. As a result, measured propene formation rates at a given residence time are different for beds of proportionately different lengths and linear fluid velocities. Propene formation rates collected at lower Péclet numbers more closely resemble protolytic dehydrogenation rates, because these conditions approach well-mixed reactors that remove axial gradients in product pressures, thus more strongly inhibiting the extrinsic dehydrogenation function (Figure 3.32, Section 3.6.8). Taken together, these data indicate that products of propane dehydrogenation (propene, H_2) inhibit propene formation events on a second active site that is unrelated to Brønsted acidic protons and which forms during reaction. These observations also illustrate how conditions typically used in lab-scale reactors can conflate kinetic and hydrodynamic effects of reactant pressure and residence time. This represents a disconcerting conclusion given that literature reports seldom consider such matters when measuring data of purported kinetic origin or document the required details when describing the methods used to collect catalytic data, thus preventing independent replication or retroactive interpretation of rate data.

3.4.3 Effects of H_2 on the removal of reaction-derived organic residues acting as an extrinsic dehydrogenation function

These results clearly point to reaction-derived organic residues as an extrinsic dehydrogenation function. Such residues may form via reactions of alkene products (e.g., oligomerization, cyclization, hydride transfer) [175] or from unsaturated impurities in reaction mixtures (e.g., propyne, 1,3-butadiene), but they can be scavenged or rendered inactive by reactions with H_2. The presence of adventitious unsaturated feed impurities in our studies was ruled out by addition of H_2 (20 kPa) to reactant streams and the placement of a Pt/SiO_2 catalyst (293 K) upstream of the zeolite bed to hydrogenate any trace unsaturated impurities (details in Section 3.6.9). Such protocols did not have any detectable effect on measured propene formation rates on H-MFI-43 (Figure 3.33).

The purposeful deposition of carbonaceous structures on H-form zeolites typically involves exposure to unsaturated hydrocarbons, such as propene, at high temperatures (~1000 K); the formation of non-volatile organic residues was evident by dissolving the zeolite in HF and detecting the zeolite-templated carbonaceous deposits formed (ZTC) [176,177]. Organic residues formed on H-FAU zeolites during reactions of benzene (773-1073 K) in an inert He environment contained H/C ratios consistent with fused aromatic rings. In these studies, H_2 inhibited the formation of carbonaceous deposits (1-5 MPa H_2), apparently because benzene and other intermediates were hydrogenated at H^+ sites to form volatile products [178]. Similar H_2 co-feed strategies have been used to mitigate the formation of unsaturated organic residues during n-C_7 cracking (543 K, 0-2 MPa H_2) [179] and methanol-to-hydrocarbon conversion (623 K, 1.6 MPa H_2) [180] on H-MFI zeolites. Exposing carbonaceous deposits to H_2 leads to the formation of CH_4 [181,182] via hydrogenation reactions that first remove methyl groups from substituted aromatics (e.g., toluene, diphenylmethane) and then lead to aromatic ring saturation and C-C bond cleavage to form C_1-C_2 hydrocarbons [183,184]. Thus, H_2 allows the scavenging and hydrogenation of unsaturated organic residues that form during acid-catalyzed reactions on zeolites.

These previous observations, taken together with the effects of product concentrations and chemical treatments on the contributions from extrinsic dehydrogenation sites, led us to explore more direct probes of the presence and involvement of organic residues as an extrinsic catalytic dehydrogenation function. Figure 3.3a shows the results of an experiment in which H-MFI-43 was first treated in H_2 (20 kPa, 803 K) and then exposed to propane (0.6 kPa C_3H_8 in He, 748 K) without co-fed H_2 until constant propene formation rate constants were achieved (~8 ks); these conditions also led to the formation of the equimolar CH_4/C_2H_4 mixtures expected from protolytic cracking. Then, H_2 (20 kPa) was added to the reactant stream without any changes in propane pressure or residence time. Propene formation rate constants decreased immediately upon co-feeding H_2 (from 2.5 to 1.9 × 10^{-3} mol (mol $H^+)^{-1}$ s^{-1} (bar $C_3H_8)^{-1}$, Figure 3.3a) and then more gradually with time over ~5 ks to reach values (1.7 × 10^{-3} mol (mol $H^+)^{-1}$ s^{-1} (bar $C_3H_8)^{-1}$, Figure 3.3a) that were similar to steady-state values measured with 20 kPa H_2 co-feeds (Figure 3.12d, SI); in contrast, ethene formation rate constants were unaffected by H_2 co-feeds and did not vary with time. These data show that H_2 inhibits an extrinsic function that mediates only dehydrogenation events and which is not associated in its formation or function with the protons that mediate protolytic cracking reactions.

CH_4 formation rate constants, however, increased sharply upon H_2 introduction (from 1.7 to 5.8 × 10^{-3} mol (mol $H^+)^{-1}$ s^{-1} (bar $C_3H_8)^{-1}$, Figure 3.3a) and then decreased with time to the same constant value obtained before H_2 introduction, at which point it formed the equimolar CH_4/C_2H_4 ratios expected from protolytic cracking. Similar experiments on H-MFI-43 samples that attained constant rates after exposure to propane at different pressures (0.6 or 2.2 kPa C_3H_8) and for different time-on-stream (2–75 ks) using packed beds of different heights (2.5 or 7.5 × 10^{-3} m; Figures 3.34-3.35; data on H-MOR-10 in Figure 3.36; Section 3.6.10), also led to the evolution of excess CH_4 (other saturated products, such as ethane, were not detected). The formation of excess amounts of CH_4 upon H_2 introduction indicates that H_2 leads to the removal of some or all reaction-derived organic residues deposited during reactions in the absence of H_2 [178].

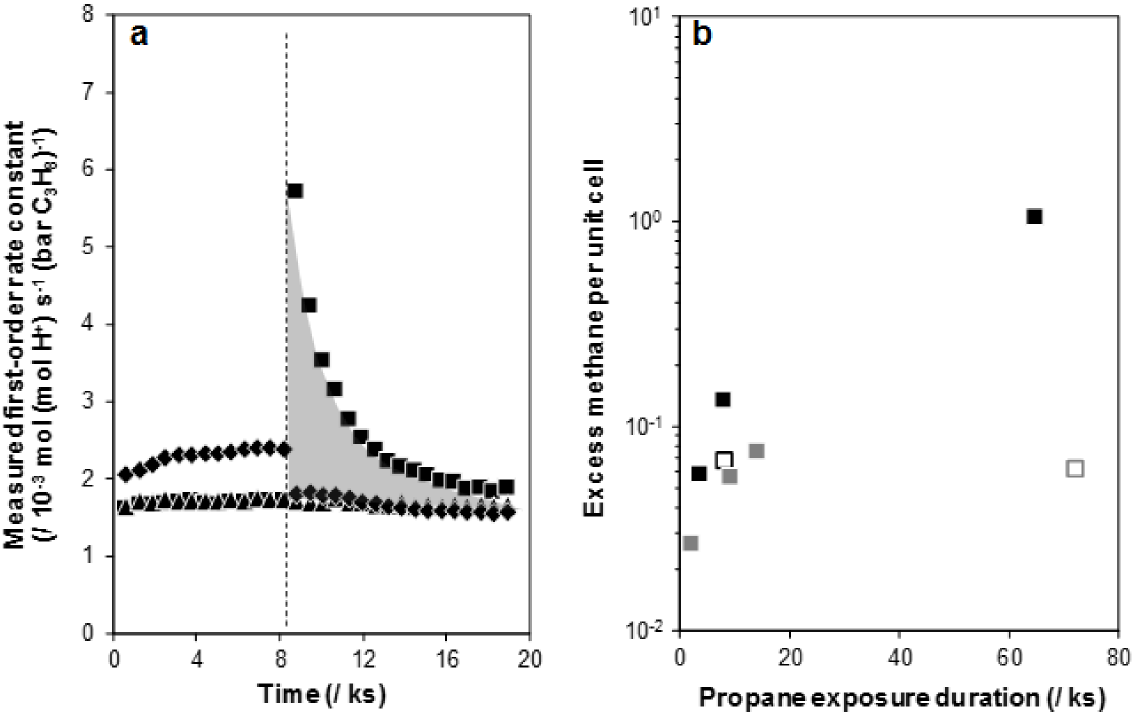

Figure 3.3.: (a) Measured rate constants of methane (■), ethene (▲), and propene (◆) formation (per H$^+$, 748 K) on H-MFI-43 (0.6 kPa C_3H_8, 17 s (mol H$^+$) m^{-3}, 2.5 × 10^{-3} m bed height). Dashed line at ∼8 ks indicates a step-change increase in co-fed H_2 from 0 to 20 kPa. Grey shaded region represents the excess methane formed. (b) Excess methane removed per unit cell (96 T-atoms) from H-MFI-43 during exposure to propane (748 K) after a step-change increase in co-fed H_2 (0 to 20 kPa). Experiments performed under 0.6 kPa (■) or 2.2 kPa (▨) C_3H_8 and with catalyst bed heights of 2.5 × 10^{-3} (closed) and 7.5 × 10^{-3} m (open) of H-MFI-43.

The excess amount of CH_4 formed upon H_2 introduction on H-MFI-43 (Figure 3.3a, grey shaded region) was 0.14 CH_4 per zeolite unit cell (2.3×10^{-5} mol CH_4 g^{-1}). Figure 3.3b shows the amount of excess CH_4 formed (per unit cell) at various propane exposure times and propane pressures before introducing H_2 to inlet streams, and on catalyst beds of different height. Longer beds (7.5 mm) formed smaller amounts of excess CH_4 (0.07 vs. 0.13 CH_4 per unit cell) than shorter beds (2.5 mm) after exposure to 0.6 kPa C_3H_8 for 8 ks at the same gas linear velocity (2.6×10^{-2} m s^{-1}), indicating that carbon deposition does not occur uniformly throughout catalyst beds. The formation of smaller amounts of excess CH_4 (per unit cell) on longer beds is consistent with reactor hydrodynamics characteristic of Péclet numbers of order $\sim 10^0$–10^1, which preserve H_2-deficient regions near the bed inlet; such H_2-deficient regions therefore represent smaller fractions of the packed beds for longer beds. As a result, the deposition of carbonaceous residues occurs chromatographically at the front of catalyst beds where H_2-deficient regions prevail, similar to the axial gradients in coke content reported along H-FAU catalyst beds during propene reactions (723 K, 10 kPa C_3H_6) [185].

Smaller amounts of CH_4 were evolved in analogous experiments performed at higher C_3H_8 pressures (2.2 kPa) but identical bed length and linear velocity (Figure 3.3b), because the higher product H_2 pressures generated *in situ* led to the more efficient hydrogenation of unsaturated intermediates, thus mitigating the formation of carbonaceous residues. After each constant propene formation rate was attained for each C_3H_8/H_2 reactant mixture, a subsequent switch to pure H_2 also led to the transient evolution of excess CH_4 (Figure 3.37, Section 3.6.10), albeit a significantly smaller amount (by three orders-of-magnitude) than was removed when C_3H_8/H_2 replaced C_3H_8/He reactants. The evolution of excess CH_4 in these experiments shows that minority amounts of organic residues are replenished from alkane reactants and thus still present on H-form zeolite surfaces even when H_2 is introduced in inlet streams, and that such residues were only fully removed when propane was removed from inlet streams.

These experiments cannot directly discern the specific nature of the reaction-derived extrinsic dehydrogenation function. Any inquiries about their structure would require fast quenching protocols that are certain to change their composition and H-content. It is evident, however, that their removal by H_2 as CH_4 decreases the rates of propene formation without detectable changes in the rates of ethene formation, via a reaction that occurs exclusively at proton sites. In fact, carbonaceous deposits have been implicated as active structures in non-oxidative dehydrogenation on VO_x/Al_2O_3 (e.g., ethylbenzene [186, 187], butane [188], and cyclohexene [189]), and the edges of these carbonaceous deposits have been proposed as plausible active sites for alkane dehydrogenation [186]. Plausible routes for these dehydrogenation events include hydrogen transfer from propane to an unsaturated residue to form a bound propyl radical or hydride transfer to form a bound propoxide, which would then undergo β-hydrogen abstraction to eliminate propene. The hydrogenated-form of these carbonaceous residues would then dehydrogenate to desorb H_2 in order to complete a turnover, restoring its unsaturation and thus its catalytic function.

The extrinsic nature and reaction-derived origins of these non-protonic dehydrogenation sites are evident from their negligible contributions during the earliest stages of exposure of H-form zeolites to propane. The transient evolution of propene formation rates appears to reflect concomitant changes in the amount and composition of these organic residues with time, in response to the prevalent chemical potentials of carbon and hydrogen in the reacting mixtures. Such changes influence, in turn, their ability to effect hydrogen transfer reactions from alkanes and the desorption of H-atoms as the H_2 co-products.

The gradual evolution of propene formation rates on H-MFI-43 after different treatments in O_2 (5 kPa) and H_2 (10 kPa) are shown in Figure 3.4. An O_2 treatment (803 K, 2 h; Figure 3.4a) led to propene formation rate constants (748 K) that decreased about two-fold (from 3.0 to 1.7 $\times$ 10^{-3} mol (mol $H^+)^{-1}$ s^{-1} (bar $C_3H_8)^{-1}$) and reached constant values after about 3 ks. A subsequent O_2 treatment (and He flush for 0.5 h at 748 K) followed by the reintroduction of propane reactants led to a lower initial rate constant (2.1×10^{-3} mol (mol H^+)$^{-1}$ s^{-1} (bar C_3H_8)$^{-1}$) and to a shorter transient (∼0.5 ks) approach to steady-state values, which were similar to those attained before this second O_2 treatment (Figure 3.4b). After these two successive O_2 treatments, H-MFI-43 was treated in H_2 (803 K, 2 h) and then flushed with He (748 K, 0.5 h) before reintroducing propane reactants (Figure 3.4c). The transient evolution of propene formation rates resembled that measured after the first O_2 treatment (Figure 3.4a), with the propene formation rate constants decreasing (from 3.0 to 1.7×10^{-3} mol (mol H^+)$^{-1}$ s^{-1} (bar C_3H_8)$^{-1}$) over a similar transient period (∼3 ks) as after the initial O_2 treatment. These data indicate that O_2 treatments do not fully remove the organic residues that form on H-form zeolites during propane reactions in the absence of co-fed H_2; in contrast, H_2 treatments at 803 K for 2 h are able to remove them (Figure 3.3; Figures 3.34-3.35) and to restore H-MFI-43 to its state before exposure to propane at reaction conditions.

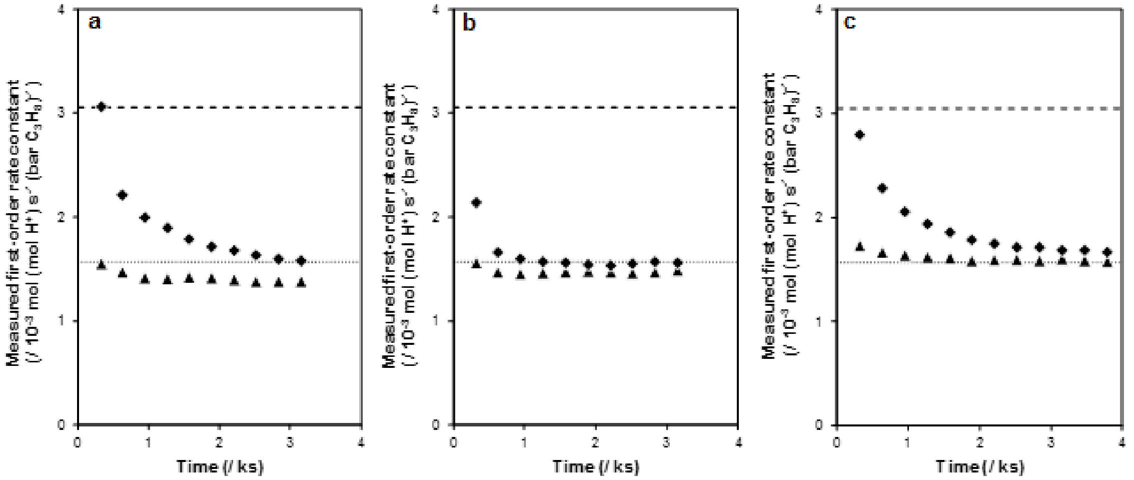

Figure 3.4.: Transients in measured first-order ethene (▲) and propene (◆) formation rate constants (748 K, per H^+) on H-MFI-43 following (a) first treatment in 5 kPa O_2/He (803 K, 2 h) and He purge (748 K, 0.5 h), (b) second treatment in 5 kPa O_2/He (803 K, 2 h) and He purge (748 K, 0.5 h), and (c) treatment in 10 kPa H_2/He (803 K, 2 h) and He purge (748 K, 0.5 h). Dashed line represents the initial propene formation rate constant after the first O_2 treatment, and the dotted line represents the steady-state propene formation rate constant.

Once steady-state propene formation rates have been attained, subsequent transients in propene formation rates are observed when inlet flow rates are changed in order to vary bed residence times. This is shown in Figure 3.5 (data collected on H-MOR-10) for rates measured in the absence of co-fed products. Step changes that increased or decreased residence times led to a gradual decrease or increase, respectively, in propene formation rate constants (748 K) over 10-20 ks (Figure 3.5); in contrast, ethene formation rate constants remained constant with time and unaffected by residence time. Changes to inlet flow rates cause changes to bed residence time and in turn to product pressures, which influence prevalent carbon and hydrogen chemical potentials in reacting mixtures. Such changes also influence linear fluid velocities and thus Péclet numbers, leading to different extents of back-mixing and to differences in the prevalent axial gradients of carbon and hydrogen chemical potentials. These different carbon and hydrogen chemical potentials would cause organic residues to evolve in composition, thus influencing their ability to catalyze dehydrogenation turnovers.

We conclude that the transient evolution in propene formation rates observed upon changes in residence time (Figure 3.5) reflects such a compositional evolution of these unsaturated surface organic residues; they retain a memory of the hydrogen and carbon chemical potential history from the previous steady-state and change their composition with time in response to new hydrogen and carbon chemical potentials in the reacting mixture. The inhibition of propene formation turnovers by products on these carbonaceous active sites cannot arise from strong adsorption of products (alkenes, H_2), which would have resulted in much faster changes in propene formation rate constants in response to changes in residence time. Such inhibition reflects instead changes in the reactivity of carbonaceous active sites in response to the effective H/C chemical potential. Sufficiently high H/C chemical potentials would increase the degree of saturation in organic residues that would limit their ability to abstract H-atoms from reactant alkanes, and sufficiently low H/C chemical potentials would increase the degree of unsaturation in organic residues that would limit their ability to desorb H_2.

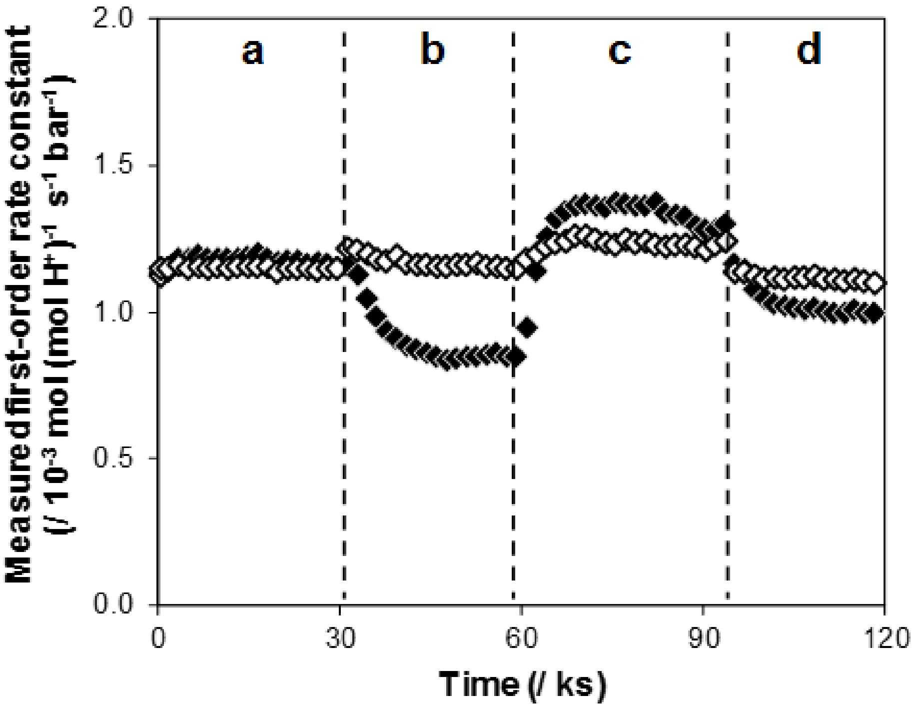

Figure 3.5.: Measured first-order ethene (◇) and propene (◆) formation rate constants (748 K, per H^+) on H-MOR-10 as a function of time-on-stream, and their response to changes in reactant site contact time (s (mol H^+) (mol C_3H_8)$^{-1}$) corresponding to (a) 43, (b) 99, (c) 29, and (d) 54.

These data clearly demonstrate that the initial transient propene formation rates when acidic zeolites are contacted with H_2-free propane reactants reflect the formation of unsaturated organic residues; they also show that such extrinsic sites vary in number and/or reactivity in response to the reaction environment. Changes in bed residence time and the resulting changes in the prevalent H_2 and propene concentrations influence dehydrogenation rates (Figure 3.5; Figure 3.30, Section 3.6.7) through changes in the number and the H-content (and thus the reactivity) of the organic residues that act as the extrinsic dehydrogenation function. These parallel pathways, catalyzed by intrinsic (protons) and extrinsic (organic residues) functions, contribute in an additive manner to measured propene formation rates, while cracking occurs exclusively on protons. Their relative contributions depend on the reaction environment, on the history of use for each sample, and even on axial dispersion effects; these dispersion effects depend sensitively on details such as bed length, aggregate size, and linear fluid velocities that are seldom considered, controlled, or reported as part of the protocols used to measure catalytic data.

Measured dehydrogenation barriers reflect additive contributions from two functions with very different kinetic parameters and disparate sensitivities to product concentrations, even under nominally “differential conditions”. Not surprisingly, the resulting inconsistent reports of dehydrogenation rates and activation barriers have brought forth widespread confusion and significant discord, and myriad hypotheses about their origins. Next, we illustrate some of the ubiquitous pitfalls inherent in rate measurements at conditions typically used to determine the rates and kinetic parameters for monomolecular dehydrogenation and cracking on H-form zeolites [49,101–105].

3.4.4 Monomolecular dehydrogenation barriers and corruptions induced by extrinsic reaction-derived active sites

Measured activation barriers for propane cracking (150-164 kJ mol^{-1}, Table 3.2) and dehydrogenation (189-210 kJ mol^{-1}, Table 3.2) obtained from initial rates on zeolites in their H-form pretreated in H_2 and with H_2 present in the inlet stream are consistent with protolytic pathways at H^+ sites, given that carbonium ion-like transition states for these parallel pathways differ in energy in a manner proportional to the difference in the ensemble-averaged proton affinity of the C-C and C-H bonds in gaseous propane (25–40 kJ mol^{-1}) [172, 173]. Such H_2 pretreatments and the presence of added H_2 represent atypical situations in the practice of protolytic alkane activation [49, 101–105].

Figure 3.6 shows steady-state ethene and propene formation rates on H-form zeolites (without co-fed products) in the semi-logarithmic form appropriate for Arrhenius-type rate dependences. The corresponding activation energies and entropies are reported in Table 3.3. Measured cracking activation energies (153-169 kJ mol^{-1}, Table 3.3) are similar to those previously attributed to protolytic cracking (150-164 kJ mol^{-1}, Table 3.2) on the four most Al-dense samples (H-MFI-17, H-MFI-43, H-MOR-10, H-CHA-16). Measured cracking activation energies were lower on the most Al-dilute sample (H-MFI-140, 143 kJ mol^{-1}, Table 3.3) that contains the highest density of H^+-free voids (Table 3.1) and thus extrinsic carbonaceous deposits, which appear to generate minority amounts of ethene that become detectable when proton sites are essentially absent. In contrast, dehydrogenation activation energies differed significantly among these samples (67-214 kJ mol^{-1}; Table 3.3) with some zeolites exhibiting deviations from Arrhenius-type behavior (Figure 3.6), in line with the literature discord about measured dehydrogenation barriers on H-form zeolites (65-202 kJ mol^{-1} [49, 101–105]).

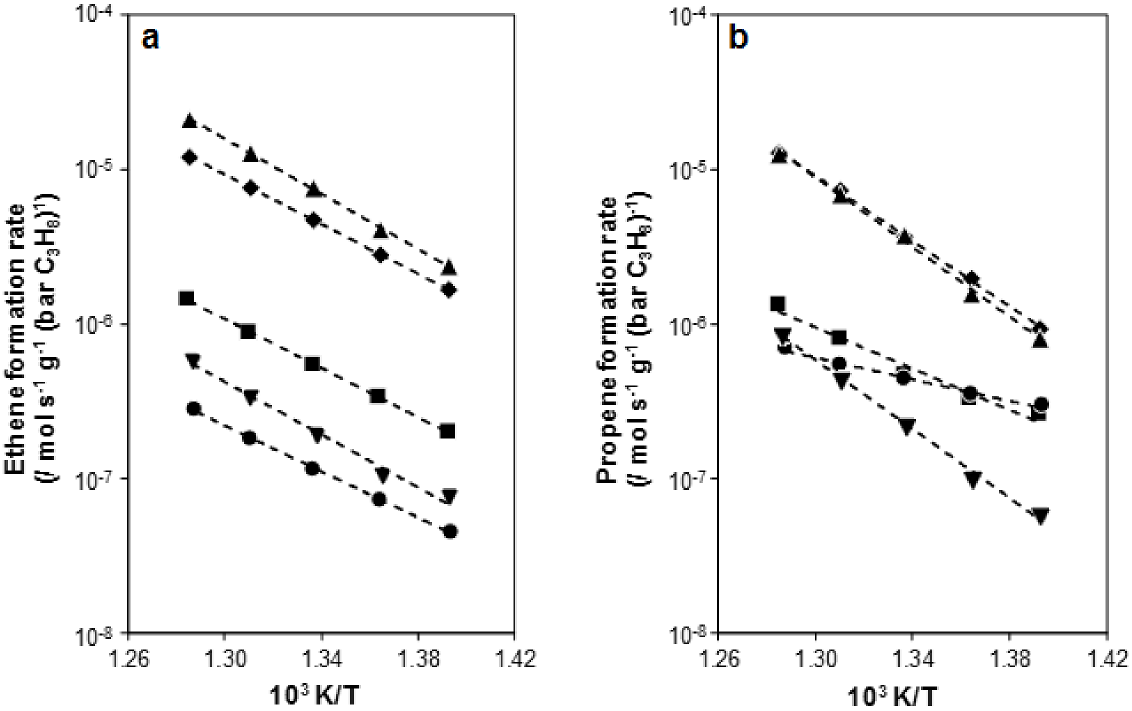

Figure 3.6.: Arrhenius plots for steady-state (a) ethene and (b) propene formation rates on H-MFI-17 (◆), H-MFI-43 (■), H-MFI-140 (●), H-MOR-10 (▲), and H-CHA-16 (▼). Rates collected from 718–778 K at propane pressures of 0.6–2.2 kPa.

Table 3.3.: Measured activation energies and entropies for steady-state propane cracking and dehydrogenation measured without co-fed products on H-form zeolites.

	H-MFI-17	H-MFI-43	H-MFI-140	H-MOR-10	H-CHA-16
			Cracking		
$E^{a}_{meas,C}$	154	153	143	169	164
$\Delta S^{b}_{meas,C}$	-89	-100	-122	-82	-103
			Dehydrogenation		
$E^{a}_{meas,C}$	202	125	67	208	214
$\Delta S^{b}_{meas,D}$	-27	-140	-210	-26	-35

[a] Units of kJ mol^{-1}; Uncertainty is ± 8 kJ mol^{-1}.

[b] Units of J mol^{-1} K^{-1}; Uncertainty is ± 10 J mol^{-1} K^{-1}.

On all samples (except H-MFI-140), measured activation entropies for propane cracking (-103 – -82 J mol^{-1} K^{-1}) are similar to values reported previously for propane cracking on H-form zeolites by Gounder and Iglesia (-109 – -89 J mol^{-1} K^{-1}) [49]. Propane adsorption at protons present within MFI voids results in significant entropy losses (-102 – -82 J mol^{-1} K^{-1}) as estimated by experiment using microcalorimetry and gravimetry [47,190], and as also calculated using statistical mechanics treatments for mobile adsorbates (-100 – -70 J mol^{-1} K^{-1}) [190]. Entropic gains are negligible when adsorbed propane subsequently forms its cracking transition state, according to statistical mechanics estimates of the entropy associated with the one-dimensional rotational degrees of freedom about the C-C bond being cleaved in propane that are accessed by product C_1 and C_2 molecular fragments in the $(C\text{-}C\text{-}H)^+$ carbonium-ion-like transition state [158]. These net changes in entropy upon propane adsorption and subsequent formation of the relevant cracking transition state are consistent with the measured activation entropies of about -100 J mol^{-1} K^{-1} (Table 3.3).

Carbonium-ion-like transition states for propane dehydrogenation occur later along their reaction coordinates than for propane cracking and are more loosely bound and product-like [191]. Consequently, dehydrogenation activation entropies are less negative than for cracking. Indeed, measured activation entropies for dehydrogenation

(-35 – -26 J mol^{-1} K^{-1}, Table 3.3) are less negative than for cracking on all samples that showed higher measured barriers for dehydrogenation than for cracking (H-MFI-17, H-MOR-10, H-CHA-16; Table 3.3), as expected from the exclusive involvement of protolytic alkane activation in such samples. In contrast, measured dehydrogenation activation entropies (-140 – -210 J mol^{-1} K^{-1}) are significantly more negative than for cracking on samples (H-MFI-43, H-MFI-140; Table 3.3) that also showed dehydrogenation barriers much lower than expected for protolytic reactions at H^+ sites. Such aberrantly low values of measured dehydrogenation activation entropies serve to diagnose the presence of non-protonic functions, and reflect both the incorrect normalization of dehydrogenation rates by proton sites and the non-carbonium-ion-like nature of the transition states formed.

These data show that the evolution of the reaction-derived extrinsic active sites in number and composition influences dehydrogenation rates and their temperature dependence; such extrinsic sites lead to significant contributions to measured rates, which tend to obscure the contributions from monomolecular proton-catalyzed events and to do so to different extents with changes in reaction temperature. Such effects account for the prevalent literature discord, but contributions from extrinsic sites cannot be retroactively extracted from such data, because the number and structure of extrinsic sites depend on the reaction environment (temperature, reactant and product concentrations), on the temporal and thermal history of the samples, and even on how axial mixing effects influence product concentrations along the catalyst bed. These are important details that are seldom reported with the detail required for such a forensic analysis.

Measured dehydrogenation activation energies and entropies (Table 3.3) from steady-state rate data also systematically decrease with increasing Si/Al ratio on H-MFI zeolites. Measured barriers on H-MFI-17, H-MOR-10, and H-CHA-16 were similar with H_2 co-feeds (189-210 kJ mol^{-1}) and without H_2 co-feeds (202-208 kJ mol^{-1}). In contrast, measured barriers on H-MFI-43 and H-MFI-140 were lower without co-fed products (67-125 kJ mol^{-1}) than with H_2 co-feeds at initial time-on-stream (193-200 kJ mol^{-1}), which are conditions that suppress extrinsic functions. These data indicate that the contributions from extrinsic reaction-derived active functions to dehydrogenation rates increase proportionally with the fraction of siliceous regions within zeolites, and become essentially undetectable on proton-dense zeolites (Si/Al $\sim$ 10-16, Table 3.3).

3.4.5 Measurements of propene hydrogenation barriers at H^+ sites and predictions of protolytic dehydrogenation barriers from De Donder relations

The rate constants for stoichiometric chemical reactions in their forward and reverse directions, when measured under different reaction conditions that lie far away from equilibrium on either side, are related by the equilibrium constant for the overall reaction, for systems in which sites are predominantly bare and the same kinetically-relevant step prevails in both directions; such requirements are met for propane dehydrogenation and propene hydrogenation rates on H-form zeolites [192].

Propene hydrogenation rates (748 K, per H^+) measured at high H_2 pressures (>60 kPa) and large H_2/C_3H_6 molar ratios (>1000) reflect exclusive contributions from proton-catalyzed pathways because contributions from extrinsic active sites for dehydrogenation (and for its reverse hydrogenation) are suppressed by H_2. Together with reversibility treatments based on De Donder relations between chemical affinities for elementary steps and their equilibrium and rate constants [192], propene hydrogenation rates can be used to confirm that propane dehydrogenation rates measured at the conditions of the experiments reported in Section 3.4.1 indeed solely reflect proton-catalyzed contributions and the high activation barriers characteristic of such routes.

Measured propene hydrogenation rates (748 K, per H^+) increased linearly with both C_3H_6 and H_2 pressures on H-form zeolites (Figure 3.38, Section 3.6.11), consistent with previous reports at similar conditions (748 K, 1-4 kPa C_3H_6, 10-100 kPa H_2) [192]. Such kinetic behavior indicates that protons remain essentially bare at the conditions of catalysis, leading to the rate equation:

$$r_H = k_{meas,H} P_{C_3H_6} P_{H_2} \tag{3.2}$$

where r_H is the propene hydrogenation rate and $k_{meas,H}$ is the second-order hydrogenation rate constant. This equation also shows that the kinetically-relevant transition state for hydrogenation contains the same number and type of atoms as a propene and H_2 molecule and an H^+ site, as is also the case for the transition state that mediates monomolecular dehydrogenation (i.e., the same number and type of atoms as in a propane molecule and an H^+ site). The essentially uncovered nature of the protons during both dehydrogenation and hydrogenation reactions and the requisite De Donder relations lead to propane dehydrogenation and propene hydrogenation rates with rate constant ratios that merely reflect the equilibrium constant for the overall dehydrogenation chemical reaction:

$$K_r = \frac{k_{meas,D}}{k_{meas,H}} \tag{3.3}$$

(K_r is the reaction equilibrium constant; 0.017 bar at 748 K [192]).

The number and/or reactivity of the extrinsic carbonaceous active sites are suppressed at the high H_2 pressures (>60 kPa) and H_2/C_3H_6 molar ratios (>2000) used to measure propene hydrogenation rates, as evident in $k_{meas,H}$ values for H-MFI-17 that remained essentially invariant (within a factor of 1.2) with time-on-stream at all reactant alkene and H_2 pressures and site contact times (Figure 3.39, Section 3.6.11). The $k_{meas,H}$ values (obtained by regression of rate data to the functional form of Eq. 3.2) are plotted on the abscissa of Figure 3.7; these values solely reflect propene hydrogenation at H^+ sites. The dashed line in Figure 3.7 represents the predicted values of $k_{meas,D}$ from propane dehydrogenation reactions at H^+ sites, using measured $k_{meas,H}$ values and K_r in the manner dictated by Equation 3.3. Values of $k_{meas,D}$ measured on the same samples, but at different inlet propane and H_2 pressures (Table 3.2), are plotted as closed symbols in Figure 3.7; these values are identical, within experimental error, to those predicted from measured $k_{meas,H}$ values and Equation 3.3, confirming that propane dehydrogenation rates measured at initial time-on-stream on H-zeolites pretreated in H_2 and with H_2 co-feeds solely reflect protolytic reactions. In contrast, propane dehydrogenation rates measured on the same samples at steady-state but without co-fed H_2 (Figure 3.31), after normalization by propane pressure to estimate values of $k_{meas,D}$, are plotted as open symbols in Figure 3.7; these values are higher than those predicted from protolytic dehydrogenation reactions at H^+ sites because they also contain additional contributions from dehydrogenation reactions at extrinsic active sites that do not contribute to hydrogenation rates at the H_2 pressures used for their measurements. Thus, the lower activation energies for propane dehydrogenation estimated from steady-state rate data (Figure 3.6) are corrupted by additional contributions from lower barrier alkane H-transfer pathways at carbonaceous active sites.

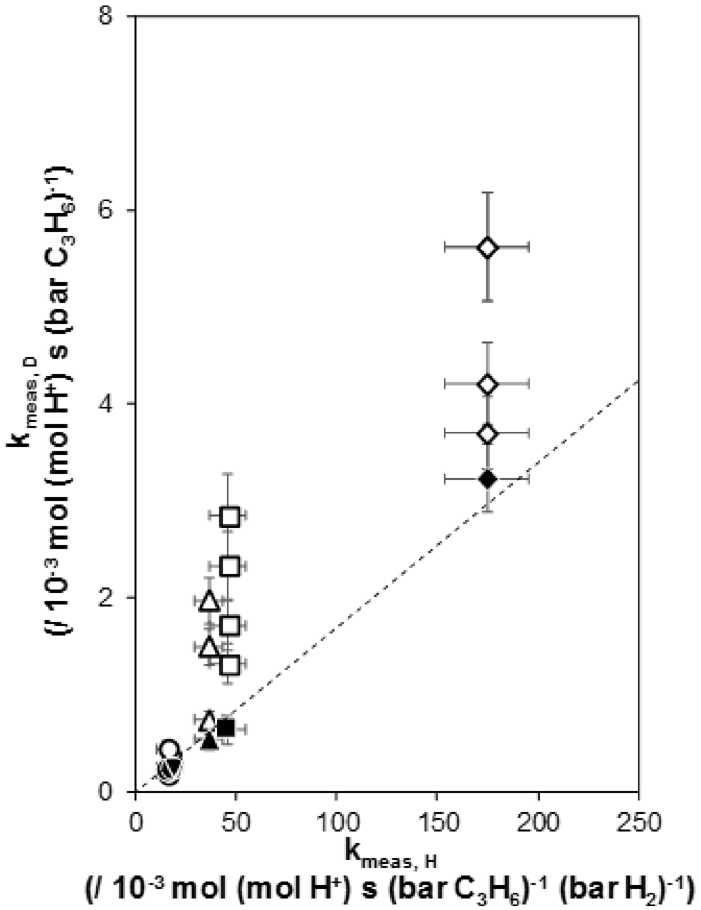

Figure 3.7.: Measured second-order rate constants for propene hydrogenation and first-order rate constants for propane dehydrogenation (748 K, per H^+) on H-MFI-17 (◆), H-MFI-43 (■), H-MFI-140 (●), H-MOR-10 (▲), and H-CHA-16 (▼) at initial time-on-stream with H_2 co-feeds (closed symbols) and at steady-state in the absence of co-fed products (open symbols). Dashed line represents the $k_{meas,D}$ values predicted from measured $k_{meas,H}$ values and K_r (0.017 bar [192]) using Equation 3.3.

3.4.6 Extrinsic dehydrogenation sites: their role in discrepancies in reported turnover rates and activation barriers and a "prescription" for isolating only proton-catalyzed dehydrogenation rates

The initial decrease in dehydrogenation rates during reactions on H-form zeolites treated in O_2 (Figure 3.4a; Figure 3.29, Section 3.6.7) has also been reported for *n*-butane dehydrogenation (773-803 K) on H-MFI and H-FAU [100, 101, 193]. In these studies, dehydrogenation rates reached constant values at shorter times when H-FAU was treated with NH_4OH to dissolve non-framework Al species, but cracking rates were unaffected by such treatments, leading to the proposal that such extraframework Al species selectively catalyze dehydrogenation before being covered by hydrogen [101,193]. Yet, butane dehydrogenation rates decreased to similar extents (about five-fold) from initial to steady-state values on both samples, suggesting that the NH_4OH treatments of H-FAU did not change the number of non-protolytic active sites. The transient decay of dehydrogenation rates to their constant values became longer with decreasing bed residence time [101], however, consistent with the transient changes in dehydrogenation rates with residence time reported here (Figure 3.30). Such residence time effects may account for the different transient dehydrogenation rates observed on H-FAU zeolites before and after NH_4OH treatments [101]. These authors proposed a non-protonic Al site that is intrinsic to the parent aluminosilicate material, and its strong titration by H_2 that would be unexpected at the high temperatures (>773 K) and low H_2 pressures (<1 kPa) typical of protolytic activation, as the source of transient decay in alkane dehydrogenation rates at initial time-on-stream before reaching steady-state rates through protolytic reactions.

The role of extraframework Al as an additional dehydrogenation function and its full titration by H_2 [101], however, are inconsistent with propene formation rates from propane/H_2 mixtures that depend on time-on-stream when 20 kPa H_2 is present in the inlet stream (Figures 3.11-3.15, Section 3.6.2); these co-fed H_2 pressures are much higher than product H_2 pressures (<1 kPa) formed from protolytic propane reactions. The previous proposal that non-protolytic active sites are fully inhibited during steady-state dehydrogenation rate measurements seems consistent with their reported first-order dependence on alkane pressure and the absence of product inhibition [101], but contradicts our findings about the strong inhibition by products of steady-state rates (Figure 3.31, Section 3.6.7), as well as the excess CH_4 evolved after propane is removed from mixed C_3H_8/H_2 reactant streams (Figure 3.37, Section 3.6.10), which provide compelling evidence for the presence and involvement of organic residues as active sites. The non-equimolar amounts of H_2 and *n*-butane dehydrogenation products (butenes, butadienes) measured in reactor effluents during initial time-on-stream reported previously [101] would also be consistent with the formation of carbonaceous deposits during transient approach to steady-state. Such deposits can undergo changes in composition (to change their H/C ratios) in response to the prevalent fluid-phase chemical potentials, which may also account for previous findings that H_2 forms for a period of time after n-butane was removed from the inlet stream on H-MFI [101].

Thus, we interpret the initial transient decrease in dehydrogenation rates after O_2 pretreatments and in the absence of co-fed H_2 (Figures 3.2a and 3.4a; Figure 3.29) to arise from the formation of organic residues [194] that evolve in composition, as steady-state carbon and hydrogen chemical potentials are attained, to forms that become less effective at catalyzing alkane dehydrogenation. The more gradual increases in dehydrogenation rates at initial times-on-stream with H_2 pretreatments and co-feeds (Figures 3.11-3.15) appear to reflect the slower buildup of unsaturated carbonaceous deposits because the high hydrogen chemical potentials result in hydrogenation of unsaturated organic residues [180, 195]. This interpretation is consistent with our findings that removal of propane from propane/H_2 mixtures results in the removal of unsaturated organic residues to restore H-form zeolites to their states before propane exposure (Figure 3.4c). Thus, we conclude that H_2 co-feeds mitigate the formation and reactivity of carbonaceous deposits at initial time-on-stream, allowing for measurement of protolytic reaction events.

The effects of bed residence time on n-butane dehydrogenation rates for H-MFI zeolites have been previously attributed to competitive binding of alkene products at protons [100]. Inhibition of dehydrogenation rates was also observed when n-butane reactant streams contained added butenes, which equilibrate over H^+ sites to a mixture of isomers [100]. This proposal led these authors to conclude that the intrinsic reactivity of protons in these samples could be captured by merely extrapolating dehydrogenation rates to zero residence time in order to minimize the prevalent concentrations of alkene products [100]. Our data show that, in fact, such an extrapolation to zero residence time leads to the strongest contributions from extrinsic dehydrogenation sites, because their reactivity is inhibited significantly by the presence of H_2 and alkene products, which exist at their lowest concentrations precisely at such short bed residence times. The proposal of competitive binding of alkene products at protons is also inconsistent with n-butane cracking rates that remained invariant with bed residence time and with co-fed butene pressures in the same report [100]. The subsequent study by Li and co-workers [105] also contradicts the proposal of competitive binding of alkenes at protons [100], through the direct *in situ* spectroscopic observations that neither the intensity nor the frequency of the acidic OH infrared bands are affected by the same changes to longer bed residence times that led to significantly lower dehydrogenation rates (618-710 K). These authors accurately concluded that a second active site, whose reactivity was inhibited by products, led to additional dehydrogenation events; they did not, however, provide any further insights into the nature or properties of such sites.

Our studies confirm the presence of an extrinsic dehydrogenation function, unrelated to protons, and consisting of organic residues that depend, in number and reactivity, on the carbon and hydrogen chemical potentials in the contacting fluid phase at each point along the catalyst bed. These findings and interpretations "prescribe" the protocols that are required in order to isolate the contributions from proton-catalyzed dehydrogenation pathways and the turnover rates and kinetic parameters for such protolytic dehydrogenation routes. H-forms of zeolites must be treated in H_2 (803 K, 101 kPa) in order to remove any adventitious residues formed upon contact with ambient air before use. Rates must be measured in the presence of sufficient H_2 (>20 kPa) in the inlet reactant stream, so as to remove (and/or suppress the formation or reactivity of) any reaction-derived dehydrogenation sites. In situations where H_2 is not co-fed, shorter catalyst beds, lower fluid linear velocities, and higher reactant partial pressures will lead to lower Péclet numbers and to higher extents of back-mixing in catalytic packed beds. Such hydrodynamics minimize axial gradients in H_2 pressure and, in turn, mitigate the formation and reactivity of the secondary active site, resulting in measured alkane dehydrogenation rates that predominantly reflect protolytic dehydrogenation events. Measurements of the reverse propene hydrogenation reaction under conditions that suppress the formation of carbonaceous active sites (H_2 >60 kPa, H_2/C_3H_6 >1000), together with predictions from the De Donder relations of non-equilibrium thermodynamics, should be used to confirm that measured propane dehydrogenation rates indeed reflect only contributions from protolytic reactions.

The broad range of dehydrogenation barriers reported here for propane reactant streams without added H_2 (67-214 kJ mol^{-1}, Table 3.3) resemble those reported in previous studies (65-202 kJ mol^{-1} [49, 101–105]), indicative of the ubiquitous but unrecognized contributions of reaction-derived extrinsic active sites and how time-on-stream, product concentrations, and flow hydrodynamics determine the contributions of such extrinsic sites to measured rates. Only the highest measured propane dehydrogenation barriers (∼200 kJ mol^{-1}; Table 3.2) reflect the true dynamics and energetics of proton-catalyzed monomolecular dehydrogenation routes, a conclusion supported by the consistency of such dehydrogenation rates with those of propene hydrogenation rates through their interconversion thermodynamics (Figure 3.7); such values of dehydrogenation barriers are higher than for proton-catalyzed monomolecular cracking (by 25-40 kJ mol^{-1}) as expected from the different proton affinities of C-H and C-C bonds in propane and their relation to measured activation energies using Born-Haber thermochemical cycles [49].

Propane dehydrogenation barriers reported here and in earlier studies indicate that barriers are much lower (by up to 100-150 kJ mol^{-1}) on the organic residues that account for the extrinsic function than on protons. Measured barriers estimated from steady-state propane dehydrogenation rates in the absence of co-fed H_2 decreased systematically from 202 to 67 kJ mol^{-1} with decreasing H^+ density (increasing Si/Al ratio) among H-MFI zeolites, and thus with increasing fractions of proton-free voids in these samples. These observations also rationalize the measurement of propane dehydrogenation barriers on the same H-zeolite samples here (H-MFI-17 and H-MOR-10, Table 3.3) and previously by Gounder and Iglesia [49] at steady-state but without co-fed products that are consistent with protolytic dehydrogenation pathways (∼200 kJ mol^{-1}), because more Al-dense frameworks have fewer proton-free voids available to host unsaturated organic residues that would subsequently contribute to measured dehydrogenation rates. Taken together, these findings indicate that contributions to measured dehydrogenation rates from carbonaceous deposits become more pronounced at lower temperatures and at more dilute Brønsted acid site densities.

The contributions to measured rates from proton-catalyzed routes increase with increasing temperature relative to those from the events mediated by extrinsic sites, because of the higher activation barriers for carbonium-ion mediated routes. As a result, temperature effects on rates can exhibit non-Arrhenius behavior (Figure 3.6b) as also reported previously for propane dehydrogenation on H-CHA [171], and specifically result in systematically decreasing slopes (and thus measured barriers) at lower temperatures as lower barrier dehydrogenation pathways catalyzed by extrinsic sites become more prevalent. This behavior has been previously attributed to new types of intrinsic active functions formed via Brønsted acid site dehydroxylation during high temperature (1073 K) treatments in inert environments; such dehydroxylation was proposed to proceed through heterolytic dehydration and homolytic dehydrogenation routes to form H_2O and H_2, respectively, leaving behind trigonally-coordinated Al sites or radical centers at lattice oxygens [196]. MFI zeolites subject to such high-temperature pretreatments and subsequent exposure to naphthalene showed UV-Visible spectral features for radical centers that was taken as evidence to support the proposal for radical sites formed at lattice O atoms upon Brønsted acid site dehydroxylation [197]. These high-temperature inert treatments resulted in measurements of low propane dehydrogenation barriers on H-CHA zeolites (84-174 kJ mol^{-1}) [171], but were not used here to reproduce these same low barriers, which are instead attributed to contributions from reaction-derived carbonaceous active sites. These high-temperature inert treatments would also cause any carbonaceous debris present to evolve H_2 and become even more unsaturated, potentially leaving behind radical centers on carbonaceous scaffolds that would participate in alkane dehydrogenation, as proposed here.

Proton-catalyzed alkane dehydrogenation reactions on H-form zeolites were originally reported by Haag and Dessau in 1984 [151]; since then, their kinetic details (reaction orders, product inhibition, turnover rates, activation energies, activation entropies) have proven challenging to replicate, with each disparate result fueling a different speculation, whether about the nature of the active function (e.g., non-framework Al) or of the kinetically-relevant steps for protolytic pathways. Our body of work provides compelling evidence for extrinsic (reaction-derived) unsaturated carbonaceous deposits as the origin of non-protolytic alkane dehydrogenation catalyzed in parallel to protolytic pathways on acidic zeolites, without requiring the need to disavow the expected kinetic behavior of proton sites.

3.5 Conclusions

Propane dehydrogenation rates measured on H-form zeolites with co-fed H_2 and extrapolated to the time of initial contact with reactants solely reflect protolytic dehydrogenation events, as evidenced by relative barriers for cracking and dehydrogenation that differ by the gas-phase proton affinities of the reactant C-C and C-H bonds and by the strict first-order dependence of rates on alkane pressure without any inhibition effects by H_2 or propene products. Zeolites acquire an extrinsic active site that forms during exposure to propane reactants and their protolytic reaction products. Such extrinsic sites catalyze propane dehydrogenation with much lower barriers than protons and are inhibited by H_2 and propene products, but they do not detectably contribute to cracking products, allowing turnover rates of cracking reactions to serve as a reporter of the state of proton sites during catalysis. The conditions that form extrinsic active sites are characterized by the essential absence of H_2, allowing samples to acquire a memory of their sojourn at those conditions. The formation and reactivity of extrinsic sites can be mitigated by high H_2 pressures and H_2/alkene ratios, conditions typically used to measure the rates of its reverse reaction (propene hydrogenation), either by the deliberate addition of H_2 to propane reactants or by increasing axial dispersion using beds with a small Péclet number. Such protocols allow the uncorrupted measurements of the rates and kinetic behavior of proton-catalyzed monomolecular alkane dehydrogenation routes.

These extrinsic active sites do not influence propane cracking rates, which at all conditions occur solely at acidic protons. Such extrinsic active sites consist of unsaturated organic residues with an intermediate affinity for H-atoms that allows them to abstract H-atoms from alkanes and then evolve such H-atoms as H_2; in doing so, they catalyze turnovers but adjust their degree of unsaturation and their affinity for H-atoms in response to the prevalent fluid-phase C and H chemical potentials, via elementary steps that resemble hydrogen transfer events. Such H-transfer processes between bound species and gaseous alkanes and alkenes are ubiquitous in zeolite acid catalysis. The findings reported herein provide specific guidance for depositing, removing, or inhibiting the reactivity of these extrinsic organocatalytic residues that mediate hydrogen transfer reactions via routes that occur in parallel with protolytic routes catalyzed by zeolitic protons.

Alkane dehydrogenation at extrinsic carbonaceous active sites provides a unifying explanation for previous observations of non-protolytic dehydrogenation events on acidic zeolites, including reports of product inhibition and measurements of activation energies that vary over a wide range and appear to be unrelated to intrinsic properties of acidic zeolites. Contributions from these reaction-derived sites become more significant at lower temperatures and on zeolites with low H^+ site densities, as well as in reactors with strong bed-scale concentration gradients of reaction products that would otherwise selectively inhibit the reactivity of the extrinsic sites. These data and their interpretation illustrate how lab-scale experimentation under non-differential conditions caused by strong product inhibition leads to hydrodynamic corruptions of kinetic data as a result of the extent of back-mixing. Such artifacts cannot be detected or corrected from literature data because of the dearth of detail about reactor configurations, extent of mixing, and sample history reported when measuring, reporting or interpreting data of purported kinetic origin. This prevents the independent reproduction and the retroactive interpretation of data, thus serving to propagate conflicting reports and hypotheses.

3.6 Supporting Information

3.6.1 Powder X-ray diffraction patterns and adsorption isotherms for zeolite samples

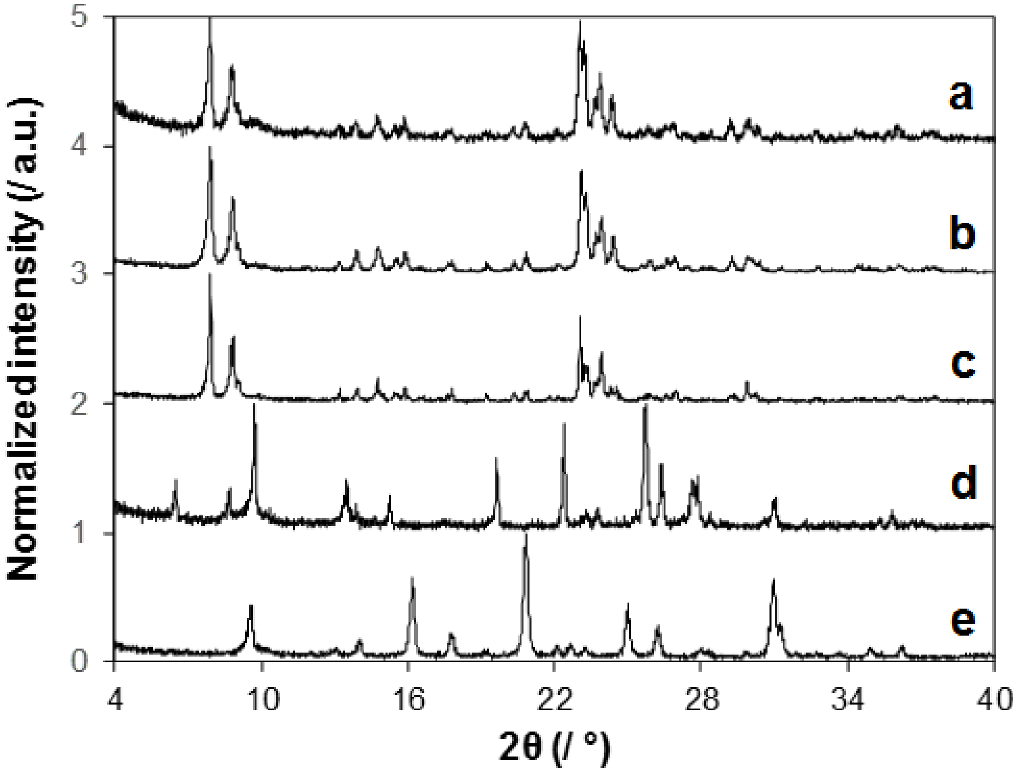

Figure 3.8.: X-ray diffraction patterns of (a) H-MFI-17, (b) H-MFI-43, (c) H-MFI-140, (d) H-MOR-10, and (e) H-CHA-16.

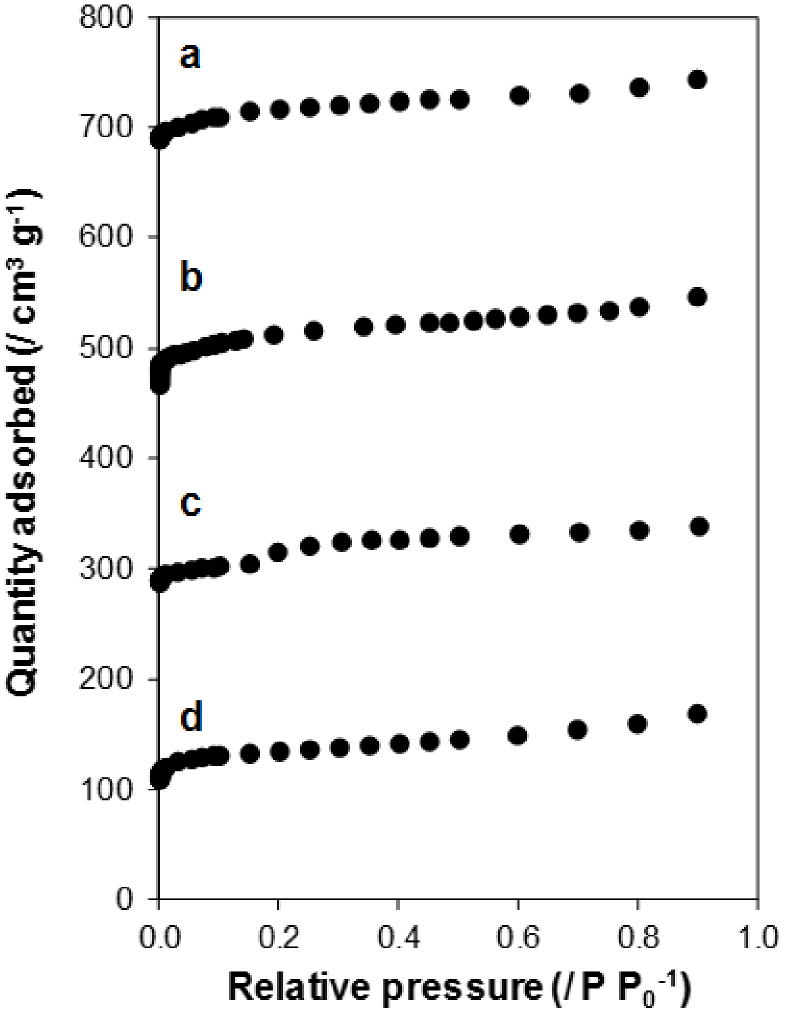

Figure 3.9.: N_2 adsorption isotherms (77 K) for (a) H-MFI-17, (b) H-MFI-43, (c) H-MFI-140, and (d) H-MOR-10. Isotherms are vertically offset by 200 cm^3 g^{-1} for clarity.

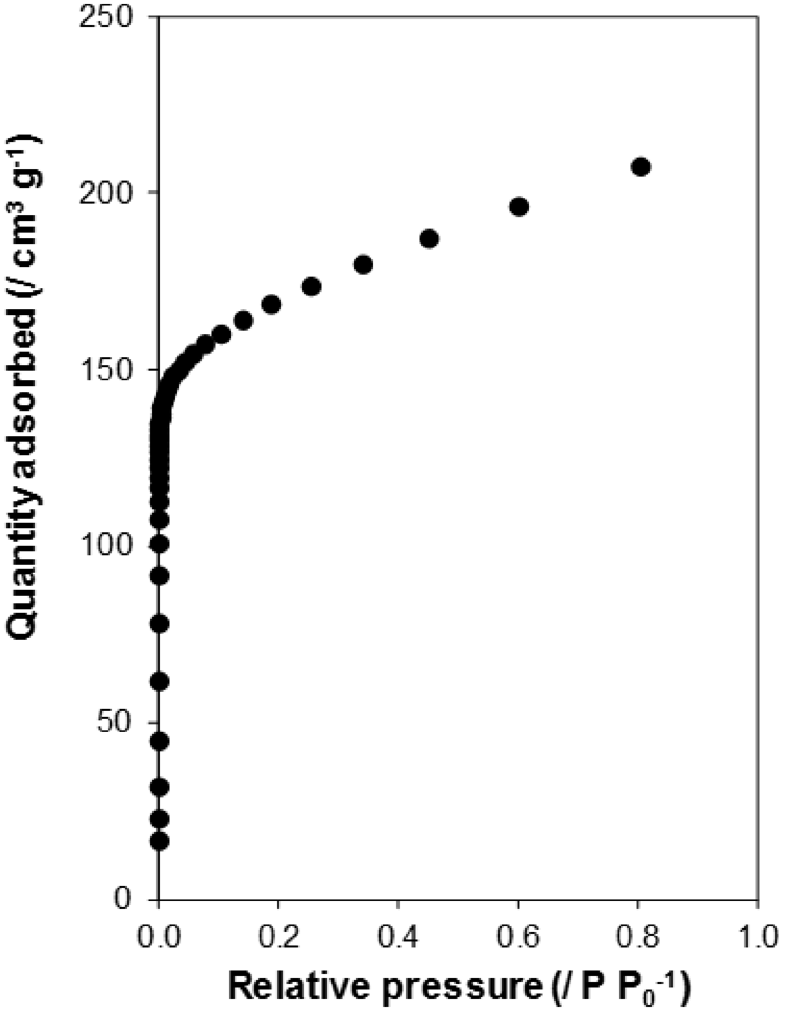

Figure 3.10.: Ar adsorption isotherm (87 K) for H-CHA-16.

3.6.2 Transient propane cracking and dehydrogenation rates on H-form zeolites with H_2 co-feeds

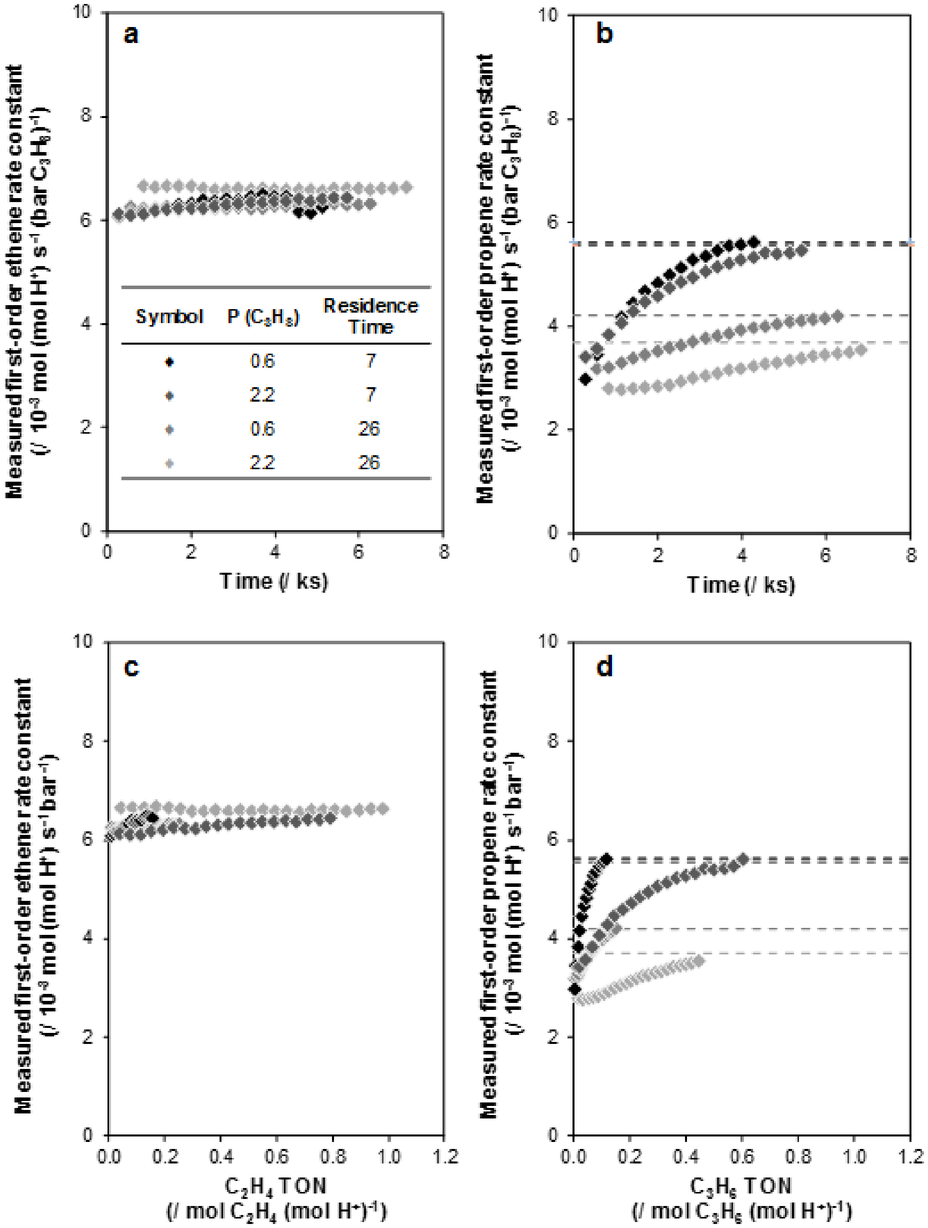

Figure 3.11.: Transient (a, c) ethene and (b, d) propene formation rates (748 K, per H^+) as a function of (a, b) time-on-stream and (c, d) turnover number on H-MFI-17 following pretreatment in 101 kPa H_2 (803 K, 2 h). Rates were measured with 20 kPa co-fed H_2 and at varying C_3H_8 pressures (kPa) and residence times (s (mol H^+) m^{-3}) indicated by the legend in panel (a). Dashed lines of different shades of gray represent steady-state propene formation rates at each respective condition.

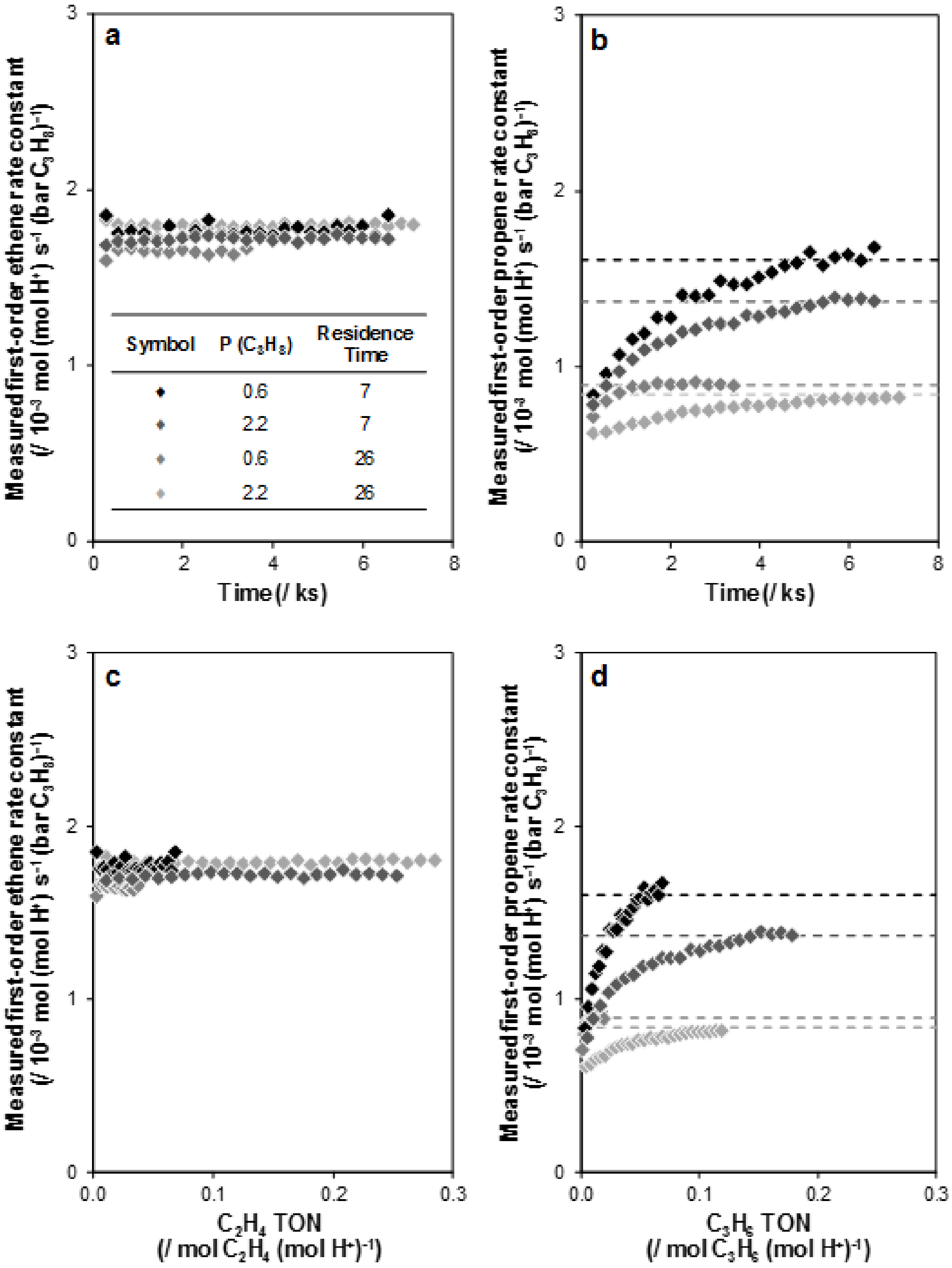

Figure 3.12.: Transient (a, c) ethene and (b, d) propene formation rates (748 K, per H^+) as a function of (a, b) time-on-stream and (c, d) turnover number on H-MFI-43 following pretreatment in 101 kPa H_2 (803 K, 2 h). Rates were measured with 20 kPa co-fed H_2 and at varying C_3H_8 pressures (kPa) and residence times (s (mol H^+) m^{-3}) indicated by the legend in panel (a). Dashed lines of different shades of gray represent steady-state propene formation rates at each respective condition.

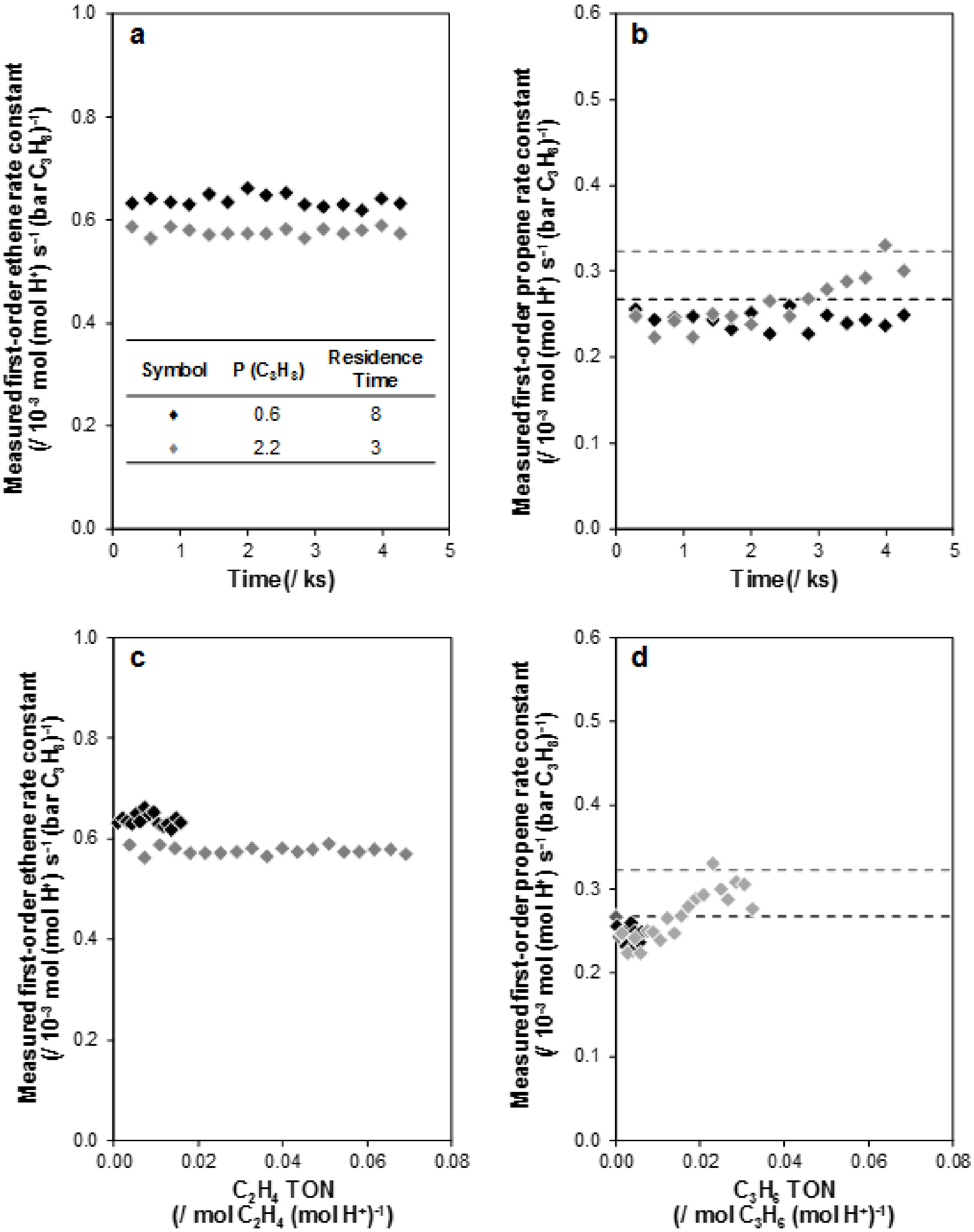

Figure 3.13.: Transient (a, c) ethene and (b, d) propene formation rates (748 K, per H^+) as a function of (a, b) time-on-stream and (c, d) turnover number on H-MFI-140 following pretreatment in 101 kPa H_2 (803 K, 2 h). Rates were measured with 20 kPa co-fed H_2 and at varying C_3H_8 pressures (kPa) and residence times (s (mol H^+) m^{-3}) indicated by the legend in panel (a). Dashed lines of different shades of gray represent steady-state propene formation rates at each respective condition.

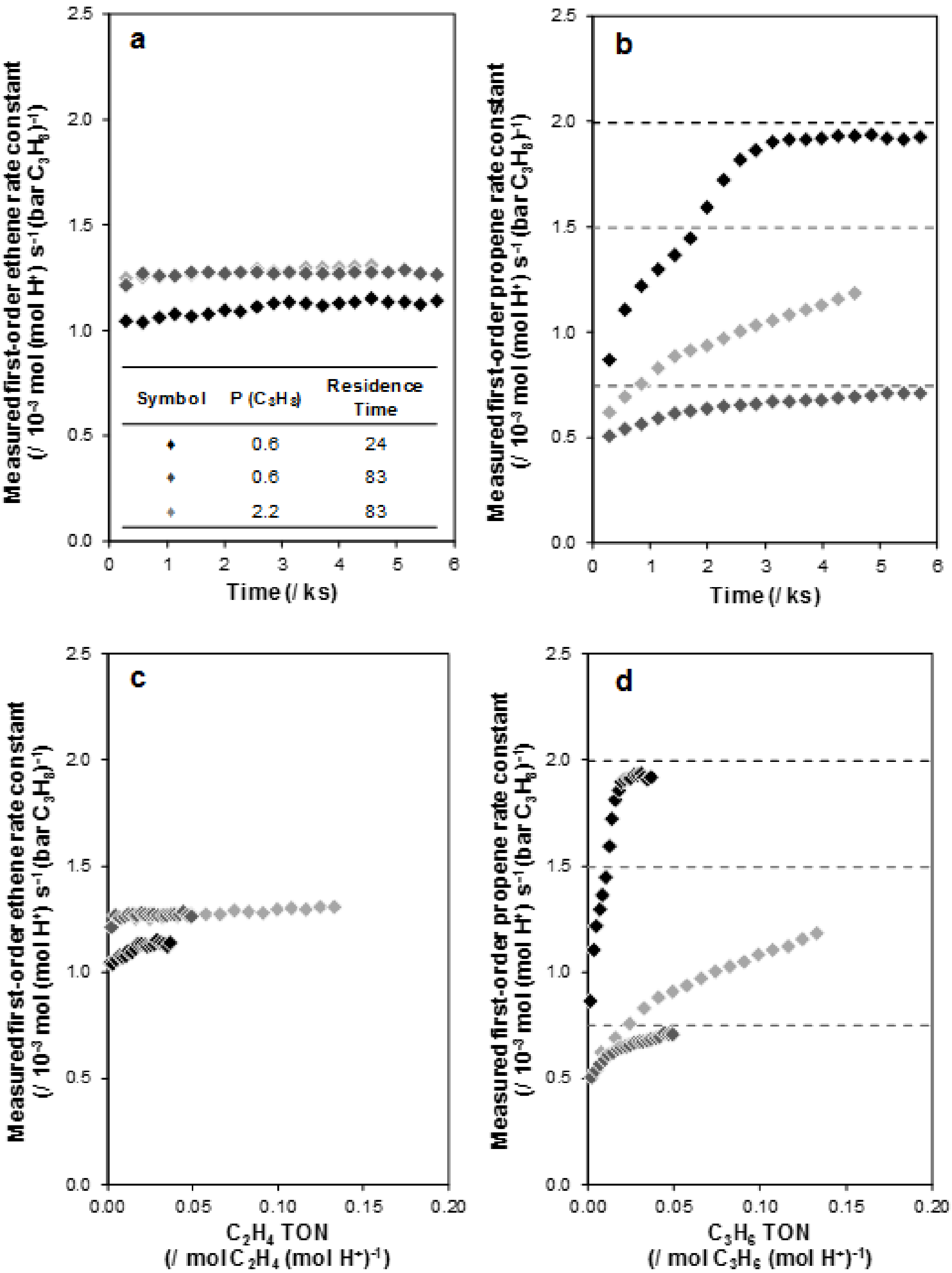

Figure 3.14.: Transient (a, c) ethene and (b, d) propene formation rates (748 K, per H$^+$) as a function of (a, b) time-on-stream and (c, d) turnover number on H-MOR-10 following pretreatment in 101 kPa H$_2$ (803 K, 2 h). Rates were measured with 20 kPa co-fed H$_2$ and at varying C$_3$H$_8$ pressures (kPa) and residence times (s (mol H$^+$) m^{-3}) indicated by the legend in panel (a). Dashed lines of different shades of gray represent steady-state propene formation rates at each respective condition.

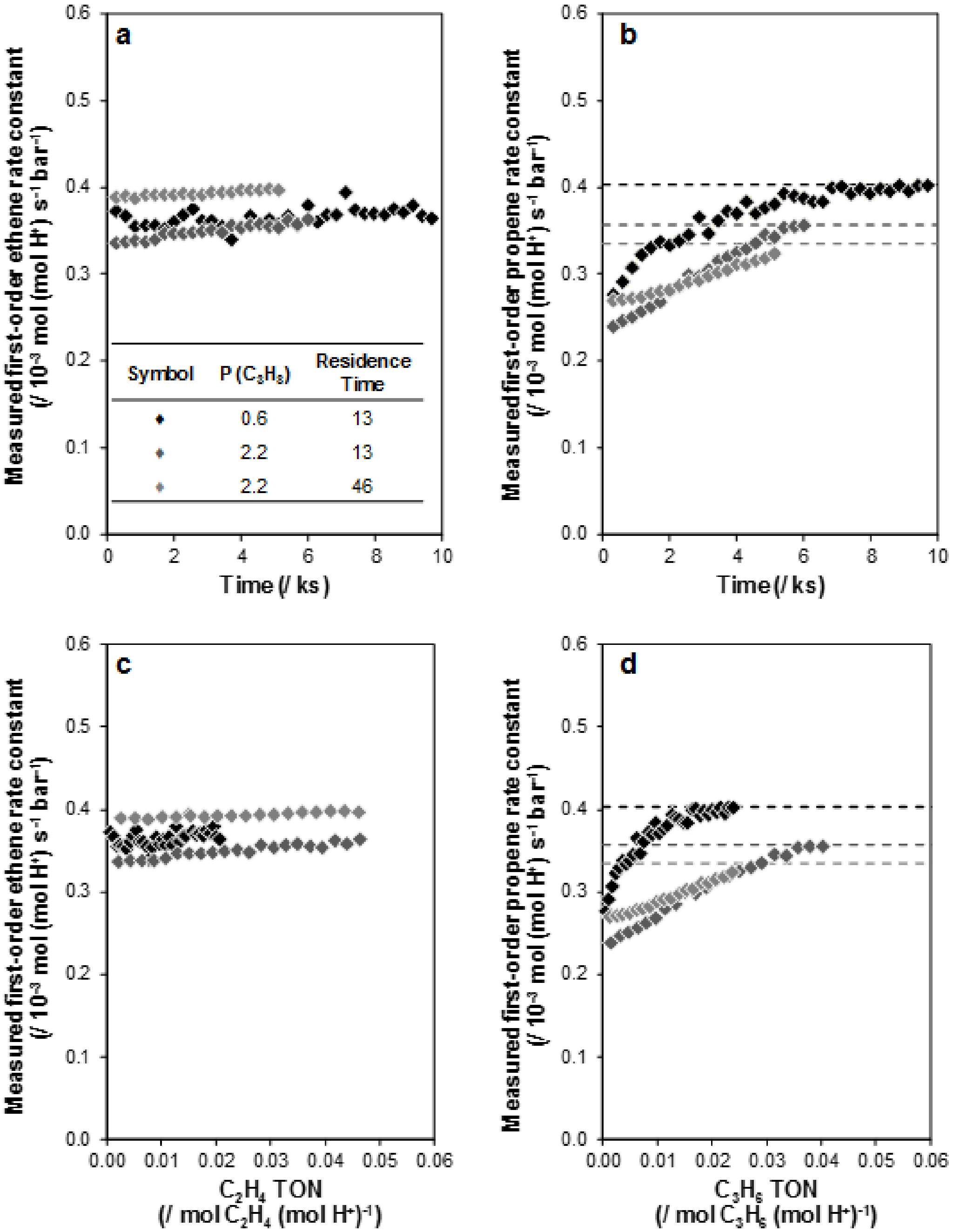

Figure 3.15.: Transient (a, c) ethene and (b, d) propene formation rates (748 K, per H$^+$) as a function of (a, b) time-on-stream and (c, d) turnover number on H-CHA-16 following pretreatment in 101 kPa H_2 (803 K, 2 h). Rates were measured with 20 kPa co-fed H_2 and at varying C_3H_8 pressures (kPa) and residence times (s (mol H$^+$) m^{-3}) indicated by the legend in panel (a). Dashed lines of different shades of gray represent steady-state propene formation rates at each respective condition.

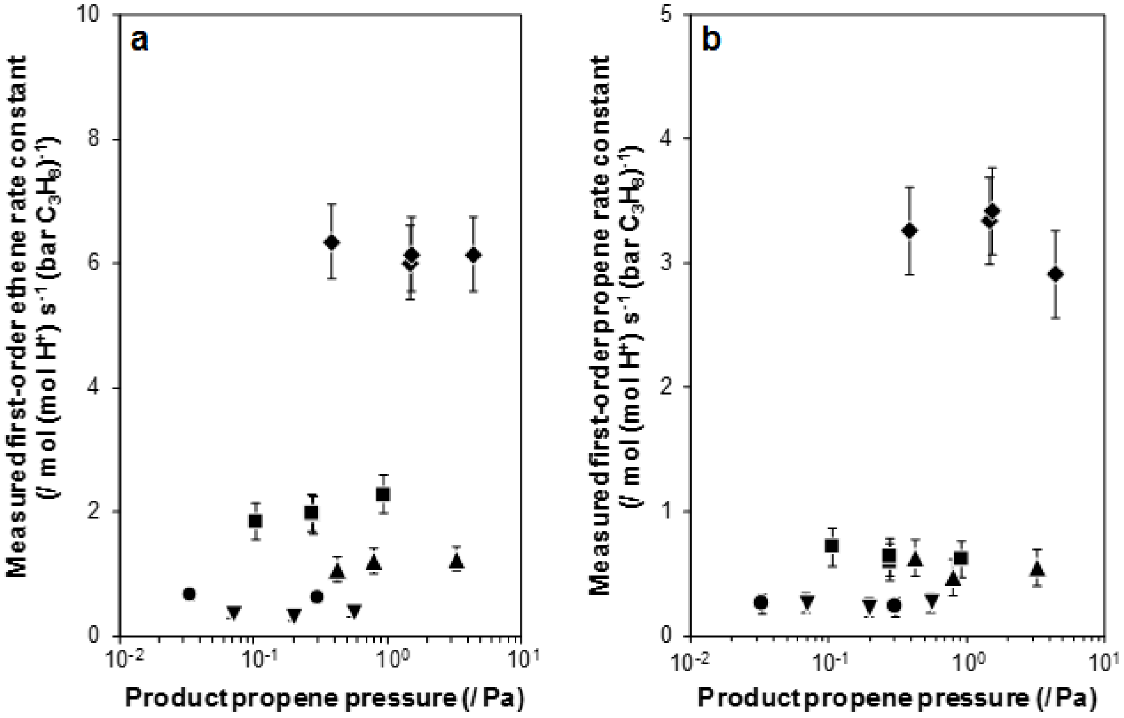

Figure 3.16.: Measured (a) cracking and (b) dehydrogenation first-order rate constants (748 K, per H^+) on H-MFI-17 (◆), H-MFI-43 (■), H-MFI-140 (●), H-MOR-10 (▲), and H-CHA-16 (▼) collected at zero cumulative turnovers following pretreatment in 101 kPa H_2 (803 K, 2 h). Reactant mixtures contained 20 kPa co-fed H_2 and varying C_3H_8 pressures (0.6-2.2 kPa) and site contact times (4-100 s (mol H^+) (mol $C_3H_8)^{-1}$).

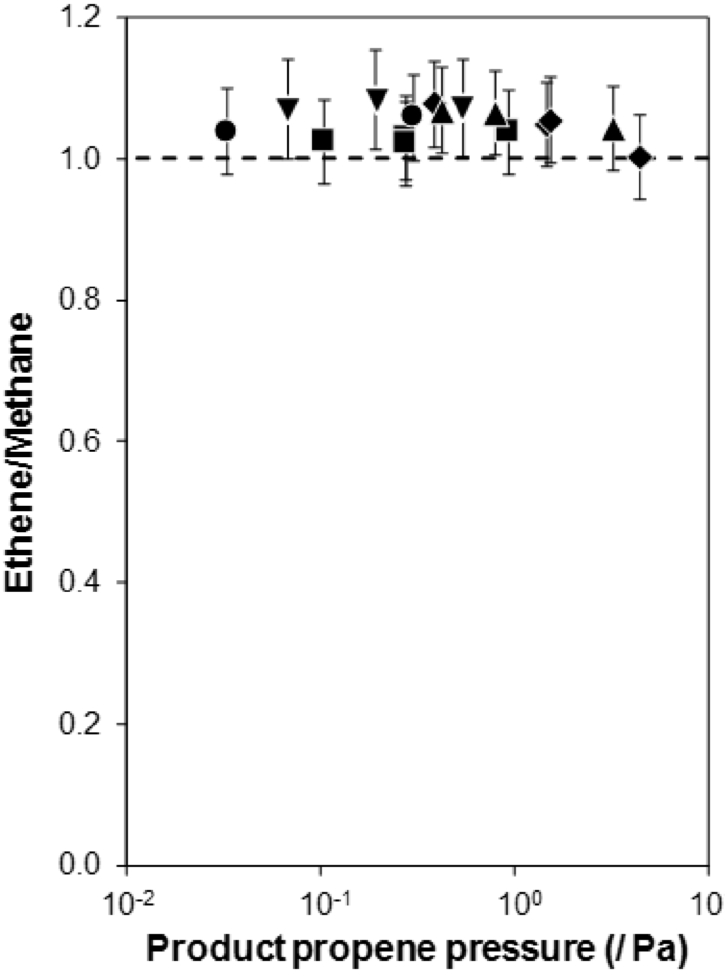

Figure 3.17.: Ethene/methane STY ratios (748 K) at initial time-on-stream on H-MFI-17 (◆), H-MFI-43 (■), H-MFI-140 (●), H-MOR-10 (▲), and H-CHA-16 (▼). Reactant mixtures contained 20 kPa co-fed H_2 and varying C_3H_8 pressures (0.6-2.2 kPa) and site contact times (4-100 s (mol H^+) (mol C_3H_8)$^{-1}$).

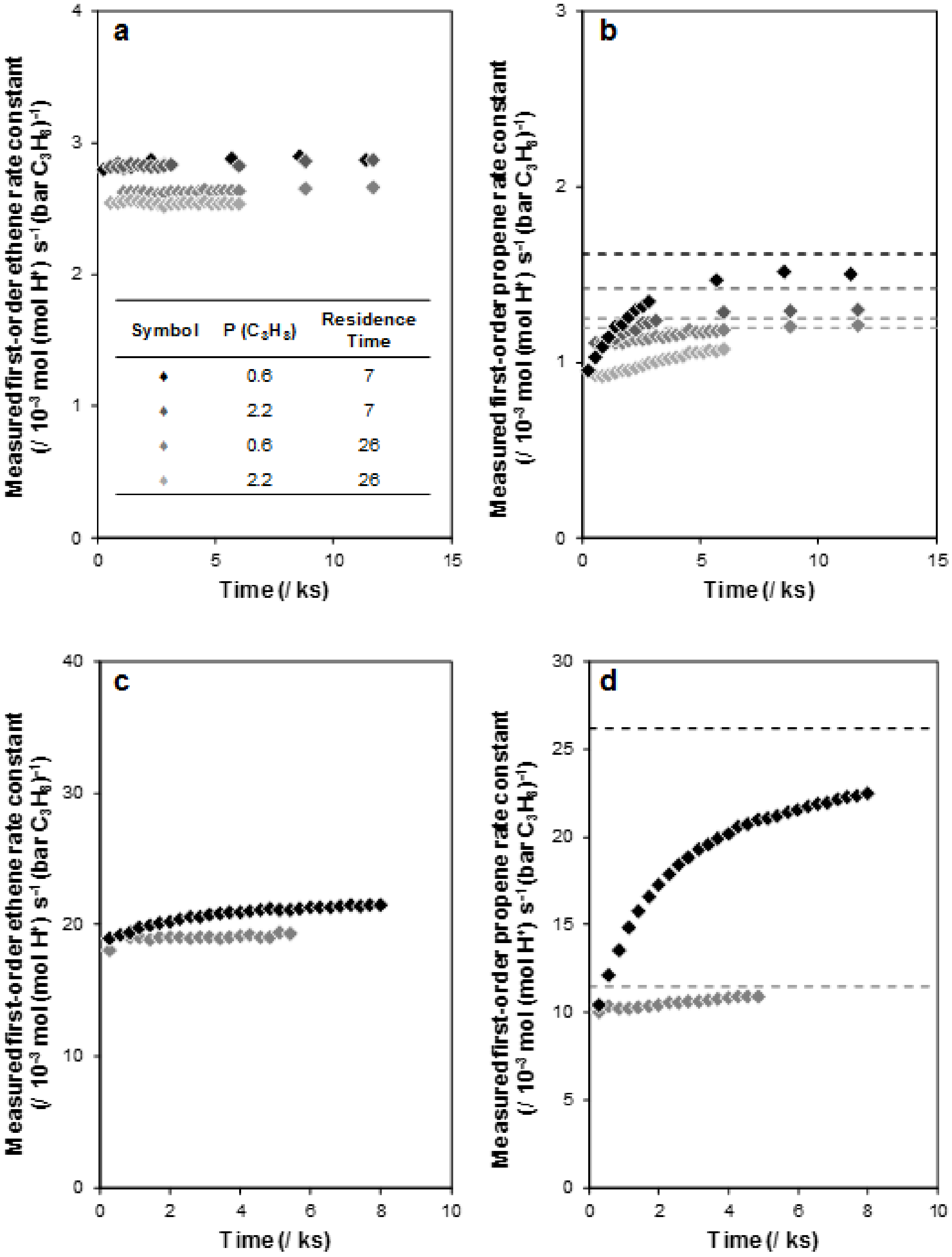

Figure 3.18.: Transient (a, c) ethene and (b, d) propene formation rates (per H^+) at (a, b) 718 K and (c, d) 778 K on H-MFI-17 following pretreatment in 101 kPa H_2 (803 K, 2 h). Rates were measured with 20 kPa co-fed H_2 and at varying C_3H_8 pressures (kPa) and residence times (s (mol H^+) m^{-3}) indicated by the legend in panel (a). Dashed lines of different shades of gray represent steady-state propene formation rates at each respective conditions.

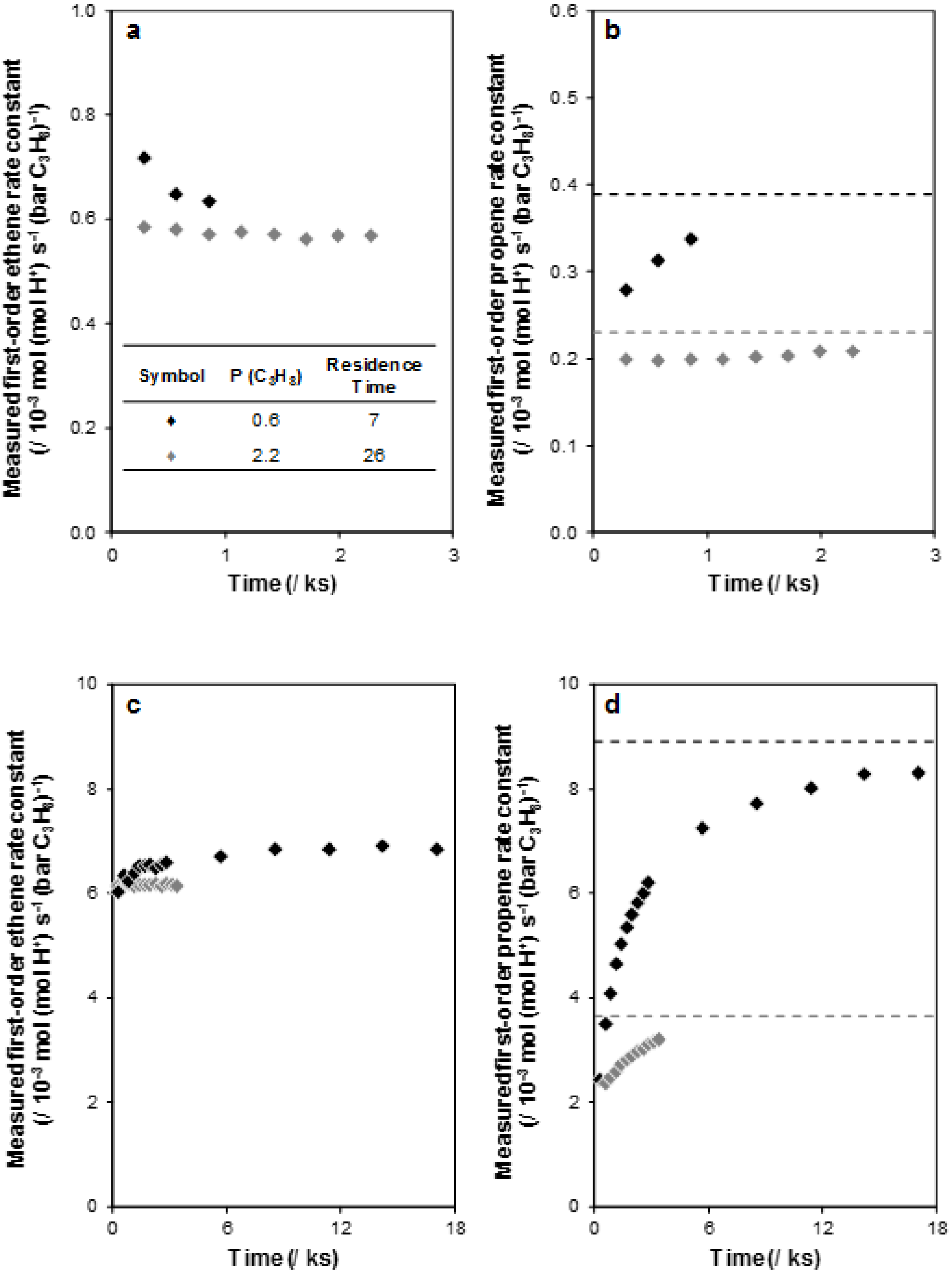

Figure 3.19.: Transient (a, c) ethene and (b, d) propene formation rates (per H^+) at (a, b) 718 K and (c, d) 778 K on H-MFI-43 following pretreatment in 101 kPa H_2 (803 K, 2 h). Rates were measured with 20 kPa co-fed H_2 and at varying C_3H_8 pressures (kPa) and residence times (s (mol H^+) m^{-3}) indicated by the legend in panel (a). Dashed lines of different shades of gray represent steady-state propene formation rates at each respective condition.

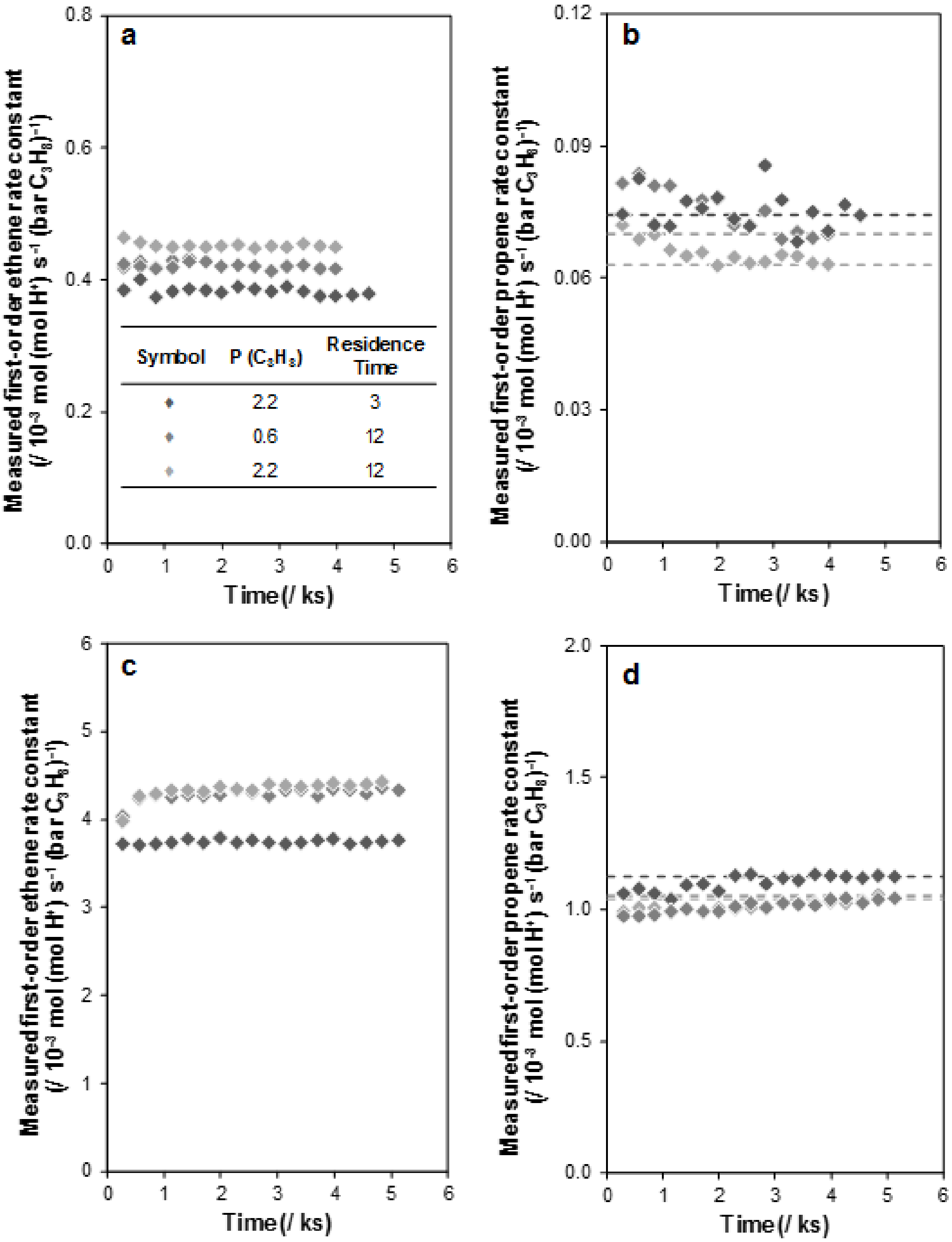

Figure 3.20.: Transient (a, c) ethene and (b, d) propene formation rates (per H^+) at (a, b) 718 K and (c, d) 778 K on H-MFI-140 following pretreatment in 101 kPa H_2 (803 K, 2 h). Rates were measured with 20 kPa co-fed H_2 and at varying C_3H_8 pressures (kPa) and residence times (s (mol H^+) m^{-3}) indicated by the legend in panel (a). Dashed lines of different shades of gray represent steady-state propene formation rates at each respective condition.

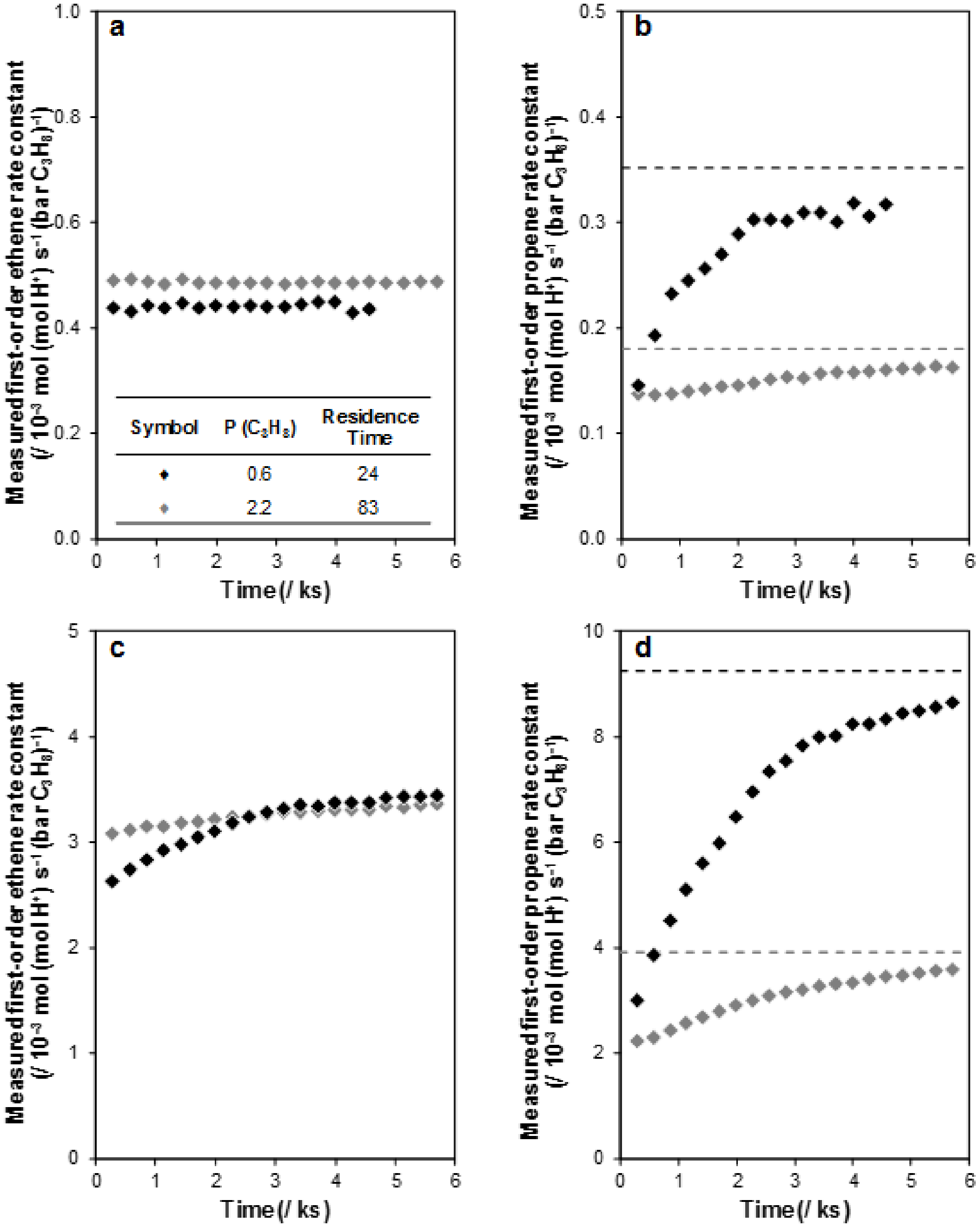

Figure 3.21.: Transient (a, c) ethene and (b, d) propene formation rates (per H^+) at (a, b) 718 K and (c, d) 778 K on H-MOR-10 following pretreatment in 101 kPa H_2 (803 K, 2 h). Rates were measured with 20 kPa co-fed H_2 and at varying C_3H_8 pressures (kPa) and residence times (s (mol H^+) m^{-3}) indicated by the legend in panel (a). Dashed lines of different shades of gray represent steady-state propene formation rates at each respective condition.

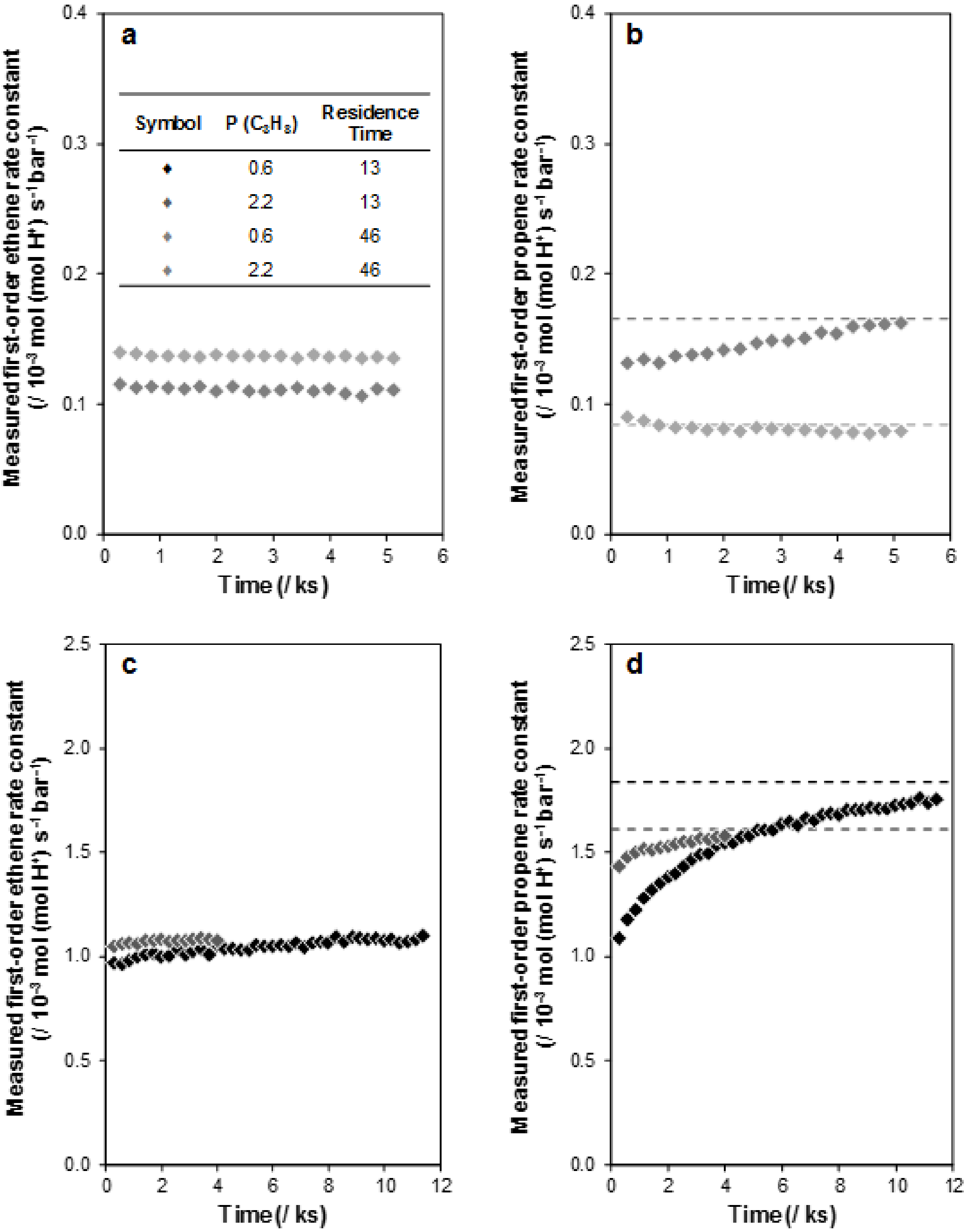

Figure 3.22.: Transient (a, c) ethene and (b, d) propene formation rates (per H^+) at (a, b) 718 K and (c, d) 778 K on H-CHA-16 following pretreatment in 101 kPa H_2 (803 K, 2 h). Rates were measured with 20 kPa co-fed H_2 and at varying C_3H_8 pressures (kPa) and residence times (s (mol H^+) m^{-3}) indicated by the legend in panel (a). Dashed lines of different shades of gray represent steady-state propene formation rates at each respective condition.

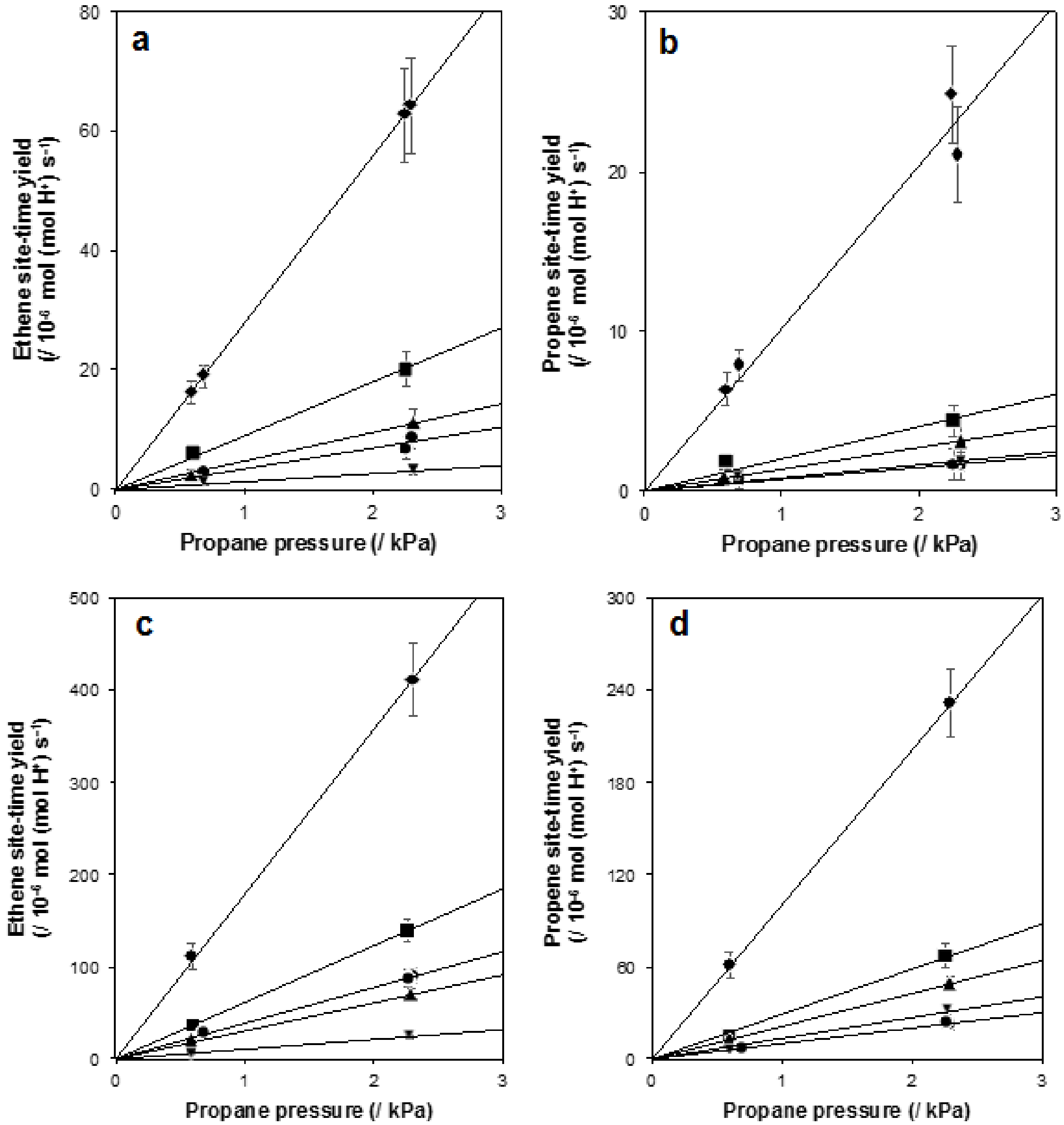

Figure 3.23.: Initial (a, c) ethene and (b, d) propene site-time yields (per H^+) at (a, b) 718 K and (c, d) 778 K on H-MFI-17 (◆), H-MFI-43 (■), H-MFI-140 (●), H-MOR-10 (▲), and H-CHA-16 (▼) following pretreatment in 101 kPa H_2 for 2 h (0.0167 K s^{-1}). Reactant mixture contained 20 kPa H_2. Lines represent regressions to the rate expression in Equation 3.1.

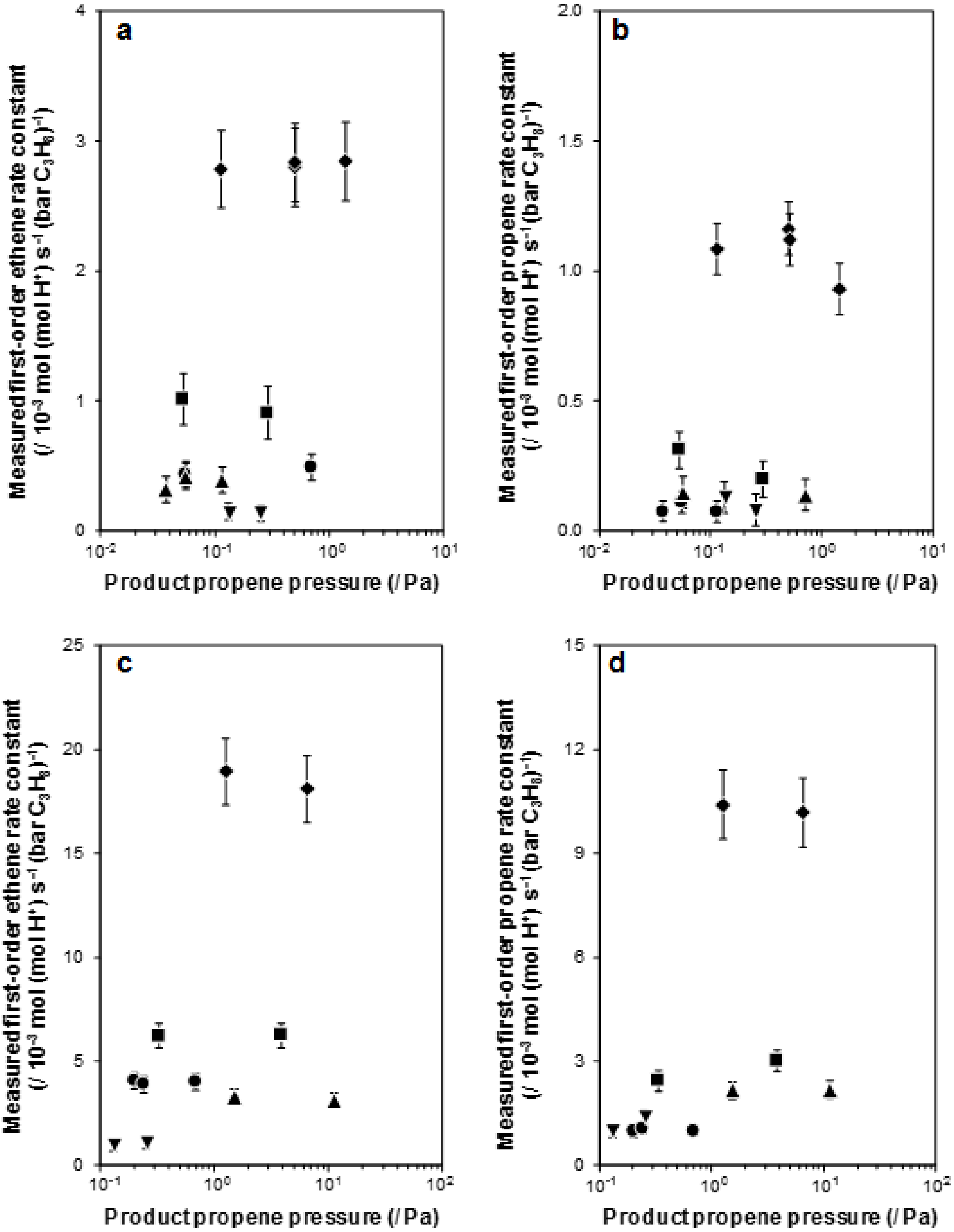

Figure 3.24.: Measured (a, c) cracking and (b, d) dehydrogenation first-order rate constants (per H^+) at (a, b) 718 K and (c, d) 778 K on H-MFI-17 (◆), H-MFI-43 (■), H-MFI-140 (●), H-MOR-10 (▲), and H-CHA-16 (▼) collected at zero cumulative turnovers following pretreatment in 101 kPa H_2 (803 K, 2 h). Reactant mixtures contained 20 kPa co-fed H_2 and varying C_3H_8 pressures (0.6-2.2 kPa) and site contact times (4-100 s (mol H^+) (mol C_3H_8)$^{-1}$).

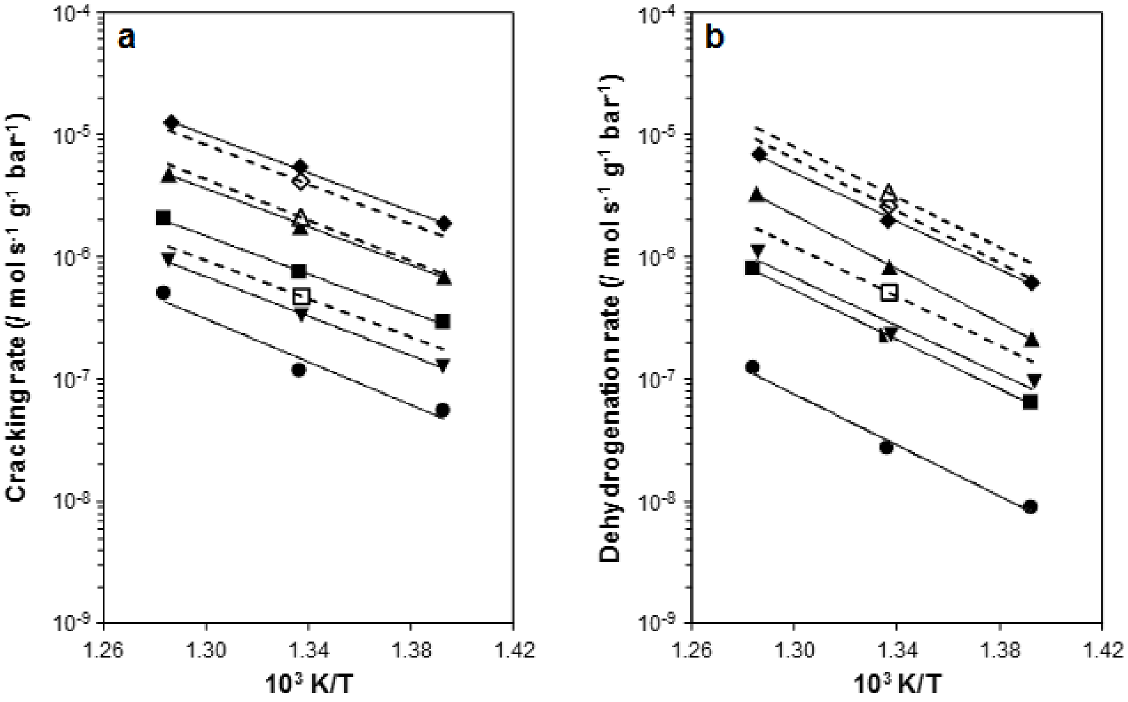

Figure 3.25.: Initial rates for propane (a) cracking and (b) dehydrogenation measured with co-fed H_2 (20 kPa) at varying temperature for H-MFI-17 (◆), H-MFI-43 (■), H-MFI-140 (●), H-MOR-10 (▲), and H-CHA-16 (▼); solid lines represent regression of the data to the Arrhenius equation. Rates reported by Gounder and Iglesia [49] at 748 K (without co-fed H_2) are shown for H-MFI-17, H-MFI-43, and H-MOR-10, with open symbols and dashed lines representing values predicted at different temperatures using the E_{meas} values reported in [49].

3.6.3 Evaluation of equilibrium limitations during propane reactions on H-form zeolites in the presence of product co-feeds

Ethene and propene site-time yields on H-form zeolites were measured in the presence of H_2 co-feeds. These site-time yields must reflect forward reaction rates, and not net rates that may be influenced by reverse reactions imposed by equilibrium limitations, to be treated as turnover frequencies. Here, we show that ethene and propene formation rates were collected far from equilibrium such that contributions of reverse reactions can be neglected, and that measured site-time yields can be treated as forward rates for propane cracking and dehydrogenation reactions.

The net rate of propene and dihydrogen formation from propane can be written as the difference between the forward dehydrogenation rate (r_D) and the reverse hydrogenation reaction (r_H). The net rate is given in equation 3.4, where the forward and reverse reactions are written in terms of their elementary rate expressions [192].

$$r_{net} = r_D - r_H = k_f P_{C_3H_8} - k_r P_{C_3H_6} P_{H_2} \tag{3.4}$$

By normalizing the forward and reverse rate terms by the forward rate, equation 3.4 can be rewritten as follows:

$$r_{net} = k_f P_{C_3H_8}(1 - \frac{k_r P_{C_3H_6} P_{H_2}}{k_f P_{C_3H_8}}) = k_f P_{C_3H_8}(1 - \frac{P_{C_3H_6} P_{H_2}}{K P_{C_3H_8}}) \tag{3.5}$$

where K is the equilibrium constant for this reaction (1.723 kPa at 748 K [192]). The approach-to-equilibrium term, η, is a dimensionless measure of the position of a multicomponent mixture (i.e., that present during catalysis) relative to its thermodynamically equilibrated composition:

$$\eta = \frac{P_{C_3H_6} P_{H_2}}{K P_{C_3H_8}} \tag{3.6}$$

Substituting Eq. 3.6 into Eq. 3.5 yields:

$$r_{net} = k_f P_{C_3H_8}(1 - \eta) = r_f(1 - \eta) \tag{3.7}$$

A value of η close to zero indicates that an experimentally measured net rate predominantly reflects the forward reaction rate. As the value of η increases to unity, the net rate approaches zero and the reaction approaches thermodynamic equilibrium.

The maximum initial C_3H_6 pressure formed in the presence of 2.2 kPa C_3H_8 and 20 kPa H_2 co-feeds was 4.5 Pa on H-MFI-17 (Figure S4). Under these conditions, the value of η is 2.4×10^{-2}. All dehydrogenation rates reported here are forward rates that have been rigorously corrected for approach-to-equilibrium terms using Eq. 3.7.

Analysis of approach-to-equilibrium limitations for propane cracking are analogous to those for propane dehydrogenation. Due to the absence of co-fed cracking products in these experiments and the low propane conversions studied (<5%), values of η for propane cracking are $<10^{-2}$ under all conditions studied.

3.6.4 Born-Haber thermochemical cycles for protolytic alkane reactions on zeolites

Thermochemical cycles provide hypothetical pathways to relate transition state energies to catalyst or molecular properties that are accessible to experimental or computational measurement. One such hypothetical path has been used by Gounder and Iglesia for protolytic alkane cracking and dehydrogenation catalysis on acidic zeolites [49], shown in Figure S1.

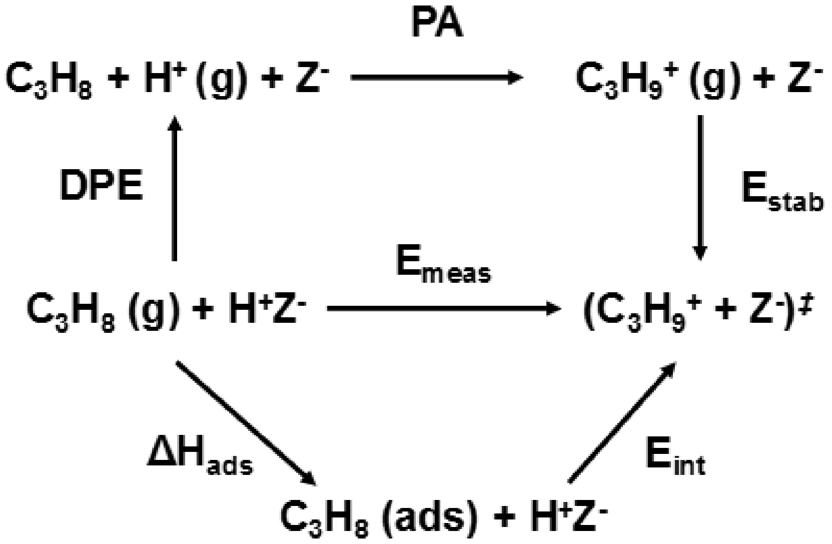

Figure 3.26.: Thermochemical cycle for protolytic propane activation on zeolites. Adapted from Gounder and Iglesia [49].

Measured activation energies (E_{meas}), referenced to gaseous propane and an uncovered active H^+ site, reflect the sum of propane adsorption enthalpies at a Brønsted acid site (ΔH_{ads}) and the protonation of a C-C (for cracking) or C-H (for dehydrogenation) bond to form the carbonium ion-like transition state (E_{int}). Contributions of adsorption enthalpies and intrinsic activation energies cannot be experimentally decoupled under the low pressure (<5 kPa C_3H_8) and high temperature (>700 K) conditions used here, because Brønsted acid protons are predominantly uncovered under reaction conditions (fractional coverage $\sim 10^{-4}$ [49]). Estimates of adsorption enthalpies are obtained experimental measurements at lower temperatures [47] or computational studies [198].

Activation energies in the hypothetical path depend on deprotonation energies (DPE) of Brønsted acid protons, the gas-phase proton affinity (PA) of a C-C (for cracking) or C-H (for dehydrogenation) bond in the reactant alkane, and the stabilization of the carbonium ion transition state through van der Waals interactions with lattice O atoms and electrostatic attraction with the conjugate base (E_{stab}) upon confinement, as given by:

$$E_{meas} = DPE + PA + E_{stab} \tag{3.8}$$

DPE values reflect the stability of the conjugate base upon separation of a proton and zeolite lattice to non-interacting distances, as given by:

$$DPE = E(H^+) + E(Z^-) - E(ZH) \tag{3.9}$$

Differences in measured activation energies for ethene and propene formation are insensitive to DPE, because DPE is independent of reaction pathway and rigorously cancels in ΔE_{meas} expressions. Theoretical treatments of gas-phase propane molecules have estimated that proton affinities of C-C bonds are $\sim$30 kJ mol^{-1} lower than those for C-H bonds [172, 173]. Stabilization of the carbonium ion by the conjugate base can be calculated by DFT, as previously shown for other cationic transition states in microporous solids [50, 52]. Carbonium ion transition states for propane cracking and dehydrogenation are similar in size and charge, and thus E_{stab} should be similar for these transition states to the extent that stabilization from van der Waals interactions with lattice O atoms and electrostatic attraction between the transition state cation and lattice anion are similar [49]. Therefore, differences in protolytic propane dehydrogenation and cracking activation energies of 25-40 kJ mol^{-1} predominantly reflect differences in proton affinity of C-H and C-C bonds in gas-phase propane, and are expected for such reactions on H-form zeolites.

3.6.5 Steady-state propane reaction rates on H-form zeolites with H_2 co-feeds

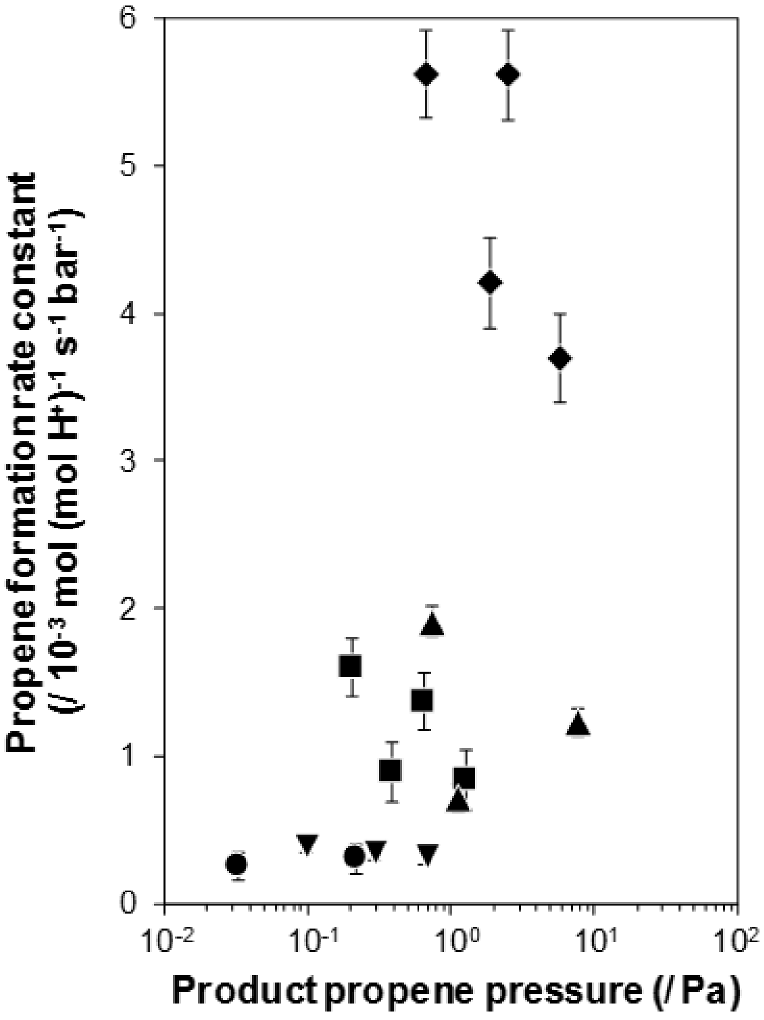

Figure 3.27.: Steady-state propene formation rate constants (748 K, per H^+) on H-MFI-17 (◆), H-MFI-43 (■), H-MFI-140 (●), H-MOR-10 (▲), and H-CHA-16 (▼) in the presence of 20 kPa H_2. Rates were collected at propane pressures of 0.6–2.2 kPa and residence times of 3–83 s (mol H^+) m^{-3}.

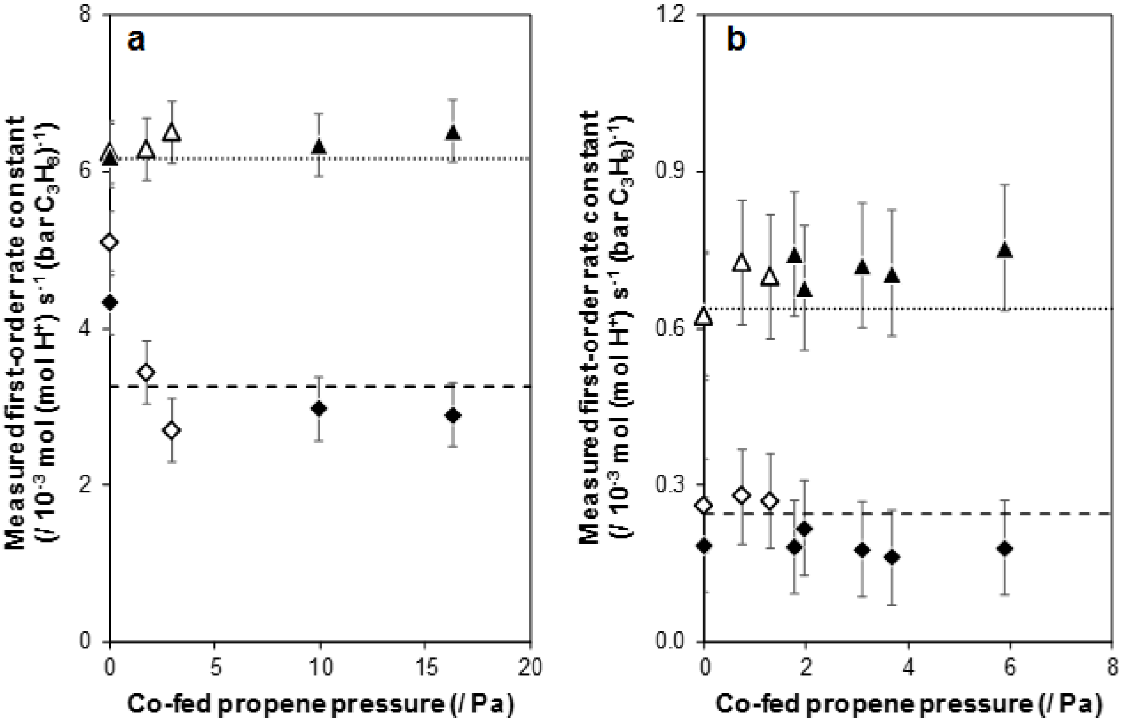

Figure 3.28.: Measured first-order rate constants (748 K, per H^+) for ethene (▲) and propene (◆) on (a) H-MFI-17 and (b) H-MFI-140 as a function of co-fed propene pressure. Rates were collected with 0.6 kPa (open symbols) and 2.2 kPa (closed symbols) C_3H_8 and residence times of 8–43 s (mol H^+) m^{-3}. Dotted and dashed lines correspond to protolytic cracking and dehydrogenation rate constants respectively, reported in Table 3.2.

3.6.7 Transient and steady-state propane reactions on H-form zeolites after oxidative pre-treatments in the absence of co-fed products

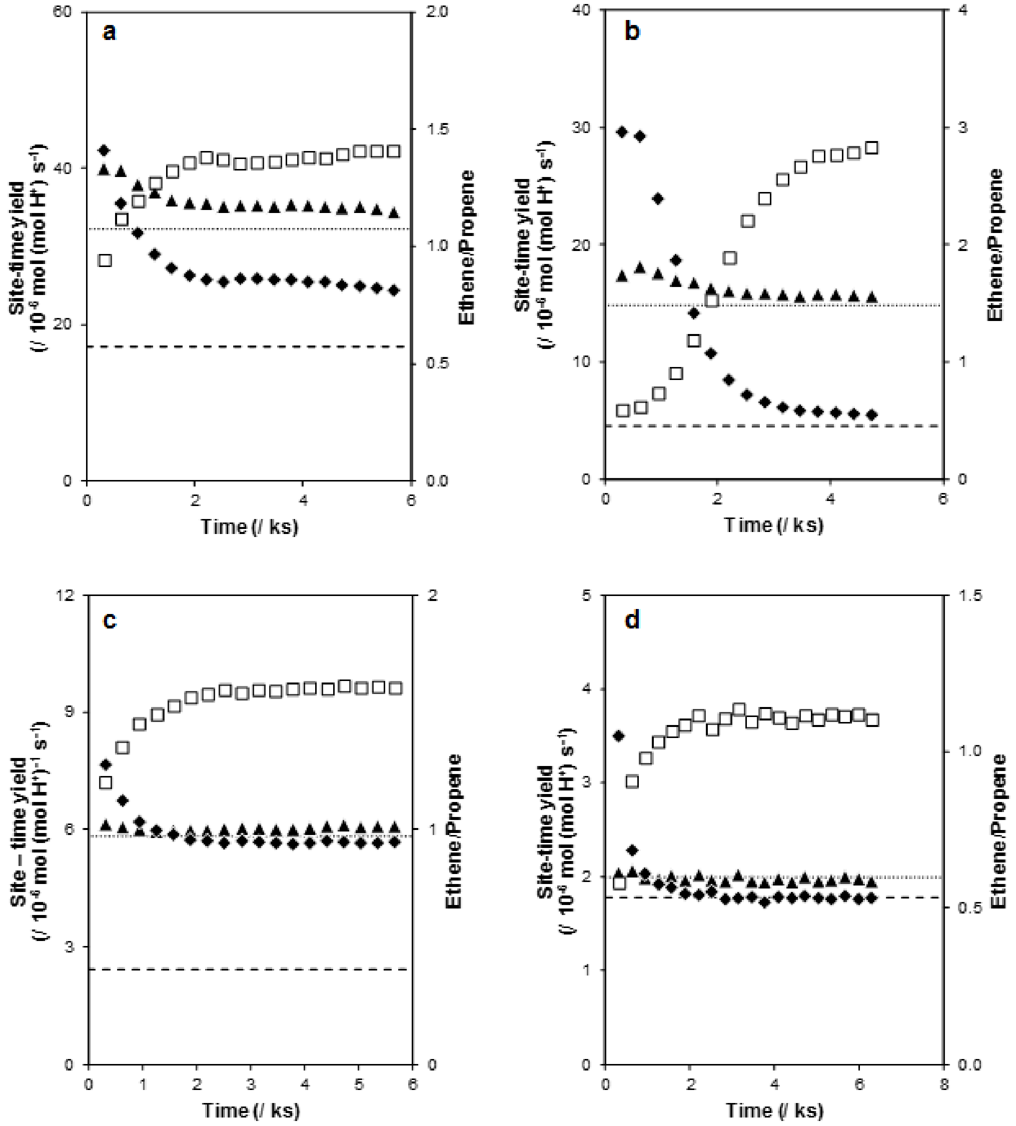

Figure 3.29.: Transient ethene (▲) and propene (◆) site-time yields (748 K, per H$^+$) and ethene/propene ratios (□) on (a) H-MFI-17, (b) H-MFI-140, (c) H-MOR-10, and (d) H-CHA-16 measured at 0.6–2.2 kPa C_3H_8 and conversions <1% following pretreatment in 5 kPa O_2 (803 K, 2 h); expected protolytic cracking (dotted line) and dehydrogenation (dashed line) turnover frequencies calculated from rate constants in Table 3.2.

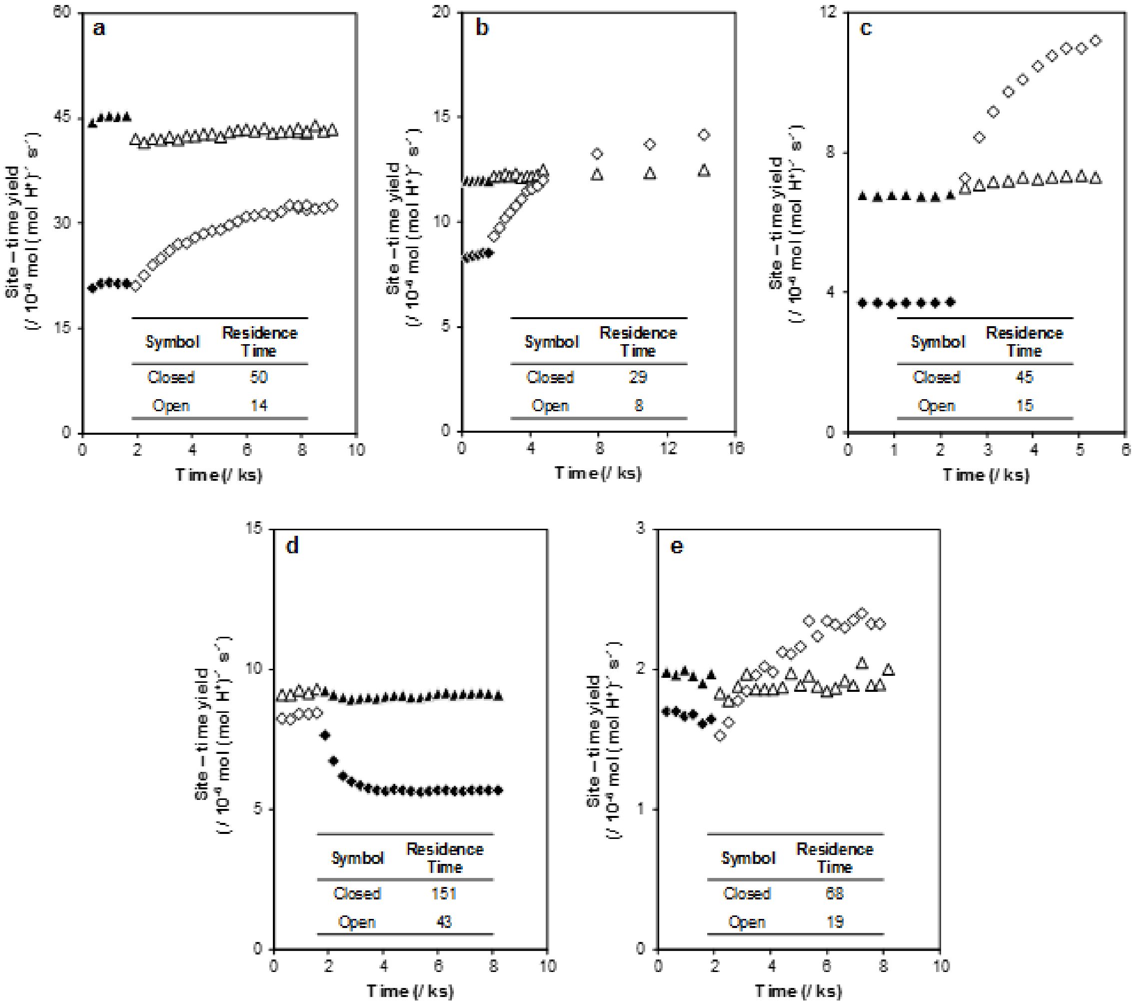

Figure 3.30.: Transient ethene (▲) and propene (◆) site-time yields (748 K, per H^+, 0.6–2.2 kPa C_3H_8) on (a) H-MFI-17, (b) H-MFI-43, (c) H-MFI-140, (d) H-MOR-10, and (e) H-CHA-16 with step changes in residence time; residence times are given in each panel.

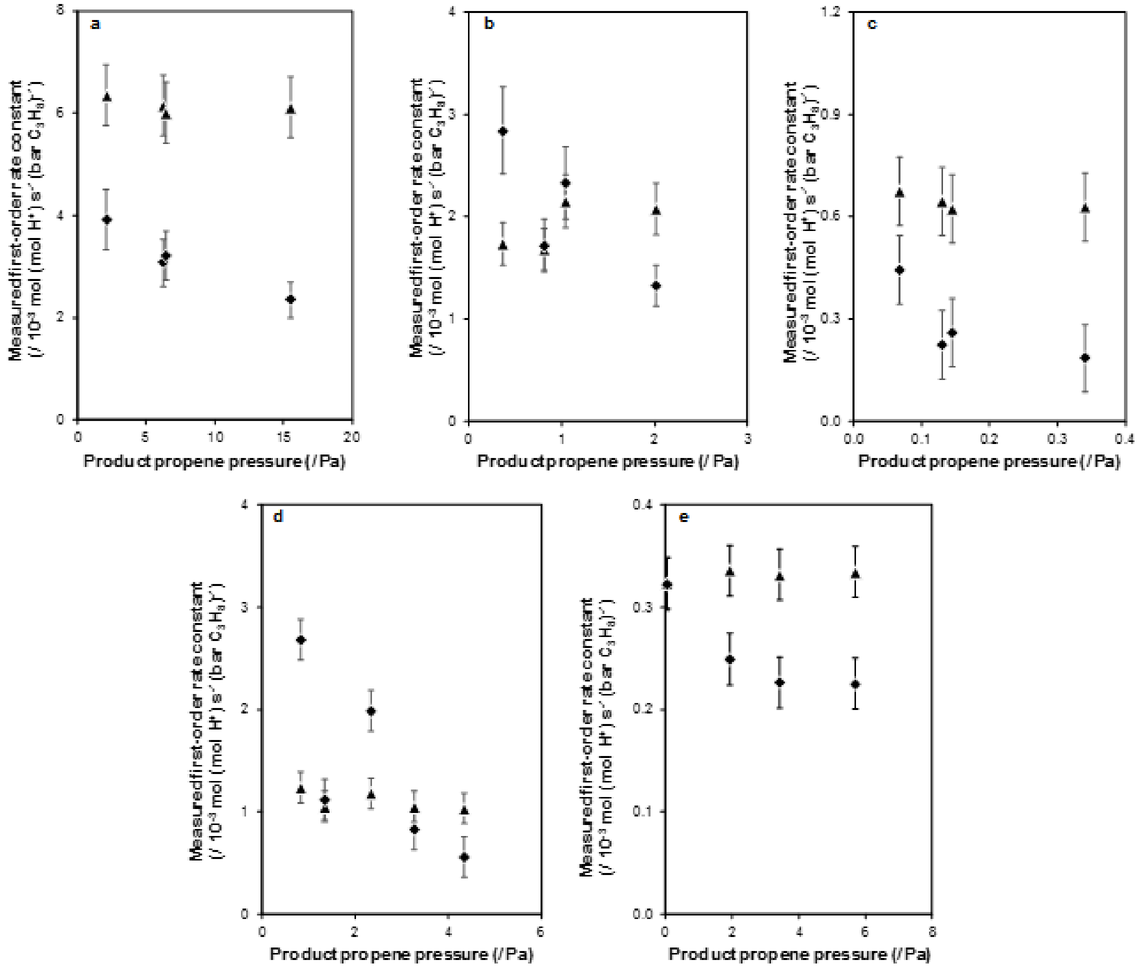

Figure 3.31.: Steady-state ethene (▲) and propene (◆) first-order rate constants (748 K, per H$^+$, 0.6–2.2 kPa C$_3$H$_8$) on (a) H-MFI-17, (b) H-MFI-43, (c) H-MFI-140, (d) H-MOR-10, and (e) H-CHA-16 as a function of propene pressure in the product mixture.

3.6.8 Evaluation of bed-scale H_2 gradients during propane reactions on H-form zeolites

Steady-state turnover rates measured in differential kinetic regimes are insensitive to reactor hydrodynamics, because differences in residence times introduced by non-ideal flow patterns (e.g., channeling, axial dispersion) are linearly averaged over the reactor volume when intregral reactor design equations are simplified to their algebraic forms. However, because propane dehydrogenation rates are not measured under differential conditions on H-form zeolites in the absence of co-fed products, non-ideal flow patterns may influence bed-scale gradients in product pressures and thus influence measured site-time yields. Figure 2c in the main text and Figure S23 (Section S7) show that, in the absence of co-fed products, propene formation rates (748 K, per H^+) on H-form zeolites generally decreased with increasing product pressure, suggesting that one or more products may inhibit propene formation on a secondary (non-proton) active site. However, propene formation rates did not decrease monotonically with increasing product partial pressures on all samples, as expected for kinetic inhibition by products when rates are measured in an ideal plug-flow reactor. This suggests that non-idealities in plug-flow hydrodynamics influence measured propene site-time yields on H-form zeolites in the absence of co-fed products.

Relative rates of convective and diffusive mass transfer in packed beds are described by the Péclet number, given by Equation S7.

$$P\acute{e} = \frac{uL}{D_e} \tag{3.10}$$

Here, u is the fluid linear velocity, L is the depth of the catalyst bed, and D_e is the effective diffusivity of a given reactant or product. Linear gas velocities and catalyst bed depths ranged from 0.01–0.10 m s^{-1} and 0.005–0.03 m, respectively. Razdan and co-workers [199] have estimated the effective diffusivity of molecular hydrogen to be $\sim$1.5 cm^2 s^{-1} from tracer pulse experiments performed under similar plug-flow conditions to those used here. Assuming a $T^{3/2}$ dependence of the effective diffusivity, we estimate that De for molecular hydrogen is 1.0 $cm^2\ s^{-1}$ at 748 K. These parameters result in Péclet numbers of 0.6–30, suggesting that transport rates of molecular H_2 via axial diffusion and convection occurred at similar orders-of-magnitude in certain cases.

Figure S24 shows propene formation rates on H-form zeolites as a function of the Péclet number at a variety of conditions. At a given partial pressure, propene formation rates decreased with decreasing Péclet number, corresponding to higher rates of axial dispersion relative to convection. Propene formation rates were not a single-valued function of the Péclet number because the Péclet number is agnostic to the extensive quantity of molecular hydrogen present. Higher dihydrogen pressures at the front of the catalyst bed (and thus lower propene formation rates) are observed at higher reactant propane pressures (resulting from protolytic dehydrogenation to form H_2 on Brønsted acid protons) and at lower Péclet numbers as dihydrogen more readily diffuses upstream against convective flow patterns. Therefore, deviations from protolytic dehydrogenation rates were most significant under conditions closer to ideal plug-flow hydrodynamics, because axial mixing of dihydrogen formed *in situ* mitigates the formation of carbonaceous deposits that predominantly form at the front of the catalyst bed (Figure 4 in the main text). We surmise that the sensitivity of measured propene formation rates to experimental parameters (e.g., reactant mixture volumetric flow rate, reactor diameter, catalyst bed depth, reactant alkane partial pressure) may contribute to differences in reported steady-state n-alkane dehydrogenation rates and activation energies reported in the literature under nominally similar conditions [101, 102, 105].

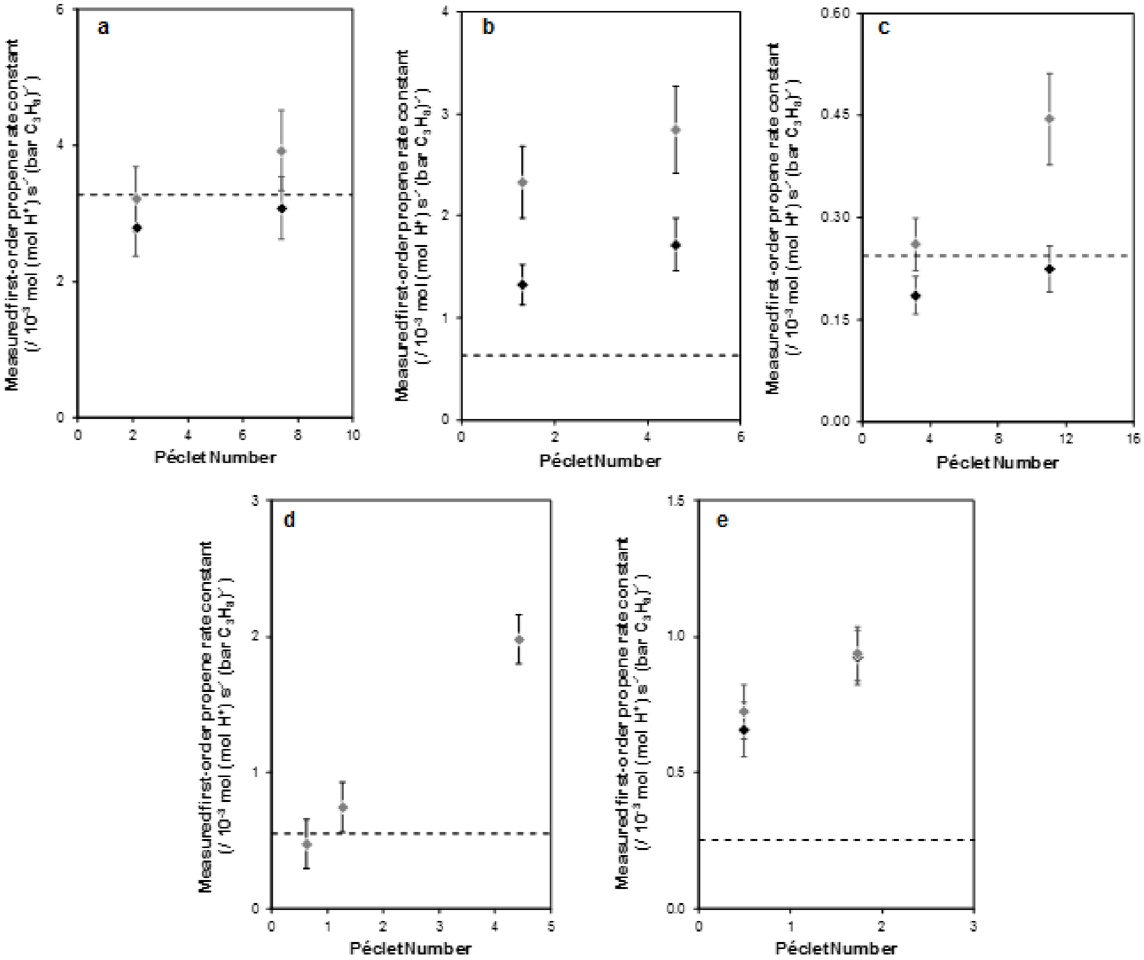

Figure 3.32.: Steady-state propene formation rates (748 K, per H^+) on (a) H-MFI-17, (b) H-MFI-43, (c) H-MFI-140, (d) H-MOR-10, and (e) H-CHA-16 as a function of the Péclet number. Rates collected with 0.6 kPa C_3H_8 (gray symbols) or 2.2 kPa C_3H_8 (black symbols). Dashed lines represent protolytic dehydrogenation rate constants collected at initial time-on-stream with 20 kPa H_2 co-feeds.

3.6.9 Role of reactant mixture impurities on propane reactions on H-form zeolites

The deposition of carbonaceous intermediates on H-form zeolites in the presence of propane (0.6-2.2 kPa) at 748 K requires secondary reactions of alkene products, or seeding of the carbon pool by unsaturated impurities in reactant mixtures. Unsaturated hydrocarbon intermediates or impurities (e.g., propyne) may be responsible for formation of carbonaceous deposits, because similar intermediates (e.g., 1,3-butadiene) lead to the formation of occluded polyaromatics during methanol-to-hydrocarbons catalysis in zeolites that lead to pore blockage and deactivation [180]. Deactivation can be mitigated by co-feeding H_2 to hydrogenate unsaturated intermediates before they form polycyclic aromatics. Here, a Pt/SiO_2 catalyst (1 wt% Pt) was placed in an upstream bed [200] and used to hydrogenate any trace unsaturated impurities in reactant mixtures prior to reaction on an H-form zeolite. At 293 K, the Pt/SiO_2 catalyst equilibrated a mixture of 0.3 kPa C_3H_6 and 50 kPa H_2 to 0.3 kPa propane and $<$1 Pa propene, conditions that should lead to hydrogenation of other unsaturated hydrocarbons that may be in the reactant mixture, given that Pt/SiO_2 hydrogenates propyne under similar conditions [201]. Figure S25 shows transient propene formation rates on H-MFI-43 following pretreatments in H_2 (803 K) and in the presence of 20 kPa co-fed H_2 under two different sets of conditions, in either the absence or presence of the upstream Pt/SiO_2 catalyst bed. Initial and steady-state propene formation rates were similar at each set of conditions, suggesting that carbonaceous deposits are likely derived from secondary reactions of product alkenes, and not from any unsaturated impurities found in reactant mixtures.

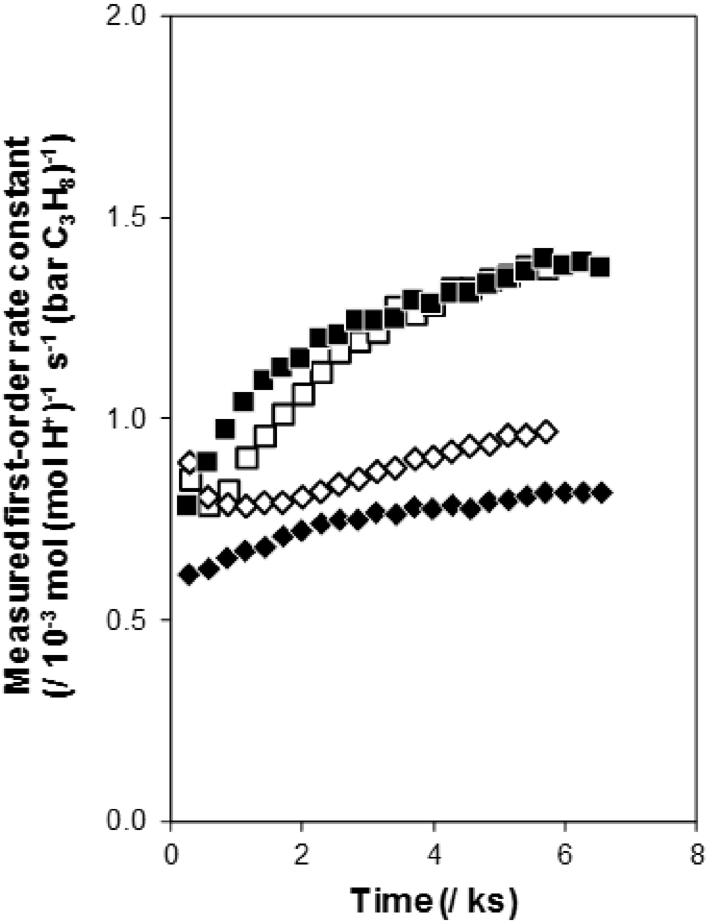

Figure 3.33.: Transient propene formation rates (748 K, per H^+) as a function of time-on-stream on H-MFI-43 following pretreatment in 101 kPa H_2 (803 K, 2 h). Rates were measured with 20 kPa co-fed H_2 and propane pressures of 0.6 kPa (■) and 2.2 kPa (◆) in the absence (closed) and presence (open) of a a 1 wt% Pt/SiO_2 catalyst (293 K) placed upstream of the H-MFI-43 bed.

3.6.10 Transient methane, ethene, and propene formation rates on H-form zeolites after a step-change in co-feeding H_2

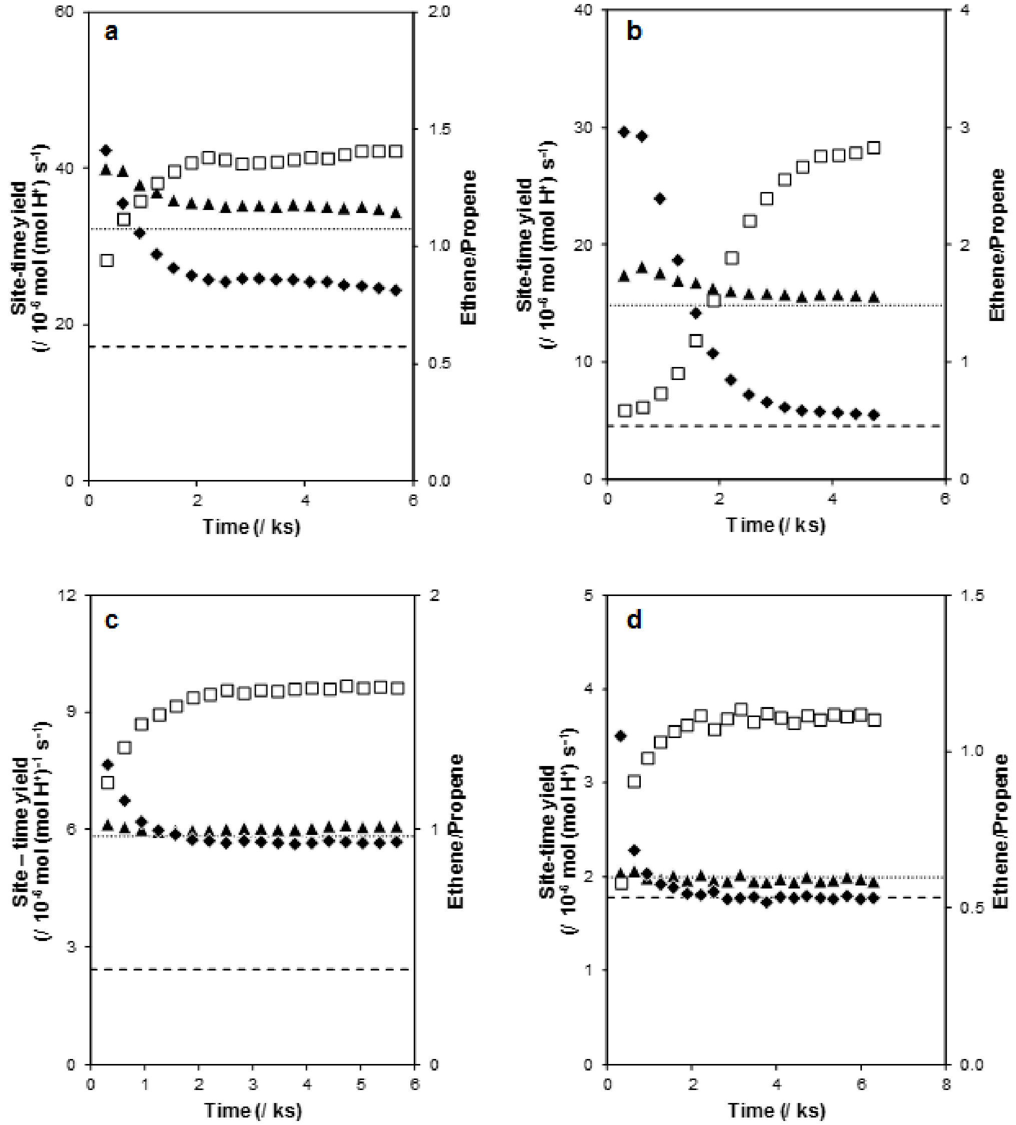

Figure 3.34.: Measured first-order rate constants for methane (■), ethene (▲), and propene (◆) formation on H-MFI-43 (per H^+, 748 K, 0.6 kPa C_3H_8). Dashed line indicates a step-change increase in co-fed H_2 pressure from 0 to 20 kPa. Catalyst bed depths were (a, b) 2.5×10^{-3} m and (c) 7.5×10^{-3} m.

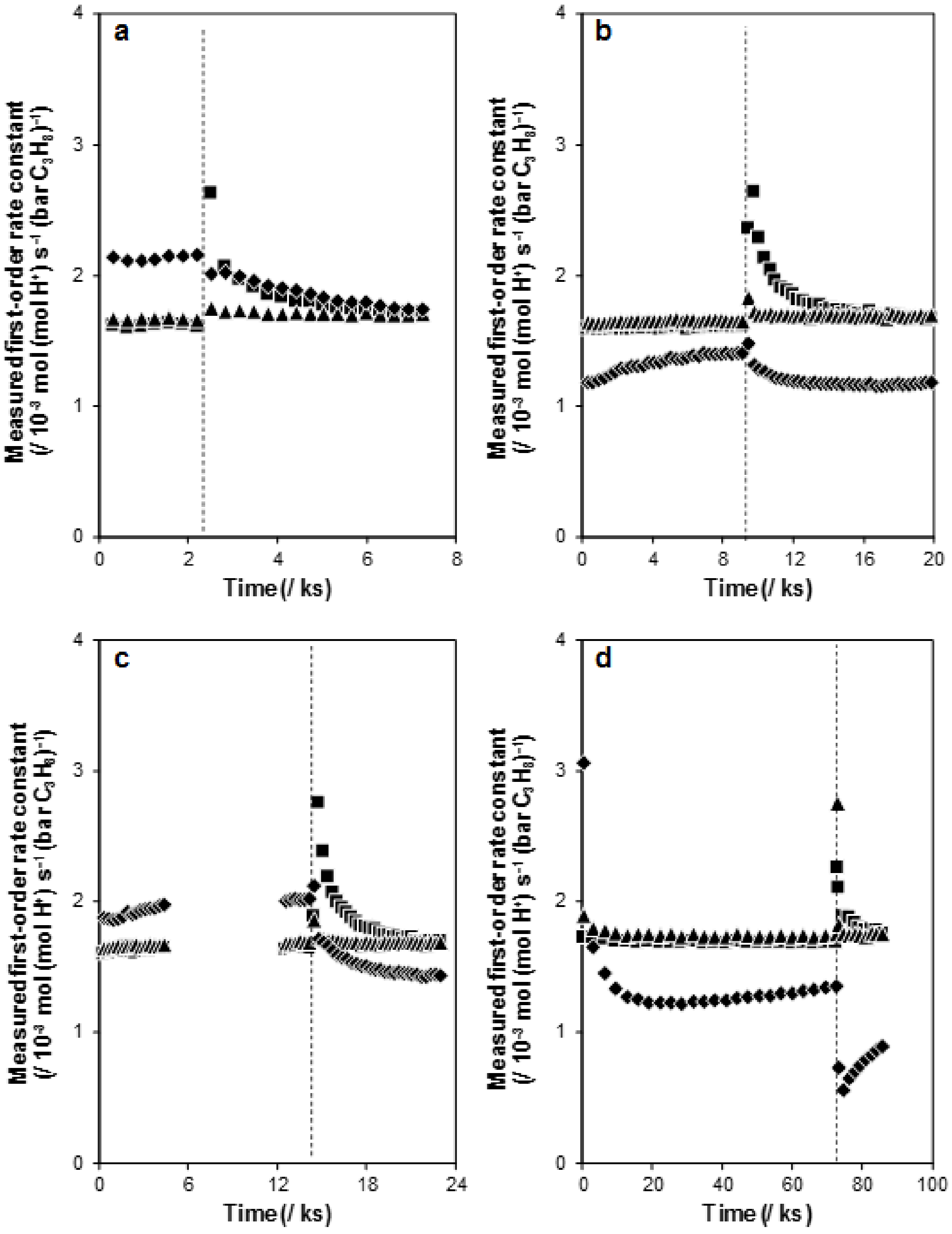

Figure 3.35.: Measured first-order rate constants for methane (■), ethene (▲), and propene (◆) formation on H-MFI-43 (per H^+, 748 K, 2.2 kPa C_3H_8). Dashed line indicates a step-change increase in co-fed H_2 pressure from 0 to 20 kPa. Catalyst bed depths were (a, b) 2.5×10^{-3} m and (c, d) 7.5×10^{-3} m.

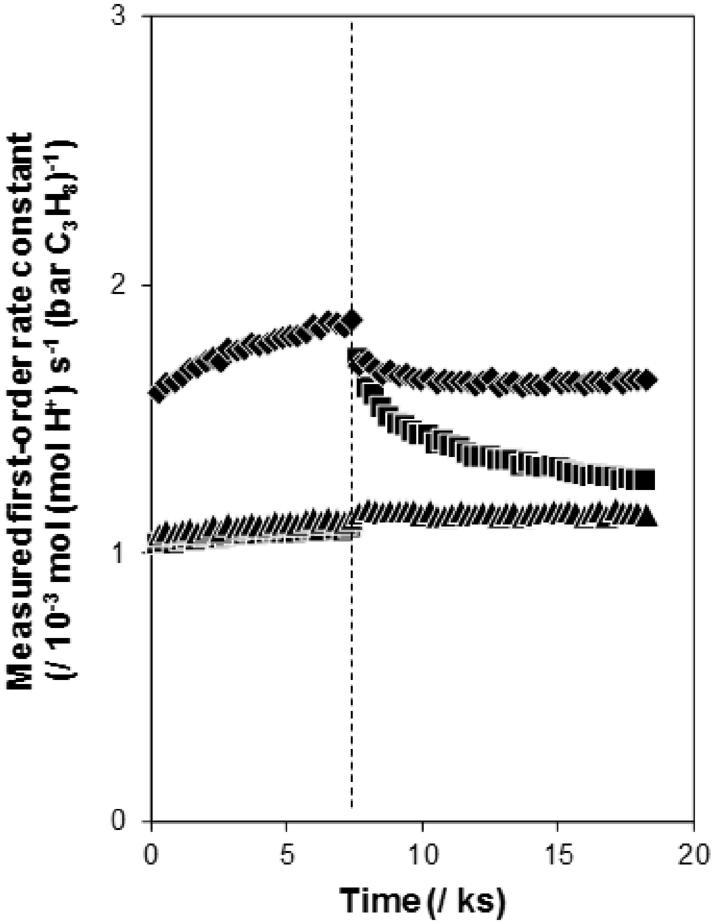

Figure 3.36.: Measured first-order rate constants for methane (■), ethene (▲), and propene (◆) formation on H-MOR-10 (per H^+, 748 K, 0.6 kPa C_3H_8). Dashed line indicates a step-change increase in co-fed H_2 pressure from 0 to 20 kPa.

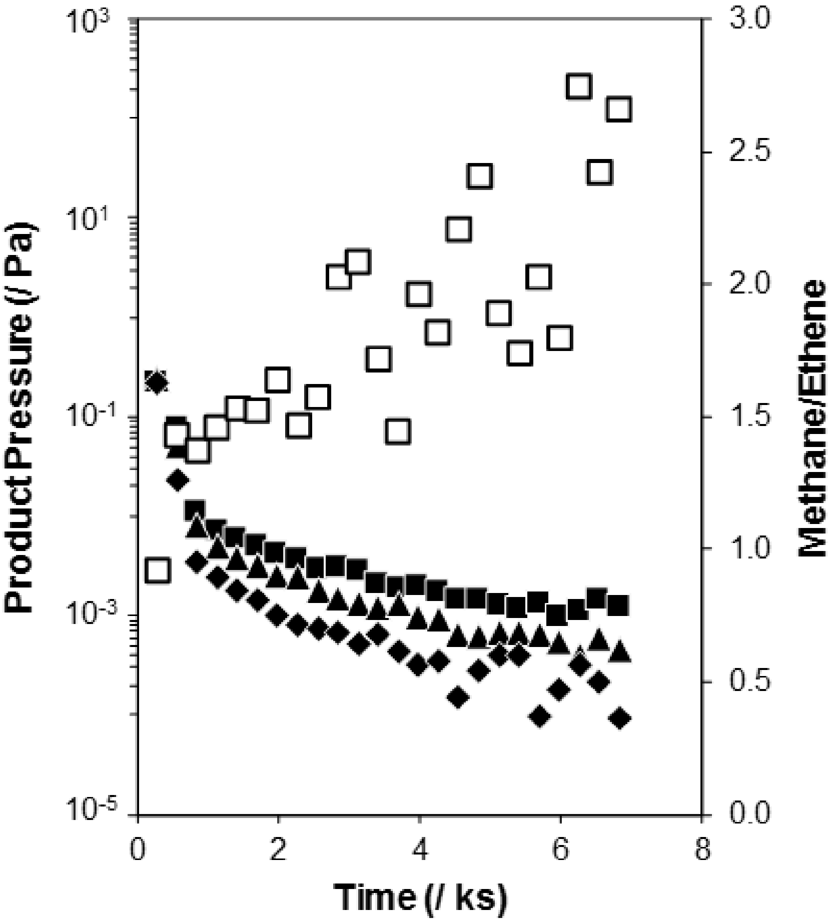

Figure 3.37.: Methane (■), ethene (▲), and propene (◆) partial pressures removed from H-MFI-43 and transfer lines in flowing H_2 following removal of C_3H_8 and He from reactant mixture containing 0.6 kPa C_3H_8 and 20 kPa H_2. Ratio of methane to ethene (□) is plotted on the secondary axis.

3.6.11 Steady-state propene hydrogenation rates on H-form zeolites

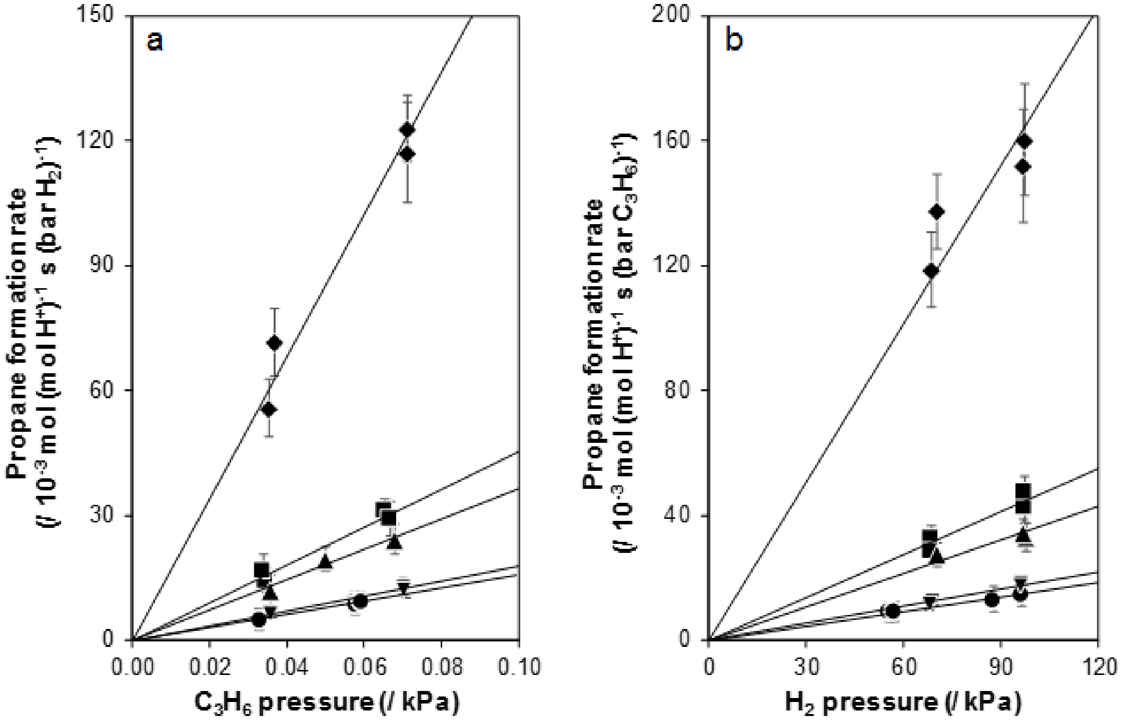

Figure 3.38.: Steady-state propene hydrogenation rates (748 K, per H^+) as a function of (a) C_3H_6 and (b) H_2 pressure on H-MFI-17 (◆), H-MFI-43 (■), H-MFI-140 (●), H-MOR-10 (▲), and H-CHA-16 (▼). Lines represent regressions to Equation 3.2 in the main text.

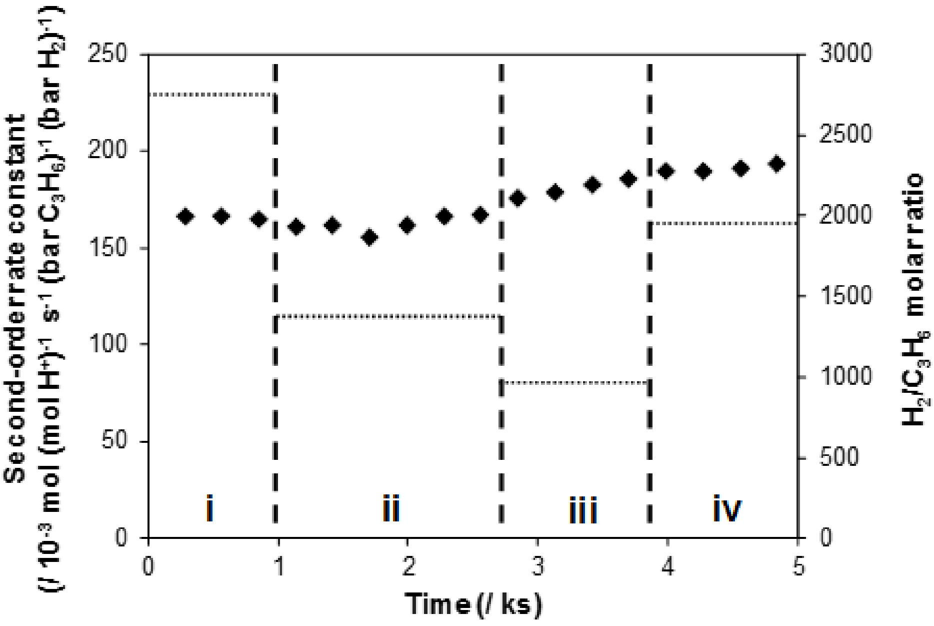

Figure 3.39.: Second-order propene hydrogenation rate constants on H-MFI-17 as a function of time under reaction conditions of (i) 0.04 kPa C_3H_6, 97 kPa H_2, 342 s (mol H^+) (mol C_3H_6)$^{-1}$; (ii) 0.07 kPa C_3H_6, 97 kPa H_2, 182 s (mol H^+) (mol C_3H_6)$^{-1}$; (iii) 0.07 kPa C_3H_6, 68 kPa H_2, 182 s (mol H^+) (mol C_3H_6)$^{-1}$; (iv) 0.04 kPa C_3H_6, 71 kPa H_2, 360 s (mol H^+) (mol C_3H_6)$^{-1}$. Dotted lines show H_2/C_3H_6 molar ratios in the reactant mixture on the secondary axis.

3.7 Acknowledgements

We acknowledge financial support from the National Science Foundation under Cooperative Agreement No. EEC-1647722, an Engineering Research Center for the Innovative and Strategic Transformation of Alkane Resources (CISTAR), and support for Prof. Enrique Iglesia from the Neil Armstrong Distinguished Visiting Fellowship (Purdue University). We thank Jiahan Xie (UC-Berkeley) for technical discussions and data collection that assisted in testing the hypotheses and in refining the conclusions described in this manuscript, and Junnan Shangguan (UC-Berkeley) for a critical reading of this manuscript. We also thank Neil Razdan (University of Minnesota) and Prof. Aditya Bhan (University of Minnesota) for helpful technical discussions during the preparation of this manuscript.

4. AMMONIA TITRATION METHODS TO QUANTIFY BRØNSTED ACID SITES IN ZEOLITES SUBSTITUTED WITH ALUMINUM AND BORON HETEROATOMS

4.1 Abstract

Ammonia titration methods were developed to discriminate and quantify Brønsted acid sites of different strength that compensate aluminum and boron heteroatoms incorporated within zeolite frameworks. Borosilicate and boroaluminosilicate MFI zeolites (B-Al-MFI) were synthesized with different Al contents and crystallite sizes, which are typically correlated structural properties in aluminosilicates synthesized hydrothermally, but independently varied here by incorporating boron as a second framework heteroatom and using ethylenediamine as a structure directing agent. Temperature programmed desorption (TPD) of ammonia from B-Al-MFI samples saturated via liquid-phase NH_4NO_3 ion-exchange resulted in quantifying the total number of Al and B heteroatoms. In contrast, TPD performed after NH_4-form B-Al-MFI samples were purged in flowing helium (433 K), or after gas-phase NH_3 adsorption (433 K) onto H-form B-Al-MFI samples, quantified only protons charge-compensating framework Al heteroatoms. Turnover rates for methanol dehydration to dimethyl ether (415 K), when measured in zero-order kinetic regimes that are sensitive predominantly to Brønsted acid strength, depended only on the number of protons compensating framework Al atoms in B-Al-MFI zeolites. The NH_3 titration methods developed here are useful in rigorously normalizing turnover rates of Brønsted acid-catalyzed reactions in boroaluminosilicate zeolites, which have been recognized previously to depend solely on Al content. The incorporation of B heteroatoms into zeolite frameworks, which generate protons that are essentially unreactive, provides a strategy to influence crystallite sizes independently of Al content, especially relevant

in cases where catalytic behavior is influenced by intracrystalline transport phenomena.

4.2 Introduction

Aluminosilicate zeolites are a class of solid Brønsted acid catalysts used widely in petrochemical refining [152, 202], of which the MFI framework has received particular attention for converting methanol [203] and alkenes (C_2-C_{12}) [23, 153] into heavier molecular weight compounds used as transportation fuels. Crystallite sizes and framework Al content influence the reactivity, selectivity, and deactivation of MFI zeolites in methanol-to-olefins [88, 89, 93, 204] and alkene oligomerization [87, 205, 206] catalysis, because longer diffusion paths and higher Al contents preferentially increase intracrystalline residence times of larger products, increasing their propensity to undergo secondary reactions to form smaller molecules that egress more readily from intracrystalline pore networks. The combined effects of crystallite size and framework Al content are reflected in a characteristic diffusion parameter (Ψ) within Thiele modulus expressions, proportional to the square of the characteristic diffusion length and to the volumetric acid site density of a given crystallite, as used by Sarazen and Iglesia to interpret changes in propene oligomerization product selectivities on different Al-MFI zeolites [87]. The location of Brønsted acidic protons among the intraporous voids present in MFI, which depends on the distribution of Al atoms among crystallographically-distinct tetrahedral site (T-site) positions, also influences reactivity and selectivity [67]. In the case of propene dimerization, turnover rates depend on the geometry of pore structures confining Brønsted acid sites, which determine the strength of van der Waals interactions between lattice oxygen atoms and carbenium ion transition states stabilized at such sites [51]. In the case of methanol-to-olefin reactions that occur via a hydrocarbon pool mechanism [203, 207], larger channel intersections in MFI (and MWW) zeolites have been reported to preferentially stabilize larger transition states of aromatic-based cycles, while smaller 10-membered ring (10-MR) channels do so for smaller transition states in olefin-based cycles [208, 209]. As a result, synthetic methods to prepare MFI zeolites with varying crystallite size, and framework Al content and distribution [64, 208], can generate materials with different catalytic properties for a variety of hydrocarbon upgrading processes [67].

Crystallite sizes tend to increase with decreasing Al content among MFI zeolites crystallized hydrothermally in the presence of tetrapropylammonium (TPA^+) cations [90–92], although using di-quaternary ammonium surfactants can restrict crystal growth to form single-unit-cell thick zeolite sheets [93], and using zeolite growth modifiers that selectively bind to certain crystal facets can inhibit crystal growth in certain dimensions [94, 210]. The synthesis of boroaluminosilicate MFI (B-Al-MFI) zeolites from mixtures containing equimolar quantities of B and Al has been reported to produce smaller crystallites (∼6 μm) than aluminosilicate MFI zeolites (∼10 μm) at fixed Al content (Si/Al = 12) [96]. ^{27}Al, ^{29}Si, and ^{11}B magic angle spinning nuclear magnetic resonance (MAS NMR) characterization has provided evidence that B competes with Al for incorporation at certain T-sites in MFI, resulting in changes to the Al distribution among different possible T-sites at a given Si/Al ratio [211]. Similar effects of B incorporation on the resulting Al distribution have been reported in MCM-22, using IR methods with adsorbed pyridine (after protons in supercages and surface pockets were selectively poisoned by *m*-xylene) and ^{27}Al NMR to identify acid sites in smaller 10-MR sinusoidal channels [209], which are less prone to deactivation by carbonaceous deposits during methanol-to-hydrocarbons catalysis than acid sites in larger voids. Although B competes with Al for incorporation in siliceous frameworks, their corresponding bridging OH groups are much weaker in Brønsted acid strength, reflected in deprotonation energies (DPE) that are ∼70 kJ mol^{-1} higher than bridging OH groups at framework Al [33]. Such large differences in deprotonation energy result in zero-order rate constants of methanol dehydration to dimethyl ether, which depend predominantly on acid strength and are essentially insensitive to confinement effects [212], estimated to be an order of magnitude higher (per H^+, 433 K) on Al-MFI than B-MFI [33]. Rates (per g) of other Brønsted acid-catalyzed reactions (*n*-hexane cracking [213], ethylbenzene dealkylation [213], cyclopropane isomerization [213], ethylene methylation [211]) in B-Al-MFI samples have been reported to correlate with their total number of Al sites (per g), even when present in trace quantities (<100 ppm Al, Al/B < 0.01) that are introduced, in certain cases, as adventitious impurities from silica precursors [214] or alumina binders [213, 215]. Thus, the incorporation of boron as a non-catalytic heteroatom in Brønsted acidic zeolites provides a strategy to influence crystallite size independently of framework Al content and distribution.

Interpreting catalytic phenomena of Brønsted acidic origin on boroaluminosilicates, especially in the normalization of rate data, requires methods to discriminate and quantify protons compensating framework Al and B. Previous methods to identify framework Al in boroaluminosilicates have used ^{27}Al, ^{29}Si, and ^{11}B MAS NMR spectroscopy [209, 211, 216], although ^{27}Al MAS NMR characterization of aluminosilicates can overestimate the number of Brønsted acidic protons, because tetrahedral Al species detected in NMR spectra are structural proxies for the number of proton active sites present during reaction [116, 217, 218]. Moreover, B atoms trigonally coordinated within *BEA frameworks have been reported to appear as tetrahedral in ^{11}B MAS NMR spectra, depending on the extent of sample hydration [219]. Infrared OH stretching vibrations of protons at framework Al and B have been observed at ~3600 and ~3700 cm^{-1} [211, 220, 221], respectively, but have not been directly quantified to our knowledge in boroaluminosilicates, which would require molar extinction coefficients for the two OH groups. Temperature-programmed desorption (TPD) of bases often results in a multitude of desorption features, as observed for ammonia desorption and attributed to acid strength differences between protons compensating framework B and Al [209, 211, 222, 223], despite ambiguities in interpreting the position of desorption features on the basis of binding strength because of convoluting effects of molecular readsorption and diffusion phenomena during egress from microporous voids [224, 225]. Gorte and co-workers have shown that alkylamine titrants (*t*-butylamine, *i*-propylamine) undergo Hoffman elimination to form ammonia and the corresponding alkene at protons associated with framework Al, but desorb intact from OH groups formed from framework B [226, 227], suggesting that such methods could distinguish framework Al and B.

Here, we adapt strategies reported previously for using ammonia titrants to discriminate and quantify sites of different binding strength that arise from Brønsted and Lewis acid sites that co-exist in H-form [228] and partially Cu-exchanged [129, 218] aluminosilicates, in order to do so for protons of different Brønsted acid strength generated from framework B and Al in boroaluminosilicates. Titration methods using ammonia are especially useful to quantify protons in porous materials of certain topology (e.g., small-pore frameworks [218]) or composition (low Si/Al with protons in close proximity [217]) that present challenges when using bulkier alkylamine titrants. We provide evidence that TPD of ammonia after liquid-phase ion-exchange to saturation allows quantifying all framework Al and B heteroatoms (either trigonal or tetrahedral [221]), while methods to purge weakly-bound ammonia (433 K, He) from framework B allow quantifying only protons at framework Al sites (H^+_{Al}) in a subsequent TPD. Gas-phase ammonia saturation of H-form B-Al-MFI samples at 433 K provides identical quantification in a subsequent TPD, because ammonia does not adsorb to protons at framework B under these conditions. These proton site quantifications are useful in normalizing rates of Brønsted acid-catalyzed reactions on boroaluminosilicates, verified here by measuring zero-order rate constants for methanol dehydration to dimethyl ether, a catalytic probe that is sensitive to acid strength and can discriminate catalytic contributions from protons at Al and B in zeolite frameworks [33].

4.3 Experimental Methods

4.3.1 Catalyst Synthesis and Preparation

B-Al-MFI zeolites were synthesized from solutions with molar ratios of 1 SiO_2/ 0.3 EDA/ X H_3BO_3/ Y $Al(NO_3)_3$/ 0.01 TPABr/ 10.2 H_2O, with values of X ranging from 0.08 to 0.40 and values of Y ranging from 0.006 to 0.012. All samples are denoted B-

Al-MFI (Si/B, Si/Al), where Si/B and Si/Al correspond to the molar ratios present in the synthesis solutions. Ethylenediamine (99.5 wt%, Sigma Aldrich) was first diluted with deionized water (18.2 MΩ) in a perfluoroalkoxy alkane (PFA) container (Savillex Corp.), followed by addition of boric acid (99.5 wt%, Sigma Aldrich). This solution was mixed for 15 minutes under ambient conditions. A separate mixture of aluminum nitrate nonahydrate (98 wt%, Sigma Aldrich) and tetra-*n*-propylammonium bromide (98 wt%, Alfa Aesar) in deionized water was also mixed for 15 minutes under ambient conditions. The two solutions were then combined into one PFA container, followed by addition of colloidal silica (Ludox HS40, 40 wt%, Sigma Aldrich). This mixture was then stirred under ambient conditions for 2 h to produce a homogeneous solution, added to a 45 mL Teflon-lined stainless steel autoclave (Parr Instruments), and heated in a forced convection oven (Yamato DKN-402C) at 448 K under rotation at 40 rpm for 5 days.

B-MFI zeolites were synthesized from solutions with molar ratios of 1 SiO_2/ 0.3 EDA/ X H_3BO_3/ 0.01 TPABr/ 10.2 H_2O, with values of X ranging from 0.08 to 0.40. Samples are denoted B-MFI (Si/B), where Si/B corresponds to the molar ratio present in the synthesis solution. Ethylenediamine (99.5 wt%, Sigma Aldrich) was first diluted with deionized water (18.2 MΩ) in a PFA container, followed by addition of boric acid (99.5 wt%, Sigma Aldrich). This solution was mixed for 15 minutes under ambient conditions. A separate mixture of tetra-*n*-propylammonium bromide (98 wt%, Alfa Aesar) in deionized water was also mixed for 15 minutes under ambient conditions. The two solutions were then combined into one PFA container, followed by addition of tetraethylorthosilicate (TEOS, 98 wt%, Sigma Aldrich) and stirred for 2 h uncovered and under flowing air to evaporate the ethanol evolved from hydrolysis of TEOS. The mixture was then added to a 45 mL Teflon-lined stainless steel autoclave (Parr Instruments), heated in a forced convection oven (Yamato DKN-402C) at 448 K under rotation at 40 rpm for 5 days.

Solid products were removed from the Teflon liners and washed with water and acetone (Sigma-Aldrich, >99.5 wt%) in alternating washes (30 cm^3 (g solid)$^{-1}$ per wash) until the pH of the supernatant solution was constant. Solids were separated by centrifugation, dried in air at 373 K for 24 h, and then treated in flowing dry air (1.67 cm^3 s^{-1} (g solid)$^{-1}$, UHP, 99.999%, Indiana Oxygen) to 853 K (0.0167 K s^{-1}) and held for 10 h in a muffle furnace (Nabertherm L/E 611 with a P300 controller) to remove organic structure directing agents from zeolite products.

B-Al-MFI and B-MFI samples were converted to their NH_4-form by aqueous phase ion-exchange (100 cm^3 (g solid)$^{-1}$) in a 1.0 M NH_4NO_3 solution (8.0 wt% in deionized H_2O; 99.9 wt%, Sigma Aldrich) for 24 h under ambient conditions, then washed with deionized water (70 cm^3 per g solids), recovered via centrifugation, and dried in air at 373 K for 24 h. NH_4-form samples were converted to their H-form by treatment in flowing dry air (1.67 cm^3 s^{-1} (g solid)$^{-1}$, UHP, 99.999%, Indiana Oxygen) to 773 K (0.0167 K s^{-1}) for 4 h in a muffle furnace (Nabertherm L/E 611 with a P300 controller).

4.3.2 Characterization of B-Al-MFI and B-MFI

Crystal structures were verified with powder X-ray diffraction (XRD) patterns collected using a Rigaku SmartLab X-ray diffractometer with a Cu Kα source operating at 1.76 kW. Typically, 0.01 g of sample was loaded into a zero-background, low dead volume sample holder (Rigaku) and diffraction patterns were measured from 4 - 40° at a scan rate of 0.0167° s^{-1} and step size of 0.01°. Micropore volumes were calculated from N_2 adsorption isotherms measured at 77 K with a Micromeritics ASAP 2020 Surface Area and Porosity Analyzer. B-MFI and B-Al-MFI samples (0.04 – 0.06 g, sieved to 180-250 μm) were degassed by heating to 393 K (0.167 K s^{-1}) under vacuum (5 μmHg) for 8 h. The linear volumetric uptake of N_2 (for 0.05 – 0.35 P/P_0) was used to estimate micropore volumes (cm^3 (g solid)$^{-1}$ at STP). These results were compared to those from a semi-log derivative plot of the isotherm, given by $\partial(V_{ads})/\partial(\ln(P/P_0))$ vs. $\ln(P/P_0)$. The volume of N_2 adsorbed at the first minimum in this plot corresponds to the point at which the micropores have been filled, from which micropore volumes were calculated [229, 230]. All reported micropore volumes agreed (± 10%) between these two methods.

Elemental analysis of aluminum in B-MFI and B-Al-MFI zeolites were performed via atomic absorption spectroscopy (AAS) with a Perkin Elmer AAnalyst 300 Atomic Absorption Spectrometer. Samples were prepared by dissolving 0.04 g of solid in 2 g of hydrofluoric acid (48 wt%, Alfa Aesar) and allowed to sit overnight, then diluted in 50 g of deionized water (18.2 MΩ). ***Caution: when working with HF acid, use appropriate personal protective equipment, ventilation, and other safety precautions.*** Absorbances were measured with radiation sources at wavelengths of 309.3 nm in a reducing acetylene/nitrous oxide flame. Elemental compositions were calculated using calibration curves generated from known solutions. Silicon and boron contents in B-Al-MFI were determined by inductively coupled plasma optical emission spectroscopy (ICP-OES, Galbraith Laboratories). Images were collected via scanning electron microscopy (SEM) on an FEI Quanta 3D FEG Dual-beam SEM. Prior to imaging, samples were coated with platinum to reduce charging. Images were taken at an accelerating voltage of 15 kV and spot size of 6 at 3,500–50,000× magnification.

4.3.3 Temperature Programmed Desorption

TPD experiments were performed with a Micromeritics AutoChem II 2920 Chemisorption analyzer and an Agilent 5975C mass selective detector (MSD) to identify the gaseous products evolved from zeolite samples. MFI samples (0.04 – 0.08 g, sieved to 180 – 250 μm) were supported between two quartz wool plugs in a U-shaped quartz cell in a clam-shell furnace. Calibration and deconvolution methods were performed according to previous reports [129]. The total number of Al and B sites was estimated by holding NH_4-form B-Al-MFI samples at 323 K for 0.5 h under flowing He (15 cm^3 s^{-1} (g solid)$^{-1}$, UHP, 99.999%, Indiana Oxygen), followed by increasing the temperature to 873 K (0.167 K s^{-1}) while the effluent gas was sent to the MSD for analysis.

Two additional methods were used to titrate only protons at framework Al in B-Al-MFI. In the first method, NH_4-form samples were held under flowing He (15 cm^3 s^{-1} (g solid)$^{-1}$, UHP, 99.999%, Indiana Oxygen), heated to 433 K (0.167 K s^{-1}), and held isothermally for 4 h. The temperature was then increased to 873 K (0.167 K s^{-1}) while the effluent gas was sent to the MSD for analysis. In the second method, prior to gas-phase NH_3 saturation, H-form B-Al-MFI samples were treated in flowing dry air (15 cm^3 s^{-1} (g solid)$^{-1}$, UHP, 99.999%, Indiana Oxygen) to 673 K (0.167 K s^{-1}) and held for 2 h, then cooled to 433 K under flowing He (15 cm^3 s^{-1} (g solid)$^{-1}$) and held for 1 h. Samples were then saturated with gaseous NH_3 (30 cm^3 s^{-1} (g solid)$^{-1}$, 500 ppm NH_3 in He, Indiana Oxygen) for 2 h, then held isothermally in flowing He (15 cm^3 s^{-1} (g solid)$^{-1}$) for 4 h. The temperature was then increased to 873 K (0.083 K s^{-1}) while the effluent gas was sent to the MSD for analysis.

4.3.4 Methanol Dehydration Kinetic Measurements

Methanol dehydration rates were measured under differential conversions (<10%) in a tubular packed-bed quartz reactor (7 mm inner diameter) with H-B-MFI samples (0.02 – 0.03 g, sieved to 180 – 250 μm) supported between two quartz wool plugs. Reaction temperatures were controlled in a resistively-heated three-zone furnace (Applied Test Systems Series 3210) and Watlow controllers (EZ-Zone series). Catalyst temperatures were measured with a K-type thermocouple placed at the external surface of the quartz tube at the middle of the catalyst bed. Methanol (99.9 wt%, Sigma Aldrich) partial pressures were controlled with a syringe pump (Legato 100, KD Scientific) and injected into a stream of flowing He (UHP, 99.999%, Indiana Oxygen) and transferred to the reactor via heated lines maintained at >373 K using resistive heating tape (BriskHeat Co.) and insulating wrap. H-B-Al-MFI samples were first treated in flowing 5% O2 with balance He (50 cm^3 s^{-1} (g solid)$^{-1}$, 99.999%, Indiana Oxygen) to 773 K (0.033 K s^{-1}) and held for 4 h before cooling to 415 K under He flow (150 cm^3 s^{-1} (g solid)$^{-1}$) prior to rate measurements. Methanol partial pressures in the reactant stream were measured in a bypass configuration. Concentrations of reactants and products were measured with a gas chromatograph equipped with a flame ionization detector (HP Plot-Q KCl column, 0.53 mm ID × 30 m × 40 μm film, Agilent). Dimethyl ether and water were the only products observed on all catalysts under all conditions. Methane (25% CH_4 in Ar, 99.999%, Indiana Oxygen) was introduced to the reactor effluent stream (0.083 $cm^3\ s^{-1}$) and used as an internal standard. First- and zero-order rate constants for methanol dehydration were calculated as previously reported [79].

4.4 Results and Discussion

4.4.1 Synthesis and bulk characterization of borosilicate and boroaluminosilicate zeolites

B-Al-MFI (Si/B, Si/Al) and B-MFI (Si/B) samples are denoted by the Si/B and Si/Al ratios present in their synthesis mixtures. The physiochemical properties and elemental compositions of the B-Al-MFI and B-MFI zeolites crystallized in this study are summarized in Table 4.1. Micropore volumes calculated from N_2 adsorption isotherms (Figs. 4.7 and 4.8, Section 4.6.1) and XRD patterns (Figs. 4.9 and 4.10, Section 4.6.2) of all samples are consistent with the MFI topology, even after washing solid products in water and removing organic structure directing agents by high temperature oxidative treatments (853 K), suggesting that any deboronation that may have occurred did not result in detectable structural degradation. The characteristic lengths of B-Al-MFI crystallites were taken as their shortest dimension, estimated from linear averages of crystallite sizes measured via SEM micrographs. B-Al-MFI (2.6, 176) and B-Al-MFI (2.6, 88) crystallites are rectangular prism-shaped and ca. 1.5 × 0.3 × 0.3 μm in dimension (Figures 4.1a and 4.1b, respectively), with solid Si/Al ratios of 142 and 88 (Table 4.1), respectively. B-Al-MFI (13, 176) and B-Al-MFI (13, 88) crystallites are coffin-shaped and ca. 10 × 10 × 15 μm in dimension (Figures 4.1c and 4.1d, respectively), with solid Si/Al ratios of 153 and 74 (Table 4.1), respectively. SEM micrographs of B-MFI samples are shown in 4.11 (4.6.3). Among the B-Al-MFI samples studied here, solid Si/Al ratios were similar (within

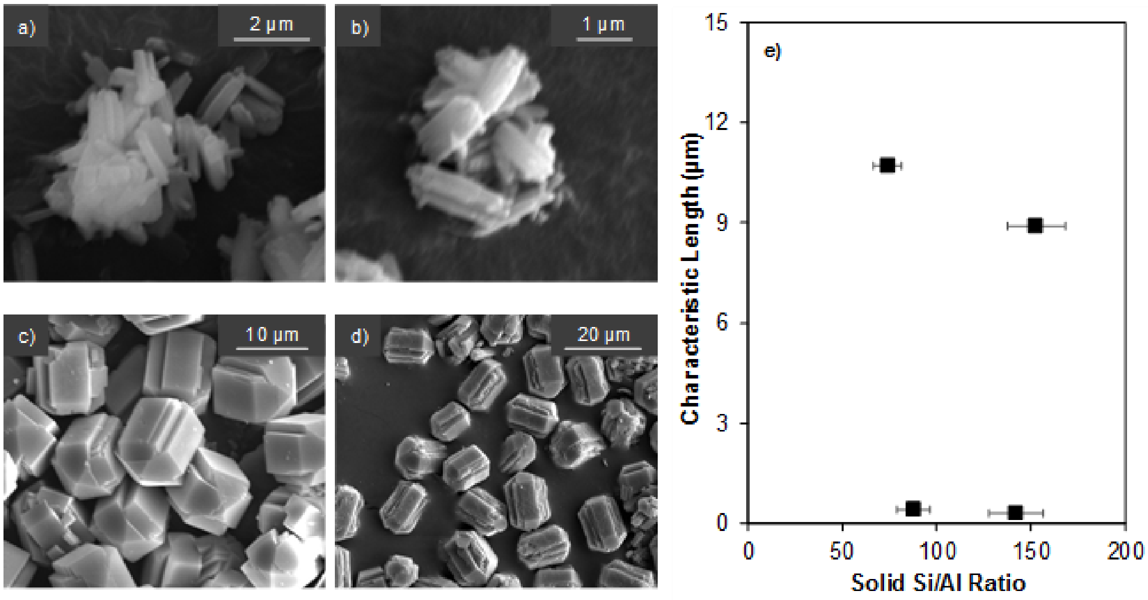

Figure 4.1.: SEM micrographs of a) B-Al-MFI (2.6, 176), b) B-Al-MFI (2.6, 88), c) B-Al-MFI (13, 176), and d) B-Al-MFI (13, 88); e) Characteristic crystallite lengths and Si/Al ratio of solid B-Al-MFI products formed.

20%) to the molar ratios present in their synthesis solutions, while solid Si/B ratios were similar (Si/B = 30–35, Table 4.1) among all samples and higher than Si/B ratios in their synthesis solutions (Si/B = 2.6–13). These findings resemble prior reports of B-Al-MCM-22 with solid Al content (Si/Al = 27) similar to that in the synthesis solution (Si/Al = 29), but with only partial incorporation of B heteroatoms [209].

Table 4.1.: Physiochemical properties and elemental compositions of B-Al-MFI and B-MFI zeolites.

Sample[a]	Solid Si/Al[b]	Solid Si/B[c]	B/EDA in synthesis	Micropore volume[d] (/ $cm^3 g^{-1}$)	Characteristic Length (/ μm)	Diffusion parameter (/ mol H^+_{Al} nm^{-1})
B-Al-MFI (2.6,176)	142	32	1.33	0.13	0.3	0.02
B-Al-MFI (2.6,88)	88	30	1.33	0.13	0.4	0.07
B-Al-MFI (13,176)	153	30	0.26	0.13	8.9	15
B-Al-MFI (13,88)	74	35	0.26	0.15	10.7	42
B-MFI (2.6)	n.d.∗	n.d.∗	1.33	0.14	0.3	n.d.∗
B-MFI (13)	n.d.∗	n.d.∗	0.26	0.13	1.0	n.d.∗

[a] Samples are denoted B-Al-MFI (Si/B, Si/Al) and B-MFI (Si/B), where Si/B and Si/Al correspond to the molar ratios ratios present in the synthesis solutions.

[b] Determined from atomic absorption spectroscopy. Errors are ± 10%.

[c] Determined from ICP-OES.

[d] Errors are ± 0.01 cm^3 g^{-1}.

∗n.d.; not determined.

Crystallite sizes are primarily influenced by the amount of B present in the synthesis solution under the conditions studied here, reminiscent of reports by Bodart et al [96] in which the addition of B (Si/B = 12) to a synthesis solution used to crystallize Al-MFI zeolites (Si/Al = 12) decreased mean crystallite sizes from 10 to 6 μm. We surmise that the smaller B-Al-MFI crystallite sizes obtained here ($\sim$0.3 μm) reflect, in part, the higher B content used in synthesis mixtures (Si/B = 2.6). We note, however, that the addition of B has also been reported to increase crystallite sizes under certain conditions for borosilicate MFI [231] and boroaluminosilicate *BEA [214], which likely reflects the influence of other precursors present in synthesis solutions on crystal morphology. Alkanolamines [232–234] act as chelating agents for Al that delay the release of Al into solution and decrease its incorporation into crystallizing oxide networks (e.g., LTA), while ethylenediamine (EDA) acts as a chelating agent for B (EDA/B = 2) [109, 235, 236] and has been reported to direct the siting of B heteroatoms into straight and sinusoidal channel locations in MFI [109]. Alkylamines (e.g., triethylenetetramine [94,210,237], ethylenediamine [95]) are also zeolite growth modifiers (ZGMs) that selectively bind to certain zeolite crystal facets during synthesis and influence their aspect ratio. The B-Al-MFI samples in this study were crystallized from solutions containing excess EDA (B/EDA $<$ 2), which appears to have influenced product crystallite sizes by serving as a ZGM, given that the amount of excess EDA present during synthesis was similar between B-Al-MFI samples that crystallized with similar size and morphology (Table 4.1). These synthesis protocols provide a strategy to vary the crystallite size of MFI zeolites independently of Al content, circumventing typical observations of crystallite size that tend to increase with Si/Al ratio [90–92].

4.4.2 Ammonia TPD methods to discriminate and quantify protons in boron and aluminum-substitued zeolites

Figure 4.2 shows the ammonia desorption rate from the four NH_4-B-Al-MFI samples of varying Al and B content, prepared by liquid-phase NH_4NO_3 ion-exchange to saturation at ambient conditions. Multiple desorption features are observed in each TPD profile, in agreement with previous reports of ammonia desorption from boroaluminosilicate MFI zeolites following adsorption of gas-phase ammonia at 373 K [211,223] or 393 K [209], and in contrast to the single desorption feature observed in TPD from aluminosilicate MFI (Fig. 4.12). The total amounts of ammonia desorbed from these four NH_4-B-Al-MFI samples are listed in Table 4.2 (0.65 – 0.91 10^{-3} mol H^+ g^{-1}) and overestimated Al contents by 3 – 8× (Figure 4.3), yet were similar to the total Al and B content (0.58 – 0.69 × 10^{-3} mol g^{-1}; Fig. 4.13 and Table S1, Section 4.6.4). This total reflects ammonia desorption from protons at framework Al and from other acidic binding sites that originate from B, given that TPD after such liquid-phase NH_4^+ ion-exchange protocols have been shown to detect only framework Al atoms in aluminosilicate CHA and MFI zeolites [129,218].

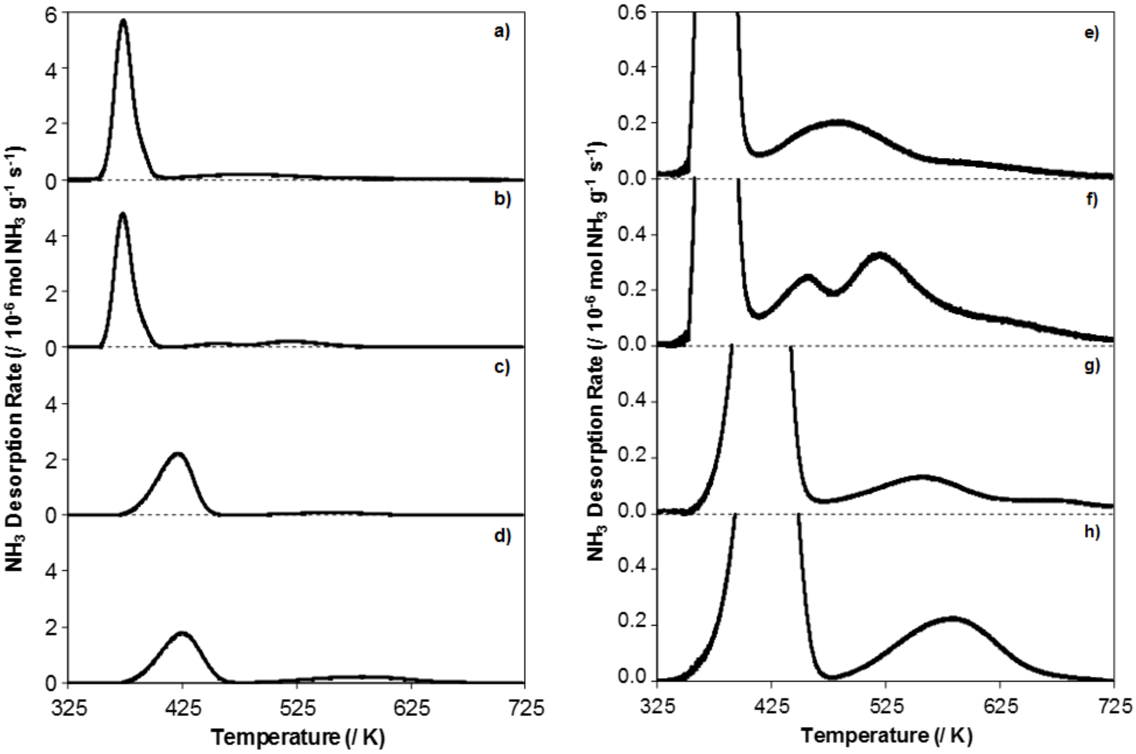

Figure 4.2.: NH$_3$ desorption rates during TPD of a) B-Al-MFI (2.6, 176), b) B-Al-MFI (2.6, 88), c) B-Al-MFI (13, 176), and d) B-Al-MFI (13, 88) after saturation in aqueous-phase NH$_4$NO$_3$. Figures e-h are the same profiles as a-d, respectively, upon magnification by 10×.

Table 4.2.: Quantification of ammonia desorbed during TPD from B-Al-MFI and B-MFI zeolites.

Sample	Al Content[a] (/ 10^{-3} mol g^{-1})	H^{+}_{Al}[b] (/ 10^{-3} mol g^{-1})			H^{+}_{Al}/Al_{tot}	
		NH_4^+ aqueous exchange, no He purge	NH_4^+ aqueous exchange, He purge (433 K)	NH_3 gas phase saturation (433 K)	NH_4^+ aqueous exchange, He purge (433 K)	NH_3 gas phase saturation (433 K)
B-Al-MFI (2.6,176)	0.12	0.86	0.10	0.11	0.90	0.98
B-Al-MFI (2.6,88)	0.19	0.91	0.20	0.17	1.06	0.90
B-Al-MFI (13,176)	0.11	0.65	0.08	0.10	0.78	0.94
B-Al-MFI (13,88)	0.22	0.79	0.16	0.18	0.75	0.83
B-MFI (2.6)	<0.01	0.50	<0.01	<0.01	n.d.*	n.d.*
B-MFI (13)	<0.01	0.58	<0.01	<0.01	n.d.*	n.d.*

[a] Determined from atomic absorption spectroscopy. Errors are ± 10%.

[b] Errors for all NH_3 TPD experiments are ± 0.03 10^{-3} mol NH_3 g^{-1}

∗n.d.; not determined.

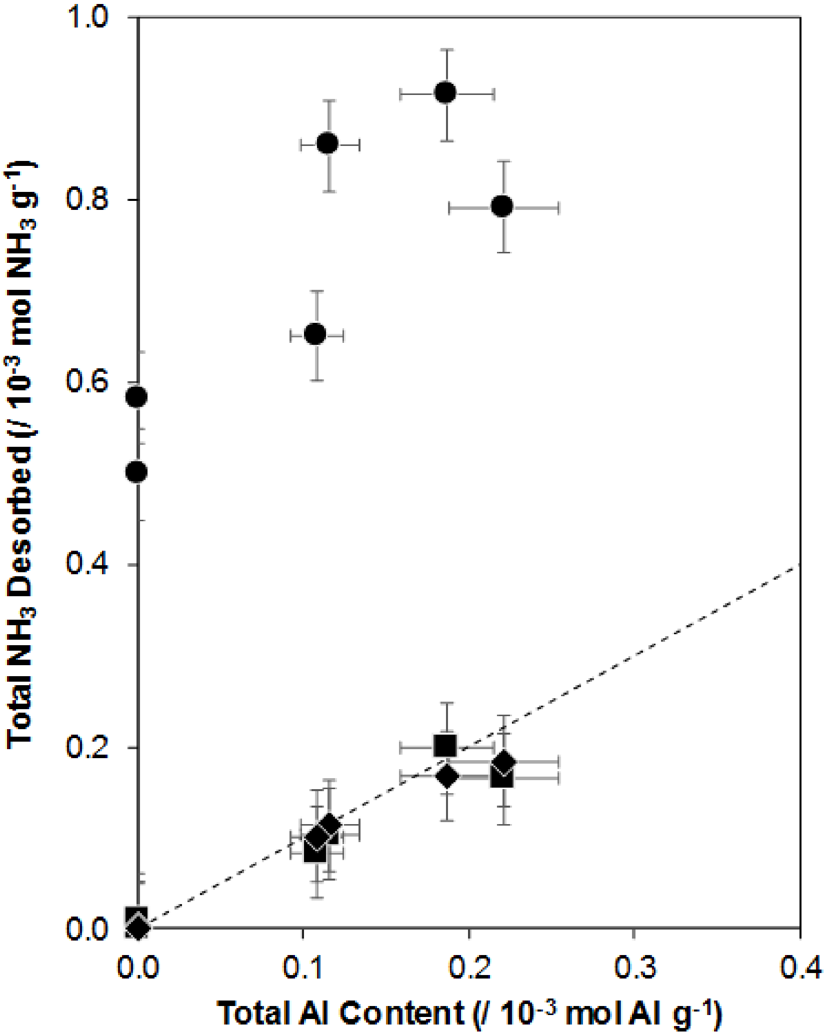

Figure 4.3.: NH_3 desorbed during TPD from B-MFI and B-Al-MFI samples after aqueous-phase NH_4NO_3 saturation without (●) and with subsequent He purge in He at 433 K (■), and after gas phase NH_3 saturation at 433 K (◆). Dashed line represents parity.

The lower-temperature desorption feature (350 – 450 K, Figure 4.2) likely reflects ammonia desorption from both trigonal and tetrahedral framework boron heteroatoms, each of which can adsorb ammonia [221]. B-MFI was synthesized using TEOS as the silicon precursor to avoid adventitious Al impurities often present in colloidal silica [214], and then subjected to liquid-phase NH_4NO_3 ion-exchange to saturation and a subsequent TPD. The TPD profiles of B-MFI (Fig. 4.14, Section 4.6.4) show a single desorption feature in a similar low temperature range as observed on B-Al-MFI (350 – 450 K), and the amount of ammonia desorbed from B-MFI (0.50 – 0.58 $\times 10^{-3}$ mol H^+ g^{-1}) is significantly larger than the trace Al contents that were below AAS detection limits ($<10^{-5}$ mol g^{-1}). The lower temperature desorption feature cannot unambiguously be assigned to weaker ammonia binding sites that originate from B heteroatoms, however, because the position of this feature is influenced by readsorption and diffusion effects that depend on crystallite size [224, 225]. This is reflected in the different temperatures corresponding to the maximum desorption rate of ammonia from ∼0.3 μm B-Al-MFI crystallites (∼375 K, Figures 4.2a and 4.2b) and ∼10 μm B-Al-MFI crystallites (∼425 K, Figures 4.2c and 4.2d), even though these data were collected with identical experimental methods.

These observations of ammonia TPD profiles of B-Al-MFI zeolites after liquid-phase saturation in NH_4NO_3 solution are similar to those reported by Woolery et al. for Al-MFI samples saturated in gas-phase NH_3 at 398 K and purged in dry flowing He (398 K, 4 h) [228]. Two prominent desorption features at ∼493 K and ∼653 K were assigned to NH_3 desorption from Lewis and Brønsted acid sites, respectively, and overestimated of the number of protons (by 1.3×) quantified from peaks in IR spectra for protonated pyridine (1545 cm^{-1}). In contrast, treatment of NH_3-saturated Al-MFI zeolites in flowing wet He (398 K) prior to TPD resulted in the disappearance of the lower temperature (∼493 K) desorption feature, and quantification of the NH_3 evolved in the higher temperature feature (∼653 K) was consistent with the number of protons quantified by IR spectroscopy. Thus, purging in wet He (398 K) was concluded to selectively remove ammonia bound to Lewis acidic Al sites because of competitive adsorption by water, a result corroborated by proton site estimates from TPD of samples saturated via aqueous-phase NH_4^+ exchange. Bates [218] and Di Iorio [129] extended these methods to differentiate between Lewis acidic copper (Cu^{2+}, Cu^+) and Brønsted acid sites in partially Cu-exchanged MFI and CHA zeolites, and quantified residual protons by ammonia saturation at elevated temperatures (433 K) and purging treatments in flowing wet He (433 K) to selectively remove Lewis-bound NH_3 prior to TPD.

We hypothesized that these methods could be adapted to quantify Brønsted acid sites of different strength compensating framework Al and B in boroaluminosilicates, given the presence of multiple desorption features in TPD profiles of B-Al-MFI observed here (Figure 4.2) and reported elsewhere [209, 211, 223], Al-MFI [228], and Cu-exchanged MFI and CHA zeolites [129, 218]. The maximum NH_3 desorption rate from B-Al-MFI after liquid-phase NH_4^+ ion-exchange to saturation was observed at ~375 K and ~425 K for samples with characteristic crystallite lengths of 0.3 and 10 μm, respectively. Based on the methodology used by Bates et al. [218], a purge step in flowing dry He at a temperature near the maximum desorption rate (433 K) of the low temperature desorption feature was used here to attempt selective removal of NH_3 associated with framework B. Water was not required in the intermediate He purge treatment to remove NH_3 from Lewis acid sites, because any Lewis acid sites present were expected to be coordinated to water after aqueous-phase NH_4NO_3 ion-exchange [228]. Ammonia desorption rates from B-Al-MFI samples after purging in dry He are shown in Figure 4.4. For all samples, the low-temperature desorption feature is absent, with a maximum desorption rate observed at ~550 K in a single primary desorption feature (and a shoulder at higher temperatures). The total amounts of ammonia evolved by this method ($0.08 - 0.20 \times 10^{-3}$ mol NH_3 g^{-1}, Table 4.2) for B-Al-MFI samples are similar to their Al content ($H^+/Al = 0.75 - 1.06$, Table 4.2), as shown in Figure 4.3. Indeed, TPD profiles measured after subjecting NH_3-saturated B-MFI zeolites to this intermediate He purge treatment at 433 K show negligible amounts of NH_3 desorbed ($<10^{-5}$ mol NH_3 g^{-1}, Figure 4.15,

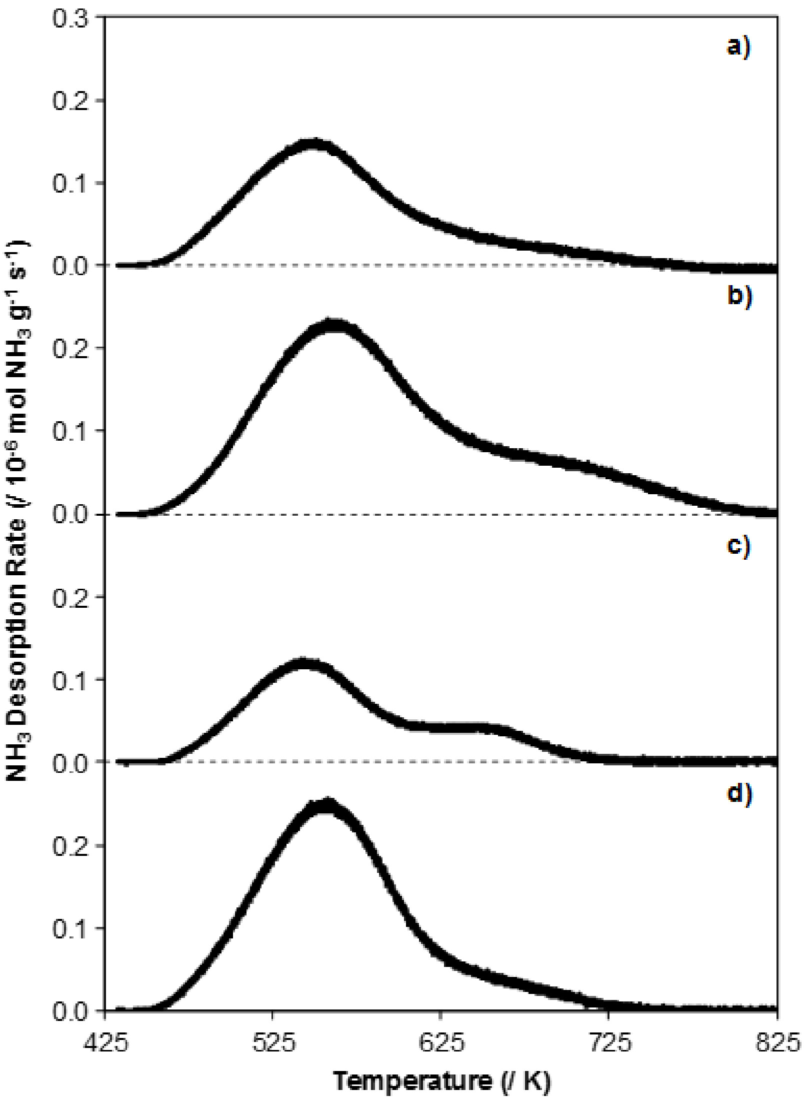

Figure 4.4.: NH_3 desorption rates from a) B-Al-MFI (2.6, 176), b) B-Al-MFI (2.6, 88), c) B-Al-MFI (13, 176), and d) B-Al-MFI (13, 88) samples after saturation in aqueous-phase NH_4NO_3 and He purge at 433 K.

Section 4.6.4). Taken together, these results suggest that NH_3 can be selectively desorbed from B heteroatoms after liquid-phase ion-exchange by purging NH_3-saturated boroaluminosilicates in flowing dry He at 433 K.

Saturation of Cu-exchanged MFI and CHA samples with gaseous NH_3 at 433 K (and subsequent purging in the presence of water) has also been used to discriminate between Lewis acidic Cu and Brønsted acid protons [129, 218], because NH_3 only adsorbs at protons under these conditions. In order to corroborate the number of Brønsted acidic protons at framework Al atoms in boroaluminosilicates, a similar gas-phase saturation procedure was performed here (without water) in which H-form B-Al-MFI samples were$_3$ stream (500 ppm NH_3 in He) at 433 K (2 h), followed by a purge in flowing dry He at 433 K (4 h). Rates of NH_3 desorption in a subsequent TPD from B-Al-MFI samples titrated using this method are shown in Figure 4.16 (Section 4.6.4). On each sample, the total amount of NH_3 evolved is similar to total Al content ($H^+/Al = 0.83 - 0.98$, Table 4.2), and to the amount of NH_3 desorbed after aqueous-phase NH_4^+-saturation and intermediate He purge, as shown in Figure 4.3. Again, NH_3 was only desorbed in trace quantities ($<10^{-5}$ mol NH_3 g^{-1}) from B-MFI zeolites after this procedure (Fig. 4.17, Section 4.6.4), verifying that the NH_3 desorbed from B-Al-MFI samples titrated with this procedure originated from H^+ associated with framework Al (H^+_{Al}). The amount of B in B-Al-MFI samples can be estimated from the difference between the NH_3 evolved in TPD after liquid-phase ion-exchange in NH_4NO_3, without and with purging in He at 433 K (Figure 4.18, Section 4.6.4). Next, we use methanol dehydration to dimethyl ether as a catalytic probe reaction to verify that these TPD protocols have accurately distinguished protons at framework Al and B.

4.4.3 Catalytic rates of methanol dehydration to dimethyl ether on boroaluminosilicates

Methanol dehydration to dimethyl ether (DME) can proceed via associative or dissociative routes on solid Brønsted acids (e.g. polyoxometalate clusters, zeolites) [212]. In the associative mechanism, methanol monomers form via adsorption of gas-phase methanol at a proton site, and a protonated dimer is formed via adsorption of a second methanol molecule that causes transfer of the proton from the oxide lattice. The protonated dimer then rearranges and dehydrates to form water and an adsorbed DME, which desorbs to regenerate the acid site. Periodic density functional theory (DFT) calculations have shown that methanol monomers and protonated dimers are the most abundant reactive intermediates (MARI) during methanol dehydration catalysis (433 K, >0.2 kPa CH_3OH) on polyoxometalate clusters and Al-*BEA zeolites, giving rise to the rate expression in Equation 4.1 [212]:

$$r = \frac{k_{first,A} P_{CH_3OH}}{1 + \frac{k_{first,A}}{k_{zero,A}} P_{CH_3OH}} \tag{4.1}$$

where $k_{first,A}$ and $k_{zero,A}$ are the first-order and zero-order rate constants for methanol dehydration in the associative pathway, respectively. *In situ* IR spectra of H-form Al-MFI (433 K, 0 – 15.3 kPa CH_3OH [238]; 415 K, 0 – 22 kPa CH_3OH [79]) show hydrogen-bonding modes for methanol monomers ($\sim$2380 cm^{-1}) and protonated dimers ($\sim$2620 cm^{-1}) present in both associative and dissociative pathways, but no peaks for surface methoxy species ($\sim$1457 cm^{-1}) involved in the dissociative mechanism [212]. Periodic DFT methods (vdW-DF functional) have estimated free energy barriers that are $\sim$40 kJ mol^{-1} lower for the associative than the dissociative pathway at Brønsted acid protons at four different T-sites in Al-MFI channels and intersections (415 K, 10 kPa CH_3OH) [239]. These results collectively indicate that the associative pathway is the predominant mechanism on Al-MFI zeolites under the conditions studied here.

First-order methanol dehydration rate constants reflect free energy differences between the DME formation transition state and an adsorbed methanol monomer and one gaseous methanol molecule, while zero-order rate constants reflect free energy differences between the same transition state and protonated methanol dimers. Zero-order rate constants are primarily sensitive to acid strength and depend weakly on the local confining environment, because van der Waals interactions with lattice oxygen atoms stabilize the similarly-sized transition state and the protonated dimer to similar extents [212, 240]. First-order rate constants depend on both acid strength and confinement, which preferentially stabilizes larger DME formation transition states over smaller methanol monomers [33, 240]. Previous data collected from our group [79] has shown quantitative agreement in first-order and zero-order rate constants (per H^+_{Al}, 415 K), and corresponding activation enthalpy and entropy values, with values of rate constants and activation parameters reported by Jones et al. (per H^+_{Al}, 433 K) [33] on a suite of commercially-available Al-MFI zeolites of different Si/Al ratio. Methanol dehydration turnover rates (per H^+, 433 K, 0.2 – 20 kPa) are two orders-of-magnitude lower on B-MFI than on Al-MFI, reflecting deprotonation energies that are $\sim$70 kJ mol^{-1} higher for protons at framework B than Al [33]. Thus, methanol dehydration turnover rates measured in zero-order regimes on B-Al-MFI zeolites should depend predominantly on the number of protons at framework Al in B-Al-MFI.

DME formation rates (per H^+_{Al}, 415 K) on the four B-Al-MFI samples, normalized by the number of protons compensating framework Al as quantified by the selective NH_3 titration methods reported here (H^+_{Al}, Table 4.2), are shown as a function of methanol partial pressure in Figure 4.5. DME formation rates on B-Al-MFI zeolites increased linearly at low methanol partial pressures ($<$ 2 kPa) and approached a zero-order kinetic regime at higher pressures ($>$ 40 kPa), in agreement with previous reports on Al-MFI zeolites under similar conditions (433 K, 0 – 20 kPa CH_3OH [33]; 415 K, 0 – 60 kPa CH_3OH [79]). These data were regressed to Eq. (1) to estimate zero-order and first-order rate constants, which are shown in Figure 4.6 as a function of H^+_{Al} content on the B-Al-MFI samples, along with data reported previously on Al-MFI samples. Zero-order rate constants are identical, within experimental error, for all B-Al-MFI samples (20 – 26 $\times$ 10^{-3} mol DME (mol H^+_{Al})$^{-1}$ s^{-1}, Fig. 4.6) and in quantitative agreement with values reported previously by Jones et al. [33] and Di Iorio et al. [79] on Al-MFI zeolites. Additionally, zero-order DME formation rates (per g) are independent of the number of B heteroatoms present (Fig. 4.19, Section 4.6.5), in agreement with previous reports for a variety of acid-catalyzed reactions in B-Al-MFI (*n*-hexane cracking [213], ethylbenzene dealkylation [213], cyclopropane isomerization [213], and ethylene methylation [211]), and DME formation rates on B-MFI (13) suggest that B contributes to less than 1% of the measured rate on B-Al-MFI samples (Fig. 4.20, Section 4.6.5). These results collectively provide rigorous verification that the ammonia titration methods developed here quantify only catalytically-relevant Brønsted acid protons in B-Al-MFI zeolites of varying B (Si/B = 20-35) and Al (Si/Al = 74 – 153) heteroatom content and diffusion parameters ($\Psi = 0.02 - 42$ mol H^+_{Al} nm^{-1}, Table 4.1).

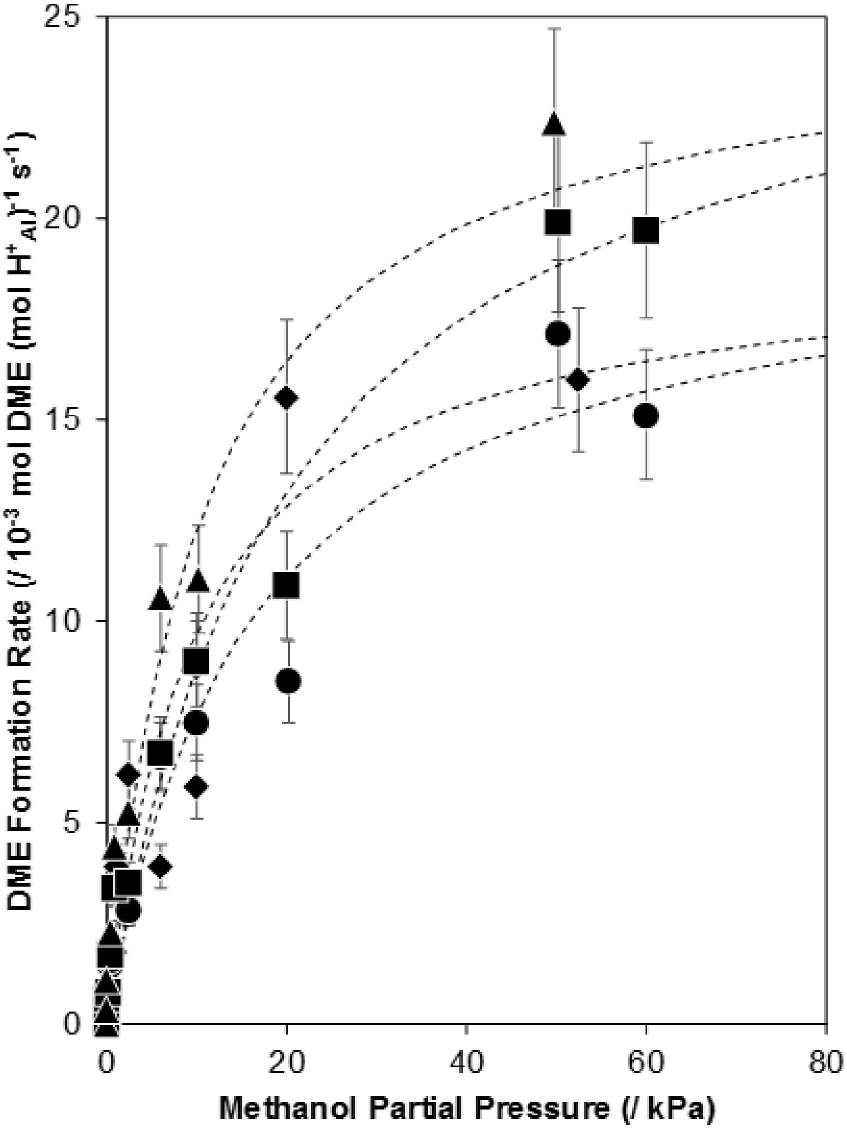

Figure 4.5.: DME formation rates on (◆) B-Al-MFI (2.6, 176), (●) B-Al-MFI (2.6, 88), (■) B-Al-MFI (13, 176), and (▲) B-Al-MFI (13, 88) samples at 415 K. Rates are normalized by the number of protons at framework Al (H^+_{Al}) quantified by NH_3 TPD after aqueous-phase saturation in NH_4NO_3 and intermediate purging in He at 433 K (Table 4.2).

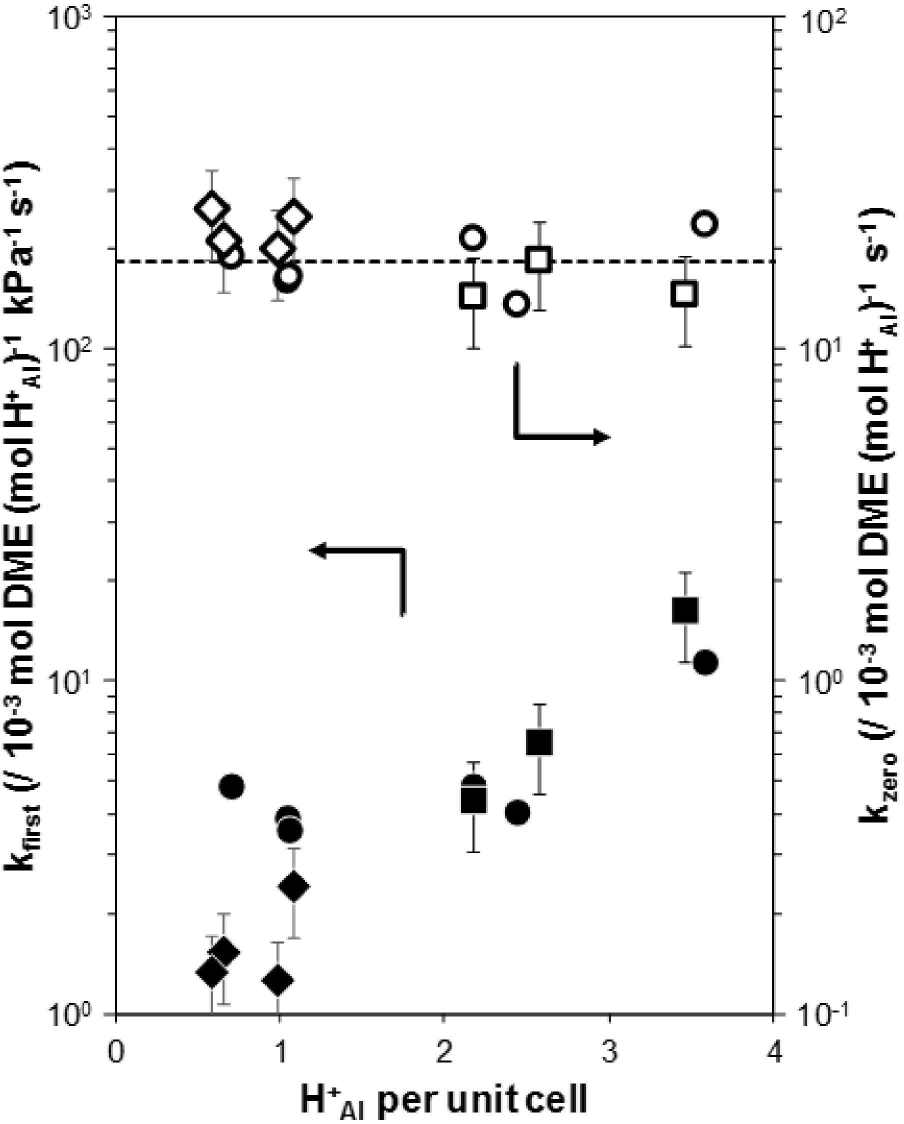

Figure 4.6.: First-order (closed symbols) and zero-order (open symbols) rate constants of methanol dehydration on Al-MFI samples reported by Jones et al. [33] at 433 K (●), Di Iorio et al. [79] at 415 K (■), and in this study on B-Al-MFI samples at 415 K (◆).

First-order rate constants (per H^+_{Al}, 415 K; Fig. 4.6) for the B-Al-MFI samples (1.3 - 2.4 × 10^{-3} mol DME (mol H^+_{Al})$^{-1}$ kPa^{-1} s^{-1}) are lower by 2 - 10× than those reported previously for Al-MFI (4 – 12 10^{-3} mol DME (mol H^+_{Al})$^{-1}$ kPa^{-1} s^{-1}, 433 K [33]; 4 – 16 10^{-3} mol DME (mol H^+_{Al})$^{-1}$ kPa^{-1} s^{-1}, 415 K [79]). Intraparticle mass transfer limitations can decrease observed rates measured in positive-order kinetic regimes by decreasing reactant concentrations at active sites [241], as previously reported during methanol dehydration catalysis (415 K) in large Al-CHA crystallites (Si/Al = 27, 6 μm, $\Psi = 50$ mol H^+ nm^{-1}) [79]. Intraparticle methanol concentration gradients were estimated in the four B-Al-MFI zeolites under the conditions studied for methanol dehydration catalysis (Figures 4.21-4.24, Section 4.6.6) using methods reported previously [79]. Methanol partial pressures decrease by less than 15% from the bulk external fluid to the center of catalyst particles in all B-Al-MFI zeolites, with effectiveness factors near unity (Figure 4.25, Section 4.6.6) that were estimated using the first-order rate constants and the physiochemical properties in Table 4.1 (additional details in Section 4.6.6).

Differences in first-order methanol dehydration rate constants among microporous aluminosilicates, when rigorously of kinetic origin, reflect differences in the stabilization of larger DME formation transition states and smaller methanol monomers by van der Waals interactions, which cause rate constants to increase as confining voids become smaller [240]. First-order rate constant values of ~7.0×10^{-3} mol DME (mol H^+_{Al})$^{-1}$ kPa^{-1} s^{-1} are characteristic of protons confined within pores of ~0.6 nm diameter, while values of ~2.0×10^{-3} mol DME (mol H^+_{Al})$^{-1}$ kPa^{-1} s^{-1} are characteristic of protons confined within ~0.8 nm voids [240]. The lower first-order methanol dehydration rate constants measured on B-Al-MFI (Fig. 4.6) may reflect the preferential siting of framework Al into T-sites located within MFI intersections (~0.7 nm voids [87]) over those in straight and sinusoidal channels (~0.55 nm voids [87]), which seems plausible considering that EDA chelates with B during conditions of synthesis (B/EDA = 2) [235] and has been characterized by XRD to locate within straight and sinusoidal channels during synthesis of B-MFI [109]. Although first-order rate constant values of ~5×10^{-3} mol DME (mol H^+_{Al})$^{-1}$ kPa^{-1} s^{-1} have been attributed previously to protons confined within MFI intersections, these materials were synthesized in the presence of both TPA^+ and Na^+ cations [33], which are synthetic mixtures that have been reported by Yokoi et al. to incorporate Al at T-sites both in MFI intersections and in straight and sinusoidal channels [68]. The first-order rate constant values measured here, which are consistent with values expected for protons confined within ~0.7 - 0.8 nm voids characteristic of MFI intersections [87, 240], suggest that B-Al-MFI zeolites synthesized in the presence of EDA and TPA^+ may contain Al preferentially sited at T-sites located within MFI intersections.

4.5 Conclusions

Ammonia titration methods were developed to distinguish between framework B and Al heteroatoms in boroaluminosilicate MFI catalysts, where the latter generate protons that are stronger acids and behave as dominant active sites for Brønsted acid-catalyzed reactions. Temperature programmed-desorption (TPD) of ammonia following aqueous phase NH_4^+ ion-exchange quantifies both framework Al and B species in B-Al-MFI. Intermediate treatments to remove weakly-bound ammonia at framework B sites (flowing dry He, 433 K) or gas-phase NH_3 saturation at intermediate temperatures (433 K), however, quantify only protons that charge compensate framework Al atoms. These methods should be adaptable to discriminate and quantify weaker and stronger protons respectively originating from B and Al in other boroaluminosilicates, and are especially useful to quantify catalytically-relevant protons in small-pore or Al-dense molecular sieves [217, 218].

The number of protons counted by these TPD methods agreed quantitatively with the amount of total Al measured by atomic absorption spectroscopy ($H^+/Al = 0.75 – 1.06$) on a series of B-Al-MFI zeolites of varying crystallite size and Al contents. Crystallite sizes (0.3 – 10 μm) and Si/Al ratios (74 – 153) were independently varied in B-Al-MFI zeolites synthesized in the presence of tetrapropylammonium cations and ethylenediamine structure directing agents, resulting in crystallites with diffusion parameters that varied by three orders of magnitude (0.02 – 42 mol H_{Al}^+ nm^{-1}). These findings differ from heuristic guidelines that crystallite sizes and Al contents are correlated structural properties for aluminosilicates synthesized hydrothermally, and the typical observations that crystallite sizes increase with Si/Al ratios, which likely reflects the dual roles of ethylenediamine as a structure directing agent and a zeolite growth modifier during MFI crystallization. The ability to vary Si/Al ratios and crystallite sizes over a range of diffusion parameters allows for independent assessments of how these properties influence rates and selectivities of catalytic reaction networks, especially where catalytic and transport phenomena are inherently coupled, such as in alkene oligomerization [87] and methanol-to-olefins [88, 89] cycles.

The number of protons compensating framework Al atoms were used to rigorously normalize zero-order rate constants for methanol dehydration to dimethyl ether, a catalytic probe that is sensitive to Brønsted acid strength and able to unambiguously discriminate contributions from protons that charge-compensate Al and B heteroatoms. We surmise that first-order dehydration rate constants (per H^+_{Al}, 415 K) on B-Al-MFI samples that are lower than values characteristic of Al-MFI zeolites may reflect the preferential siting of Al in T-sites located in MFI intersections, wherein preferential stabilization of larger DME formation transition states relative to smaller methanol precursors by van der Waals interactions is less effective than within smaller MFI channels. Zero-order dehydration rate constants (per H^+_{Al} , 415 K) were identical on all B-Al-MFI zeolites with varying crystallite size and Al content, and identical to values characteristic of Al-MFI zeolites [33, 79], providing confirmation that the NH_3 titration and TPD methods developed here selectively quantify protons at Al atoms, as required for rigorous normalization of turnover rates. These findings are consistent with prior reports of rates for Brønsted acid-catalyzed reactions on borosilicates that depend solely on residual trace Al content, often present as adventitious impurities introduced from inorganic precursors used in zeolite crystallization or from contact with binders in formulated catalytic solids.

4.6 Supporting Information

4.6.1 N_2 adsorption isotherms of B-MFI and B-Al-MFI zeolites

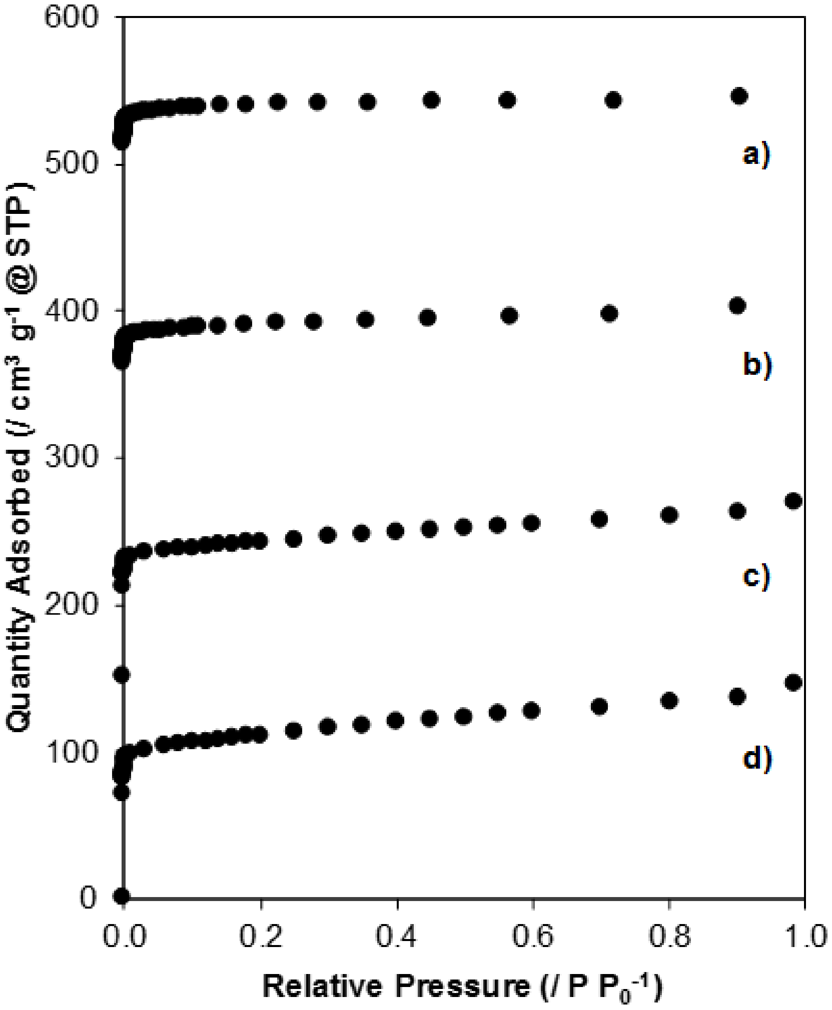

Figure 4.7.: N_2 adsorption isotherms for a) B-Al-MFI (2.6, 176), b) B-Al-MFI (2.6,88), c) B-Al-MFI (13, 176), and d) B-Al-MFI (13,88). Isotherms are vertically offset by 150 cm^3 g^{-1} @ STP for clarity.

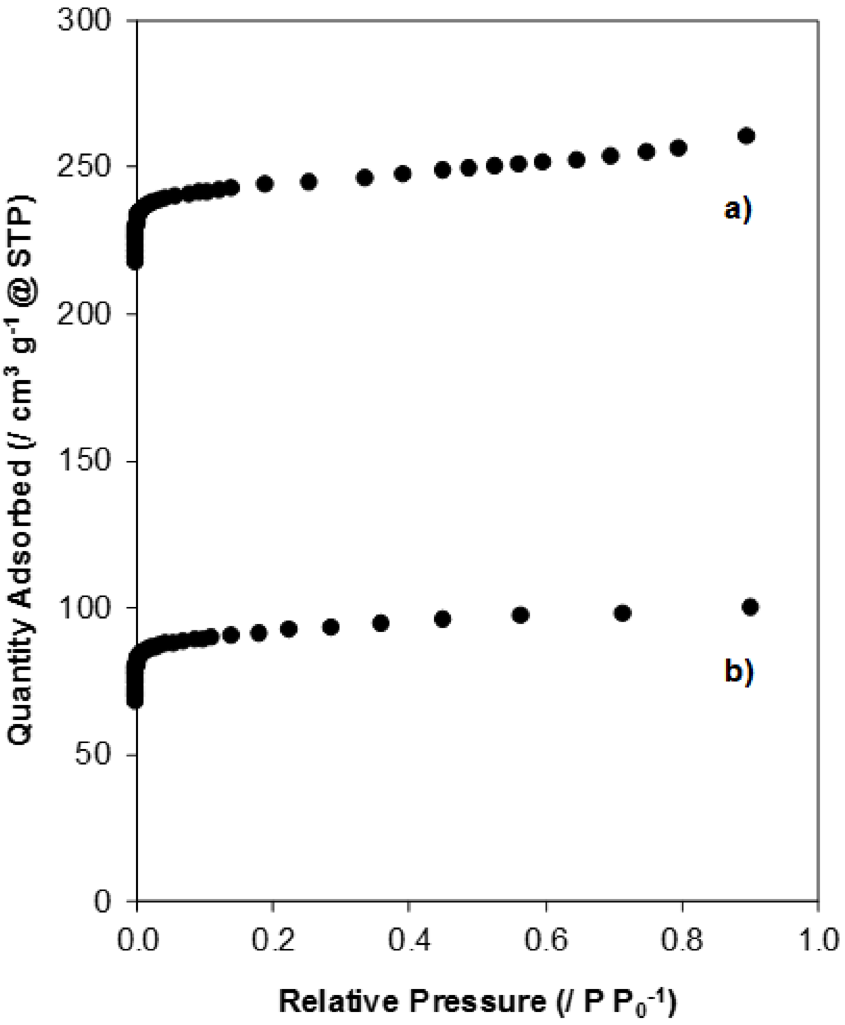

Figure 4.8.: N_2 adsorption isotherms for a) B-MFI (2.6) and b) B-MFI (13). Isotherms are vertically offset by 150 cm^3 g^{-1} @ STP for clarity.

4.6.2 XRD patterns of B-MFI and B-Al-MFI zeolites

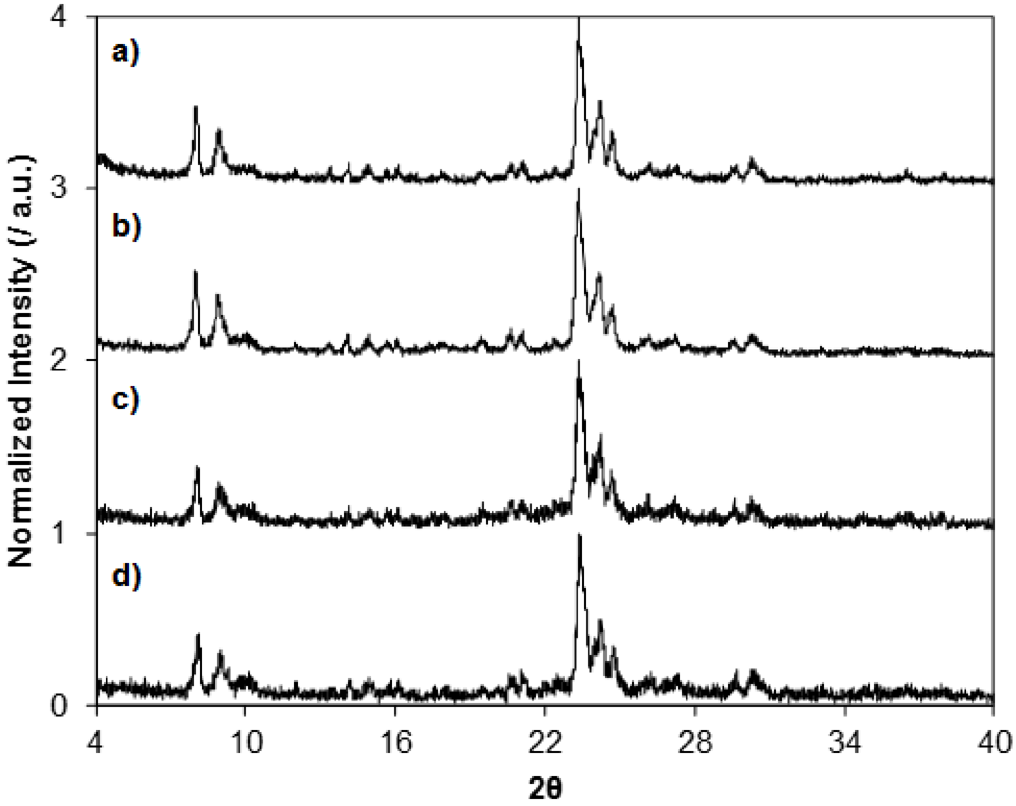

Figure 4.9.: XRD patterns of a) B-Al-MFI (2.6, 176), b) B-Al-MFI (2.6, 88), c) B-Al-MFI (13, 176), and d) B-Al-MFI (13, 88).

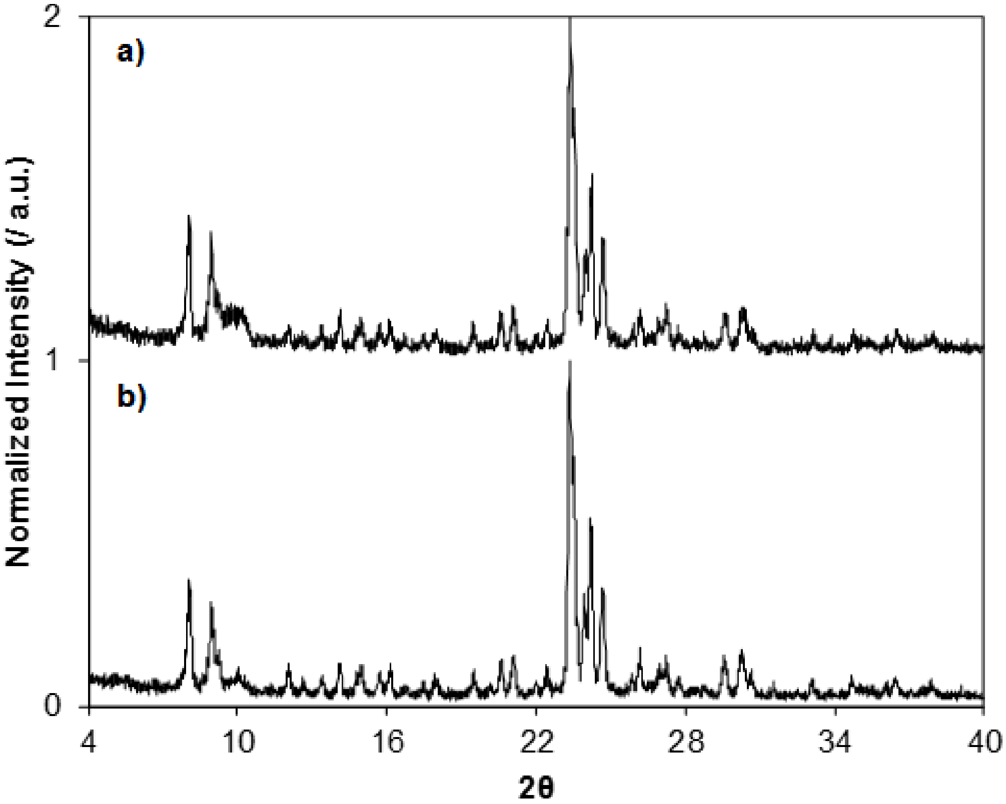

Figure 4.10.: XRD patterns of a) B-MFI (2.6) and b) B-MFI (13).

4.6.3 SEM micrographs of B-MFI zeolites

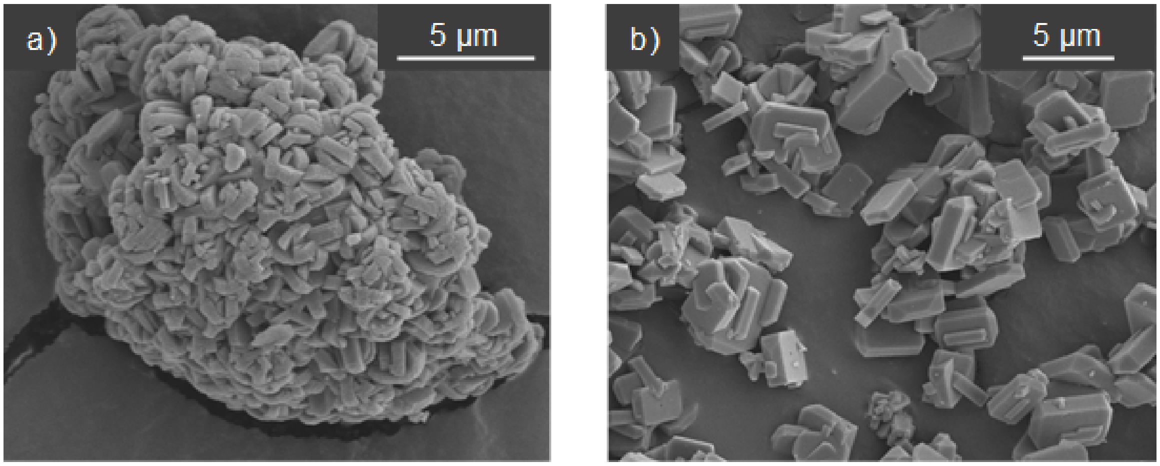

Figure 4.11.: SEM micrographs of a) B-MFI (2.6) and b) B-MFI (13).

4.6.4 Ammonia TPD of Al-MFI, B-Al-MFI, and B-MFI zeolites

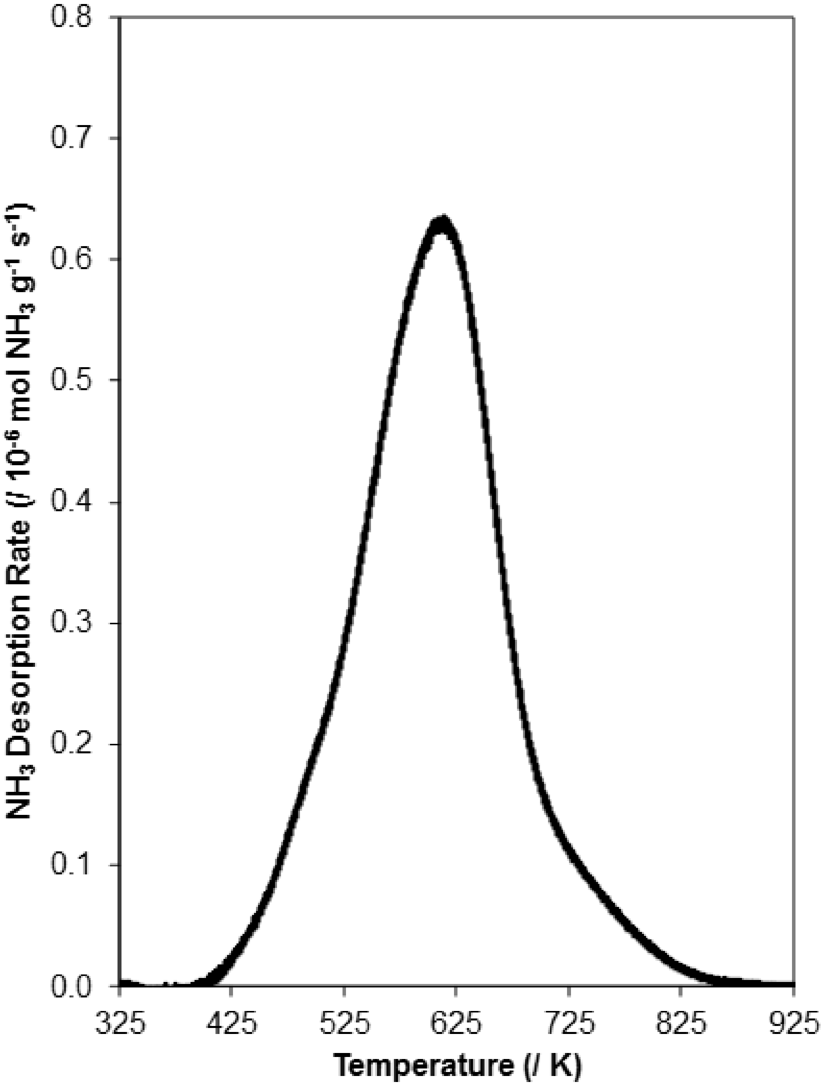

Figure 4.12.: NH_3 desorption rates from NH_4-Al-MFI (Zeolyst CBV 5524G, Si/Al = 25).

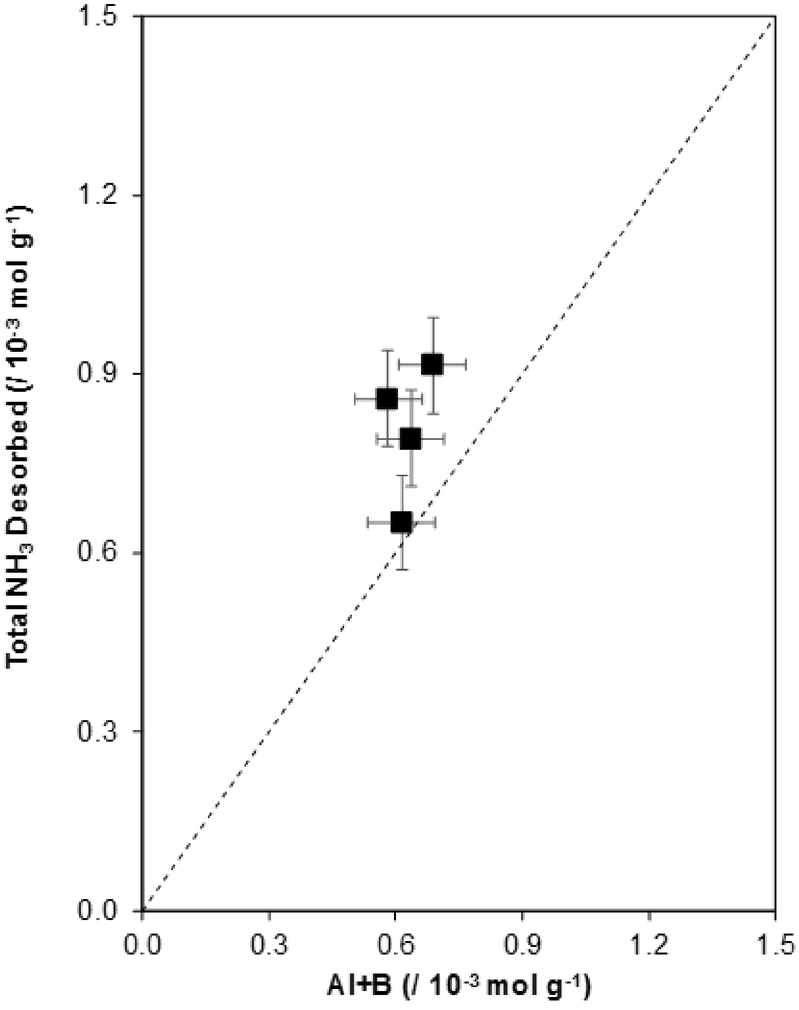

Figure 4.13.: Total amount of NH_3 desorbed during TPD after saturation in liquid-phase NH_4NO_3 solution (y-axis) and total Al and B content from elemental analysis (x-axis).

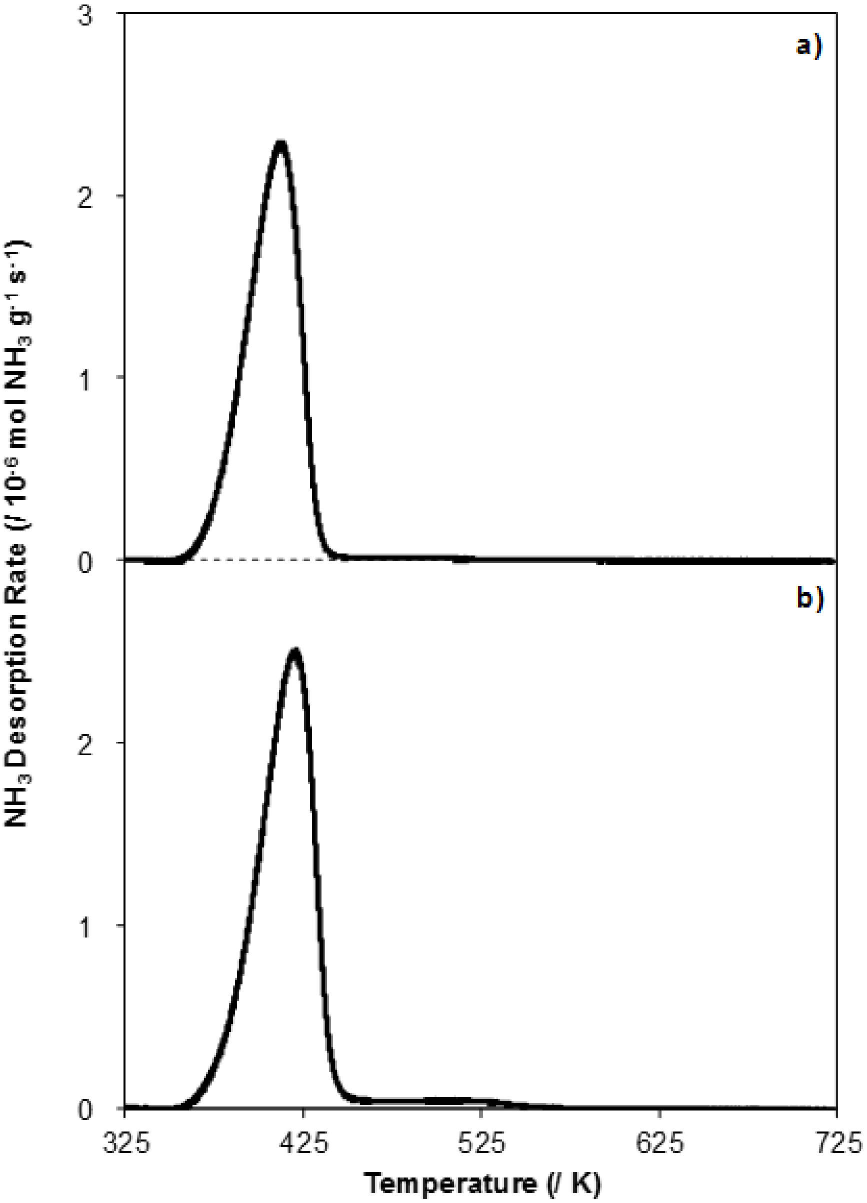

Figure 4.14.: NH_3 desorption rates from a) B-MFI (2.6) and b) B-MFI (13) after liquid-phase saturation with NH_4NO_3.

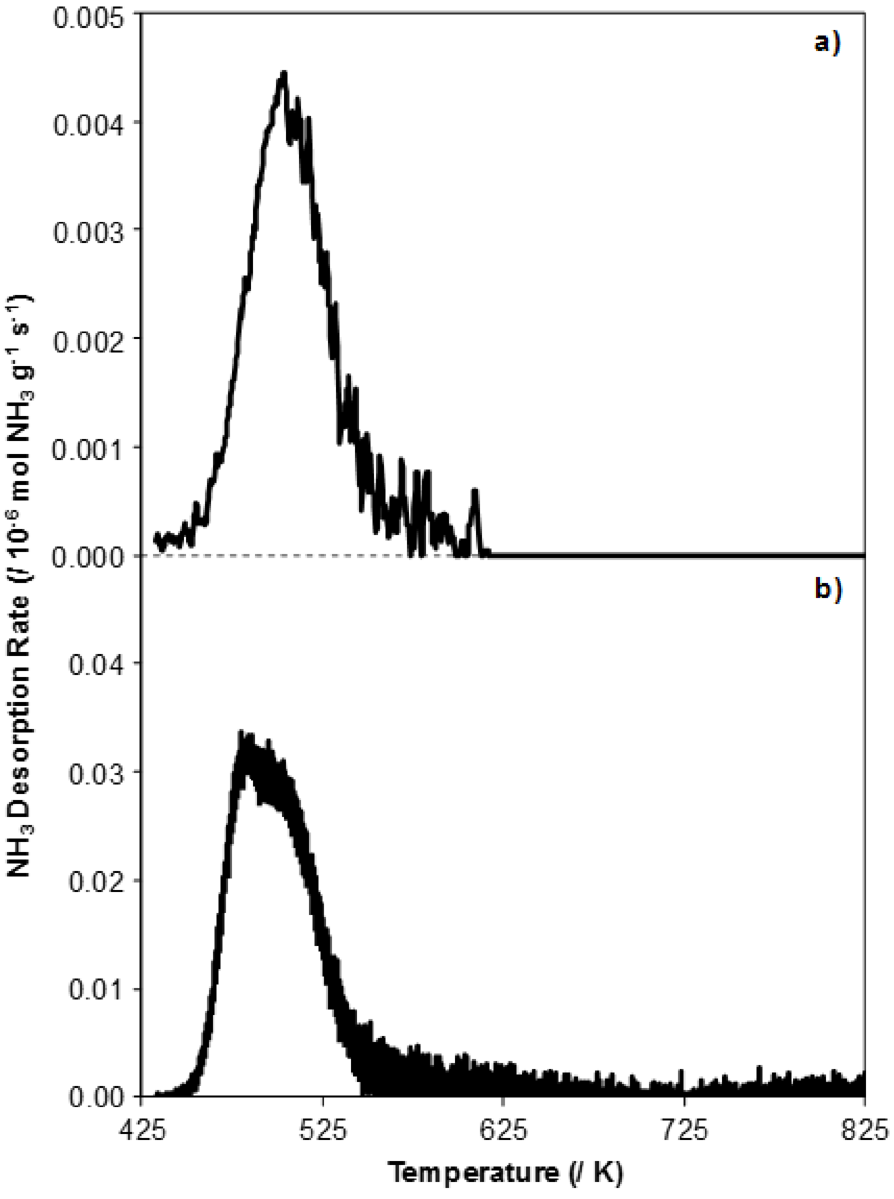

Figure 4.15.: NH_3 desorption rates from a) B-MFI (2.6) and b) B-MFI (13) after liquid-phase saturation with NH_4NO_3 and intermediate He purge at 433 K.

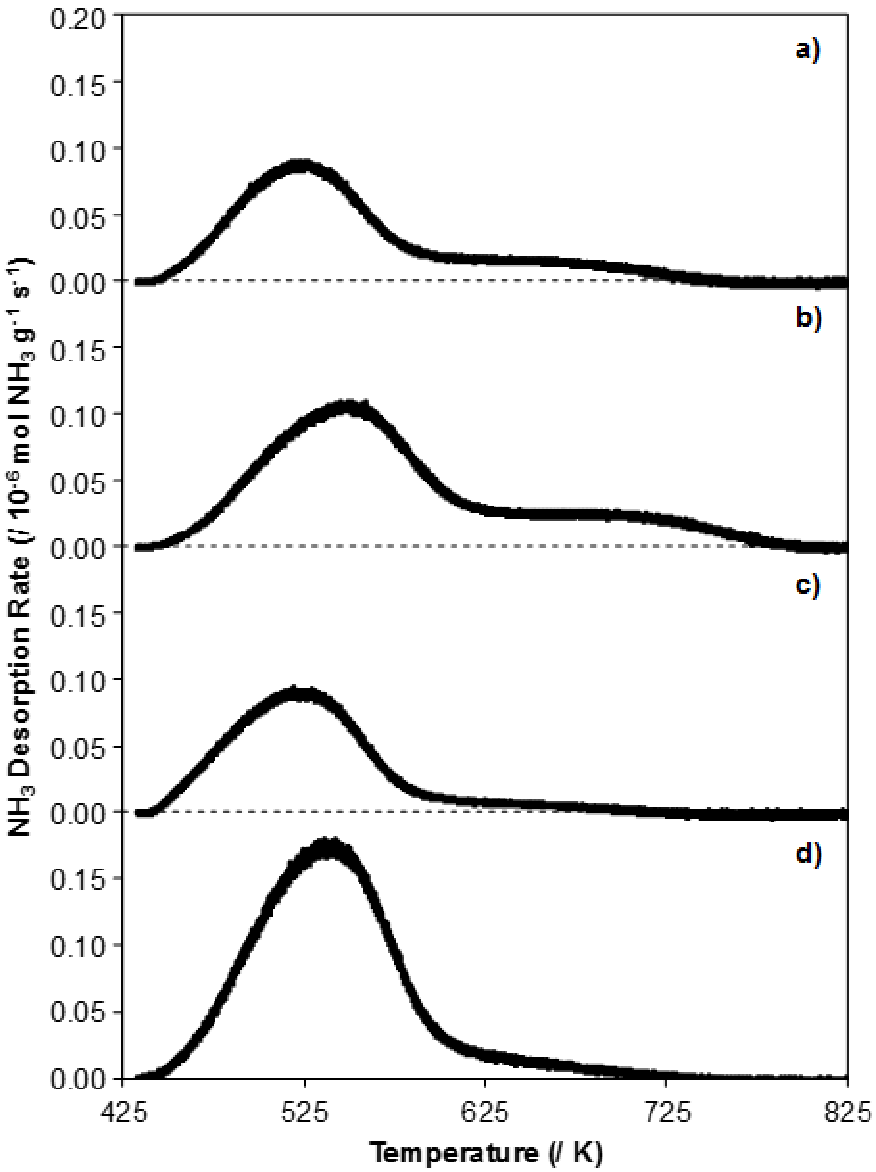

Figure 4.16.: NH_3 desorption rates from a) B-Al-MFI (2.6, 176), b) B-Al-MFI (2.6,88), c) B-Al-MFI (13, 176), and d) B-Al-MFI (13,88) after gas-phase NH_3 saturation at 433 K and intermediate He purge at 433 K.

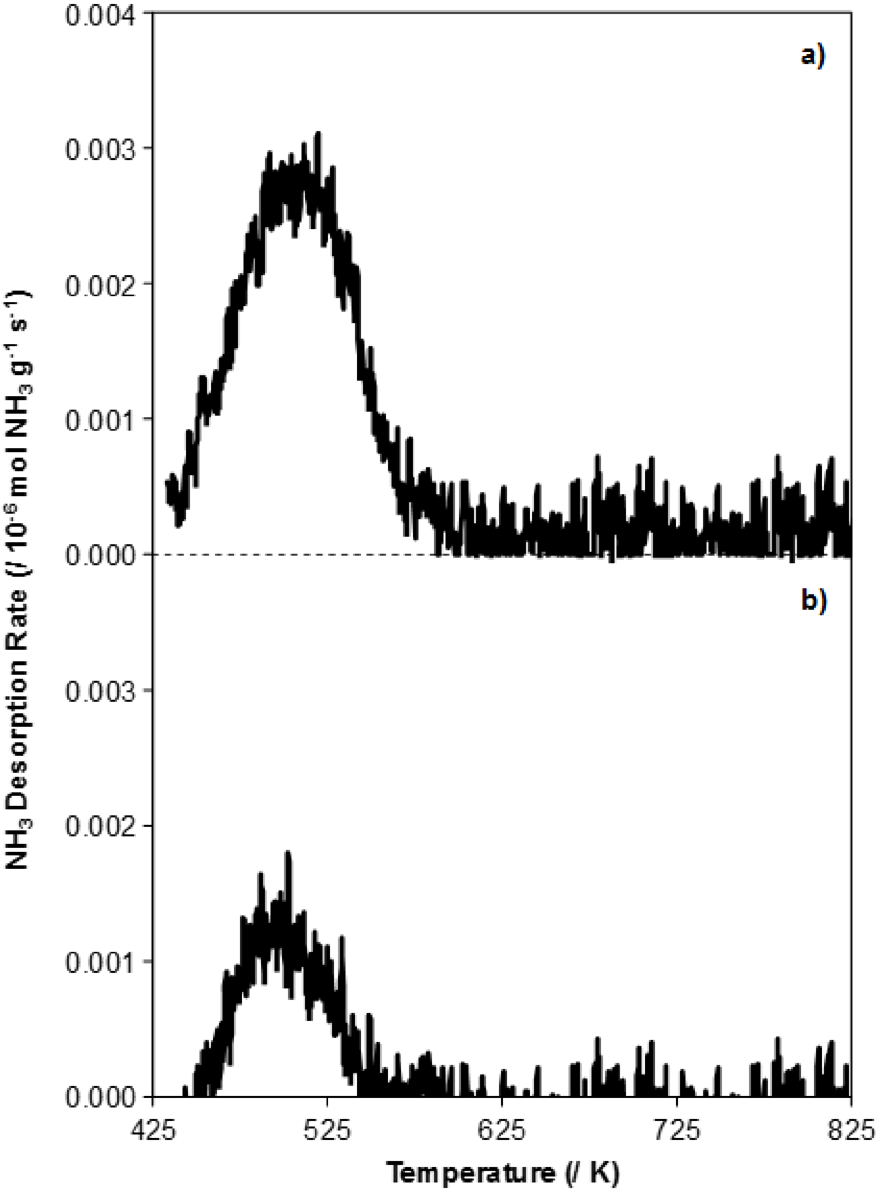

Figure 4.17.: NH$_3$ desorption rates from a) B-MFI (2.6) and b) B-MFI (13) after saturation gas-phase NH$_3$ saturation at 433 K and intermediate He purge at 433 K.

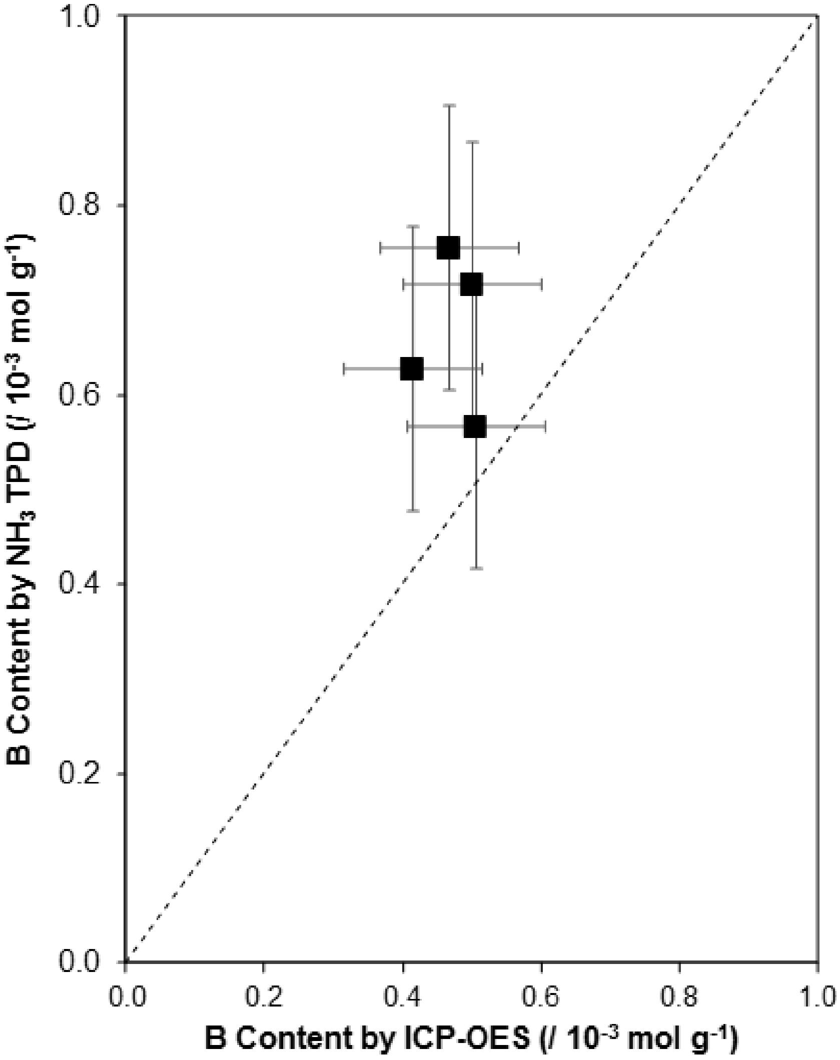

Figure 4.18.: B content estimated by the difference between NH_3 desorbed in TPD after non-selective titrations and after liquid-phase saturation and He purge at 433 K, plotted against B content of B-Al-MFI measured by ICP-OES. Dashed line represents parity.

4.6.5 Estimation of methanol dehydration turnover frequencies at B in B-Al-MFI zeolites

Zero-order DME formation rates (per g) are shown in Figure S13, as a function of protons at framework Al (quantified from NH_4NO_3 ion-exchange and subsequent He purge at 433 K) or at B sites in B-Al-MFI samples. DME formation rates (per g) increase linearly with the number of protons at framework Al (H^+_{Al}) and extrapolate to the origin, without any discernable dependence on B content. DME formation rates (415 K, per mol B) measured on B-MFI (13) are shown in Figure 4.19, and increase linearly with methanol pressure up to 60 kPa, in agreement with previous reports of methanol dehydration on B-MFI under similar conditions [33]. The first-order rate constant on this sample is 3.1×10^{-6} mol DME (mol B)$^{-1}$ kPa^{-1} s^{-1}, which is three orders of magnitude smaller than that at H^+_{Al}. These data conclusively show that the observed methanol dehydration rates on B-Al-MFI are primarily due to protons compensating framework Al, even though B contents are 2 – 5× greater than Al contents, and reflect previous reports of acid-catalyzed reactions in boroaluminosilicates [213].

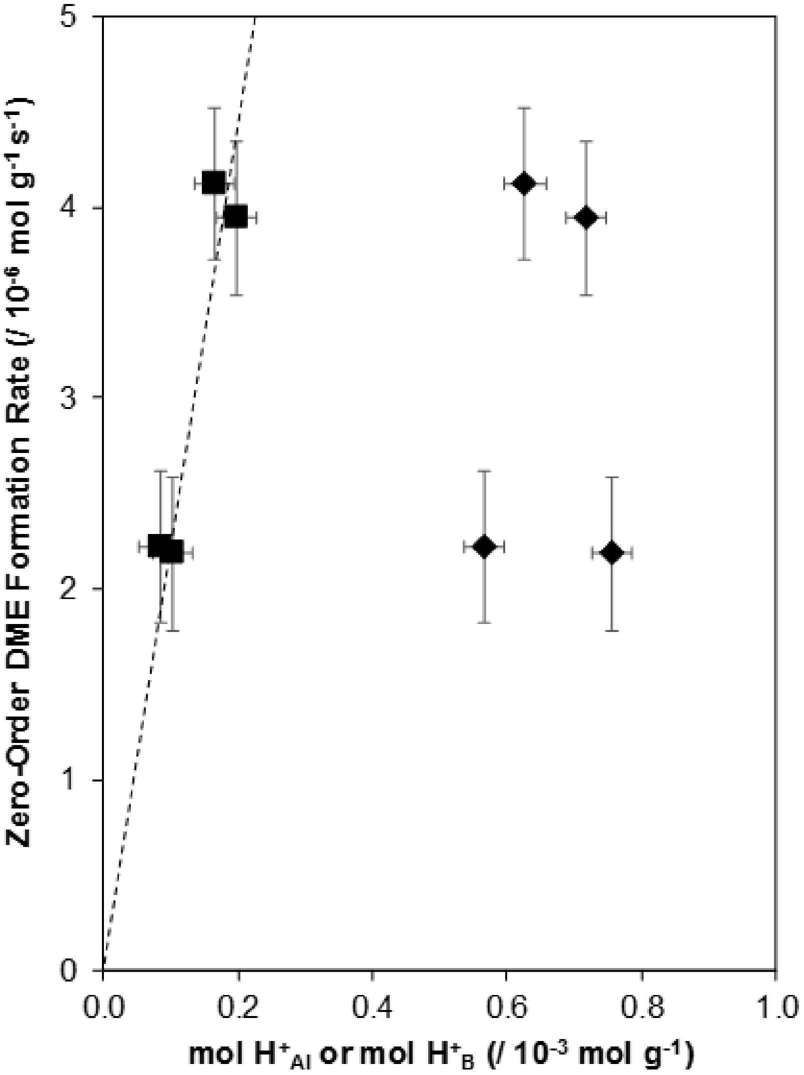

Figure 4.19.: Zero-order DME formation rates (per g) as a function of the number of protons at framework Al (■) or B (◆). Dotted line is a fit through the origin for rates as a function of protons at framework Al.

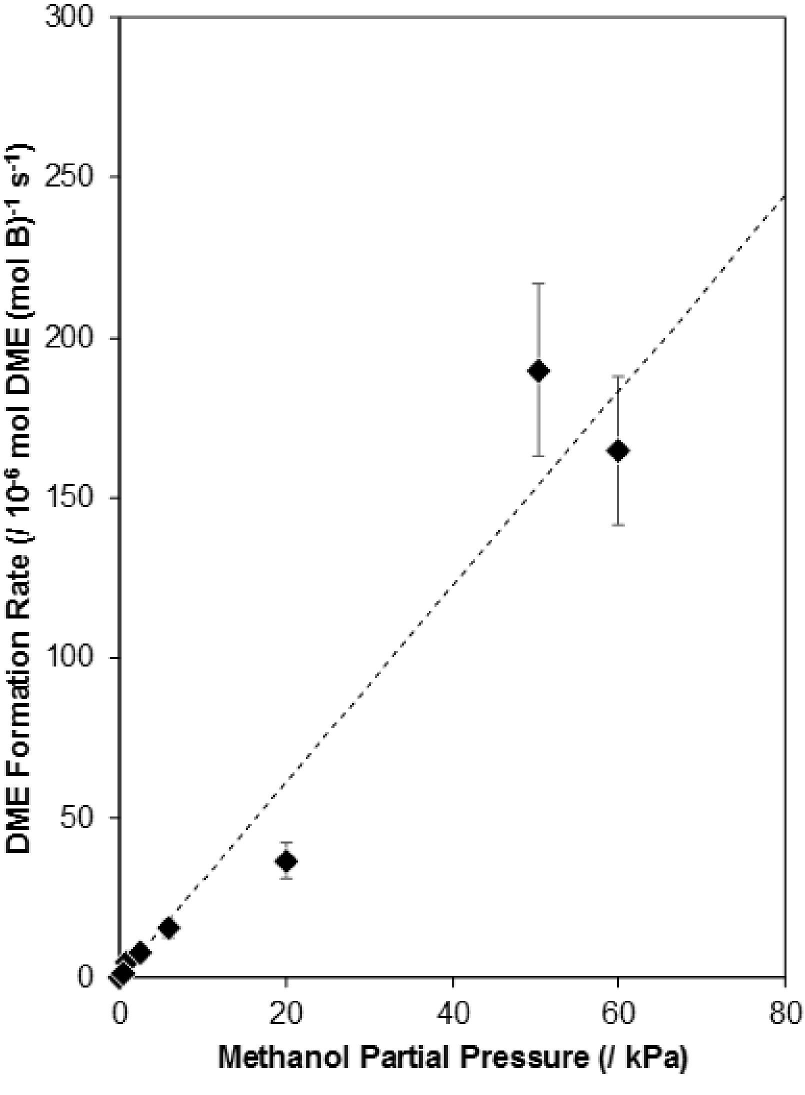

Figure 4.20.: DME formation rates (415 K, per mol B) on B-MFI (13). Dashed line represents fit of the associative dehydration rate law to experimental data.

4.6.6 Evaluation of intraparticle mass transfer limitations in B-Al-MFI during methanol dehydration catalysis

Intraparticle methanol concentration profiles were calculated according to methods previously described by Di Iorio et al. [79]. Concentration profiles can be calculated from models for coupled reaction and molecular transport in spherical particles at steady state in the absence of external diffusion limitations with Equation 4.2.

$$\frac{d^2C_m}{d^2r} + \frac{2}{r}\frac{dC_m}{dr} - \frac{2\rho_s}{D_e}r_{DME} = 0 \tag{4.2}$$

In this expression, C_m is the concentration of methanol (mol m^{-3}), r is the distance from the center of the particle, ρ_s is the volumetric density of Brønsted acid protons at framework Al, D_e is the effective self-diffusivity of methanol in MFI pores (m^2 s^{-1}), and r_{DME} is the rate of DME formation (m^3 (mol $H^+)^{-1}$ s^{-1}). The rate of DME formation via associative methanol dehydration is given as a function of pressure (concentration) by Equation 4.1 in the main text. D_e was estimated from molecular dynamics simulations for methanol diffusion in MFI (1.4×10^{-10} m^2 s^{-1}, 300 K) and extrapolated to 415 K (2.3×10^{-10} m^2 s^{-1}) using Chapman-Enskog theory as given by Equation 4.3.

$$D_e(T_2) = D_e(T_1)(\frac{T_2}{T_1})^{\frac{3}{2}} \tag{4.3}$$

Figures 4.21–4.24 show the calculated concentration profiles of methanol in the four B-Al-MFI zeolites at 415 K over a range of methanol partial pressures (0.05 - 51.2 kPa). Methanol concentrations in B-Al-MFI (2.6, 176), B-Al-MFI (2.6, 88), and B-Al-MFI (13, 176) are invariant with intraparticle location at all pressures, providing evidence that first-order methanol dehydration rate constants are not corrupted by mass transfer limitations under these conditions. Mass transfer limitations become apparent in B-Al-MFI (13, 88) due to its larger crystallite size and proton density, as methanol concentrations decrease from 0.05 kPa at the external surface to 0.04 kPa at the center of the particle. Effectiveness factors calculated for spherical particles are also near unity for all B-Al-MFI samples, as shown in Figure 4.25. These results show that measured first-order rate constants of methanol dehydration are unaffected by intraparticle concentration gradients.

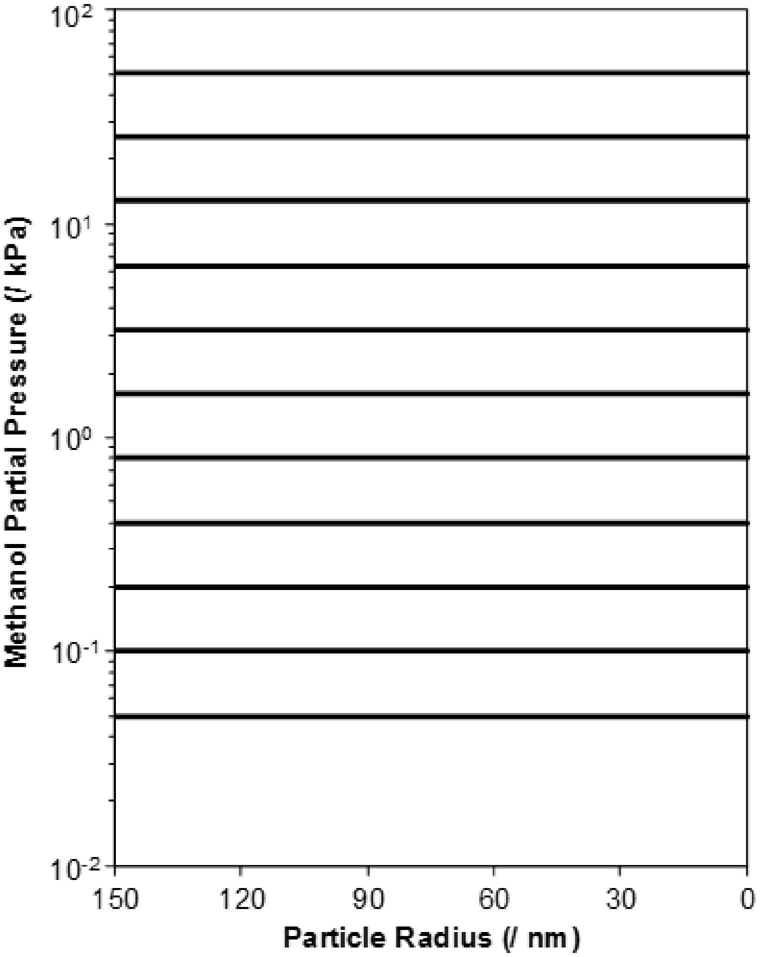

Figure 4.21.: Calculated methanol partial pressure in B-Al-MFI (2.6, 176) as a function of particle radius for bulk methanol pressures of 0.05, 0.1, 0.2, 0.4, 0.8, 1.6, 3.2, 6.4, 12.8, 25.6, and 51.2 kPa at 415 K.

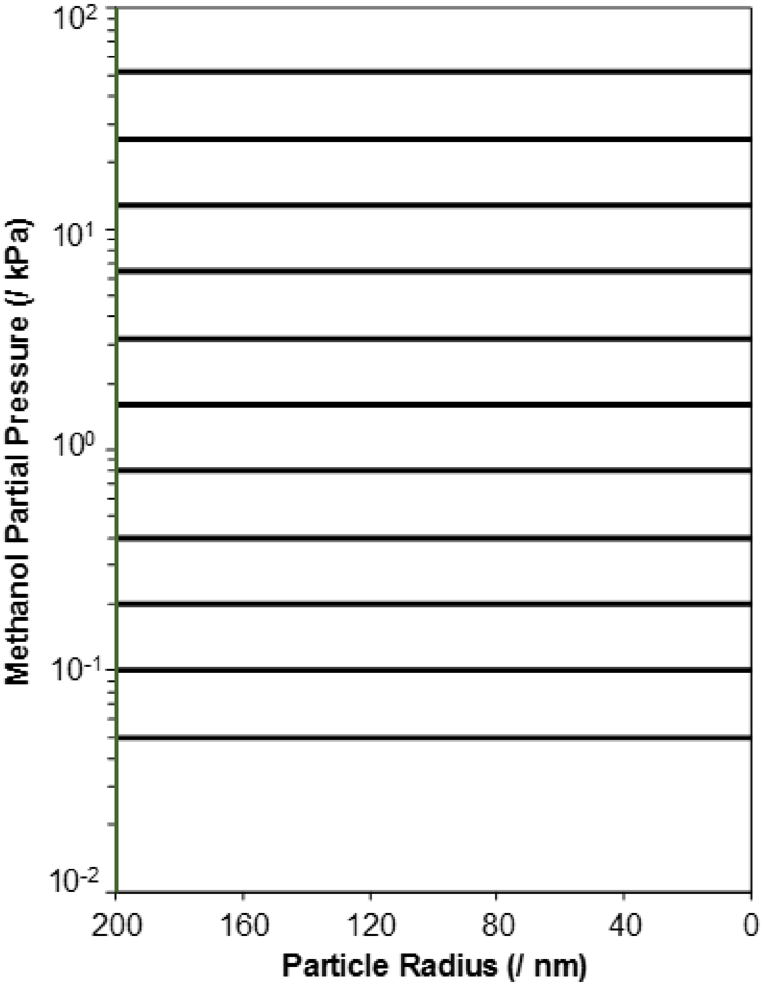

Figure 4.22.: Calculated methanol partial pressure in B-Al-MFI (2.6, 88) as a function of particle radius for bulk methanol pressures of 0.05, 0.1, 0.2, 0.4, 0.8, 1.6, 3.2, 6.4, 12.8, 25.6, and 51.2 kPa at 415 K.

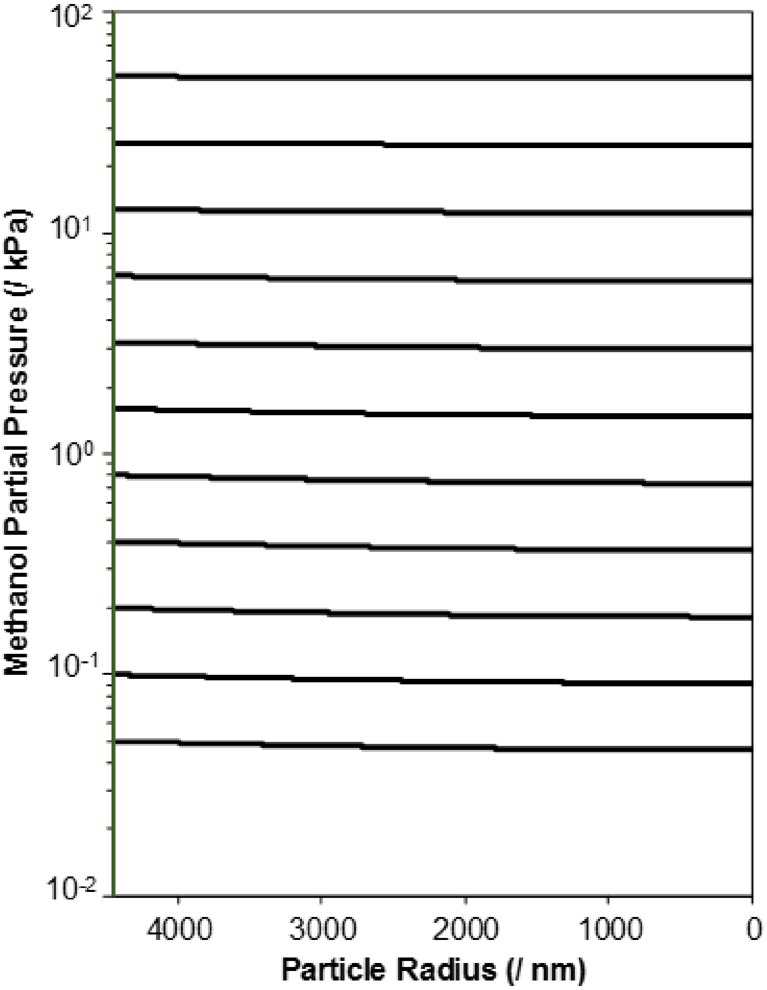

Figure 4.23.: Calculated methanol partial pressure in B-Al-MFI (13, 176) as a function of particle radius for bulk methanol pressures of 0.05, 0.1, 0.2, 0.4, 0.8, 1.6, 3.2, 6.4, 12.8, 25.6, and 51.2 kPa at 415 K.

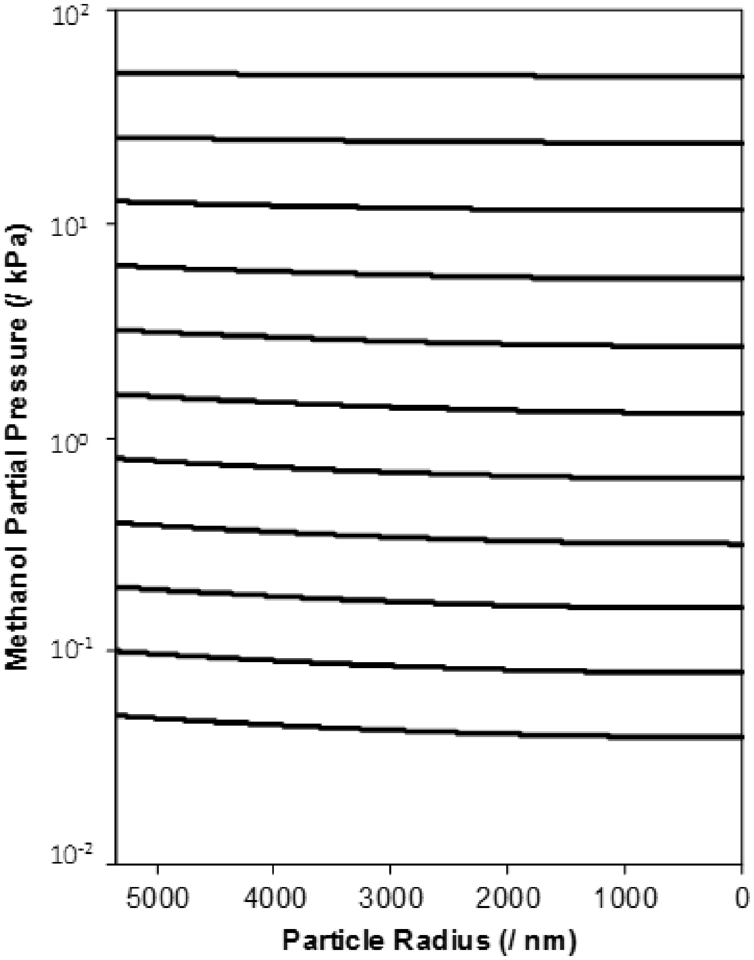

Figure 4.24.: Calculated methanol partial pressure in B-Al-MFI (13, 88) as a function of particle radius for bulk methanol pressures of 0.05, 0.1, 0.2, 0.4, 0.8, 1.6, 3.2, 6.4, 12.8, 25.6, and 51.2 kPa at 415 K.

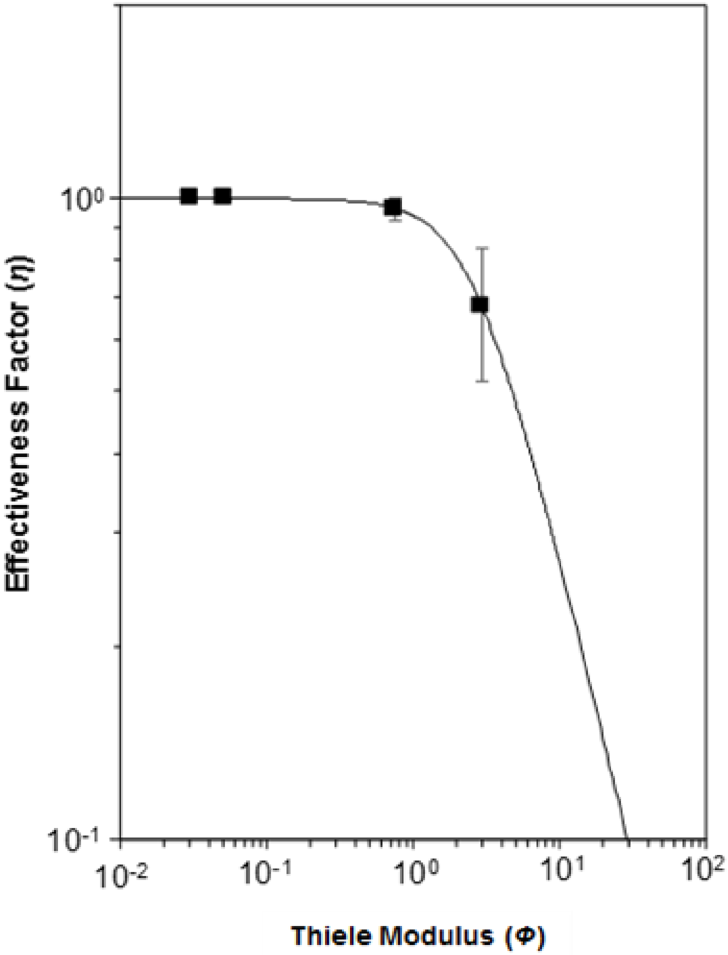

Figure 4.25.: Calculated effectiveness factors from experimentally determined Thiele moduli.

4.7 Acknowledgements

We thank YoonRae Cho for assistance with zeolite synthesis, Dr. Young Gul Hur for assistance with SEM imaging, and Claire Nimlos and John Di Iorio for assistance collecting methanol dehydration kinetic data. We also thank John, Claire, and Young for technical discussions and feedback on this manuscript. We acknowledge the support for this work provided by the National Science Foundation under Cooperative Agreement No. EEC-1647722, an Engineering Research Center for the Innovative and Strategic Transformation of Alkane Resources (CISTAR).

4.8 Rights and Permissions

Reprinted with permission from P.M. Kester, J.T. Miller, and R. Gounder. Ind. Eng. Chem. Res. 57 (2018) 6673-6683. Copyright 2018 American Chemical Society.

5. INFLUENCE OF TETRAPROPYLAMMONIUM AND ETHYLENEDIAMINE STRUCTURE-DIRECTING AGENTS ON THE FRAMEWORK AL DISTRIBUTION IN B-AL-MFI ZEOLITES

5.1 Abstract

We report synthetic protocols to independently influence composition and crystallite sizes of MFI zeolites, properties that contribute to Thiele modulus expressions, and the proximity of Al heteroatoms at fixed composition (Si/Al $\sim$ 50). When only tetra-*n*-propylammonium (TPA^+) is used as a structure-directing agent (SDA) to crystallize MFI, a nonzero percentage of framework Al atoms (20 – 40%) are in proximal configurations, while mixtures of ethylenediamine (EDA) and TPA^+ ($EDA/TPA^+ = 15$) crystallize MFI with nearly all (>95%) Al in isolated configurations. Crystallite sizes decrease with the addition of non-catalytic B heteroatoms. B-Al-MFI zeolites crystallized without EDA retain one TPA^+ per channel intersection, while those crystallized with EDA and TPA^+ contain EDA that displaces some TPA^+, which is linked to the isolation of framework Al. These findings indicate how adding B and EDA to zeolite synthesis solutions provides a route to crystallizing MFI zeolites of similar composition but framework Al distributed at varying relative proximity, or with similar Al distributions but different diffusion pathlengths.

5.2 Introduction

Zeolites are a class of microporous solid acid catalysts that influence reactivity by regulating the access and egress of reactants and products within intracrystalline pores via shape selectivity concepts [202], and by stabilizing confined reactive intermediates and transition states via van der Waals interactions with lattice oxygen atoms [47, 53]. MFI zeolites [20] are often used in catalytic hydrocarbon upgrading routes (e.g., methanol-to-olefins (MTO) [203] and olefin oligomerization [23,153]) because their three-dimensional pore interconnectivity attenuates deactivation from micropore blocking by carbonaceous deposits compared to one-dimensional zeolites (e.g., MOR) or to zeolites with larger differences between their largest cavity diameters and diffusion-limiting apertures (e.g., ERI) [242]. Carbonaceous deposits formed during propene oligomerization on MFI zeolites (473 K) that cause deactivation become increasingly aromatic in nature with increasing crystallite size [205], because secondary reactions on Brønsted acid sites that produce aromatics become more prevalent with increasing intracrystalline residence time [242]. The size of zeolite crystallites and the volumetric density of Brønsted acid sites contribute to a characteristic diffusion parameter (Ψ, Equation 5.1), found in Thiele modulus expressions that relate reaction and diffusion rates within porous catalysts.

$$\Psi = [H^+]L^2 \tag{5.1}$$

The preferential increase in intracrystalline residence times of bulky intermediates, imparted by the diffusion parameter, leads to increases in selectivity towards products formed from these larger reactive intermediates. Such phenomena are reflected in the increased selectivity to ethene produced from substituted aromatic intermediates during MTO [88,89] and to products of secondary β-scission of longer hydrocarbon intermediates during propene oligomerization [87] in MFI zeolites.

Product selectivities in such reactions can thus be influenced by synthetic methods to vary the diffusion parameter of zeolitic crystallites, either by changing the density of Brønsted acid protons via framework Al or the characteristic crystallite size, yet these two material properties are generally correlated in conventional hydrothermal synthesis. Linear crystal growth rates have been shown to decrease with increasing Al content in MFI synthesis solutions [243,244], although the size of the resulting crystallites depends on the alkalinity of the synthesis media because of competition between crystal growth and dissolution, which are both catalyzed by hydroxide anions [244]. Hydroxide anions are often present in structure directing agent (SDA) precursors, including tetra-n-propylammonium (TPA^+) and Na^+ cations that are commonly used in MFI synthesis. In the case of MFI zeolites, TPA^+ cations form clathrate structures with water molecules in solution, which are isomorphously replaced by silicate precursors with a Si/TPA^+ ratio of ~24, corresponding to one TPA^+ per intersection in MFI [60]. Al incorporation into the lattice is proposed to occur via aluminate substitution into TPA^+ clathrates and S_N2-type nucleophilic attack of a deprotonated oxygen within a silicate tetrahedron on an aluminate species, to form Al-O-Si bonds [245]. Other SDAs (e.g., Na^+) compete with TPA^+ to balance the charge in anionic aluminate species [245], and may influence the siting of Al at crystallographically-unique locations in MFI zeolite frameworks [68]. Therefore, characteristic diffusion lengths and framework Al siting in MFI zeolites depend on the identity and quantity of organic and inorganic precursors in synthetic solutions, which provide alternative strategies to independently influence material properties that define characteristic diffusion parameters of zeolites.

Indeed, several alternative methods have been studied previously to influence either the size and morphology of zeolite crystallites or the siting of Al heteroatoms within their frameworks. Alcohol and amine additives (termed "zeolite growth modifiers", or ZGMs) in hydrothermal synthesis solutions bind to certain crystallite facets of silicalite-1 (Si-MFI), thereby inhibiting crystal growth in certain directions, which decreases the size of crystalline products and influences their aspect ratios [94]. Ethylenediamine (EDA) is one such additive [95], and has also been used as a template for borosilicate [109, 246] and boroaluminosilicate MFI [247] compositions. Competition between B and Al for incorporation into MWW frameworks has been implicated to bias Al siting away from T-site locations in larger voids, which are more prone to deactivation during MTO catalysis [209]. Brønsted acidic protons that compensate B heteroatoms are catalytically irrelevant in comparison to those compensating framework Al [213], because the former have ~70 kJ mol^{-1} higher deprotonation energies [33]; therefore, such protons do not contribute to zeolite characteristic diffusion parameters. We have recently reported the synthesis of B-Al-MFI zeolites using mixtures of organic TPA^+ and EDA molecules to independently influence crystallite size (∼0.3 – 10 μm) and bulk Al content (Si/Al $>$ 70) [247]. Here, we build upon this prior work to synthesize B-Al-MFI zeolites from mixtures containing TPA^+ as the only organic SDA and from mixtures of TPA^+ and EDA as co-SDAs, to provide evidence that this strategy can enable independently varying the fraction of Al in proximal or isolated locations of MFI (at fixed Si/Al) in samples with different characteristic diffusion parameters.

5.3 Experimental Methods

5.3.1 Synthesis of B-Al-MFI zeolites

Two methods were used to synthesize B-Al-MFI zeolites of varying elemental composition (Si/B and Si/Al ratio). In the first route, B-Al-MFI-TPA zeolites were synthesized as reported by Zhu et. al. [211] using tetra-*n*-propylammonium (TPA^+) as the organic SDA. Synthesis gels comprising a molar ratio of X H_3BO_3/ 0.01 Al_2O_3/ 1 SiO_2/ 0.32 TPAOH/ 30.45 H_2O were prepared, where X was varied from 0 to 0.4. The synthesis procedure involved adding aluminum hydroxide ($Al(OH)_3$, 99 wt %, SPI Pharma), tetra-*n*-propylammonium hydroxide (TPAOH, 40 wt %, Alfa Aesar), and boric acid (H_3BO_3, 99.5 wt %, Sigma-Aldrich) to deionized H2O (18.2 MΩ) in a perfluoroalkoxy alkane (PFA) container (Savillex Corp.), and stirring the solution under ambient conditions for 0.25 h. Next, fumed silica (SiO_2, 99 wt %, Cabot) was added to the solution, and the mixture was stirred under ambient conditions for 2 h to homogenize the contents. The synthesis solution was then transferred to a 45 mL Teflon-lined stainless-steel autoclave and placed in a forced convection oven at 443 K and rotated at 50 rpm for 168 h. These B-Al-MFI samples are referred as B-Al-MFI-TPA(a,b) to denote that TPA^+ was the only organic SDA present during synthesis, where a is the Si/B molar ratio and b is the Si/Al molar ratio used in the synthesis solution.

In the second route, B-Al-MFI-EDA zeolites were synthesized by adapting methods reported in Kester et al. [247] that use ethylenediamine (EDA) and TPA^+ as organic SDAs during crystallization. Synthesis gels comprising a molar ratio of 0.3 EDA/ X H_3BO_3/ Y Al_2O_3/ 1 SiO_2/ 0.02 TPAOH/ 10.2 H_2O were prepared, where X was varied from 0 – 0.4 and Y from 0 – 0.01. The synthesis procedure involved adding EDA (99.5 wt %, Sigma-Aldrich) and H3BO3 (99.5 wt %, Sigma-Aldrich) to deionized H2O (18.2 MΩ) in a PFA container and stirring the solution under ambient conditions for 0.25 h. Next, aluminum nitrate nonahydrate ($Al(NO_3)_3$, 98 wt %, Alfa Aesar) and TPAOH (40 wt %, Alfa Aesar) were added to the EDA-containing solution, and the mixture was stirred under ambient conditions for 0.25 h to homogenize the contents. Finally, colloidal silica (Ludox HS-40, 40 wt %, Sigma-Aldrich) was added to the mixture and stirred for 2 h under ambient conditions. The synthesis solution was then transferred to a 45 mL Teflon-lined stainless-steel autoclave and placed in a forced convection oven at 448 K and rotated at 50 rpm for 120 h. These B-Al-MFI samples are denoted B-Al-MFI-EDA(a,b) to denote that EDA was also present as an organic SDA in the synthesis solution, where a is the Si/B molar ratio and b is the Si/Al molar ratio used in the synthesis.

5.3.2 Preparation of cation-exchanged zeolites

Zeolite products were recovered from autoclaves and washed with deionized water (18.2 MΩ) and acetone (Sigma-Aldrich, 99.9 wt%) in alternating steps until the pH of the supernatant remained constant between washes. Solids then were recovered via centrifugation, dried at 373 K under stagnant air for 24 h, and then treated in flowing dry air ($1.67\ cm^3\ s^{-1}\ g_{cat}^{-1}$, 99.999% UHP, Indiana Oxygen) at 853 K ($0.0167\ K\ s^{-1}$) for 10 h. B-Al-MFI zeolites were converted to NH4-form via aqueous phase ion-exchange using 150 cm^3 of a 1.0 M NH_4NO_3 solution (8.0 wt% in deionized water, 99.9 wt %, Sigma-Aldrich), followed by washing four times with deionized water (70 cm^3 per g solids). NH_4-form zeolites were converted to their proton form via treatment in flowing dry air ($1.67\ cm^3\ s^{-1}\ g_{cat}^{-1}$, 99.999% UHP, Indiana Oxygen) at 773 K (0.0167

K s^{-1}) for 4 h. Na-form B-Al-MFI zeolites were prepared by aqueous-phase ion-exchange using 150 cm^3 of a 1.0 M NaCl solution (5.8 wt% in deionized water, 99.9 wt%, Sigma-Aldrich) per g zeolite for 24 h under ambient conditions, followed by washing the solids four times with deionized water (70 cm^3 per g solids). Na-form zeolites were recovered using centrifugation, dried at 373 K under stagnant air for 24 h, and then treated in flowing dry air (1.67 cm^3 s^{-1} g_{cat}^{-1}, 99.999% UHP, Indiana Oxygen) at 773 K (0.0167 K s^{-1}) for 4 h. Na-form B-Al-MFI zeolites were converted to their Co^{2+} form by ion-exchange by stirring samples with 0 – 0.5 M $Co(NO_3)_2$ solutions (0 – 9.1 wt% in deionized water, 99 wt%, Sigma-Aldrich) at 293 – 353 K for 24 h. Samples were then washed four times with deionized water until the pH was constant between washes, recovered via centrifugation, and dried at 373 K under stagnant air for 24 h. Co-zeolites were then treated in flowing dry air (1.67 cm^3 s^{-1} g_{cat}^{-1}, 99.999% UHP, Indiana Oxygen) at 773 K (0.0167 K s^{-1}) for 4 h.

5.3.3 Zeolite characterization

Powder X-ray diffraction (XRD) patterns collected using a Rigaku SmartLab X-ray diffractometer with a Cu Kα source operated at 1.76 kW. Approximately 0.01 g of zeolite was loaded into a zero-background, low dead-volume sample holder (Rigaku) and diffraction patterns were measured from 4 – 40° with a step size of 0.01° and a scan rate of 0.0167° s^{-1}. The MFI topology was confirmed via comparison with reference patterns.

Micropore volumes were calculated from N_2 adsorption isotherms measured at 77 K using a Micromeritics ASAP 2020 surface area and porosity analyzer. B-Al-MFI samples (0.04 – 0.06 g, sieved to 180 - 250 μm) were degassed by heating to 393 K (0.167 K s^{-1}) under vacuum (5 μmHg) for 2 h, then heating to 623 K (0.167 K s^{-1}) under vacuum (<5 mmHg) and holding for 9 h. The linear volumetric uptake of N_2 at 0.05 - 0.35 P/P_0 was extrapolated to zero pressure to estimate micropore volumes.

Elemental analysis of Al and Co in B-Al-MFI zeolites were performed via atomic absorption spectroscopy (AAS) using a PerkinElmer Model AAnalyst 300 atomic absorption spectrometer. Samples were prepared by dissolving 0.04 - 0.06 g of solid in 2 g of hydrofluoric acid (48 wt%, Alfa Aesar) and allowed to sit overnight, then diluted with 50 g of deionized water (18.2 MΩ). Radiation sources with wavelengths of 309.3 and 240.7 nm were used to measure absorbances for Al and Co in a reducing acetylene/nitrous oxide flame and oxidizing acetylene/air flame, respectively. Elemental compositions were calculated using calibration curves generated from standard solutions. B contents in B-Al-MFI zeolites were determined by inductively coupled plasmaoptical emission spectroscopy (ICP-OES, Galbraith Laboratories).

^{27}Al and ^{11}B magic angle spinning nuclear magnetic resonance (MAS NMR) spectra were recorded under ambient conditions on the H-form of B-Al-MFI zeolites to probe the coordination of Al and B heteroatoms. Spectra were recorded on a Chemagnetics CMX-Infinity 400 spectrometer in a wide-bore 9.4 T magnet (Purdue Interdepartmental NMR Facility). Prior to collecting NMR spectra, samples were hydrated for >48 h in a hydrator containing a saturated potassium chloride (KCl) solution. Spectra were normalized such that the maximum intensity in each spectrum is unity.

Ammonia temperature programmed desorption (TPD) experiments were performed using a Micromeritics AutoChem II 2920 Chemisorption analyzer and an Agilent 5973N mass-selective detection (MSD) system to identify the gaseous products evolved from zeolite samples. Methods to titrate protons at Al heteroatoms (H^+_{Al}) in B-Al-MFI zeolites have been reported by Kester et al [247]. In short, NH_4-form B-Al-MFI samples (0.04 – 0.06 g, sieved to 180 - 250 μm) were supported between two quartz wool plugs in a U-shaped quartz cell and placed in a clam-shell furnace. Samples were then heated under flowing He (15 cm^3 s^{-1} (g solid)$^{-1}$, UHP, 99.999%, Indiana Oxygen) to 433 K (0.167 K s^{-1}) and held isothermally for 4 h to remove NH_3 bound to B heteroatoms. The temperature was then increased to 873 K (0.167 K s^{-1}) and evolved gases were sent to the MSD for quantification. Calibration and deconvolution methods were performed according to previous reports [129]. Methods previously reported to titrate residual protons on partially metal-exchanged zeolites were used here to measure residual protons on Co-B-Al-MFI [129]. The Co-forms of B-Al-MFI samples (0.04 – 0.06 g, sieved to 180250 μm) were heated under flowing dry air (15 cm^3 s^{-1} g$^1_{cat}$, 99.999% UHP, Indiana Oxygen) to 673 K, held for 2 hours, then cooled to 433 K, at which point gas-phase NH_3 was introduced for 4 hours. A subsequent wet He purge at 433 K was used to purge NH_3 adsorbed at non-Brønsted sites associated with framework Al, prior to TPD.

UV-visible spectroscopy was used to determine the oxidation state of Co^{2+} ions and to detect the presence of Co-oxides on zeolite samples following exchange with $Co(NO_3)_2$ solutions. Diffuse reflectance UV-vis (DRUV-Vis) spectra were recorded under *in-situ* conditions using a Varian Cary 5000 UV-vis-NIR Spectrophotometer attached with a Harrick Scientific Praying Mantis diffuse reflectance accessory. Baseline spectra were recorded for every sample using poly (tetrafluoroethylene) (PTFE, 1 μm powder, Sigma–Aldrich) as the 100% reflectance standard, and then converted to an absorption spectrum using the Kubelka–Munk (F(R)) function. Spectra were recorded from 12,500 to 50,000 cm^{-1} at a scan rate of 167 cm^{-1} s^{-1} at 673 K.

Crystallites were imaged using scanning electron microscopy (SEM) using an FEI Quanta 3D FEG Dual-beam SEM system. Prior to imaging, samples were coated with platinum to reduce charging. Images were taken at 5 000 - 15 000× magnification with an accelerating voltage of 15 kV and spot size of 6 μm.

The amount of TPA^+ and EDA organic SDAs occluded in solid zeolite products was estimated from the C and N elemental compositions of as-synthesized zeolites measured with CHN analysis (Galbraith Laboratories, PerkinElmer 2400 Series II CHNS/O Analyzer).

Thermogravimetric analysis (TGA) experiments were performed on as-synthesized B-Al-MFI-TPA zeolites using a TA Instruments SDT Q600 thermogravimetric analyzer and differential scanning calorimeter (TGA-DSC) by heating 0.02 g of as-synthesized B-Al-MFI in flowing dry air (83.3 cm^3 s^{-1} $g_{cat}{}^{-1}$, UHP, 99.999%, Indiana Oxygen) to 523 K (0.167 K s^{-1}) and holding for 0.5 h to remove physisorbed water before further heating to 1073 K (0.167 K s^{-1}).

5.3.4 Methanol dehydration kinetic measurements

Detailed experimental methods and calculations for first-order and zero-order rate constants for methanol dehydration are reported in our prior publications [79]; here, we provide an abridged summary. Methanol dehydration rates were measured in a tubular quartz reactor (7 mm inner diameter) with a packed bed supported by quartz wool plugs. All rates were measured under differential conversions ($<$15%) at 415 K. Temperatures were measured by Type K thermocouple placed on the external surface of the quartz reactor aligned with the center of the catalyst bed and the temperature was controlled with resistively heated, three-zone furnaces (Applied Test Systems Series 3210) and Watlow controllers (EZ-Zone series). In a typical experiment, 0.02-0.03 g of H-B-Al-MFI were pelleted and sieved to retain particles 180-250 μm in diameter and treated in 5% O_2 with balance He (50 cm^3 s^{-1} (g solid)$^{-1}$, 99.999%, Indiana Oxygen) to 773 K (0.033 K s^{-1}) for 4 h before cooling to reaction temperature under flowing He (200 cm^3 s^{-1} (g solid)$^{-1}$, UHP 99.999%, Indiana Oxygen). Methanol (99 wt.%, Sigma Aldrich) was introduced via syringe pump (Legato 100, KD Scientific) into flowing He at varying flow rates to change the partial pressure. Partial pressures were measured in a reactor bypass and all reactant and product concentrations were measured via a gas chromatograph equipped with a flame ionization detector (HP Plot-Q KCl column, 0.53 mm inner diameter (ID) × 30 m × 40 μm film, Agilent). Dimethyl ether and water were the only products observed on all catalysts tested under all conditions. Methane (25% CH_4 in argon, 99.999%, Indiana Oxygen) was used as an internal standard, and introduced into the reactor effluent stream (0.83 cm^3 s^{-1}).

5.4 Results and Discussion

5.4.1 Synthesis of B-Al-MFI zeolites and structural characterization

B-Al-MFI samples with varying Si/B and Si/Al ratios were synthesized by two different methods, one using tetra-*n*-propylammonium (TPA^+) as the only organic SDA (denoted B-Al-MFI-TPA) and the other using both TPA^+ and ethylenediamine (EDA) as organic SDAs (denoted B-Al-MFI-EDA). Powder XRD patterns of all B-Al-MFI samples were consistent with the MFI topology (Figs. 5.10 - 5.12, Section 5.6.1). Micropore volumes calculated from N_2 adsorption isotherms (0.13 – 0.15 cm^3 g^{-1}, Figs. 5.13 and 5.14, Section 5.6.2) were also consistent with the MFI topology for all samples. The elemental compositions of synthesis solutions and crystalline solids are summarized in Table 5.1.

Table 5.1.: Elemental composition of B-Al-MFI zeolites of varying Al and B content.

B-Al-MFI-SDA (Si/B,Si/Al)	Si/Al$_{gel}$	Si/Al$^{a}_{tot}$	Si/B$_{gel}$	Si/B$^{b}_{tot}$	Si/(Al+B)$_{tot}$	H$^{+}_{Al}$/Al$^{c}_{tot}$
B-Al-MFI-TPA (2.5,50)	50	59	2.5	48	26.4	0.84
B-Al-MFI-TPA (10,50)	50	57	10	n.d.*	n.d.*	0.98
B-Al-MFI-TPA (25,50)	50	66	25	120	43.2	0.98
B-Al-MFI-TPA (50,50)	50	54	50	n.d.*	n.d.*	1.03
B-Al-MFI-TPA (100,50)	50	51	100	n.d.*	n.d.*	0.95
B-Al-MFI-TPA (200,50)	50	69	200	340	57.4	1.09
B-Al-MFI-TPA (500,50)	50	42	500	n.d.*	n.d.*	0.81
B-Al-MFI-TPA (B-free,50)	50	52	∞ B-free	∞ B-free	52	0.96
B-Al-MFI-EDA (2.5,50)	50	53	2.5	26	52	1.02
B-Al-MFI-EDA (10,50)	50	58	10	n.d.*	n.d.*	1.09
B-Al-MFI-EDA (25,50)	50	51	25	39	22.2	0.95
B-Al-MFI-EDA (50,50)	50	60	50	n.d.*	n.d.*	1.08
B-Al-MFI-EDA (200,50)	50	58	200	240	46.5	n.d.*
B-Al-MFI-EDA (500,50)	50	53	500	n.d.*	n.d.*	0.78
B-Al-MFI-EDA (B-free,50)	50	58	∞ B-free	∞ B-free	58	0.92
B-MFI-EDA	∞ Al-free	∞ Al-free	2.6	30.0	n.d.*	n.d.*

[a] Determined by atomic absorption spectroscopy. Errors are ± 10%.
[b] Determined by ICP-OES. Errors are ± 10%.
[c] Determined by NH_3 TPD. Errors are ± 15%.

The coordination of Al and B heteroatoms in MFI frameworks was probed using ^{27}Al MAS NMR (Fig. 5.15) and ^{11}B MAS NMR (Fig. 5.16). ^{27}Al MAS NMR spectra of all samples showed a resonance centered at 53 ppm for tetrahedrally-coordinated framework Al [211, 248] and a small feature at 0 ppm for octahedrally-coordinated extraframework Al. These features were used to estimate the fraction of Al incorporated into framework positions, which was close to unity for all samples ($\mathrm{Al}_f/\mathrm{Al}_{tot}$ = 0.90 – 0.98, Table 5.5, Section 5.6.3). ^{11}B MAS NMR spectra of all samples showed a resonance centered at -3 ppm for tetrahedrally-coordinated boron [249], and only minor features for trigonal B at ∼15 ppm in some B-Al-MFI-TPA samples. This suggests that B heteroatoms are predominantly tetrahedrally coordinated under hydrated conditions at ambient temperature in the B-Al-MFI samples studied here. Tetrahedral B in B-MFI can be partially removed from the framework to form trigonal B species through a series of reversible hydrolysis reactions of B-O-Si bonds upon dehydration [249, 250], and features in ^{11}B MAS NMR at -3 ppm for tetrahedral B can persist when B has less than four framework bonds, often from hydroxide or water ligands bound during hydration. Given the hydrated conditions used in ^{11}B MAS NMR experiments, we cannot comment further on the number of B-O-Si bonds retained in B-Al-MFI zeolites after oxidative treatments and aqueous-phase ion-exchange procedures.

Although both tetrahedral Al and B heteroatoms can be charge-compensated by Brønsted acid protons in zeolite frameworks, protons associated with framework Al are stronger acids than those associated with B, reflected in deprotonation energies (DPE) that are ∼70 kJ mol^{-1} lower for protons at Al than at B [33]. Therefore, rigorous normalization of acid-catalyzed turnover rates in boroaluminosilicates requires discrimination between Brøønsted acidic OH groups associated with Al and B heteroatoms, even when the quantity of B heteroatoms is much greater than Al (Al/B < 0.01), because observed catalytic reactivity originates predominantly from protons at framework Al (e.g. *n*-hexane cracking) [213]. Temperature-programmed desorption (TPD) of NH_3 from B-Al-MFI following saturation in aqueous-phase NH_4NO_3

solution overestimates the number of framework Al heteroatoms [247], because NH_3 also binds to trigonal and tetrahedral B heteroatoms [221] and thus the NH_3 evolved during TPD may originate from B or Al heteroatoms. NH_3 titrants can be used to quantify the number protons at framework Al heteroatoms (H^+_{Al}) in B-Al-MFI zeolites either by saturation of B and Al sites with NH_4^+ by aqueous-phase ion-exchange and selective removal of NH_3 from B via purging in flowing dry He (433 K), or by saturation in gaseous NH_3 at temperatures that result in selective adsorption at H^+_{Al} sites (433 K) [247]. These procedures were used to quantify H^+_{Al} in the suite of B-Al-MFI zeolites synthesized here, and the results are summarized in Table 5.1. These values agree quantitatively with the total amount of Al measured by atomic absorption spectroscopy ($H^+_{Al}/Al_{tot} = 0.78–1.09$) in all B-Al-MFI samples (Fig. 5.1),consistent with the predominant incorporation of Al into framework positions as evidenced by ^{27}Al MAS NMR. Only negligible NH_3 (<0.01 mmol g^{-1}) is evolved from B-MFI-EDA samples in these procedures because ammonia associated with B heteroatoms desorbs at 443 K.

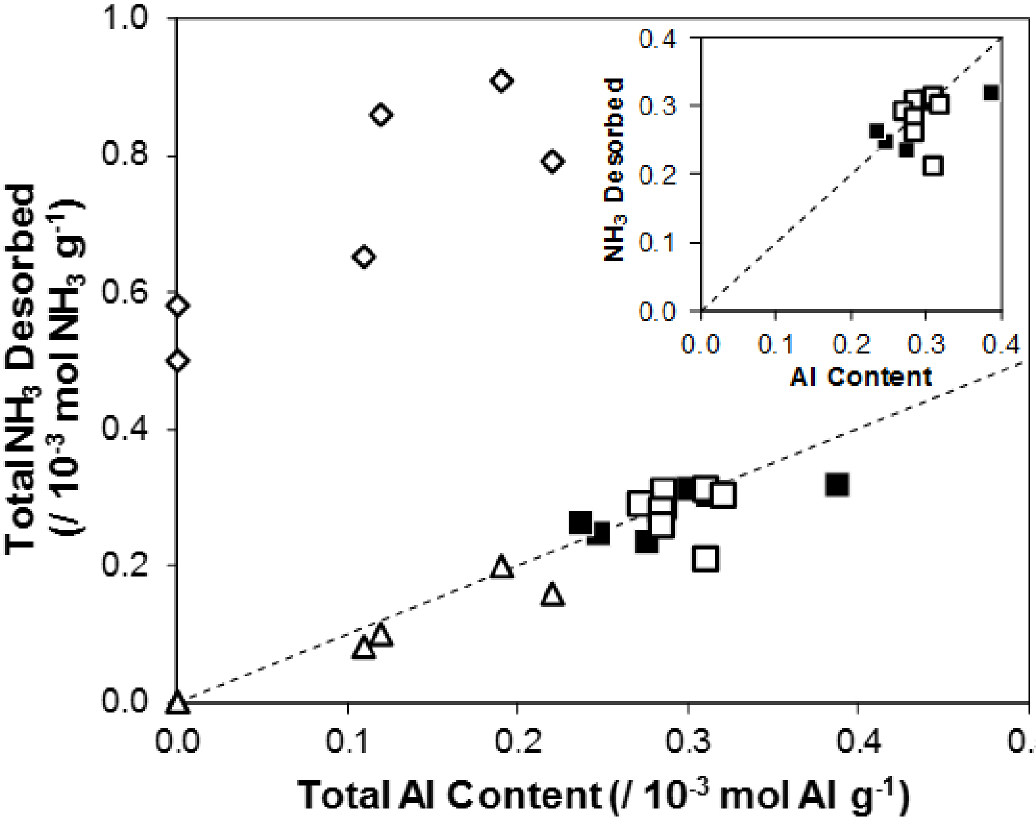

Figure 5.1.: NH_3 desorbed during TPD from B-Al-MFI-TPA (□) and B-Al-MFI-EDA (■) samples after aqueous-phase NH_4NO_3 saturation and subsequent helium purge; NH_3 desorbed from B-Al-MFI-EDA zeolites [247] after aqueous-phase NH_4NO_3 saturation with (△, reported by Kester et al. [247]) and without (◇, reported by Kester et al. [247]) purging in He at 433 K. The inset shows selective titration data for a clear visual description. Dashed line represents parity.

Representative SEM images of B-Al-MFI-EDA samples are shown in Fig. 5.2. Images shown in Figures 5.2a-5.2d correspond to B-Al-MFI-EDA samples made from synthesis gels with relatively low B content (Si/B = 25) and varying Al content (Si/Al = 50, 150, 300, 500), and those shown in Figures 5.2e-5.2h were made with synthesis gels with higher B content (Si/B = 2.5) and varying Al content (Si/Al = 50, 150, 300, 500). Elemental composition of the crystalline solids, mean crystallite lengths, and diffusion parameters of these samples are given in Table 5.2. Crystallite size distributions obtained by measuring at least 250 particles per sample (Figure 5.17, Section 5.6.4) are unimodal and symmetric. Among samples of fixed Si/B ratio in the synthesis solution (either 2.5 or 25), mean crystallite sizes are similar (within 1.5×) with varying Al content (Table 5.6). In contrast, among samples of similar Si/Al ratio (Si/Al of either 50, 150, 300, or 500), mean crystallite sizes increased with decreasing B content by a larger factor of ∼10× (Table 2). Crystallites synthesized from solutions containing Si/B = 25 are coffin-shaped (Fig. 5.2a-5.2d), while those from solutions with Si/B = 2.5 are rod-shaped and often aggregated into small clusters (Fig. 5.2e-5.2h). These findings are consistent with previous reports of B-Al-MFI zeolites made with similar synthetic protocols [247], where it was hypothesized that ethylenediamine acts as both a structure directing agent during B-Al-MFI synthesis and as a zeolite growth modifier (ZGM) by binding to MFI crystal facets during synthesis to influence anisotropic crystal growth [94,95]. Similar observations describe changes in the morphology of B-Al-MFI-TPA samples crystallized from synthesis solutions of fixed Si/Al ratio (50) and decreasing B content (Si/B = 2.5 – 500, Figure 5.18, Section 5.6.4). These findings are similar to those for Al-MFI with increasing Al content [243, 244], indicating that it may be plausible that the smaller crystallites in B-Al-MFI-EDA zeolites with increasing B content are not solely due to the binding of EDA to external crystallite surfaces during growth. These results collectively indicate that B-Al-MFI crystallite sizes are predominantly influenced by the Si/B ratios present in synthesis solutions for the conditions studied here, when using either TPA^+ only or EDA/TPA^+ mixtures as the organic SDAs.

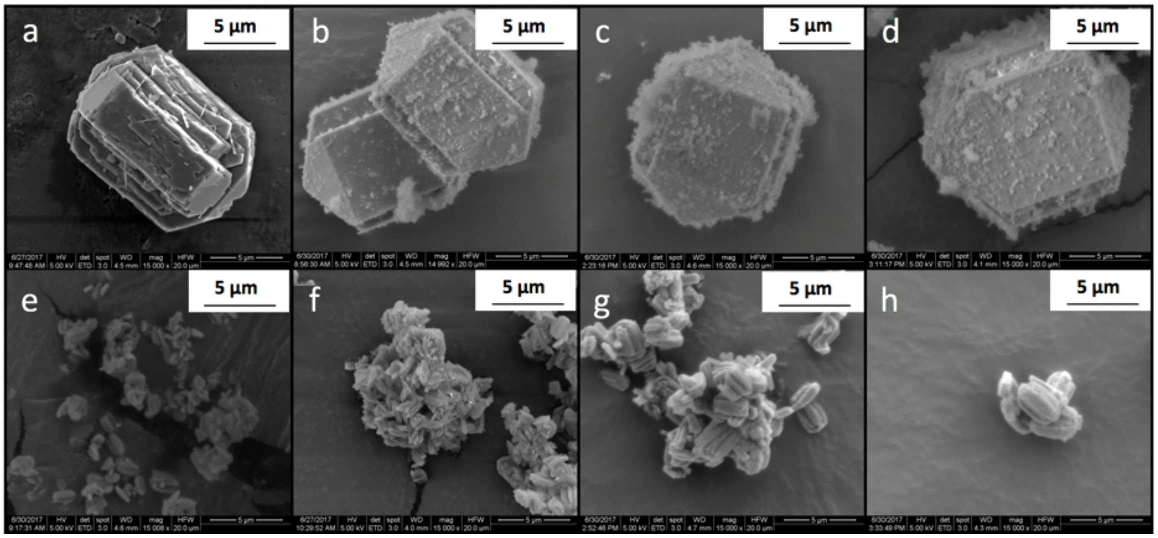

Figure 5.2.: SEM micrographs of MFI zeolite samples: (a) B-Al-MFI-EDA (25, 50), (b) B-Al-MFI-EDA (25, 150), (c) B-Al-MFI-EDA (25, 300), (d) B-Al-MFI-EDA (25, 500), (e) B-Al-MFI-EDA (2.5, 50), (f) B-Al-MFI-EDA (2.5, 150), (g) B-Al-MFI-EDA (2.5, 300), and (h) B-Al-MFI-EDA (2.5, 500).

Table 5.2.: Mean crystallite lengths and diffusion parameters for B-Al-MFI-EDA samples crystallized from synthesis gels containing low ($Si/B_{gel} = 25$) and high ($Si/B_{gel} = 2.5$) B content.

Sample	Si/Al[a]	Mean crystallite length (L)[b] (/ μm)	Diffusion parameter (/ 10^{-6} mol H^{+}_{Al} nm^{-1})
B-Al-MFI-EDA (25,50)	51	12.6 ±1.7	42
B-Al-MFI-EDA (25,150)	184	13.2 ±0.9	13
B-Al-MFI-EDA (25,300)	229	14.1 ±1.0	12
B-Al-MFI-EDA (25,500)	494	15.2 ±0.8	6
B-Al-MFI-EDA (2.5,50)	53	1.3 ±0.3	0.4
B-Al-MFI-EDA (2.5,150)	181	1.6 ±0.3	0.2
B-Al-MFI-EDA (2.5,300)	303	1.9 ±0.5	0.2
B-Al-MFI-EDA (2.5,500)	466	2.6 ±0.5	0.2

[a] Determined by atomic absorption spectroscopy. Errors are ± 10%.
[b] Determined by analyzing $>$ 250 particles per sample imaged by SEM; uncertainty given as the standard deviation in crystallite size distribution.

5.4.2 Validation of Co^{2+} ion-exchange methods to quantify proximal Al sites in MFI zeolites

The use of Co^{2+} cations as titrants to quantify proximal (or “paired”) $AlO_{4/2}^{-}$ ensembles in zeolite frameworks requires methods to verify that saturation Co^{2+}-exchange capacities have been attained, that cation site balances satisfy the expected stoichiometry of two monovalent cations (e.g., H^+ or Na^+) replaced per divalent Co^{2+} cation, and spectroscopic evidence of the presence of Co^{2+} species and the absence of other phases (e.g., Co-oxides). A variety of conditions have been reported in the literature for Co^{2+} ion exchange to titrate proximal Al sites in MFI zeolites. Dědeček and co-workers have reported using different Co^{2+} precursors, concentrations (0.0002–0.1 M), number of sequential exchanges, and temperatures (298 – 350 K) to saturate Na-form MFI zeolites with Co^{2+} cations [115, 251]. Bell and co-workers report using 0.05 M $Co(NO_3)_2$ solutions in a single exchange for 24 h on Na-form samples [100], and Corma and co-workers report using three sequential exchanges using a 0.05 M $Co(NO_3)_2$ solution at room temperature for 8 h [252]. Given the diverse range of Co^{2+} ion-exchange procedures reported previously for MFI zeolites, we first determined the conditions required for Co^{2+} saturation of Na-form Al-MFI zeolites by performing experiments with varying $Co(NO_3)_2$ concentrations in solution, duration of each exchange, temperature, and number of sequential repetitions with fresh $Co(NO_3)_2$ solutions.

A commercially-available Al-MFI zeolite sample (Zeolyst CBV2314, Si/Al = 11.5) was used for validation of Co^{2+} saturation protocols. At 293 K, the amount of Co^{2+} exchanged onto this Na-form MFI sample increased at low concentrations and reached a constant value of $2\times Co^{2+}/Al_{tot} \sim 0.14$ for $Co(NO_3)_2$ concentrations above 0.05 M (Fig. 5.3). Additionally, the amount of ion-exchanged Co^{2+} did not vary systematically with durations longer than 20 h in 0.25 M $Co(NO_3)_2$ solutions (Fig. 5.19, Section 5.6.5, suggesting that Na-MFI samples were saturated after 20 h of exposure to 0.25 M $Co(NO_3)_2$ solutions at 293 K. However, upon repeating exchange protocols up to eight times with fresh $Co(NO_3)_2$ solutions (0.25 or 0.50 M) after washing and drying samples between repetitions, the amount of Co^{2+} exchanged onto the solid increased systematically and approached an asymptotic value of $2\times Co^{2+}/Al_{tot}$ ~ 0.30 (Fig. 4.3). These systematic trends were independent of the concentration of $Co(NO_3)_2$ solution (0.25 or 0.5 M) (Fig. 5.3) and a 2:1 exchange of Na^+ for Co^{2+} was confirmed with NH_3 TPD (Fig. 5.3 inset), indicating that single repetitions of Co^{2+} ion-exchange procedures at 293 K did not saturate all proximal Al sites with Co^{2+} cations.

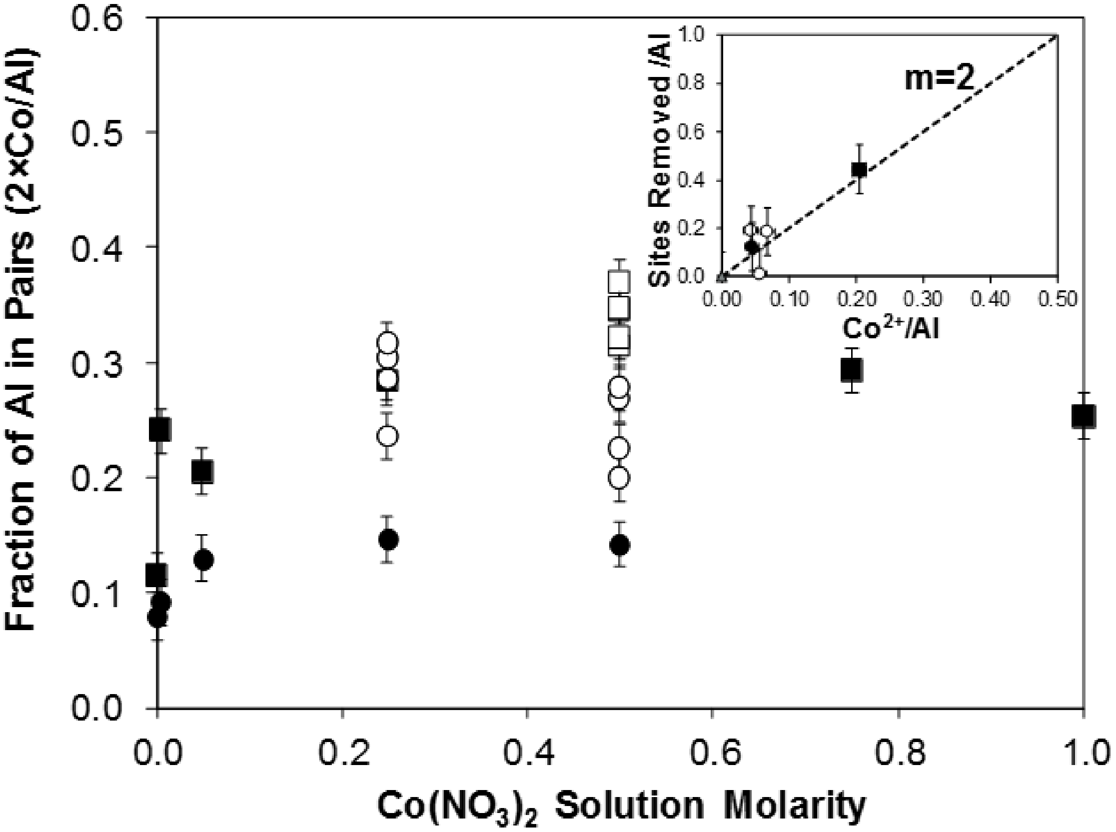

Figure 5.3.: Aqueous-phase Co^{2+} ion exchange capacity of Al-MFI (Zeolyst CBV2314, Si/Al = 11.5) with $Co(NO_3)_2$ solutions (0.001 – 1.0 M) for 24 hours at 293 K (●) and 353 K (■); Single (closed) and multiple repetitions (open, 2-8 replicate exchanges). Inset shows the site balances of divalent Co^{2+} and residual monovalent (H^+ and Na^+) cations compared to the Na-form (▲). The dashed line corresponds to of the removal of two monovalent cations with each divalent Co^{2+} ion.

Next, we equilibrated Na-form Al-MFI with aqueous $Co(NO_3)_2$ solutions at 353 K for 24 h. The number of Co^{2+} ions increased with $Co(NO_3)_2$ concentration following Langmuirian-type behavior with saturation $2\times Co^{2+}/Al_{tot}$ values of $\sim$0.30 reached by 0.25 M (Fig. 5.3) after a single ion exchange. Additional repetitions using 0.25 and 0.50 M $Co(NO_3)_2$ solutions at 353 K did not increase the amount of Co^{2+} retained (Fig. 5.3). DRUV-vis spectra collected at 673 K for dehydrated Co-MFI zeolites with varying Co^{2+} content ($2\times Co/Al_{tot}$ = 0.12 - 0.30) show features for the d-d charge transition of bare Co^{2+} ions to lattice O atoms (15,100 - 22,000 cm^{-1}, Fig. 5.20, Section 5.6.6 [251]). Absorption bands in the region reflecting charge transfer transitions in Co-oxides (around 30,000 cm^{-1}) [208] do not appear in the spectra of any Co-MFI samples (Fig. 5.21, Section 5.6.6), indicating the higher Co content resulting from higher temperature ion-exchange conditions were not a result of oxide formation.

The closure of cation-exchange site balances between Co-Na-exchanged Al-MFI samples and the parent H-Al-MFI sample was verified by temperature programmed desorption of NH_3 from Brønsted acidic protons in Al-MFI. The quantification of residual H^+ and Na^+ on Co-Na-exchanged Al-MFI samples, when compared to the number of H^+ sites on the parent H-Al-MFI sample, are shown in the inset of Figure 5.3. Al-MFI samples that were exchanged at both 298 K and 353 K showed agreement with stoichiometry expected (parity line in Fig. 5.3) for each Co^{2+} cation replacing two Na^+ or H^+ sites. These results indicate that Co^{2+} can be used to quantify proximal Al arrangements within MFI zeolites, upon verifying that Co ion-exchange protocols indeed lead to saturation of all exchange sites with Co^{2+}.

5.4.3 Effect of Structure-Directing Agents on Al Distributions in B-Al-MFI Zeolites

Using the ion-exchange methods described in Section 5.4.2, B-Al-MFI-TPA and B-Al-MFI-EDA zeolites were saturated with Co^{2+} cations in aqueous solution (0.5 M $Co(NO_3)_2$ solution at 353 K for 24 h). B-Al-MFI-TPA samples contain 20 - 40% Al in proximal configurations ($2\times Co^{2+}/Al_{tot} = 0.20 - 0.40$), and no systematic trend in the fraction of proximal Al was observed with increasing B content in the synthesis solution (Fig. 5.4). Absorption bands in the region reflecting charge transfer transitions in Co-oxides (ca. 30,000 cm^{-1} [208]) do not appear in the spectra of Co^{2+}-exchanged B-Al-MFI-TPA samples, as expected for samples saturated with Co^{2+} ions (Fig. 5.22, Section 5.16). In contrast, B-Al-MFI-EDA samples of similar bulk composition contain >95% of their framework Al present as isolated sites across a range of Si/B ratios (Fig. 5.4). The use of $Al(OH)_3$ instead of $Al(NO_3)_3$ as the Al precursor did not affect the number of proximal Al in B-Al-MFI-EDA zeolites (Table 5.6, Section 5.6.8), however, using colloidal silica instead of fumed silica in B-Al-MFI-TPA (25, 50) zeolites decreased the percentage of Al in proximal configurations from 40% to 16% (Table 5.6, Section 5.6.8). Different Al and Si precursors have also been reported to influence the fraction of Al in proximal configurations in MFI [77] and CHA [79] zeolites, and the specific Al and Si precursors used in synthetic solutions may affect framework Al arrangements in B-Al-MFI zeolites in ways that are not currently well-understood.

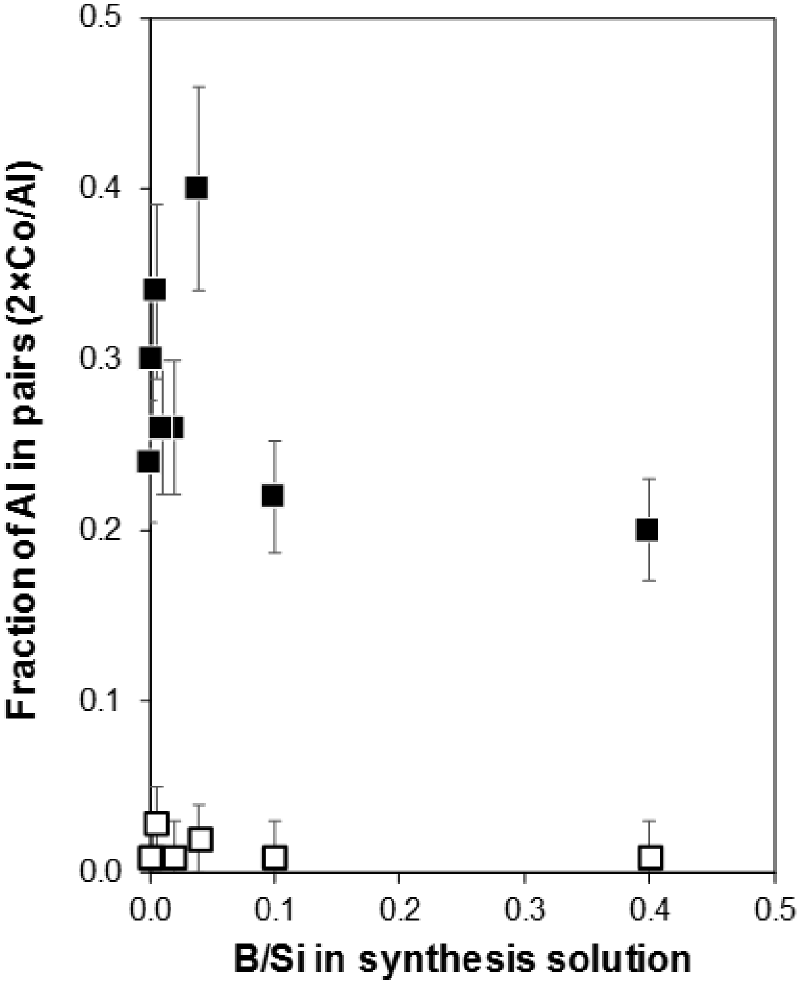

Figure 5.4.: Fraction of Al in proximal configurations measured by Co^{2+} titration (353 K, 24 h, 0.5 M $Co(NO_3)_2$), for a suite of B-Al-MFI samples of similar Al composition (Si/Al ∼ 50) prepared using two different synthesis methods (B-Al-MFI-TPA (closed), B-Al-MFI-EDA (open)) as a function of the B/Si ratio in the synthesis solution.

Among the samples in this study, we note that the most significant difference in the percentage of Al in proximal configurations is observed between zeolites made with TPA^+ only (finite values, in the range of 16-40%) or EDA/TPA^+ mixtures (essentially zero values, <5%). Therefore, differences in Co^{2+} saturation values between B-Al-MFI-TPA and B-Al-MFI-EDA samples appear to reflect the influence of TPA^+ and EDA/TPA^+ mixtures on the relative proximity of framework Al heteroatoms. The amounts of EDA and TPA^+ molecules occluded within B-Al-MFI crystallites were determined using carbon-hydrogen-nitrogen (CHN) elemental analysis to estimate the fraction of this organic content comprising either TPA^+ ($C/N = 12$) or EDA ($C/N = 1$). Among B-Al-MFI-TPA samples, approximately four TPA^+ molecules were occluded per MFI unit cell (3.7 – 3.9 TPA^+ per unit cell, Table 5.3, Figure 5.5), corresponding to one TPA^+ molecule per channel intersection in the MFI topology [253], independent of the B content in the synthesis solution. Organic contents measured by thermogravimetric analysis (TGA) showed a loss of $\sim$12 wt% in B-Al-MFI-TPA samples, consistent with $\sim$4 TPA^+ molecules per MFI unit cell. C/N ratios of occluded organics in these samples ranged from 10.9 – 11.8 (Table 5.3), close to the expected ratio of 12 for TPA^+. Framework Al contents were similar among these samples (1.3 – 1.8 Al_f per unit cell, Fig. 5.5) and close to that expected for nearly complete Al incorporation from synthesis solutions ($\sim$ 1.9 Al_f per unit cell) into crystalline products. Only a fraction of the B from synthesis solutions was incorporated into the solid B-Al-MFI-TPA crystallites (Fig. 5.5), consistent with previous reports on the partial incorporation of B into MFI zeolites from synthesis solutions containing TPA^+ [209,254,255]. Boric acid ($B(OH)_3$) precursors equilibrate with borate ($B(OH)_4^-$) in aqueous media, and borate species are predominant under the basic conditions used in hydrothermal synthesis ($pH > 11$). Unlike $Al(OH)_4^-$ species that condense with Si precursors to form Al-O-Si bonds, however, borate species are unable to undergo nucleophilic S_N2-type attack by $Si(OH)_4$ groups to form B-O-Si bonds, because B cannot adopt the pentacoordinate transition state required for this condensation reaction [245]. Hydrophobic domains near alkyl groups in TPA^+ molecules are proposed to decrease the local concentration of water and hydroxide ligands with free lone pairs around clathrated TPA^+ molecules [256], thereby shifting equilibrium towards boric acid that can undergo S_N2-type reactions with Si precursors to incorporate B [245]. The maximum amount of B and Al incorporated in B-Al-MFI-TPA (3.3 per unit cell) is similar to the TPA^+ content (3.7 per unit cell), consistent with the charge-compensation of a single framework heteroatom per TPA^+ cation (Fig. 5.5). Therefore, we surmise that B incorporation in B-Al-MFI-TPA zeolites is limited by the equilibrium between boric acid and borate, where boric acid is likely associated with TPA^+ during hydrothermal synthesis, and by the inability for TPA^+ to charge-compensate more than one framework heteroatom per MFI intersection.

Table 5.3.: Quantities of occluded organic SDAs and Co^{2+} ion-exchange capacity in B-Al-MFI-TPA zeolites.

B-Al-MFI-SDA (Si/B, Si/Al)	C/N[a]	TPA^+ (/ mmol g^{-1})	TPA^+/Al_{tot}	$2\times Co^{2+}/Al_{tot}^{b}$
B-Al-MFI-TPA (2.5,50)	11.0	0.68	2.48	0.20
B-Al-MFI-TPA (10,50)	11.2	0.54	1.86	0.22
B-Al-MFI-TPA (25,50)	11.5	0.54	2.26	0.40
B-Al-MFI-TPA (50,50)	11.8	0.66	2.19	0.26
B-Al-MFI-TPA (100,50)	11.3	0.66	2.08	0.26
B-Al-MFI-TPA (200,50)	11.5	0.65	2.41	0.34
B-Al-MFI-TPA (500,50)	10.9	0.67	1.75	0.30
B-Al-MFI-TPA (B-free,50)	11.3	0.63	2.00	0.24

[a] Determined by CHN elemental analysis. Errors are ± 10%.
[b] Determined by atomic absorption spectroscopy. Errors are ± 15%.

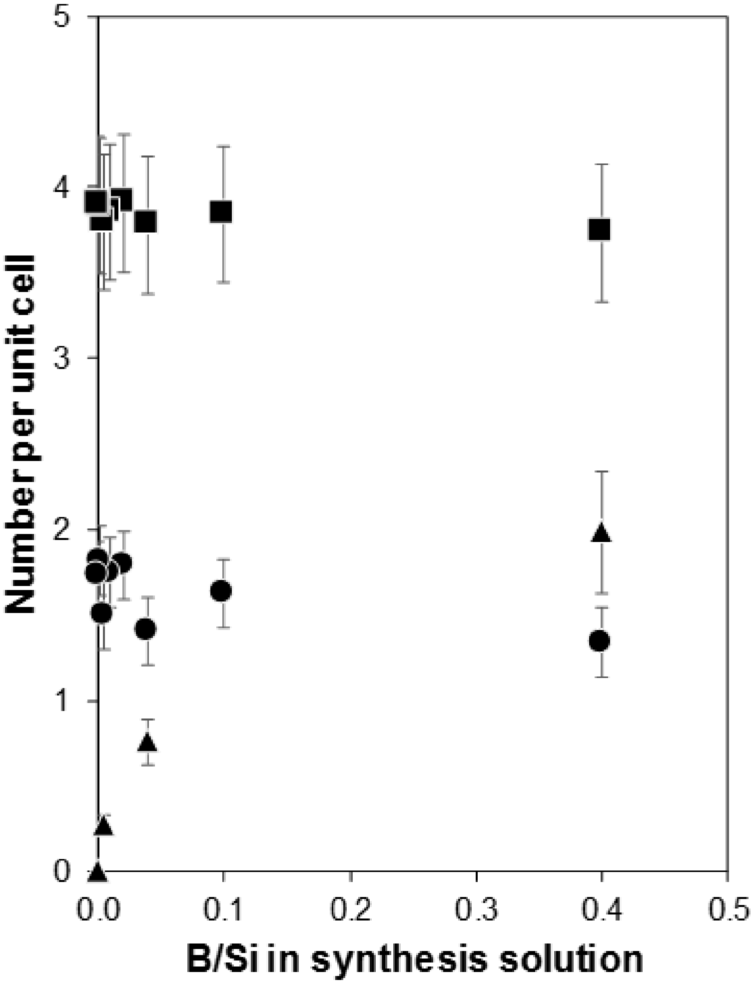

Figure 5.5.: Number of TPA$^+$ molecules (■), Al heteroatoms (•), and B heteroatoms (▲) incorporated into B-Al-MFI-TPA zeolites.

Al-MFI zeolites that do not contain boron and synthesized from solutions containing TPA^+ as the sole SDA contain framework Al sited in proximal locations that can charge-compensate Co^{2+}, and the addition of B to such synthesis solutions does not systematically affect the population of proximal Al sites in the resulting crystalline products (Fig. 5.4). This finding is consistent with previous Al-MFI syntheses using TPA^+ as the only SDA that contain Al pairs that compensate Co^{2+} cations [77]. Therefore, a fraction of framework Al heteroatoms sited by TPA^+ cations occluded in adjacent MFI channel intersections must be close enough to charge-compensate Co^{2+} cations. In the case of B-Al-MFI-TPA zeolites with Si/Al $\sim$ 50, approximately half of these TPA^+ cations compensate Al heteroatoms in the lattice, giving rise to adjacent intersections that contain TPA^+-$AlO_{4/2}^-$ ion pairs. The presence of framework B heteroatoms does not affect Co^{2+} saturation values because B heteroatoms likely do not have four framework bonds under the acidic conditions (pH $\sim$ 5) used in Co^{2+} ion-exchange [257].

Among B-Al-MFI-EDA samples, molar C/N ratios were lower (C/N = 2.3 – 4.8) than in B-Al-MFI-TPA samples and decreased with increasing B content in the synthesis solution (Table 5.4), reflecting the incorporation of EDA (C/N = 1) into crystalline products. Equation 5.2 was used to calculate the occluded EDA/TPA ratio in B-Al-MFI-EDA samples (Table 5.4), assuming that both TPA^+ and EDA remain intact during hydrothermal synthesis.

$$\frac{EDA}{TPA^+} = \frac{12 - \frac{C}{N}}{2(\frac{C}{N} - 1)} \tag{5.2}$$

Only $\sim$2 TPA^+ molecules are occluded per unit cell in B-Al-MFI-EDA zeolites (Fig. 5.6), which is approximately half of that occluded per unit cell in B-Al-MFI-TPA zeolites, likely a result of the TPA^+/Si ratio of 0.02 (corresponding to $\sim$2 TPA^+ per unit cell) that was used in synthesis solutions to crystallize B-Al-MFI-EDA zeolites. These results resemble those for MFI zeolites made from TPA^+-Na+ mixtures with similar TPA^+/Si ratios [258] to those reported here. TPA^+/Al ratios are $\sim$1 in B-Al-MFI-EDA zeolites (Fig. 5.6), independent of B content, again reflecting the molar composition of the synthesis solution. In the absence of B, approximately 2 EDA molecules are occluded per unit cell in Al-MFI-EDA zeolites (Fig. 5.7). Therefore, we conclude that EDA can also act as an SDA for the MFI framework [109] when Si/TPA$^+$ ratios in synthesis solutions are greater than 24, and not all silicate precursors can exchange with water contained in TPA$^+$-clathrate structures [60]. We surmise that TPA$^+$ cations are responsible for siting Al in B-Al-MFI-EDA zeolites, given their near-stoichiometric presence in all samples. With increasing B/Si in synthesis mixtures, a slight decrease in the amount of TPA$^+$ retained on the solid to 1.4 per unit cell is observed, while EDA contents increase systematically to 5.2 per unit cell. B retained in the solid product increases in parallel with EDA, up to 3.7 per unit cell (Fig. 5.7), and more B is retained in B-Al-MFI-EDA than in B-Al-MFI-TPA zeolites (Fig. 5.5) for a given B/Si ratio used in the synthesis solutions. Similar observations of TPA$^+$ exclusion have been reported for B-MFI zeolites made with TPA$^+$ and alkali metal cations (e.g., K$^+$, Cs$^+$), where these cations replace some TPA$^+$ and enable incorporating more than 4 B heteroatoms per MFI unit cell [259]. The amount of EDA retained in the crystalline products increases with the B content in the solid (Fig. 5.8) with a ratio of approximately two B heteroatoms per EDA molecule, consistent with EDA-boric acid complexes containing two B atoms that have previously been shown to behave as structure directing agents for B-MFI zeolites [109, 246].

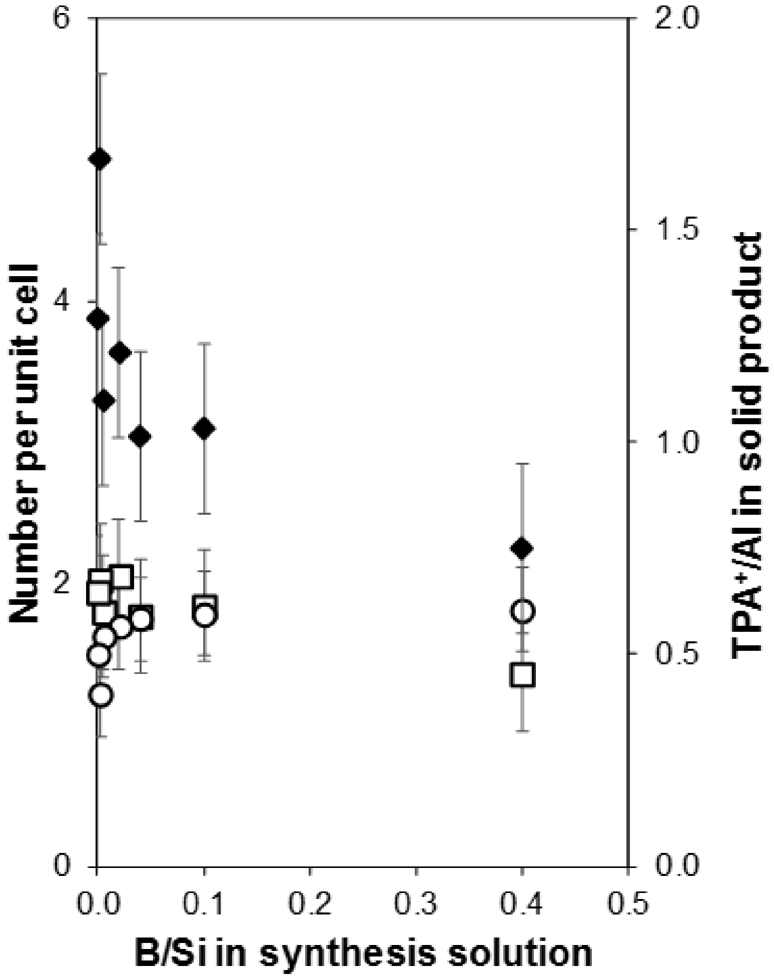

Figure 5.6.: Number of TPA$^+$ molecules (□) and Al heteroatoms (○) incorporated into B-Al-MFI-EDA zeolites. Ratio of TPA$^+$/Al (◆) is given on the secondary axis.

Table 5.4.: Quantities of occluded organic SDAs and Co^{2+} ion-exchange capacity in B-Al-MFI-EDA zeolites.

B-Al-MFI-SDA (Si/B,Si/Al)	C/N[a]	EDA/TPA^+	TPA^+ (/ mmol g^{-1})	EDA (/ mmol g^{-1})	TPA^+/Al_{tot}	$2xCo^{2+}/Al^{b}_{tot}$
B-Al-MFI-EDA (2.5,50)	2.3	3.8	0.21	0.80	0.74	0.01
B-Al-MFI-EDA (10,50)	2.9	2.4	0.27	0.64	0.87	0.01
B-Al-MFI-EDA (25,50)	3.3	1.9	0.30	0.55	0.94	0.02
B-Al-MFI-EDA (50,50)	4.2	1.2	0.37	0.45	1.1	0.01
B-Al-MFI-EDA (200,50)	4.2	1.2	0.37	0.45	1.3	0.03
B-Al-MFI-EDA (500,50)	4.8	1.0	0.38	0.36	1.2	0.01
B-Al-MFI-EDA (B-free,50)	4.2	1.2	0.31	0.39	0.91	0.01

[a] Determined by CHN elemental analysis. Errors are ± 10%.

[b] Determined by atomic absorption spectroscopy. Errors are ± 15%.

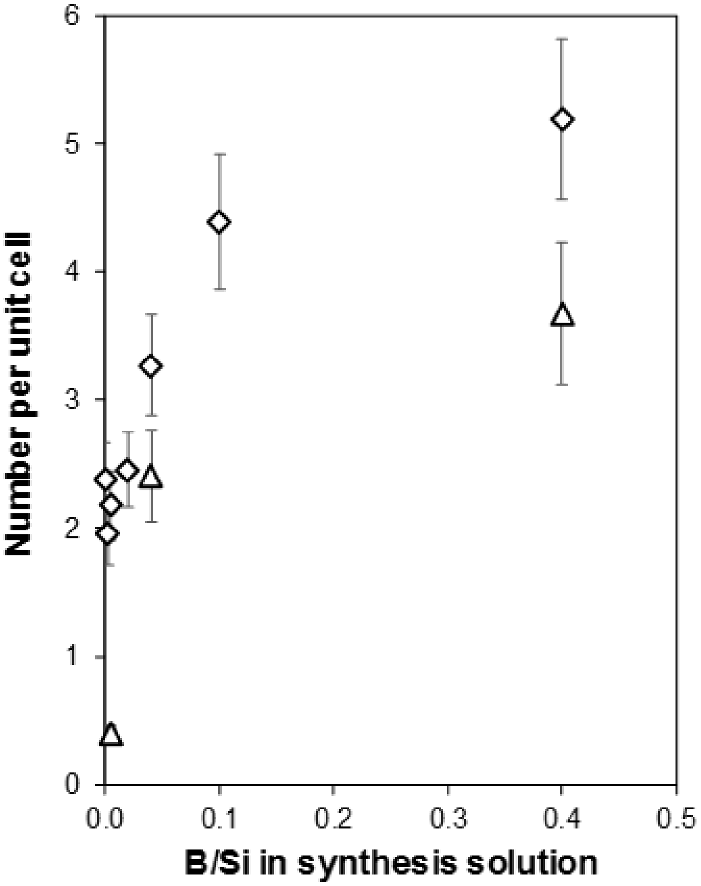

Figure 5.7.: Number of EDA molecules (◇) and B heteroatoms (△) retained in B-Al-MFI-EDA zeolites as a function of B/Si in the synthesis solution.

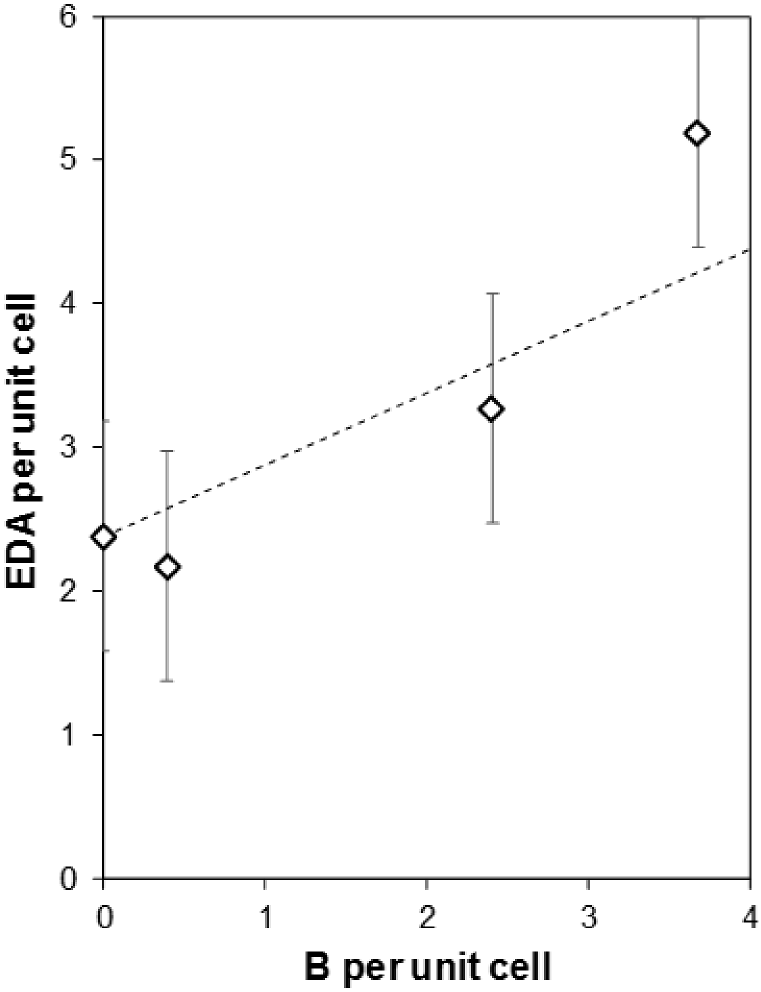

Figure 5.8.: Number of EDA molecules retained in B-Al-MFI-EDA zeolites as a function of B content. Dashed line denotes a slope of 0.5 (corresponding to a B/EDA stoichiometry of 2).

The presence of predominantly isolated Al heteroatoms in B-Al-MFI-EDA zeolites contrasts the 20-40% of Al in pairs found in B-Al-MFI-TPA zeolites of similar bulk composition. Given that approximately half of MFI intersections are occupied by TPA^+ in B-Al-MFI-EDA zeolites, the number of adjacent intersections containing TPA^+ is lower, on average, than in B-Al-MFI-TPA zeolites. Therefore, we surmise that the presence of predominantly isolated Al in B-Al-MFI-EDA zeolites is a consequence of the dilution of TPA^+ occupancy of intracrystalline void spaces in the crystalline solids by co-occluded EDA, which does not appear to site Al heteroatoms under the conditions studied. This finding provides a link between the fractional occlusion of TPA^+ within MFI frameworks (∼1.5 per unit cell) and the resulting isolation of framework Al. In this case, EDA is occluded within void spaces not occupied by TPA^+ in Al-MFI-EDA zeolites, and the addition of B to synthesis solutions forms B-EDA complexes that exclude some TPA^+ molecules and concurrently incorporate approximately two B heteroatoms per EDA into the MFI framework. These conclusions highlight the roles of TPA^+ and EDA SDAs on the siting and prevalence of Al and B heteroatoms in MFI zeolites by relating the compositions of the synthesis solutions to those of crystalline products.

5.4.4 Probing Al Location in Different Void Environments of B-Al-MFI Zeolites via Kinetics of Methanol Dehydration to Dimethyl Ether

Methanol dehydration catalysis occurs via an associative mechanism on MFI zeolites (433 K, 0.01 – 60 kPa MeOH [212]), which proceeds via adsorption of gaseous methanol at Brønsted acid sites to form hydrogen-bonded methanol monomers, followed by adsorption of a second methanol to form protonated dimers that rearrange to form dimethyl ether and water. Periodic density functional theory calculations (DFT) calculations show the most abundant reactive intermediates during methanol dehydration catalysis under these conditions (433 K, >0.2 kPa CH_3OH) are methanol monomers and protonated dimers [212]. *In situ* IR spectra (415-433 K, 0.2 – 16 kPa CH_3OH) of Al-MFI has shown the presence of hydrogen bonding modes for methanol monomers (~2380 cm^{-1}) and protonated dimers (~2620 cm^{-1} [238]) characteristic of associative and dissociative pathways, but no surface methoxy species (~1457 cm^{-1}) that are involved in the dissociative pathway [79, 238]. The Langmuirian rate expression derived for associative dehydration where methanol monomers and protonated dimers are the MARI, and DME formation is the kinetically-relevant step, is given by Equation 5.3.

$$r = \frac{k_{first,A} P_{CH_3OH}}{1 + \frac{k_{first,A}}{k_{zero,A}} P_{CH_3OH}} \tag{5.3}$$

In this expression, $k_{first,A}$ and $k_{zero,A}$ are apparent rate constants for kinetic regimes when methanol monomers and protonated dimers are the MARI, respectively.

First-order rate constants reflect the free energy difference between hydrogen-bonded methanol monomers and the transition state that differ in relative size and charge, while zero-order rate constants reflect the difference between the protonated dimers and the same transition state of similar size and charge as the dimer. This renders zero-order rate constants primarily sensitive to differences in acid strength and essentially independent of the local confining environment, because of the similar size of DME formation transition states and protonated methanol dimer intermediates, while the first-order rate constant is sensitive to both acid strength and confinement [212, 240]. Prior reports from our group [79] show first- and zero-order rate constants (per H^+_{Al}, 415 K), along with corresponding activation enthalpies and entropies, that are in quantitative agreement with those reported by Jones et al. (per H^+_{Al}, 433 K) [33] for a suite of commercially-sourced Al-MFI zeolites. DME formation rates on H-B-Al-MFI (415 K) predominantly reflect contributions from protons that charge compensate framework Al, as evidenced by zero-order rate constants (per H^+_{Al}) that are similar to those on Al-MFI, allowing for quantitative comparison of DME formation rates between Al-MFI and B-Al-MFI zeolites [33].

DME formation rates were measured on four B-Al-MFI zeolites (415 K) and normalized by the number of protons at Al heteroatoms (H^+_{Al}), as quantified by selective titration with NH_3 (Table 5.1). Turnover rates increased linearly at low methanol partial pressures (<1 kPa) before approaching a zero-order dependence at higher pressures (>20 kPa), consistent with previous reports on Al-MFI [33, 79] and B-Al-MFI [247] zeolites. Zero- and first-order rate constants (415 K, per H^+_{Al}, Table 5.7, Section 5.6.9) for the samples studied here are plotted as a function of H^+_{Al} content in Figure 5.9 along with those for a series of commercial Al-MFI samples reported previously [33], and B-Al-MFI samples synthesized in the presence of TPA^+ and EDA reported previously [247]. Zero-order rate constants were similar among all B-Al-MFI samples studied here and in quantitative agreement with values previously reported for Al-MFI (433 K, 0 20 kPa CH_3OH [33]; 415 K, 0 60 kPa CH_3OH [79]), providing validation for the NH_3 titration techniques to selectively quantify H^+_{Al} sites in B-Al-MFI zeolites and that protons of equivalent acid strength that charge-compensate framework Al contribute predominantly to measured DME formation rates.

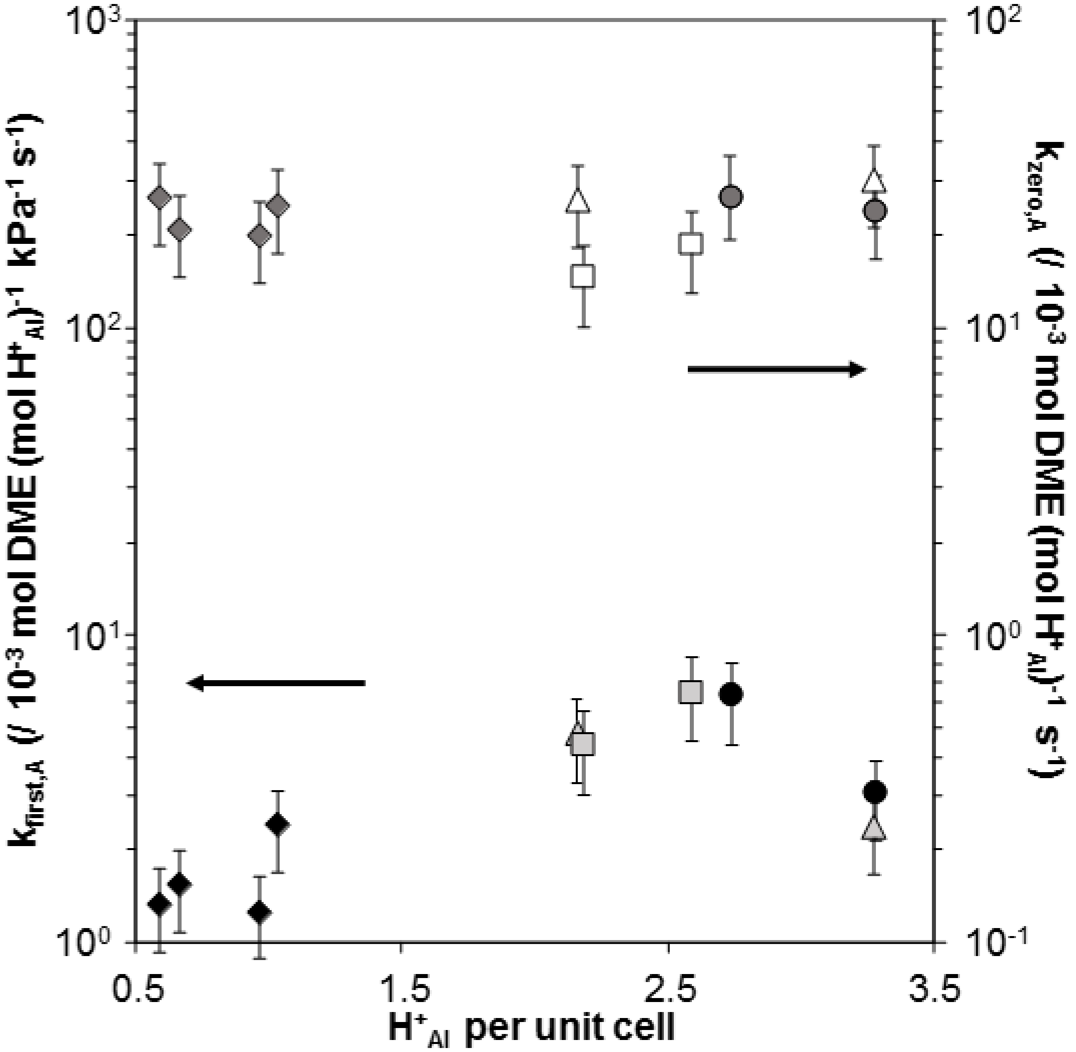

Figure 5.9.: First- (left axis) and zero-order (right axis) methanol dehydrationrate constants (415 K) on MFI samples. Samples crystallized in this study in the presence of TPA^+ (▲) or a mixture of TPA^+ and EDA (•), and previously reported B-Al-MFI samples crystallized with TPA^+ and EDA at lower Al content (◆ [247]) and commercially available Al-MFI (■ [79]).

First-order rate constants reflect the acid strength of protons and the local void geometry around active sites in MFI zeolites, as the larger transition state is preferentially stabilized over methanol monomers [33]. Higher rate constants indicate confinement within smaller voids as a consequence of van der Waals interactions between the oxide lattice and organic guests. First-order rate constants on B-Al-MFI zeolites (Si/Al $\sim$ 50) were comparable to those on commercial Al-MFI materials previously reported (Fig. 5.9, [79]) and did not trend systematically with B content, synthesis method, or the fraction of Al counted by Co^{2+} titration (Table 5.7). Additionally, these rates were not affected by intracrystalline mass transfer limitations, as evidenced by effectiveness factors close to unity (Figure 5.23, Section 5.6.9) estimated with first order rate constants and physiochemical properties (Table 5.7) similar to prior reports [79, 247].

Previously reported first-order rate constants on B-Al-MFI were lower and closer to a value of $\sim 2.0 \times 10^{-3}$ mol DME (mol $H^+_{Al})^{-1}$ kPa^{-1} s^{-1}, which is characteristic of a confining environment of approximately 0.8 nm in diameter [247, 254]. These lower first-order rate constants on B-Al-MFI zeolites (Si/Al = 74 – 153) were interpreted as the preferential siting of Al in MFI channel intersections ($\sim$0.7 nm in diameter) compared to the sinusoidal and straight channels ($\sim$0.55 nm in diameter). This was attributed to the occlusion of EDA-B complexes in MFI channels, which may bias Al incorporation to T-sites in larger intersections [247]. At higher Al content reported here, the preferential siting of Al at T-sites accessible via channel intersections may be disrupted, as evidenced by first order rate constants that are between those predicted for protons confined within 0.55 nm or 0.70 nm diameter voids, consistent with the commercial Al-MFI samples studied previously [33, 79].

5.5 Conclusions

The methods reported herein provide a strategy to crystallize MFI zeolites containing B and Al heteroatoms with independent influence over bulk zeolite properties (elemental composition, crystallite size) and active site arrangements, defined as Al in isolated or proximal framework locations. The addition of B heteroatoms to MFI synthesis solutions of fixed Al content decreases characteristic crystallite sizes when either TPA^+ or mixtures of EDA and TPA^+ are used as organic SDAs. This observation may reflect different relative rates of nucleation, growth, and dissolution during hydrothermal synthesis, influenced by the alkalinity of synthetic solutions that are less basic with the addition of boric acid precursors, and the ability of EDA to modify MFI crystallite growth rates. While crystallite sizes are predominantly influenced by Si/B ratios in the synthesis solutions, protons at B heteroatoms are irrelevant for most Brønsted acid catalyzed reactions, and thus would not contribute to characteristic diffusion parameters that range from $0.2 - 42 \times 10^{-6}$ mol H^+_{Al} nm^{-1} among MFI zeolites synthesized in this work.

The percentage of Al heteroatoms in proximal configurations was measured with Co^{2+} saturation via liquid phase ion-exchange at 353 K in a 0.5 M $Co(NO_3)_2$ solution for 24 h, and these procedures were validated by cation site balances and UV-Visible spectra to verify a 2:1 replacement of monovalent cations by Co2+ and the absence of Co-oxide phases, respectively. Using only TPA^+ as an organic SDA during B-Al-MFI synthesis (Si/Al $\sim$ 50) resulted in 20 – 40% of Al located in proximal configurations, irrespective of B content or crystallite size. B-Al-MFI zeolites of similar Al content, but instead crystallized from EDA/TPA^+ mixtures, contain <5% of Al in paired configurations, again independent of B content and crystallite size. While one TPA^+ molecule is occluded per channel intersection in MFI zeolites crystallized using only TPA^+, those crystallized with EDA/TPA^+ = 15 and excess Si relative to TPA^+, as required for substitution of all silicate precursors in TPA^+ clathrates (Si/TPA^+ > 24), result in occlusion of approximately one TPA^+ for every two channel intersections.

Intracrystalline voids not occupied by TPA$^+$ contain EDA, and EDA-B complexes incorporate two B heteroatoms per EDA with increasing B concentrations in synthesis solutions.

Ammonia titration methods can discriminate between protons at framework Al and B heteroatoms, and catalytic turnovers occur predominantly at the former protons that have lower deprotonation energies. This is demonstrated with methanol dehydration catalysis (415 K, per H^+_{Al}) in first-order and zero-order kinetic regimes, as previously shown for boroaluminosilicates. We hypothesize that these titrations could be used to normalize site-time yields and turnover numbers during hydrocarbon reactions catalyzed by Brønsted acid sites (e.g., methanol-to-hydrocarbons, alkene oligomerization) to decouple the effects of intracrystalline residence times imparted by characteristic diffusion parameters and reactivity differences between active site ensembles in MFI zeolites.

5.6 Supporting Information

5.6.1 XRD Patterns of B-Al-MFI Zeolites

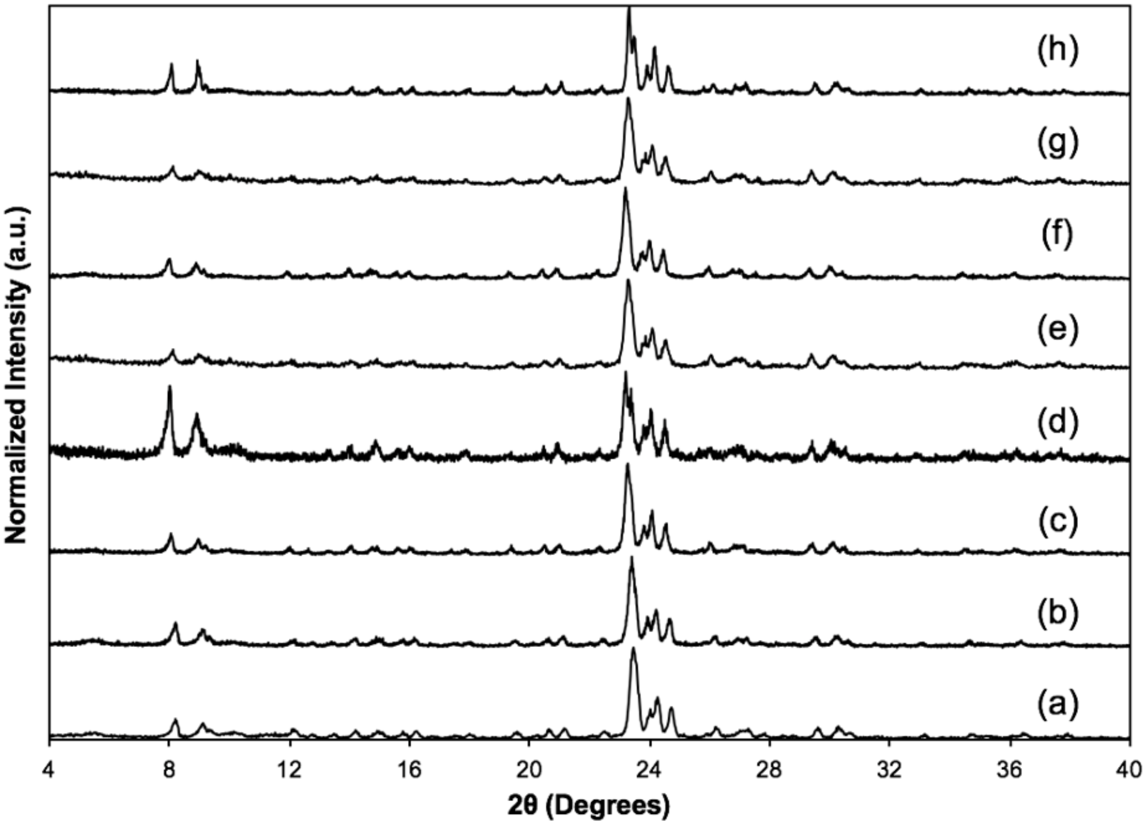

Figure 5.10.: XRD patterns for B-Al-MFI-EDA samples of varying Si/Al and Si/B ratios. (a) B-Al-MFI-EDA(2.5, 50), (b) B-Al-MFI-EDA(25, 50), (c) B-Al-MFI-EDA(2.5, 150), (d) B-Al-MFI-EDA(25, 150), (e) B-Al-MFI-EDA(2.5, 300), (f) B-Al-MFI-EDA(25, 300), (g) B-Al-MFI-EDA(2.5, 500), (h) B-Al-MFI-EDA(25, 500).

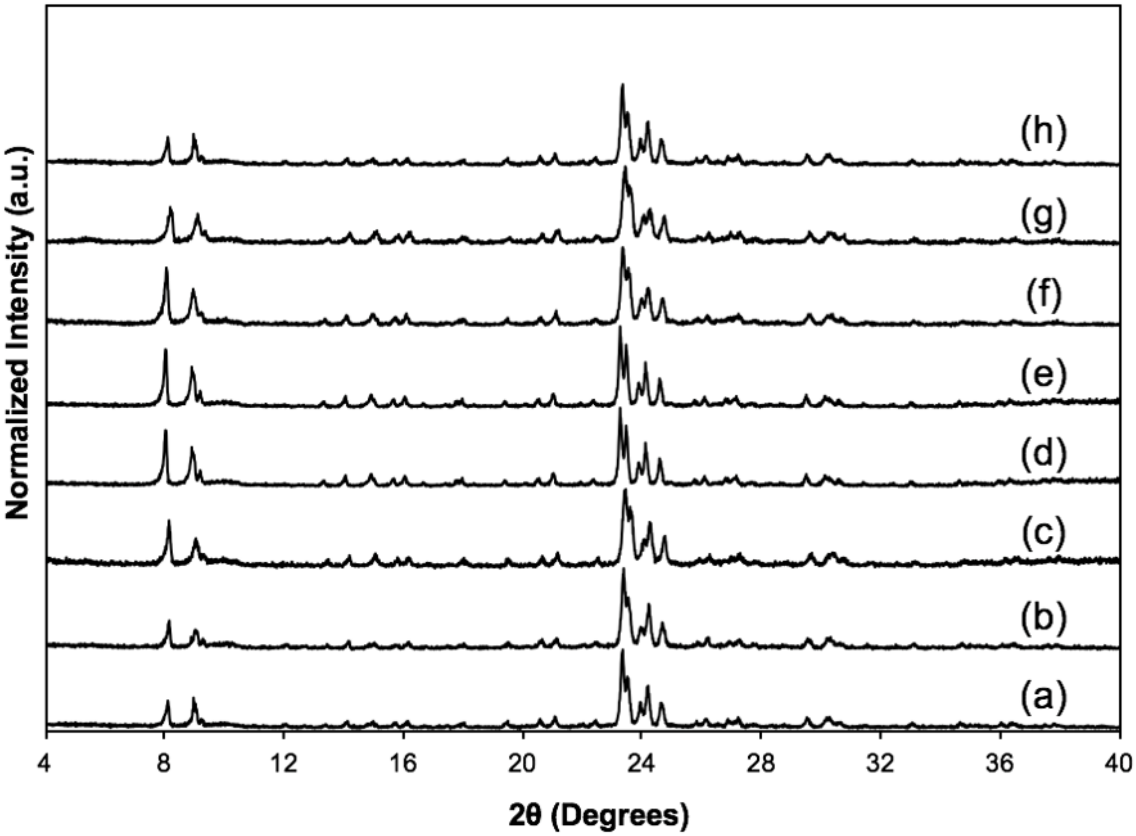

Figure 5.11.: XRD patterns for B-Al-MFI-TPA samples of Si/Al=50 and varying Si/B ratios. (a) B-Al-MFI-TPA(2.5, 50), (b) B-Al-MFI-TPA(10, 50), (c) B-Al-MFI-TPA(25, 50), (d) B-Al-MFI-TPA(50, 50), (e) B-Al-MFI-TPA(100, 50), (f) B-Al-MFI-TPA(200, 50), and (g) B-Al-MFI-TPA(500, 50), (h) B-Al-MFI-TPA(B-free, 50).

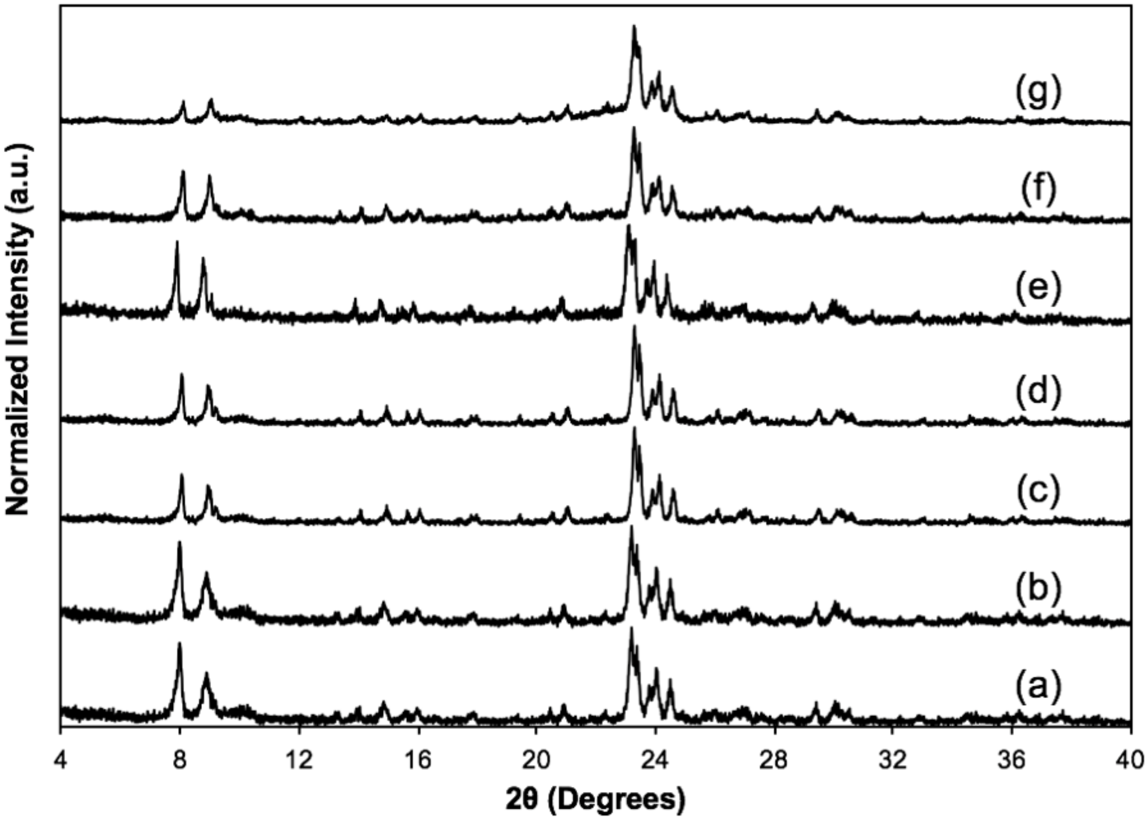

Figure 5.12.: XRD patterns for B-Al-MFI-EDA samples of Si/Al=50 and varying Si/B ratios. (a) B-Al-MFI-EDA(2.5, 50), (b) B-Al-MFI-EDA(10, 50), (c) B-Al-MFI-EDA(25, 50), (d) B-Al-MFI-EDA(50, 50), (e) B-Al-MFI-EDA(200, 50), (f) B-Al-MFI-EDA(500, 50), and (g) B-Al-MFI-EDA(B-free, 50).

5.6.2 N_2 Adsorption Isotherms of B-Al-MFI Zeolites

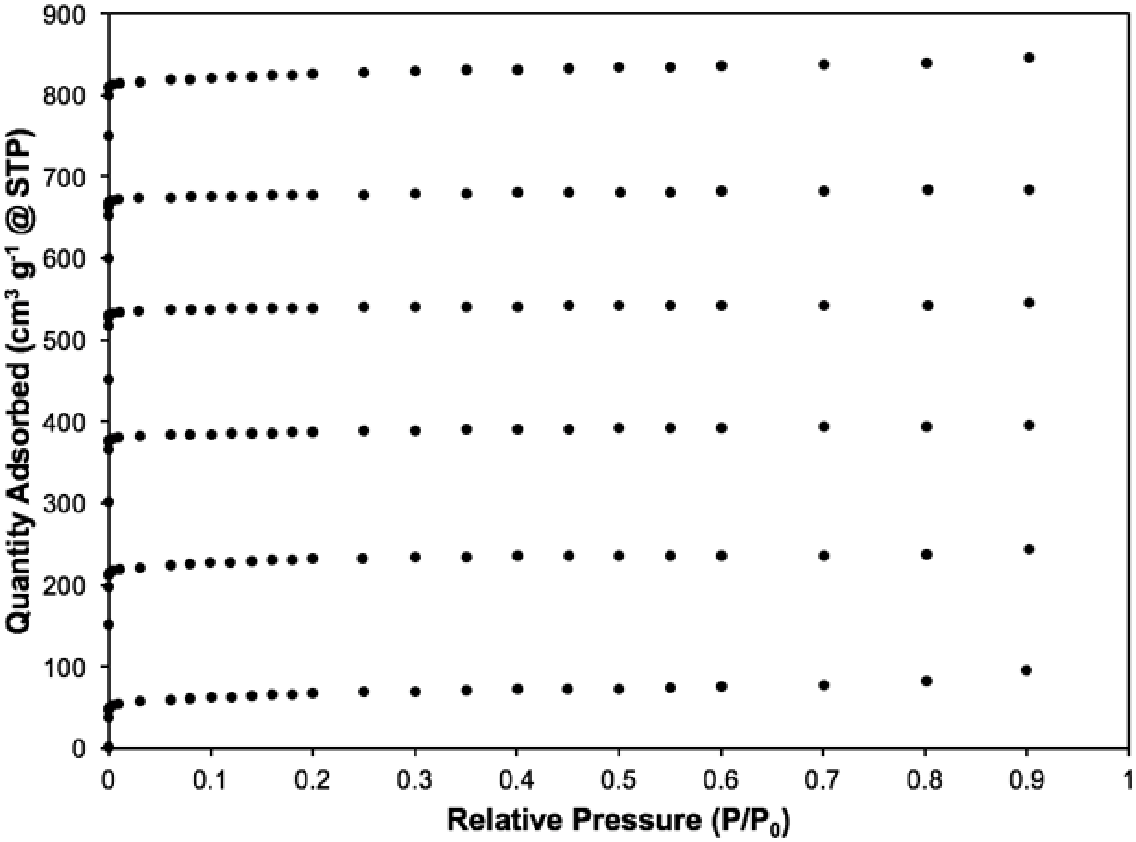

Figure 5.13.: N_2 adsorption isotherms for B-Al-MFI-EDA samples of Si/Al=50 and varying Si/B content. (a) B-Al-MFI-EDA(2.5, 50), b) B-Al-MFI-EDA(10, 50), c) B-Al-MFI-EDA(25, 50), d) B-Al-MFI-EDA(50, 50), e) B-Al-MFI-EDA(200, 50) and f) B-Al-MFI-EDA(500, 50). Isotherms are vertically offset by 150 cm^3 g^{-1} @ STP for clarity.

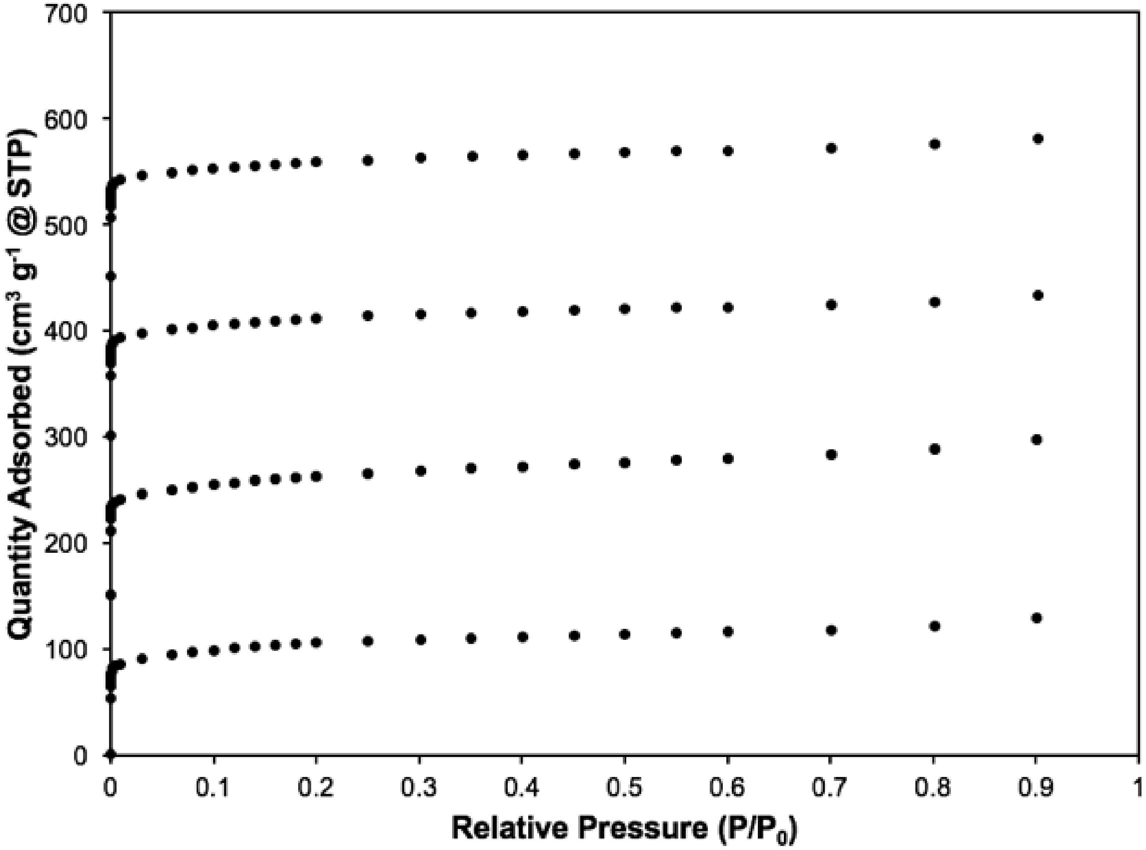

Figure 5.14.: N_2 adsorption isotherms for B-Al-MFI-TPA samples of Si/Al=50 and varying Si/B content. (a) B-Al-MFI-TPA(2.5, 50), (b) B-Al-MFI-TPA(25, 50), (c) B-Al-MFI-TPA(50, 50) and (d) B-Al-MFI-TPA(200, 50). Isotherms are vertically offset by 150 cm^3 g^{-1} @ STP for clarity.

5.6.3 ^{27}Al and ^{11}B Magic Angle Spinning Nuclear Magnetic Resonance (MAS NMR) of B-Al-MFI Zeolites

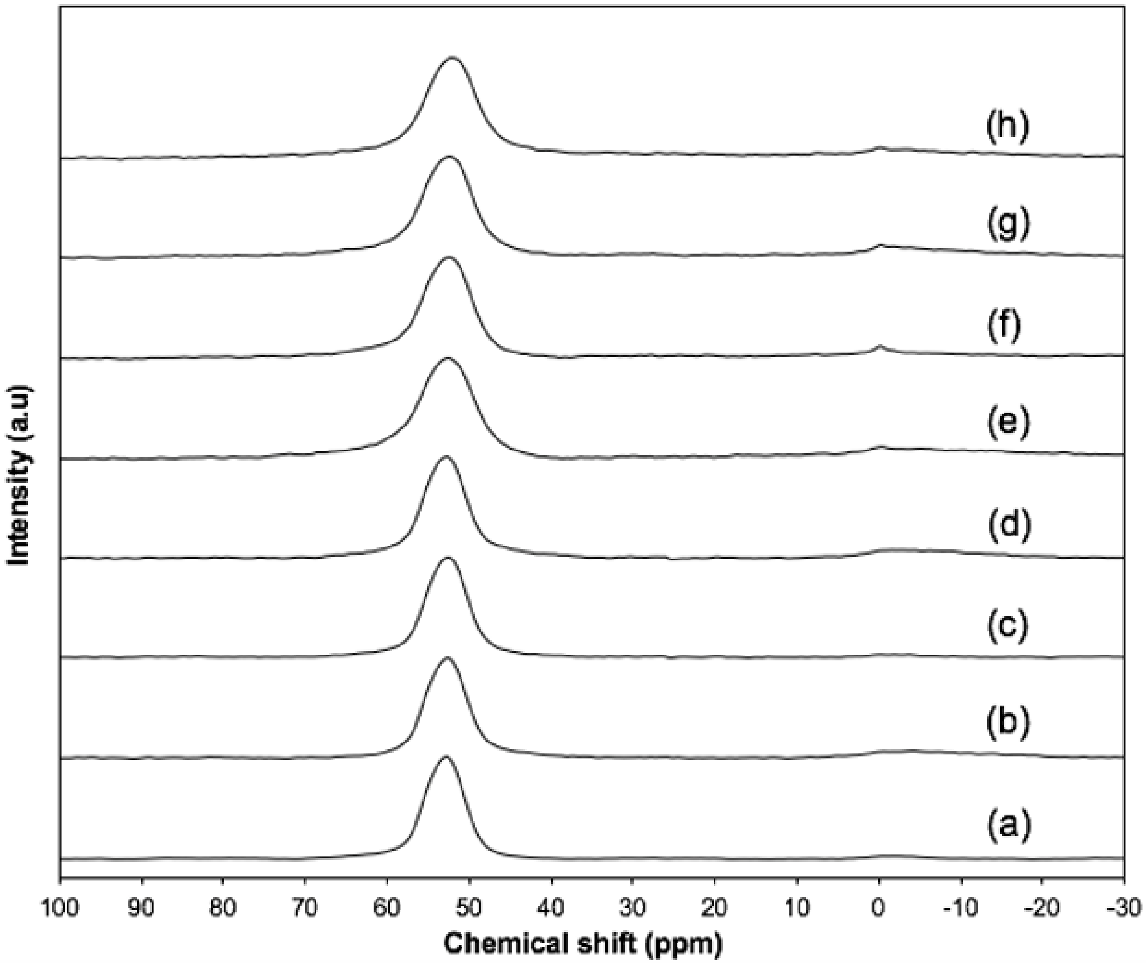

Figure 5.15.: B-Al-MFI samples for ^{27}Al NMR spectra on (a) B-Al-MFI-EDA (2.5, 50), (b) B-Al-MFI-EDA (50, 200), (c) B-Al-MFI-EDA (500, 50), (d) B-Al-MFI-EDA (1000, 50), (e) B-Al-MFI-TPA (2.5, 50), (f) B-Al-MFI-TPA (50, 50), (g) B-Al-MFI-TPA (100, 50) and (h) B-Al-MFI-TPA (500, 50).

Table 5.5.: Estimated fraction of framework Al from integrated area of 53 ppm resonance, relative to total integrated areas of 53 and 0 ppm resonances from ^{27}Al NMR spectra.

B-Al-MFI-SDA (Si/B,Si/Al)	Si/Al$_{solid}$	Si/B$_{gel}$	Al$_f/Al_{tot}$
B-Al-MFI-EDA(25,50)	51	25	0.98
B-Al-MFI-EDA(50,50)	60	50	0.95
B-Al-MFI-EDA(500,50)	58	200	0.97
B-Al-MFI-EDA(1000,50)	53	500	0.95
B-Al-MFI-EDA(2.5,50)	59	2.5	0.90
B-Al-MFI-EDA(50,50)	54	50	0.92
B-Al-MFI-EDA(100,50)	51	100	0.92
B-Al-MFI-EDA(500,50)	42	500	0.91

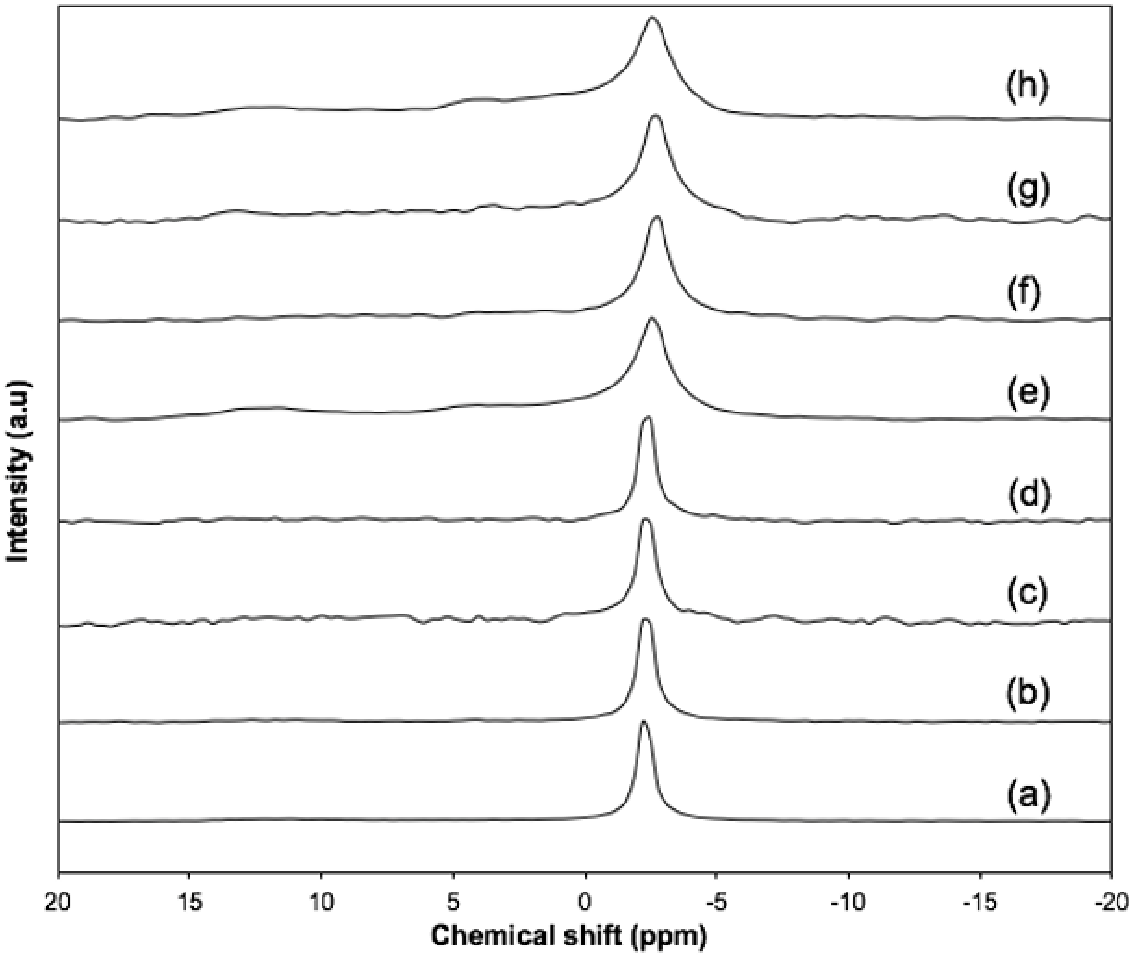

Figure 5.16.: B-Al-MFI samples for ^{11}B NMR spectra on (a) B-Al-MFI-EDA (2.5, 50), (b) B-Al-MFI-EDA (50, 200), (c) B-Al-MFI-EDA (500, 50), (d) B-Al-MFI-EDA (1000, 50), (e) B-Al-MFI-TPA (2.5, 50), (f) B-Al-MFI-TPA (50, 50), (g) B-Al-MFI-TPA (100, 50) and (h) B-Al-MFI-TPA (500, 50).

5.6.4 SEM Images and Crystallite Size Distributions of B-Al-MFI Zeolites

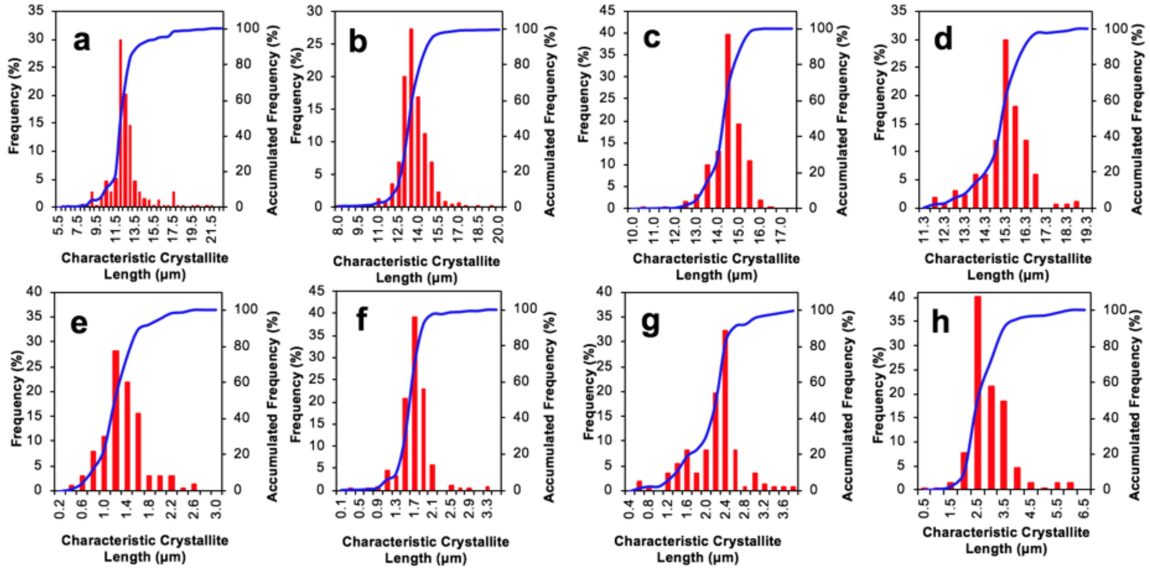

Figure 5.17.: Crystallite size distribution of B-Al-MFI zeolite samples: (a) B-Al-MFI-EDA (25, 50), (b) B-Al-MFI-EDA (25, 150), (c) B-Al-MFI-EDA (25, 300), (d) B-Al-MFI-EDA (25, 500), (e) B-Al-MFI-EDA (2.5, 50), (f) B-Al-MFI-EDA (2.5, 150), (g) B-Al-MFI-EDA (2.5, 300), and (h) B-Al-MFI-EDA (2.5, 500).

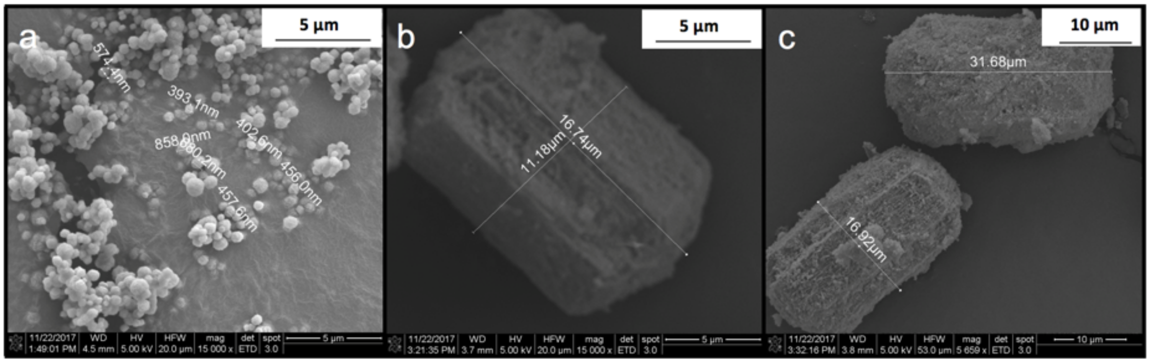

Figure 5.18.: SEM images for B-Al-MFI-TPA samples of Si/Al=50 and varying Si/B content. (a) B-Al-MFI-TPA(2.5, 50), (b) B-Al-MFI-TPA(100, 50) and (c) B-Al-MFI-TPA(500, 50).

5.6.5 Co^{2+} Ion-Exchange Experiments on Commercial Al-MFI Zeolites

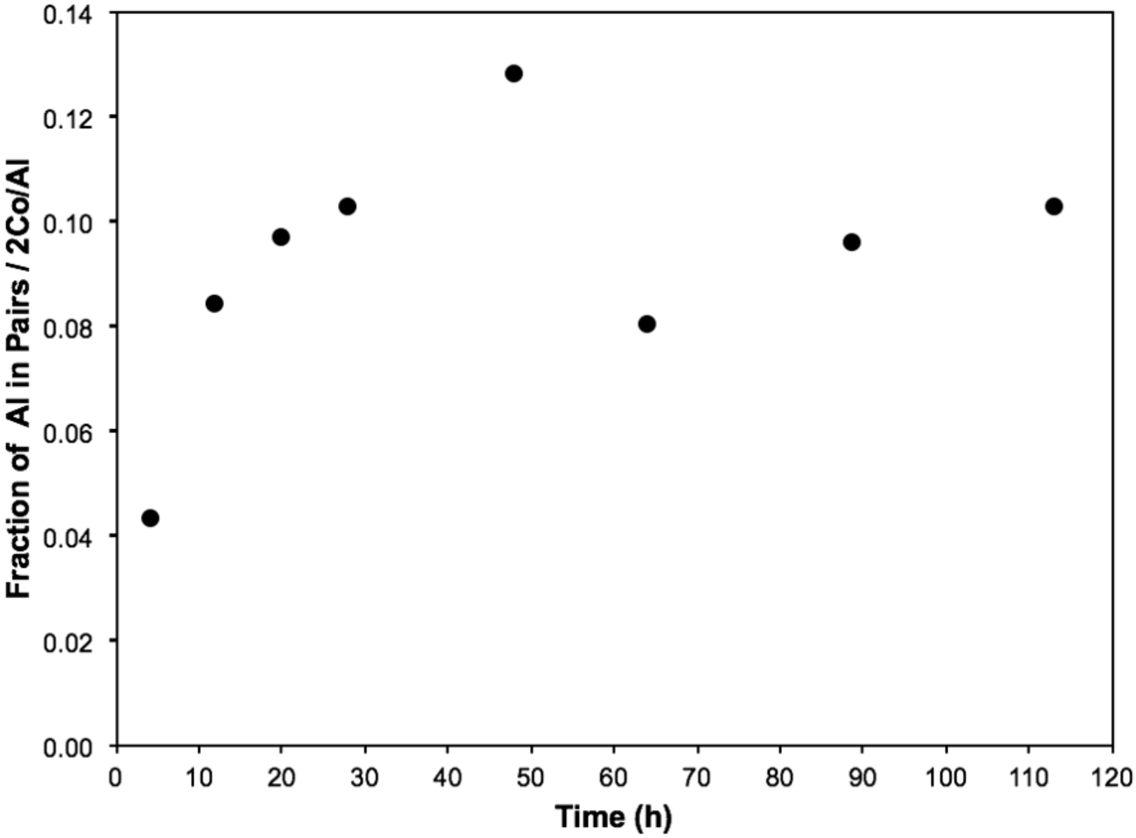

Figure 5.19.: Amount of Co^{2+} ions exchanged on a commercial Al-MFI sample (Zeolyst CBV2314, ZSM-5, Si/Al = 11.5) upon contact of sample (150 mL solution per g solid) under ambient conditions with a 0.25 M $Co(NO_3)_2$ as a function of time.

5.6.6 UV-Visible Spectra of Co^{2+}-MFI Zeolites

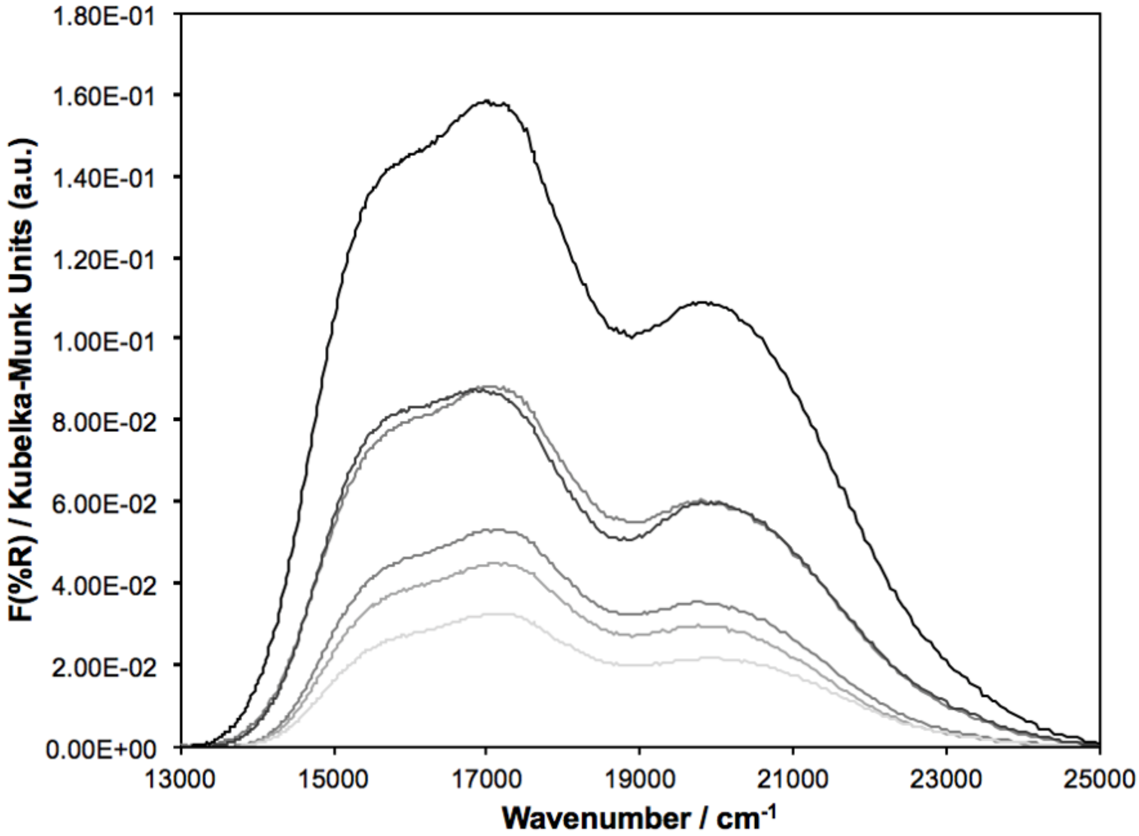

Figure 5.20.: DRUV-visible absorption spectra for d-d transition region (15,100 - 22,000 cm^1) of Co^{2+}-MFI samples (353 K for 24 h) at 673 K with increasing Co^{2+} concentration (0.05, 0.5, 0.25, 1.0, 0.75, and 0.001 M from dark to light).

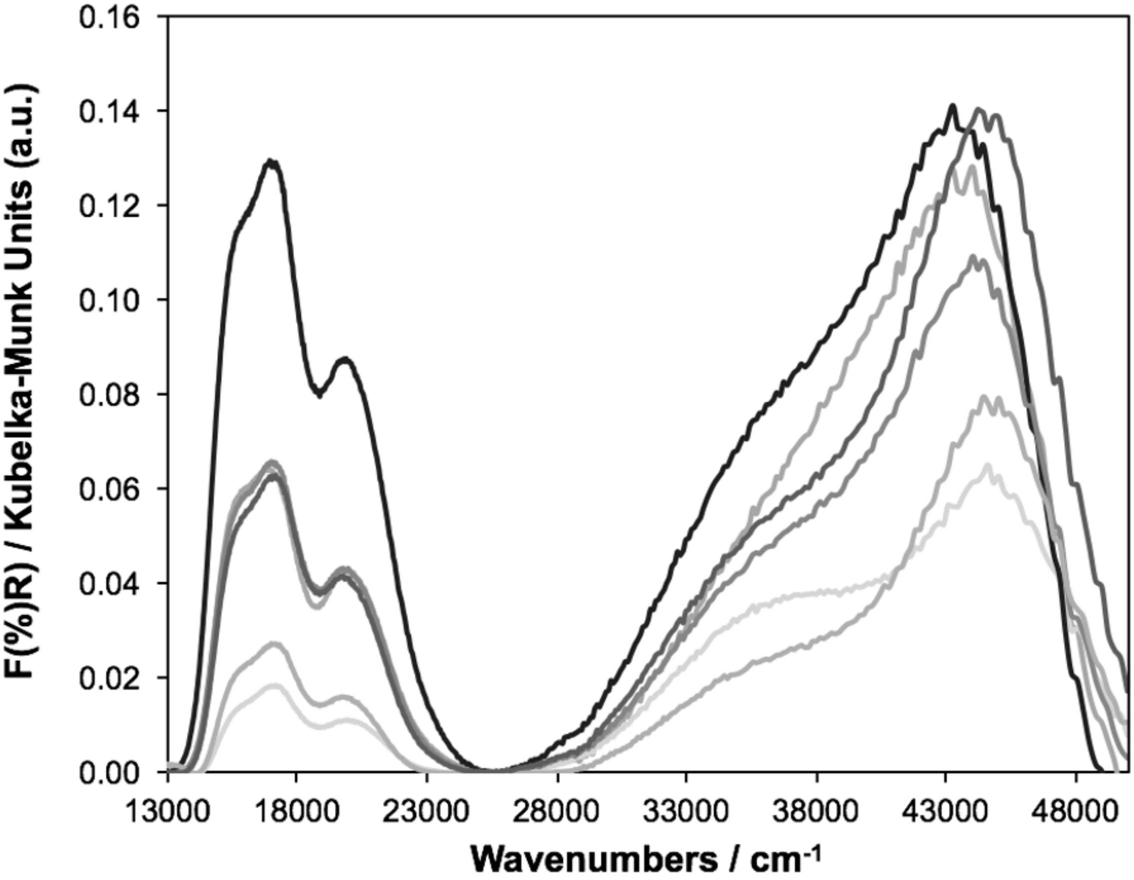

Figure 5.21.: DRUVvisible absorption spectra for full spectra of Co^{2+}-MFI samples (353 K for 24 h) at 673 K with increasing Co^{2+} concentration (0.05, 0.5, 0.25, 1.0, 0.75, and 0.001 M from dark to light).

5.6.7 Co^{2+} Ion-Exchange Experiments on B-Al-MFI-TPA Zeolites

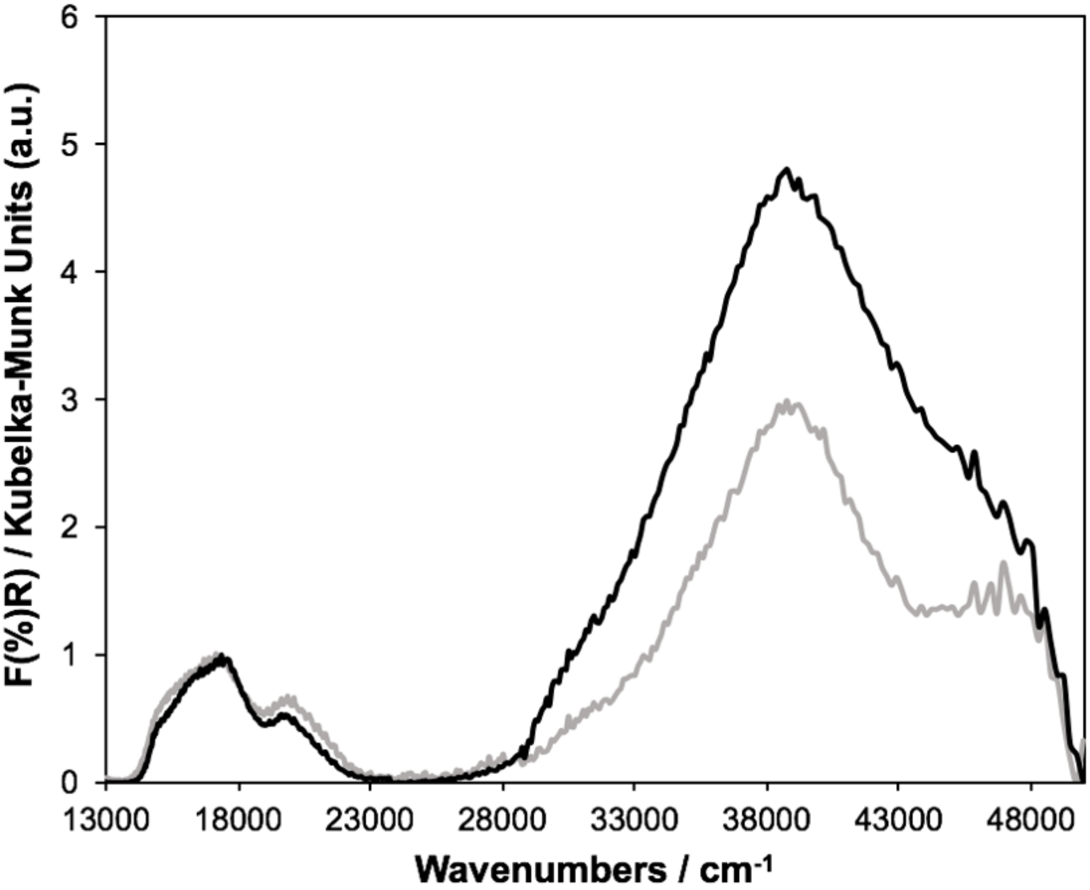

Figure 5.22.: DRUVvisible absorption spectra for full spectra of Co^{2+} exchanged (353 K for 24 h) B-Al-MFI-TPA (2.5, 50)(blanck trace) and Co^{2+}-exchanged B-Al-MFI-TPA (50, 50)(grey trace) samples at 673 K.

5.6.8 Fraction of Al in Pairs in B-Al-MFI Samples Synthesized with Different Precursors

Table 5.6.: Characterization of B-Al-MFI samples made with different Si and Al precursors

B-Al-MFI-SDA (Si/B,Si/Al) - changed parameter	Elemental composition			Precursors	
	Si/Al$_{solid}$	TPA$^+$/Al$_{gel}$	2×Co^{2+}/Al$_{solid}$	SiO$_2$	Al$_2$O$_3$
B-Al-MFI-EDA (25,50)	51.2	0.82	0.02	colloidal silica	Al(OH)$_3$
B-Al-MFI-EDA (25,50) - Al	55.8	0.82	0.01	colloidal silica	Al(NO$_3$)$_2$
B-Al-MFI-TPA (25,50)	66.0	15.4	0.40	fumed silica	Al(OH)$_3$
B-Al-MFI-TPA (25,50) - Si	51.3	15.4	0.12	colloidal silica	Al(OH)$_3$

5.6.9 Methanol Dehydration Kinetics on B-Al-MFI Zeolites

Table 5.7.: First- and Zero-order Methanol Dehydration Rate Constants on B-Al-MFI Zeolites.

B-Al-MFI-SDA (Si/B,Si/Al)	H^+_{Al}/Al^a_{tot}	H^+_{Al} per unit cell	Mean crystallite length (L)^b (/ μm)	Rate Constants (415 K, per H^+_{Al})	
				k^c_{first}	k^d_{zero}
B-Al-MFI-TPA (2.5,50)	1.08	3.3	0.5	2.4	30.1
B-Al-MFI-TPA (500,50)	0.71	2.2	15.3	4.8	26.1
B-Al-MFI-EDA (25,50)	0.95	2.7	12.6	6.4	26.2
B-Al-MFI-EDA (50,50)	1.08	3.3	17.7	3.0	23.9

[a] Determined by NH_3 TPD. Errors are ± 15%.

[b] Determined by measuring >250 particles per sample imaged by SEM.

[c] Units for k_{first} are 10^{-3} mol DME (mol H^+_{Al})$^{-1}$ kPa^{-1} s^{-1}.

[d] Units for k_{zero} are 10^{-3} mol DME (mol H^+_{Al})$^{-1}$ s^{-1}.

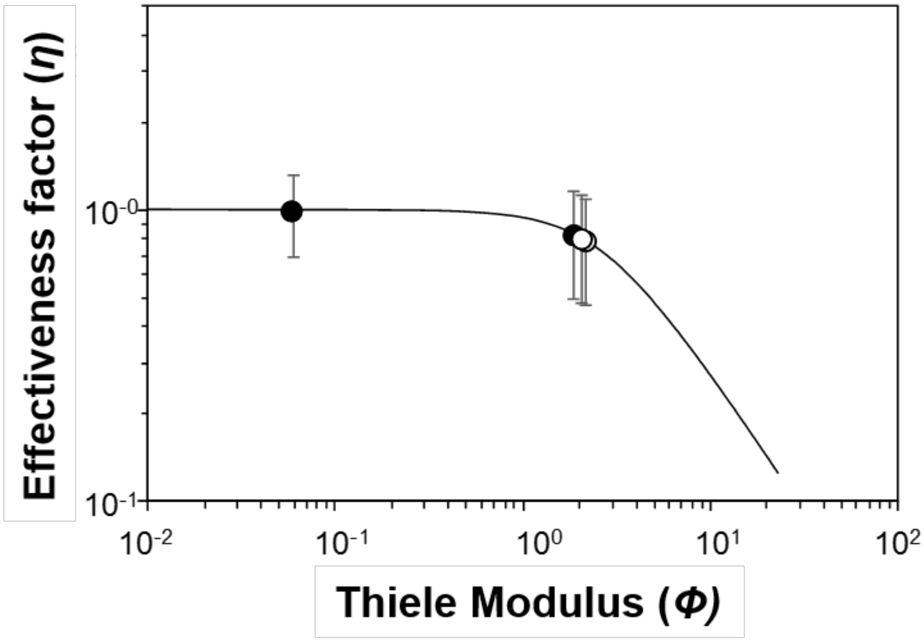

Figure 5.23.: Calculated effectiveness factors from experimentally-determined Thiele moduli for B-Al-MFI-TPA (•) and B-Al-MFI-EDA (○) zeolites

5.7 Acknowledgements

We thank co-authors Dr. Young Gul Hur, Claire Nimlos, YoonRae Cho, and Prof. Jeff Miller for experimental assistance and tecnhical feedback in the preparation of this work. We acknowledge the support for this work provided by the National Science Foundation under Cooperative Agreement No. EEC-1647722, an Engineering Research Center for the Innovative and Strategic Transformation of Alkane Resources (CISTAR). We thank Laura Wilcox for assistance collecting methanol dehydration kinetic data, and for technical discussions and feedback on this manuscript. We also thank Dr. John Harwood (Purdue Interdepartmental NMR Facility) for assistance collecting NMR spectra.

5.8 Rights and Permissions

REFERENCES

[1] Colin S. Cundy and Paul A. Cox. The Hydrothermal Synthesis of Zeolites: History and Development from the Earliest Days to the Present Time. *Chemical Reviews*, 103(3):663–702, March 2003.

[2] Li-Chiang Lin, Adam H. Berger, Richard L. Martin, Jihan Kim, Joseph A. Swisher, Kuldeep Jariwala, Chris H. Rycroft, Abhoyjit S. Bhown, Michael W. Deem, Maciej Haranczyk, and Berend Smit. In silico screening of carbon-capture materials. *Nature Materials*, 11(7):633–641, July 2012.

[3] Vasant R. Choudhary and S. Mayadevi. Adsorption of methane, ethane, ethylene, and carbon dioxide on silicalite-l. *Zeolites*, 17(5):501–507, November 1996.

[4] E. T. C. Vogt and B. M. Weckhuysen. Fluid catalytic cracking: recent developments on the grand old lady of zeolite catalysis. *Chemical Society Reviews*, 44(20):7342–7370, 2015.

[5] Christopher P. Nicholas. Applications of light olefin oligomerization to the production of fuels and chemicals. *Applied Catalysis A: General*, 543:82–97, August 2017.

[6] L. B. Young, S. A. Butter, and W. W. Kaeding. Shape selective reactions with zeolite catalysts: III. Selectivity in xylene isomerization, toluene-methanol alkylation, and toluene disproportionation over ZSM-5 zeolite catalysts. *Journal of Catalysis*, 76(2):418–432, August 1982.

[7] Christopher Paolucci, Ishant Khurana, Atish A. Parekh, Sichi Li, Arthur J. Shih, Hui Li, John R. Di Iorio, Jonatan D. Albarracin-Caballero, Aleksey Yezerets, Jeffrey T. Miller, W. Nicholas Delgass, Fabio H. Ribeiro, William F. Schneider, and Rajamani Gounder. Dynamic multinuclear sites formed by mobilized copper ions in NOx selective catalytic reduction. *Science*, August 2017.

[8] Weiping Ding, Senzi Li, George D Meitzner, and Enrique Iglesia. Methane Conversion to Aromatics on Mo/H-ZSM5: Structure of Molybdenum Species in Working Catalysts. *The Journal of Physical Chemistry B*, 105(2):506–513, January 2001.

[9] Y. Li and J. N. Armor. Ammoxidation of ethane: V. Solid-state ion exchange to prepare cobalt zeolite catalysts. *Applied Catalysis A: General*, 188(1):211–217, November 1999.

[10] Cronstedt, A. F. Om en oberkant barg art, som kallas Zeolites. *Kongl Vetenskaps Academiens Handlingar Stockholm*, 17:120, 1756.

[11] Carmine Colella and Alessandro F. Gualtieri. Cronstedt's zeolite. *Microporous and Mesoporous Materials*, 105(3):213–221, October 2007.

[12] de St. Claire Deville, H. *Compt. Rend.*, 54:324, 1862.

[13] R. M. Barrer. 33. Synthesis of a zeolitic mineral with chabazite-like sorptive properties. *Journal of the Chemical Society (Resumed)*, (0):127–132, January 1948.

[14] Robert M. Milton. Molecular sieve adsorbents, April 1959.

[15] Robert M. Milton. Molecular sieve adsorbents, April 1959.

[16] Edith M. Flanigen. Chapter 2 Zeolites and Molecular Sieves an Historical Perspective. In H. van Bekkum, E. M. Flanigen, and J. C. Jansen, editors, *Studies in Surface Science and Catalysis*, volume 58 of *Introduction to Zeolite Science and Practice*, pages 13–34. Elsevier, January 1991.

[17] R. M. Barrer and P. J. Denny. 201. Hydrothermal chemistry of the silicates. Part IX. Nitrogenous aluminosilicates. *Journal of the Chemical Society (Resumed)*, 0(0):971–982, January 1961.

[18] Robert L. Wadlinger, George T. Kerr, and Edward J. Rosinski. Catalytic composition of a crystalline zeolite, March 1967.

[19] Robert J. Argauer and George R. Landolt. Crystalline zeolite zsm-5 and method of preparing the same, November 1972.

[20] N. Y. Chen and W. E. Garwood. Some catalytic properties of ZSM-5, a new shape selective zeolite. *Journal of Catalysis*, 52(3):453–458, May 1978.

[21] Robert A. Innes, Stacey I. Zones, and Gerald J. Nacamuli. Liquid phase alkylation or transalkylation process using zeolite beta, January 1992.

[22] G. Bellussi, G. Pazzuconi, C. Perego, G. Girotti, and G. Terzoni. Liquid-Phase Alkylation of Benzene with Light Olefins Catalyzed by -Zeolites. *Journal of Catalysis*, 157(1):227–234, November 1995.

[23] W. E. Garwood. Conversion of C2-C10 to Higher Olefins over Synthetic Zeolite ZSM-5. In *Intrazeolite Chemistry*, volume 218 of *ACS Symposium Series*, pages 383–396. AMERICAN CHEMICAL SOCIETY, May 1983.

[24] Hartley Owen, Samuel A. Tabak, and Bernard S. Wright. Process for converting olefins to gasoline, distillate and alkylate liquid hydrocarbons, December 1986.

[25] S. A. Tabak, F. J. Krambeck, and W. E. Garwood. Conversion of propylene and butylene over ZSM-5 catalyst. *AIChE Journal*, 32(9):1526–1531, September 1986.

[26] Robert L. Gorring and George F. Shipman. Catalytic dewaxing of gas oils, July 1975.

[27] Raul F. Lobo, Stacey I. Zones, and Mark E. Davis. Structure-direction in zeolite synthesis. *Journal of inclusion phenomena and molecular recognition in chemistry*, 21(1):47–78, March 1995.

[28] Ramdas Pophale, Frits Daeyaert, and Michael W. Deem. Computational prediction of chemically synthesizable organic structure directing agents for zeolites. *Journal of Materials Chemistry A*, 1(23):6750–6760, 2013.

[29] Manuel Moliner, Fernando Rey, and Avelino Corma. Towards the Rational Design of Efficient Organic Structure-Directing Agents for Zeolite Synthesis. *Angewandte Chemie International Edition*, 52(52):13880–13889, 2013.

[30] Richard M. Barrer and Edouard F. Freund. Hydrothermal chemistry of silicates. Part XVI. Replacement of aluminium by boron during zeolite growth. *Journal of the Chemical Society, Dalton Transactions*, 0(10):1049–1053, 1974.

[31] M. A. Camblor, J. Perez-Pariente, and V. Fornes. Synthesis and characterization of gallosilicates and galloaluminosilicates isomorphous to zeolite Beta. *Zeolites*, 12(3):280–286, March 1992.

[32] R. Kumar, A. Thangaraj, R. N. Bhat, and P. Ratnasamy. Synthesis of iron-silicate analogs of zeolite beta. *Zeolites*, 10(2):85–89, February 1990.

[33] Andrew J. Jones, Robert T. Carr, Stacey I. Zones, and Enrique Iglesia. Acid strength and solvation in catalysis by MFI zeolites and effects of the identity, concentration and location of framework heteroatoms. *Journal of Catalysis*, 312:58–68, April 2014.

[34] Manuel Moliner. State of the art of Lewis acid-containing zeolites: lessons from fine chemistry to new biomass transformation processes. *Dalton Transactions*, 43(11):4197–4208, February 2014.

[35] Manuel Moliner, Yuriy Román-Leshkov, and Mark E. Davis. Tin-containing zeolites are highly active catalysts for the isomerization of glucose in water. *Proceedings of the National Academy of Sciences*, 107(14):6164–6168, April 2010.

[36] Stavros Caratzoulas, Mark E. Davis, Raymond J. Gorte, Rajamani Gounder, Raul F. Lobo, Vladimiros Nikolakis, Stanley I. Sandler, Mark A. Snyder, Michael Tsapatsis, and Dionisios G. Vlachos. Challenges of and Insights into Acid-Catalyzed Transformations of Sugars. *The Journal of Physical Chemistry C*, 118(40):22815–22833, October 2014.

[37] P. B. Weisz and V. J. Frilette. Intracrystalline and molecular-shape-selective catalysis by zeolite salts. *The Journal of Physical Chemistry*, 64(3):382–382, March 1960.

[38] Eric G. Derouane. New Aspects of Molecular Shape-Selectivity: Catalysis by Zeolite ZSM - 5. In B. Imelik, C. Naccache, Y. Ben Taarit, J. C. Vedrine, G. Coudurier, and H. Praliaud, editors, *Studies in Surface Science and Catalysis*, volume 5 of *Catalysis by Zeolites*, pages 5–18. Elsevier, January 1980.

[39] N. Y. Chen, W. W. Kaeding, and F. G. Dwyer. Para-directed aromatic reactions over shape-selective molecular sieve zeolite catalysts. *Journal of the American Chemical Society*, 101(22):6783–6784, October 1979.

[40] A. B. Pinar, C. Márquez-Álvarez, M. Grande-Casas, and J. Pérez-Pariente. Template-controlled acidity and catalytic activity of ferrierite crystals. *Journal of Catalysis*, 263(2):258–265, April 2009.

[41] L. D. Rollmann and D. E. Walsh. Shape selectivity and carbon formation in zeolites. *Journal of Catalysis*, 56(1):139–140, January 1979.

[42] Eric G. Derouane. Shape selectivity in catalysis by zeolites: The nest effect. *Journal of Catalysis*, 100(2):541–544, August 1986.

[43] Eiichi Kikuchi, Hiroshi Nakano, Kei Shimomura, and Yoshiro Morita. Cracking of Hydrocarbons on Zeolite Catalysts (Part 1). *Journal of The Japan Petroleum Institute*, 28(3):210–213, May 1985.

[44] W. J. Mortier. Zeolite electronegativity related to physicochemical properties. *Journal of Catalysis*, 55(2):138–145, November 1978.

[45] Eric G. Derouane, Jean-Marie André, and Amand A. Lucas. A simple van der waals model for molecule-curved surface interactions in molecular-sized microporous solids. *Chemical Physics Letters*, 137(4):336–340, June 1987.

[46] Eric G. Derouane and Janos B. Nagy. Surface curvature effects on the NMR chemical shift for molecules trapped in microporous solids. *Chemical Physics Letters*, 137(4):341–344, June 1987.

[47] F. Eder, M. Stockenhuber, and J. A. Lercher. Brønsted Acid Site and Pore Controlled Siting of Alkane Sorption in Acidic Molecular Sieves. *J. Phys. Chem. B*, 101(27):5414–5419, July 1997.

[48] Aditya Bhan, Ayman D. Allian, Glenn J. Sunley, David J. Law, and Enrique Iglesia. Specificity of Sites within Eight-Membered Ring Zeolite Channels for Carbonylation of Methyls to Acetyls. *Journal of the American Chemical Society*, 129(16):4919–4924, April 2007.

[49] Rajamani Gounder and Enrique Iglesia. Catalytic Consequences of Spatial Constraints and Acid Site Location for Monomolecular Alkane Activation on Zeolites. *Journal of the American Chemical Society*, 131(5):1958–1971, February 2009.

[50] Michele L. Sarazen and Enrique Iglesia. Experimental and theoretical assessment of the mechanism of hydrogen transfer in alkane-alkene coupling on solid acids. *Journal of Catalysis*, 354:287–298, October 2017.

[51] Michele L. Sarazen, Eric Doskocil, and Enrique Iglesia. Catalysis on solid acids: Mechanism and catalyst descriptors in oligomerization reactions of light alkenes. *Journal of Catalysis*, 344:553–569, December 2016.

[52] Stanley Herrmann and Enrique Iglesia. Elementary steps in acetone condensation reactions catalyzed by aluminosilicates with diverse void structures. *Journal of Catalysis*, 346:134–153, February 2017.

[53] Rajamani Gounder and Enrique Iglesia. The catalytic diversity of zeolites: confinement and solvation effects within voids of molecular dimensions. *Chem. Commun.*, 49(34):3491–3509, April 2013.

[54] Colin S. Cundy and Paul A. Cox. The hydrothermal synthesis of zeolites: Precursors, intermediates and reaction mechanism. *Microporous and Mesoporous Materials*, 82(1):1–78, July 2005.

[55] Patrick M. Piccione, Christel Laberty, Sanyuan Yang, Miguel A. Camblor, Alexandra Navrotsky, and Mark E. Davis. Thermochemistry of Pure-Silica Zeolites. *The Journal of Physical Chemistry B*, 104(43):10001–10011, November 2000.

[56] Ivan Petrovic, Alexandra Navrotsky, Mark E. Davis, and Stacy I. Zones. Thermochemical study of the stability of frameworks in high silica zeolites. *Chemistry of Materials*, 5(12):1805–1813, December 1993.

[57] Patrick M. Piccione, Sanyuan Yang, Alexandra Navrotsky, and Mark E. Davis. Thermodynamics of Pure-Silica Molecular Sieve Synthesis. *The Journal of Physical Chemistry B*, 106(14):3629–3638, April 2002.

[58] Avelino Corma and Mark E. Davis. Issues in the Synthesis of Crystalline Molecular Sieves: Towards the Crystallization of Low Framework-Density Structures. *ChemPhysChem*, 5(3):304–313, 2004.

[59] Jeffrey D. Rimer, Olga Trofymluk, Alexandra Navrotsky, Raul F. Lobo, and Dionisios G. Vlachos. Kinetic and Thermodynamic Studies of Silica Nanoparticle Dissolution. *Chemistry of Materials*, 19(17):4189–4197, August 2007.

[60] Clarence D. Chang and Alexis T. Bell. Studies on the mechanism of ZSM-5 formation. *Catal Lett*, 8(5):305–316, September 1991.

[61] Sandra L. Burkett and Mark E. Davis. Mechanism of Structure Direction in the Synthesis of Si-ZSM-5: An Investigation by Intermolecular 1h-29si CP MAS NMR. *The Journal of Physical Chemistry*, 98(17):4647–4653, April 1994.

[62] Viet Q. Nguyen, X. G. Chen, and Alfred L. Yergey. Observations of magic numbers in gas phase hydrates of alkylammonium ions. *Journal of the American Society for Mass Spectrometry*, 8(11):1175–1179, November 1997.

[63] Hubert Koller, Raul F. Lobo, Sandra L. Burkett, and Mark E. Davis. SiO-.cntdot. .cntdot. .cntdot.HOSi Hydrogen Bonds in As-Synthesized High-Silica Zeolites. *The Journal of Physical Chemistry*, 99(33):12588–12596, August 1995.

[64] J. Dědeček, Z. Sobalík, and B. Wichterlová. Siting and Distribution of Framework Aluminium Atoms in Silicon-Rich Zeolites and Impact on Catalysis. *Catalysis Reviews*, 54(2):135–223, April 2012.

[65] Ana B. Pinar, Luis Gómez-Hortigüela, Lynne B. McCusker, and Joaquín Pérez-Pariente. Controlling the Aluminum Distribution in the Zeolite Ferrierite via the Organic Structure Directing Agent. *Chemistry of Materials*, 25(18):3654–3661, September 2013.

[66] Yuriy Román-Leshkov, Manuel Moliner, and Mark E. Davis. Impact of Controlling the Site Distribution of Al Atoms on Catalytic Properties in Ferrierite-Type Zeolites. *The Journal of Physical Chemistry C*, 115(4):1096–1102, February 2011.

[67] Brandon C. Knott, Claire T. Nimlos, David J. Robichaud, Mark R. Nimlos, Seonah Kim, and Rajamani Gounder. Consideration of the Aluminum Distribution in Zeolites in Theoretical and Experimental Catalysis Research. *ACS Catal.*, 8(2):770–784, February 2018.

[68] Toshiyuki Yokoi, Hiroshi Mochizuki, Seitaro Namba, Junko N. Kondo, and Takashi Tatsumi. Control of the Al Distribution in the Framework of ZSM-5 Zeolite and Its Evaluation by Solid-State NMR Technique and Catalytic Properties. *J. Phys. Chem. C*, 119(27):15303–15315, July 2015.

[69] Toshiyuki Yokoi, Hiroshi Mochizuki, Turgen Biligetu, Yong Wang, and Takashi Tatsumi. Unique Al Distribution in the MFI Framework and Its Impact on Catalytic Properties. *Chemistry Letters*, 46(6):798–800, March 2017.

[70] V. J. Frillette, W. O. Haag, and R. M. Lago. Catalysis by crystalline aluminosilicates: Characterization of intermediate pore-size zeolites by the "Constraint Index". *Journal of Catalysis*, 67(1):218–222, January 1981.

[71] Anton N. Mlinar, Paul M. Zimmerman, Fuat E. Celik, Martin Head-Gordon, and Alexis T. Bell. Effects of Brønsted-acid site proximity on the oligomerization of propene in H-MFI. *Journal of Catalysis*, 288:65–73, April 2012.

[72] M. Bernauer, E. Tabor, V. Pashkova, D. Kaucký, Z. Sobalík, B. Wichterlová, and J. Dedecek. Proton proximity – New key parameter controlling adsorption, desorption and activity in propene oligomerization over H-ZSM-5 zeolites. *Journal of Catalysis*, 344:157–172, December 2016.

[73] Chenhai Song, Yueying Chu, Meng Wang, Hui Shi, Li Zhao, Xuefeng Guo, Weimin Yang, Jianyi Shen, Nianhua Xue, Luming Peng, and Weiping Ding. Cooperativity of adjacent Brønsted acid sites in MFI zeolite channel leads to enhanced polarization and cracking of alkanes. *Journal of Catalysis*, 349(Supplement C):163–174, May 2017.

[74] Richard W. Borry, Young Ho Kim, Anne Huffsmith, Jeffrey A. Reimer, and Enrique Iglesia. Structure and Density of Mo and Acid Sites in Mo-Exchanged H-ZSM5 Catalysts for Nonoxidative Methane Conversion. *The Journal of Physical Chemistry B*, 103(28):5787–5796, July 1999.

[75] Mark J. Rice, Arup K. Chakraborty, and Alexis T. Bell. Site Availability and Competitive Siting of Divalent Metal Cations in ZSM-5. *Journal of Catalysis*, 194(2):278–285, September 2000.

[76] Jiri Dedecek, Vendula Balgová, Veronika Pashkova, Petr Klein, and Blanka Wichterlová. Synthesis of ZSM-5 Zeolites with Defined Distribution of Al Atoms in the Framework and Multinuclear MAS NMR Analysis of the Control of Al Distribution. *Chemistry of Materials*, 24(16):3231–3239, August 2012.

[77] Veronika Pashkova, Petr Klein, Jiri Dedecek, Věnceslava Tokarová, and Blanka Wichterlová. Incorporation of Al at ZSM-5 hydrothermal synthesis. Tuning of Al pairs in the framework. *Microporous and Mesoporous Materials*, 202:138–146, January 2015.

[78] John R. Di Iorio and Rajamani Gounder. Controlling the Isolation and Pairing of Aluminum in Chabazite Zeolites Using Mixtures of Organic and Inorganic Structure-Directing Agents. *Chemistry of Materials*, 28(7):2236–2247, April 2016.

[79] John R. Di Iorio, Claire T. Nimlos, and Rajamani Gounder. Introducing Catalytic Diversity into Single-Site Chabazite Zeolites of Fixed Composition via Synthetic Control of Active Site Proximity. *ACS Catal.*, 7(10):6663–6674, October 2017.

[80] S. I. Zones. Conversion of faujasites to high-silica chabazite SSZ-13 in the presence of N,N,N-trimethyl-1-adamantammonium iodide. *Journal of the Chemical Society, Faraday Transactions*, 87(22):3709–3716, January 1991.

[81] Stacey I. Zones, Son-Jong Hwang, and Mark E. Davis. Studies of the Synthesis of SSZ-25 Zeolite in a "Mixed-Template" System. *Chemistry – A European Journal*, 7(9):1990–2001, 2001.

[82] S. I. Zones and Son-Jong Hwang. Synthesis of High Silica Zeolites Using a Mixed Quaternary Ammonium Cation, Amine Approach: Discovery of Zeolite SSZ-47. *Chemistry of Materials*, 14(1):313–320, January 2002.

[83] Qinming Wu, Ye Ma, Sai Wang, Xiangju Meng, and Feng-Shou Xiao. 110th Anniversary: Sustainable Synthesis of Zeolites: From Fundamental Research to Industrial Production. *Industrial & Engineering Chemistry Research*, 58(27):11653–11658, July 2019.

[84] Bin Xie, Jiangwei Song, Limin Ren, Yanyan Ji, Jixue Li, and Feng-Shou Xiao. Organotemplate-Free and Fast Route for Synthesizing Beta Zeolite. *Chemistry of Materials*, 20(14):4533–4535, July 2008.

[85] Jonas Hedlund. Control of the Preferred Orientation in MFI Films Synthesized by Seeding. *Journal of Porous Materials*, 7(4):455–464, June 2000.

[86] Manjesh Kumar, Zachariah J. Berkson, R. John Clark, Yufeng Shen, Nathan A. Prisco, Qi Zheng, Zhiyuan Zeng, Haimei Zheng, Lynne B. McCusker, Jeremy C. Palmer, Bradley F. Chmelka, and Jeffrey D. Rimer. Crystallization of Mordenite Platelets using Cooperative Organic Structure-Directing Agents. *Journal of the American Chemical Society*, 141(51):20155–20165, December 2019.

[87] Michele L. Sarazen, Eric Doskocil, and Enrique Iglesia. Effects of Void Environment and Acid Strength on Alkene Oligomerization Selectivity. *ACS Catal.*, 6(10):7059–7070, October 2016.

[88] Rachit Khare, Dean Millar, and Aditya Bhan. A mechanistic basis for the effects of crystallite size on light olefin selectivity in methanol-to-hydrocarbons conversion on MFI. *Journal of Catalysis*, 321:23–31, January 2015.

[89] Rachit Khare, Zhaohui Liu, Yu Han, and Aditya Bhan. A mechanistic basis for the effect of aluminum content on ethene selectivity in methanol-to-hydrocarbons conversion on HZSM-5. *Journal of Catalysis*, 348:300–305, April 2017.

[90] Wha Jung Kim, Myung Churl Lee, and David T Hayhurst. Synthesis of ZSM-5 at low temperature and atmospheric pressure in a pilot-scale batch reactor. *Microporous and Mesoporous Materials*, 26(1):133–141, December 1998.

[91] T. Armaroli, L. J. Simon, M. Digne, T. Montanari, M. Bevilacqua, V. Valtchev, J. Patarin, and G. Busca. Effects of crystal size and Si/Al ratio on the surface properties of H-ZSM-5 zeolites. *Applied Catalysis A: General*, 306:78–84, June 2006.

[92] L. Shirazi, E. Jamshidi, and M. R. Ghasemi. The effect of Si/Al ratio of ZSM-5 zeolite on its morphology, acidity and crystal size. *Cryst. Res. Technol.*, 43(12):1300–1306, December 2008.

[93] Minkee Choi, Kyungsu Na, Jeongnam Kim, Yasuhiro Sakamoto, Osamu Terasaki, and Ryong Ryoo. Stable single-unit-cell nanosheets of zeolite MFI as active and long-lived catalysts. *Nature*, 461(7261):246–249, September 2009.

[94] Alexandra I. Lupulescu and Jeffrey D. Rimer. Tailoring Silicalite-1 Crystal Morphology with Molecular Modifiers. *Angew. Chem. Int. Ed.*, 51(14):3345–3349, April 2012.

[95] Jeffrey D. Rimer. Zeolite compositions and methods for tailoring zeolite crystal habits with growth modifiers, August 2012. International Classification C01B39/02, C01B39/50, C01B39/54, C07C211/63; Cooperative Classification C01B39/40, C01B37/08, C01B39/32, C01B39/265, C01B39/445, C01B37/02, C01B39/54, Y10T428/24273.

[96] P. Bodart, J. B. Nagy, Z. Gabelica, and E. G. Derouane. Competitive lattice incorporation of aluminium and boron during crystallization of ZSM-5 type zeolites. *Applied Catalysis*, 24(1):315–318, July 1986.

[97] R. A Schoonheydt and J. B Uytterhoeven. Influence of temperature on the OH-band intensity in the infrared spectra of decationated zeolites X and Y. *Journal of Catalysis*, 19(1):55–63, October 1970.

[98] P. A. Jacobs and J. B. Uytterhoeven. Assignment of the hydroxyl bands in the infrared spectra of zeolites X and Y. Part 1.—Na—H zeolites. *Journal of the Chemical Society, Faraday Transactions 1: Physical Chemistry in Condensed Phases*, 69(0):359–372, 1973.

[99] Ryota Osuga, Toshiyuki Yokoi, Kazuki Doitomi, Hajime Hirao, and Junko N. Kondo. Infrared Investigation of Dynamic Behavior of Brønsted Acid Sites on Zeolites at High Temperatures. *The Journal of Physical Chemistry C*, 121(45):25411–25420, November 2017.

[100] Amber Janda and Alexis T. Bell. Effects of Si/Al Ratio on the Distribution of Framework Al and on the Rates of Alkane Monomolecular Cracking and Dehydrogenation in H-MFI. *J. Am. Chem. Soc.*, 135(51):19193–19207, December 2013.

[101] Thomas F. Narbeshuber, Axel Brait, Kulathuyier Seshan, and Johannes A. Lercher. Dehydrogenation of Light Alkanes over Zeolites. *Journal of Catalysis*, 172(1):127–136, November 1997.

[102] Bin Xu, Carsten Sievers, Suk Bong Hong, Roel Prins, and Jeroen A. van Bokhoven. Catalytic activity of Brønsted acid sites in zeolites: Intrinsic activity, rate-limiting step, and influence of the local structure of the acid sites. *Journal of Catalysis*, 244(2):163–168, December 2006.

[103] J. A. van Bokhoven and B. Xu. Towards predicting catalytic performances of zeolites. In Ruren Xu, Zi Gao, Jiesheng Chen, and Wenfu Yan, editors, *Studies in Surface Science and Catalysis*, volume 170 of *From Zeolites to Porous MOF Materials - The 40th Anniversary of International Zeolite Conference*, pages 1167–1173. Elsevier, January 2007.

[104] Dongxia Liu, Aditya Bhan, Michael Tsapatsis, and Saleh Al Hashimi. Catalytic Behavior of Brønsted Acid Sites in MWW and MFI Zeolites with Dual Meso- and Microporosity. *ACS Catalysis*, 1(1):7–17, January 2011.

[105] Haoguang Li, Shashikant A. Kadam, Alexandre Vimont, Richard F. Wormsbecher, and Arnaud Travert. Monomolecular Cracking Rates of Light Alkanes over Zeolites Determined by IR Operando Spectroscopy. *ACS Catalysis*, 6(7):4536–4548, July 2016.

[106] C. H. Collett and J. McGregor. Things go better with coke: the beneficial role of carbonaceous deposits in heterogeneous catalysis. *Catalysis Science & Technology*, 6(2):363–378, 2016.

[107] Wentian Gu and Gleb Yushin. Review of nanostructured carbon materials for electrochemical capacitor applications: advantages and limitations of activated carbon, carbide-derived carbon, zeolite-templated carbon, carbon aerogels, carbon nanotubes, onion-like carbon, and graphene. *WIREs Energy and Environment*, 3(5):424–473, 2014.

[108] Stefano Zanardi, Alberto Alberti, Roberto Millini, Giuseppe Bellussi, and Giovanni Perego. Structural characterization of borosilicates synthesized in the presence of ethylenediamine. In R. Aiello, G. Giordano, and F. Testa, editors, *Studies in Surface Science and Catalysis*, volume 142 of *Impact of Zeolites and other Porous Materials on the new Technologies at the Beginning of the New Millennium*, pages 1923–1930. Elsevier, January 2002.

[109] Giovanni Perego, Giuseppe Bellussi, Roberto Millini, Alberto Alberti, and Stefano Zanardi. B-containing molecular sieves crystallized in the presence of ethylenediamine. Part II: crystal structure of as-synthesized B-MFI. *Microporous and Mesoporous Materials*, 58(3):213–223, March 2003.

[110] Benjamin E. R. Snyder, Max L. Bols, Robert A. Schoonheydt, Bert F. Sels, and Edward I. Solomon. Iron and Copper Active Sites in Zeolites and Their Correlation to Metalloenzymes. *Chemical Reviews*, 118(5):2718–2768, March 2018.

[111] M. M. Mestdagh, W. E. Stone, and J. J. Fripiat. Proton mobility in solids. IV. Study of proton motion in the decationated Y zeolite by nuclear magnetic resonance. *The Journal of Physical Chemistry*, 76(8):1220–1226, April 1972.

[112] Priit Sarv, Tiit Tuherm, Endel Lippmaa, Kari Keskinen, and Andrew Root. Mobility of the Acidic Proton in Broensted Sites of H-Y, H-Mordenite, and H-ZSM-5 Zeolites, Studied by High-Temperature 1h MAS NMR. *The Journal of Physical Chemistry*, 99(38):13763–13768, September 1995.

[113] Christopher Paolucci, Atish A. Parekh, Ishant Khurana, John R. Di Iorio, Hui Li, Jonatan D. Albarracin Caballero, Arthur J. Shih, Trunojoyo Anggara, W. Nicholas Delgass, Jeffrey T. Miller, Fabio H. Ribeiro, Rajamani Gounder, and William F. Schneider. Catalysis in a Cage: Condition-Dependent Speciation and Dynamics of Exchanged Cu Cations in SSZ-13 Zeolites. *Journal of the American Chemical Society*, 138(18):6028–6048, May 2016.

[114] Jiří Dědeček and Blanka Wichterlová. Co2+ Ion Siting in Pentasil-Containing Zeolites. I. Co2+ Ion Sites and Their Occupation in Mordenite. A VisNIR Diffuse Reflectance Spectroscopy Study. *The Journal of Physical Chemistry B*, 103(9):1462–1476, March 1999.

[115] J. Dědeček, D. Kaucký, and B. Wichterlová. Co2+ ion siting in pentasil-containing zeolites, part 3.: Co2+ ion sites and their occupation in ZSM-5: a VIS diffuse reflectance spectroscopy study. *Microporous and Mesoporous Materials*, 35-36:483–494, April 2000.

[116] Rajamani Gounder, Andrew J. Jones, Robert T. Carr, and Enrique Iglesia. Solvation and acid strength effects on catalysis by faujasite zeolites. *Journal of Catalysis*, 286:214–223, February 2012.

[117] Sichi Li, Hui Li, Rajamani Gounder, Anthony Debellis, Imke B. Müller, Subramanian Prasad, Ahmad Moini, and William F. Schneider. First-Principles Comparison of Proton and Divalent Copper Cation Exchange Energy Landscapes in SSZ-13 Zeolite. *The Journal of Physical Chemistry C*, 122(41):23564–23573, October 2018.

[118] Jiří Dědeček, Stepan Sklenak, Chengbin Li, Fei Gao, Jiří Brus, Qingjun Zhu, and Takashi Tatsumi. Effect of Al/Si Substitutions and Silanol Nests on the Local Geometry of Si and Al Framework Sites in Silicone-Rich Zeolites: A Combined High Resolution 27al and 29si NMR and Density Functional Theory/Molecular Mechanics Study. *The Journal of Physical Chemistry C*, 113(32):14454–14466, August 2009.

[119] Einar A. Eilertsen, Bjørnar Arstad, Stian Svelle, and Karl P. Lillerud. Single parameter synthesis of high silica CHA zeolites from fluoride media. *Microporous and Mesoporous Materials*, 153:94–99, May 2012.

[120] Thomas Robert Hughes and Harry M. White. A study of the surface structure of decationized Y zeolite by quantitative infrared spectroscopy. *The Journal of Physical Chemistry*, 71(7):2192–2201, June 1967.

[121] Peter A. Jacobs and Wilfried J. Mortier. An attempt to rationalize stretching frequencies of lattice hydroxyl groups in hydrogen-zeolites. *Zeolites*, 2(3):226–230, July 1982.

[122] C. A. Emeis. Determination of Integrated Molar Extinction Coefficients for Infrared Absorption Bands of Pyridine Adsorbed on Solid Acid Catalysts. *Journal of Catalysis*, 141(2):347–354, June 1993.

[123] Marina A. Makarova, Vladimir L. Zholobenko, Khalid M. Al-Ghefaili, Nicholas E. Thompson, John Dewing, and John Dwyer. Brønsted acid sites in zeolites. FTIR study of molecular hydrogen as a probe for acidity testing. *Journal of the Chemical Society, Faraday Transactions*, 90(7):1047–1054, January 1994.

[124] M. A. Makarova, A. E. Wilson, B. J. van Liemt, C. M. A. M. Mesters, A. W. de Winter, and C. Williams. Quantification of Brønsted Acidity in Mordenites. *Journal of Catalysis*, 172(1):170–177, November 1997.

[125] Silvia Bordiga, Carlo Lamberti, Francesca Bonino, Arnaud Travert, and Frédéric Thibault-Starzyk. Probing zeolites by vibrational spectroscopies. *Chemical Society Reviews*, 44(20):7262–7341, October 2015.

[126] M. Maache, A. Janin, J. C. Lavalley, and E. Benazzi. FT infrared study of Brønsted acidity of H-mordenites: Heterogeneity and effect of dealumination. *Zeolites*, 15(6):507–516, August 1995.

[127] Hiroshi Tsubomura. Nature of the Hydrogen Bond. III. The Measurement of the Infrared Absorption Intensities of Free and Hydrogen-Bonded OH Bands. Theory of the Increase of the Intensity Due to the Hydrogen Bond. *The Journal of Chemical Physics*, 24(5):927–931, May 1956.

[128] Bijyalaxmi Athokpam, Sai G. Ramesh, and Ross H. McKenzie. Effect of hydrogen bonding on the infrared absorption intensity of OH stretch vibrations. *Chemical Physics*, 488-489:43–54, May 2017.

[129] John R. Di Iorio, Shane A. Bates, Anuj A. Verma, W. Nicholas Delgass, Fabio H. Ribeiro, Jeffrey T. Miller, and Rajamani Gounder. The Dynamic Nature of Brønsted Acid Sites in Cu–Zeolites During NOx Selective Catalytic Reduction: Quantification by Gas-Phase Ammonia Titration. *Top Catal*, 58(7):424–434, May 2015.

[130] Viktor J. Cybulskis, James W. Harris, Yury Zvinevich, Fabio H. Ribeiro, and Rajamani Gounder. A transmission infrared cell design for temperature-controlled adsorption and reactivity studies on heterogeneous catalysts. *Review of Scientific Instruments*, 87(10):103101, October 2016.

[131] John P. Perdew, Kieron Burke, and Matthias Ernzerhof. Generalized Gradient Approximation Made Simple. *Physical Review Letters*, 77(18):3865–3868, October 1996.

[132] G. Kresse and J. Furthmüller. Efficient iterative schemes for ab initio total-energy calculations using a plane-wave basis set. *Physical Review B*, 54(16):11169–11186, October 1996.

[133] G. Kresse and D. Joubert. From ultrasoft pseudopotentials to the projector augmented-wave method. *Physical Review B*, 59(3):1758–1775, January 1999.

[134] P. E. Blöchl. Projector augmented-wave method. *Physical Review B*, 50(24):17953–17979, December 1994.

[135] Baerlocher, C. and McCusker, L. B. *Database of Zeolite Structures*.

[136] Xavier Gonze and Changyol Lee. Dynamical matrices, Born effective charges, dielectric permittivity tensors, and interatomic force constants from density-functional perturbation theory. *Physical Review B*, 55(16):10355–10368, April 1997.

[137] Ask Hjorth Larsen, Jens Jørgen Mortensen, Jakob Blomqvist, Ivano E. Castelli, Rune Christensen, Marcin Du\lak, Jesper Friis, Michael N. Groves, Bjørk Hammer, Cory Hargus, Eric D. Hermes, Paul C. Jennings, Peter Bjerre Jensen, James Kermode, John R. Kitchin, Esben Leonhard Kolsbjerg, Joseph Kubal, Kristen Kaasbjerg, Steen Lysgaard, Jón Bergmann Maronsson, Tristan Maxson, Thomas Olsen, Lars Pastewka, Andrew Peterson, Carsten Rostgaard, Jakob Schiøtz, Ole Schütt, Mikkel Strange, Kristian S. Thygesen, Tejs Vegge, Lasse Vilhelmsen, Michael Walter, Zhenhua Zeng, and Karsten W. Jacobsen. The atomic simulation environment—a Python library for working with atoms. *Journal of Physics: Condensed Matter*, 29(27):273002, June 2017.

[138] L. J. Smith, A. Davidson, and A. K. Cheetham. A neutron diffraction and infrared spectroscopy study of the acid form of the aluminosilicate zeolite, chabazite (H- SSZ-13). *Catalysis Letters*, 49(3-4):143–146, December 1997.

[139] John W. Ward. The nature of active sites on zeolites: II. Temperature dependence of the infrared spectra of hydrogen Y zeolite. *Journal of Catalysis*, 9(4):396–402, December 1967.

[140] Andrew J. Jones and Enrique Iglesia. The Strength of Brønsted Acid Sites in Microporous Aluminosilicates. *ACS Catalysis*, pages 5741–5755, August 2015.

[141] Steven Nystrom, Alexander Hoffman, and David Hibbitts. Tuning Brønsted Acid Strength by Altering Site Proximity in CHA Framework Zeolites. *ACS Catalysis*, 8(9):7842–7860, September 2018.

[142] Florian Göltl, Alyssa M. Love, Sarah C. Schuenzel, Patrick Wolf, Manos Mavrikakis, and Ive Hermans. Computational description of key spectroscopic features of zeolite SSZ-13. *Physical Chemistry Chemical Physics*, 21(35):19065–19075, September 2019.

[143] M. Boudart. Turnover Rates in Heterogeneous Catalysis. *Chemical Reviews*, 95(3):661–666, May 1995.

[144] Michael Zeets, Daniel E. Resasco, and Bin Wang. Enhanced Chemical Activity and Wettability at Adjacent Brønsted Acid Sites in HZSM-5. *Catalysis Today*, March 2018.

[145] M. T. Aronson, R. J. Gorte, and W. E. Farneth. The influence of oxonium ion and carbenium ion stabilities on the Alcohol/H-ZSM-5 interaction. *Journal of Catalysis*, 98(2):434–443, April 1986.

[146] Marek Sierka, Uwe Eichler, Jerzy Datka, and Joachim Sauer. Heterogeneity of Brønsted Acidic Sites in Faujasite Type Zeolites due to Aluminum Content and Framework Structure. *The Journal of Physical Chemistry B*, 102(33):6397–6404, August 1998.

[147] Prashant Deshlahra, Robert T. Carr, and Enrique Iglesia. Ionic and Covalent Stabilization of Intermediates and Transition States in Catalysis by Solid Acids. *Journal of the American Chemical Society*, 136(43):15229–15247, October 2014.

[148] A. M. Rigby, G. J. Kramer, and R. A. van Santen. Mechanisms of Hydrocarbon Conversion in Zeolites: A Quantum Mechanical Study. *Journal of Catalysis*, 170(1):1–10, August 1997.

[149] J. Dědeček, D. Kaucký, and B. Wichterlová. Al distribution in ZSM-5 zeolites: an experimental study. *Chemical Communications*, 0(11):970–971, 2001.

[150] David Karhanek. *Self-assembled monolayers studied by density-functional theory*. phd, uniwien, wien, 2010.

[151] W. O. Haag and R. M. Dessau. In *Proceedings of the 8th International Congress on Catalysis*, page 305, Berlin, July 1984.

[152] A. Corma. Inorganic Solid Acids and Their Use in Acid-Catalyzed Hydrocarbon Reactions. *Chem. Rev.*, 95(3):559–614, May 1995.

[153] Samuel A. Tabak. Oligomerization of olefins, March 1981. U.S. Classification 585/533, 585/510; International Classification C07C11/02, B01J29/00, C07C67/00, C07C2/12, C07B61/00, C07C1/00; Cooperative Classification C07C2/12, C07C2529/70; European Classification C07C2/12.

[154] M. Guisnet, N. S. Gnep, and F. Alario. Aromatization of short chain alkanes on zeolite catalysts. *Applied Catalysis A: General*, 89(1):1–30, September 1992.

[155] B. S. Greensfelder, H. H. Voge, and G. M. Good. Catalytic and Thermal Cracking of Pure Hydrocarbons: Mechanisms of Reaction. *Industrial & Engineering Chemistry*, 41(11):2573–2584, November 1949.

[156] S. Kotrel, H. Knözinger, and B. C. Gates. The Haag–Dessau mechanism of protolytic cracking of alkanes. *Microporous and Mesoporous Materials*, 35–36:11–20, April 2000.

[157] Rajamani Gounder and Enrique Iglesia. Effects of Partial Confinement on the Specificity of Monomolecular Alkane Reactions for Acid Sites in Side Pockets of Mordenite. *Angewandte Chemie International Edition*, 49(4):808–811, January 2010.

[158] Rajamani Gounder and Enrique Iglesia. The Roles of Entropy and Enthalpy in Stabilizing Ion-Pairs at Transition States in Zeolite Acid Catalysis. *Accounts of Chemical Research*, 45(2):229–238, February 2012.

[159] B. C. Gates. Supported Metal Clusters: Synthesis, Structure, and Catalysis. *Chemical Reviews*, 95(3):511–522, May 1995.

[160] Alper Uzun and Bruce C. Gates. Dynamic Structural Changes in a Molecular Zeolite-Supported Iridium Catalyst for Ethene Hydrogenation. *Journal of the American Chemical Society*, 131(43):15887–15894, November 2009.

[161] W. A. Weber, A. Zhao, and B. C. Gates. NaY Zeolite-Supported Rhodium and Iridium Cluster Catalysts: Characterization by X-ray Absorption Spectroscopy during Propene Hydrogenation Catalysis. *Journal of Catalysis*, 182(1):13–29, February 1999.

[162] Minkee Choi, Zhijie Wu, and Enrique Iglesia. Mercaptosilane-Assisted Synthesis of Metal Clusters within Zeolites and Catalytic Consequences of Encapsulation. *Journal of the American Chemical Society*, 132(26):9129–9137, July 2010.

[163] Bi-Zeng Zhan and Enrique Iglesia. RuO2 Clusters within LTA Zeolite Cages: Consequences of Encapsulation on Catalytic Reactivity and Selectivity. *Angewandte Chemie International Edition*, 46(20):3697–3700, 2007.

[164] L. J. Simon, J. G. van Ommen, A. Jentys, and J. A. Lercher. Sulfur tolerance of Pt/mordenites for benzene hydrogenation: Do Brønsted acid sites participate in hydrogenation? *Catalysis Today*, 73(1):105–112, April 2002.

[165] Minachev, K. M., Garanin, V. I., Kharlamov, V. V., and Isakova, T. A. *Kinet. Catal.*, 13:1101, 1972.

[166] Junichi Kanai, Johan A. Martens, and Peter A. Jacobs. On the nature of the active sites for ethylene hydrogenation in metal-free zeolites. *Journal of Catalysis*, 133(2):527–543, February 1992.

[167] C. F. Heylen, P. A. Jacobs, and J. B. Uytterhoeven. Active sites in zeolites: 5. Hydrogen-deuterium equilibration over synthetic faujasites. *Journal of Catalysis*, 43(1):99–110, June 1976.

[168] Peter A. Jacobs and Jan B. Uytterhoeven. Active sites in zeolites: Part 7. Isopropanol dehydrogenation over alkali cation-exchanged X and Y zeolites. *Journal of Catalysis*, 50(1):109–114, October 1977.

[169] Ville Nieminen, Marek Sierka, Dmitry Yu. Murzin, and Joachim Sauer. Stabilities of C3–C5 alkoxide species inside H-FER zeolite: a hybrid QM/MM study. *Journal of Catalysis*, 231(2):393–404, April 2005.

[170] Khalid A. Al-majnouni, Jang Ho Yun, and Raul F. Lobo. High-Temperature Produced Catalytic Sites Selective for n-Alkane Dehydrogenation in Acid Zeolites: The Case of HZSM-5. *ChemCatChem*, 3(8):1333–1341, 2011.

[171] J. H. Yun and R. F. Lobo. Effects of temperature pretreatment on propane cracking over H-SSZ-13 zeolites. *Catalysis Science & Technology*, 5(1):264–273, December 2014.

[172] Simon J. Collins and Patrick J. O'Malley. Density functional studies of the carbonium ion species CH+5, C2h+7 and C3h+9. *Chemical Physics Letters*, 228(1):246–251, September 1994.

[173] Pierre M. Esteves, Claudio J. A. Mota, A. Ramírez-Solís, and R. Hernández-Lamoneda. Potential Energy Surface of the C3h9+ Cations. Protonated Propane. *Journal of the American Chemical Society*, 120(13):3213–3219, April 1998.

[174] Gilbert F. Froment and Kenneth B. Bischoff. *Chemical reactor analysis and design*. Wiley, 1979. Google-Books-ID: XnNdAAAAIAAJ.

[175] M Guisnet and P Magnoux. Organic chemistry of coke formation. *Applied Catalysis A: General*, 212(1):83–96, April 2001.

[176] Takashi Kyotani, Takayuki Nagai, Sanjuro Inoue, and Akira Tomita. Formation of New Type of Porous Carbon by Carbonization in Zeolite Nanochannels. *Chemistry of Materials*, 9(2):609–615, February 1997.

[177] Takashi Kyotani, Zhixin Ma, and Akira Tomita. Template synthesis of novel porous carbons using various types of zeolites. *Carbon*, 41(7):1451–1459, January 2003.

[178] Aly Moustafa Radwan, Takashi Kyotani, and Akira Tomita. Characterization of coke deposited from cracking of benzene over USY zeolite catalyst. *Applied Catalysis A: General*, 192(1):43–50, February 2000.

[179] J. Meusinger and A. Corma. Activation of Hydrogen on Zeolites: Kinetics and Mechanism of n-Heptane Cracking on H-ZSM-5 Zeolites Under High Hydrogen Pressure. *Journal of Catalysis*, 152(1):189–197, March 1995.

[180] Sukaran S. Arora, Zhichen Shi, and Aditya Bhan. Mechanistic Basis for Effects of High-Pressure H2 Cofeeds on Methanol-to-Hydrocarbons Catalysis over Zeolites. *ACS Catalysis*, 9(7):6407–6414, July 2019.

[181] S. A. Eliason and C. H. Bartholomew. Temperature-programmed reaction study of carbon transformations on iron fischer-tropsch catalysts during steady-state synthesis. In C. H. Bartholomew and G. A. Fuentes, editors, *Studies in Surface Science and Catalysis*, volume 111 of *Catalyst Deactivation*, pages 517–526. Elsevier, January 1997.

[182] Jian Xu and Calvin H. Bartholomew. Temperature-Programmed Hydrogenation (TPH) and in Situ Mössbauer Spectroscopy Studies of Carbonaceous Species on Silica-Supported Iron FischerTropsch Catalysts. *The Journal of Physical Chemistry B*, 109(6):2392–2403, February 2005.

[183] Wolf-Dieter Gräber and Klaus J. Hüttinger. Chemistry of methane formation in hydrogasification of aromatics. 1. Non-substituted aromatics. *Fuel*, 61(6):499–504, June 1982.

[184] Wolf-Dieter Gräber and Klaus J. Hüttinger. Chemistry of methane formation in hydrogasification of aromatics. 2. Aromatics with aliphatic groups. *Fuel*, 61(6):505–509, June 1982.

[185] Henrique S. Cerqueira, Patrick Magnoux, Dominique Martin, and Michel Guisnet. Coke formation and coke profiles during the transformation of various reactants at 450C over a USHY zeolite. *Applied Catalysis A: General*, 208(1):359–367, February 2001.

[186] Christian Nederlof, Freek Kapteijn, and Michiel Makkee. Catalysed ethylbenzene dehydrogenation in CO2 or N2—Carbon deposits as the active phase. *Applied Catalysis A: General*, 417-418:163–173, February 2012.

[187] Housseinou Ba, Giulia Tuci, Claudio Evangelisti, Matteo Ceppatelli, Lam Nguyen-Dinh, Vladimiro Dal Santo, Filippo Bossola, Jean-Mario Nhut, Andrea Rossin, Pascal Granger, Giuliano Giambastiani, and Cuong Pham-Huu. Second Youth of a Metal-Free Dehydrogenation Catalyst: When -Al2o3 Meets Coke Under Oxygen- and Steam-Free Conditions. *ACS Catalysis*, 9(10):9474–9484, October 2019.

[188] James McGregor, Zhenyu Huang, Edward P. J. Parrott, J. Axel Zeitler, K. Lien Nguyen, Jeremy M. Rawson, Albert Carley, Thomas W. Hansen, Jean-Philippe Tessonnier, Dang Sheng Su, Detre Teschner, Elaine M. Vass, Axel Knop-Gericke, R. Schlögl, and Lynn F. Gladden. Active coke: Carbonaceous materials as catalysts for alkane dehydrogenation. *Journal of Catalysis*, 269(2):329–339, February 2010.

[189] Hidefumi Amano, Satoshi Sato, Ryoji Takahashi, and Toshiaki Sodesawa. Dehydrogenation of cyclohexene over carbon deposited on alumina. *Physical Chemistry Chemical Physics*, 3(5):873–879, January 2001.

[190] Bart A. De Moor, Marie-Françoise Reyniers, Oliver C. Gobin, Johannes A. Lercher, and Guy B. Marin. Adsorption of C2C8 n-Alkanes in Zeolites. *The Journal of Physical Chemistry C*, 115(4):1204–1219, February 2011.

[191] Xiaobo Zheng and Paul Blowers. Reactivity of Alkanes on Zeolites: A Computational Study of Propane Conversion Reactions. *The Journal of Physical Chemistry A*, 109(47):10734–10741, December 2005.

[192] Rajamani Gounder and Enrique Iglesia. Catalytic hydrogenation of alkenes on acidic zeolites: Mechanistic connections to monomolecular alkane dehydrogenation reactions. *Journal of Catalysis*, 277(1):36–45, January 2011.

[193] T. F. Narbeshuber, A. Brait, K. Seshan, and J. A. Lercher. The influence of extraframework aluminum on H-FAU catalyzed cracking of light alkanes. *Applied Catalysis A: General*, 146(1):119–129, October 1996.

[194] Hirotomo Nishihara, Katsuaki Imai, Hiroyuki Itoi, Keita Nomura, Kazuyuki Takai, and Takashi Kyotani. Formation mechanism of zeolite-templated carbons. *TANSO*, 2017(280):169–174, November 2017.

[195] Mykela DeLuca, Christina Janes, and David Hibbitts. Mechanisms of Alkene and Diene Hydrogenation Reactions in H-MFI and H-CHA Zeolite Frameworks During MTO. August 2019.

[196] Michael J. Nash, Anne Marie Shough, Dustin W. Fickel, Douglas J. Doren, and Raul F. Lobo. High-Temperature Dehydrogenation of Brønsted Acid Sites in Zeolites. *Journal of the American Chemical Society*, 130(8):2460–2462, February 2008.

[197] Jang Ho Yun and Raul F. Lobo. Formation and evolution of naphthalene radical cations in thermally treated H-ZSM-5 zeolites. *Microporous and Mesoporous Materials*, 155:82–89, June 2012.

[198] Amber Janda, Bess Vlaisavljevich, Li-Chiang Lin, Shaama Mallikarjun Sharada, Berend Smit, Martin Head-Gordon, and Alexis T. Bell. Adsorption Thermodynamics and Intrinsic Activation Parameters for Monomolecular Cracking of n-Alkanes on Brønsted Acid Sites in Zeolites. *The Journal of Physical Chemistry C*, 119(19):10427–10438, May 2015.

[199] Neil K. Razdan, Anurag Kumar, and Aditya Bhan. Controlling kinetic and diffusive length-scales during absorptive hydrogen removal in methane dehydroaromatization on MoCx/H-ZSM-5 catalysts. *Journal of Catalysis*, 372:370–381, April 2019.

[200] Evan C. Wegener, Zhenwei Wu, Han-Ting Tseng, James R. Gallagher, Yang Ren, Rosa E. Diaz, Fabio H. Ribeiro, and Jeffrey T. Miller. Structure and reactivity of Pt–In intermetallic alloy nanoparticles: Highly selective catalysts for ethane dehydrogenation. *Catalysis Today*, 299:146–153, January 2018.

[201] S. D. Jackson and G. Kelly. Hydrogenation of propyne to propene over platinum/silica. *Journal of Molecular Catalysis*, 87(2):275–285, February 1994.

[202] Thomas F Degnan. The implications of the fundamentals of shape selectivity for the development of catalysts for the petroleum and petrochemical industries. *Journal of Catalysis*, 216(1):32–46, May 2003.

[203] Clarence D. Chang. Hydrocarbons from Methanol. *Catalysis Reviews*, 25(1):1–118, January 1983.

[204] Michio Sugimoto, Hisashi Katsuno, Kozo Takatsu, and Noboru Kawata. Correlation between the crystal zize and catalytic properties of ZSM-5 zeolites. *Zeolites*, 7(6):503–507, November 1987.

[205] Avelino Corma, Cristina Martínez, and Eric Doskocil. Designing MFI-based catalysts with improved catalyst life for oligomerization to high-quality liquid fuels. *Journal of Catalysis*, 300:183–196, April 2013.

[206] A. G. Popov, V. S. Pavlov, and I. I. Ivanova. Effect of crystal size on butenes oligomerization over MFI catalysts. *Journal of Catalysis*, 335:155–164, March 2016.

[207] Morten Bjørgen, Stian Svelle, Finn Joensen, Jesper Nerlov, Stein Kolboe, Francesca Bonino, Luisa Palumbo, Silvia Bordiga, and Unni Olsbye. Conversion of methanol to hydrocarbons over zeolite H-ZSM-5: On the origin of the olefinic species. *Journal of Catalysis*, 249(2):195–207, July 2007.

[208] Tingyu Liang, Jialing Chen, Zhangfeng Qin, Junfen Li, Pengfei Wang, Sen Wang, Guofu Wang, Mei Dong, Weibin Fan, and Jianguo Wang. Conversion of Methanol to Olefins over H-ZSM-5 Zeolite: Reaction Pathway Is Related to the Framework Aluminum Siting. *ACS Catal.*, 6(11):7311–7325, November 2016.

[209] Jialing Chen, Tingyu Liang, Junfen Li, Sen Wang, Zhangfeng Qin, Pengfei Wang, Lizhi Huang, Weibin Fan, and Jianguo Wang. Regulation of Framework Aluminum Siting and Acid Distribution in H-MCM-22 by Boron Incorporation and Its Effect on the Catalytic Performance in Methanol to Hydrocarbons. *ACS Catal.*, 6(4):2299–2313, April 2016.

[210] Alexandra I. Lupulescu, Manjesh Kumar, and Jeffrey D. Rimer. A Facile Strategy To Design Zeolite L Crystals with Tunable Morphology and Surface Architecture. *J. Am. Chem. Soc.*, 135(17):6608–6617, May 2013.

[211] Qingjun Zhu, Junko N. Kondo, Toshiyuki Yokoi, Tooru Setoyama, Masashi Yamaguchi, Takahiko Takewaki, Kazunari Domen, and Takashi Tatsumi. The influence of acidities of boron- and aluminium-containing MFI zeolites on co-reaction of methanol and ethene. *Phys. Chem. Chem. Phys.*, 13(32):14598–14605, August 2011.

[212] Robert T. Carr, Matthew Neurock, and Enrique Iglesia. Catalytic consequences of acid strength in the conversion of methanol to dimethyl ether. *Journal of Catalysis*, 278(1):78–93, February 2011.

[213] Cynthia T-W. Chu, Guenther H. Kuehl, Rudolph M. Lago, and Clarence D. Chang. Isomorphous substitution in zeolite frameworks: II. Catalytic properties of [B]ZSM-5. *Journal of Catalysis*, 93(2):451–458, June 1985.

[214] Miroslaw Derewinski, Francesco Di Renzo, Pierre Espiau, Francois Fajula, and Marie-Agnes Nicolle. Synthesis of Zeolite Beta in Boron-Aluminium Media. In P. A. Jacobs, N. I. Jaeger, L. Kubelková, and B. Wichterlov, editors, *Studies in Surface Science and Catalysis*, volume 69 of *Zeolite Chemistry and Catalysis*, pages 127–134. Elsevier, January 1991.

[215] David S. Shihabi, William E. Garwood, Pochen Chu, Joseph N. Miale, Rudolph M. Lago, Cynthia T-W. Chu, and Clarence D. Chang. Aluminum insertion into high-silica zeolite frameworks: II. Binder activation of high-silica ZSM-5. *Journal of Catalysis*, 93(2):471–474, June 1985.

[216] Z. Gabelica, J. B. Nagy, P. Bodart, and G. Debras. High resolution solid state mas 11b-nmr evidence of boron incorporation in tetrahedral sites of zeolites. *Chem. Lett.*, 13(7):1059–1062, July 1984.

[217] A. I. Biaglow, D. J. Parrillo, G. T. Kokotailo, and R. J. Gorte. A Study of Dealuminated Faujasites. *Journal of Catalysis*, 148(1):213–223, July 1994.

[218] Shane A. Bates, W. Nicholas Delgass, Fabio H. Ribeiro, Jeffrey T. Miller, and Rajamani Gounder. Methods for NH3 titration of Brønsted acid sites in Cu-zeolites that catalyze the selective catalytic reduction of NOx with NH3. *Journal of Catalysis*, 312:26–36, April 2014.

[219] Son-Jong Hwang, Cong-Yan Chen, and Stacey I. Zones. Boron Sites in Borosilicate Zeolites at Various Stages of Hydration Studied by Solid State NMR Spectroscopy. *J. Phys. Chem. B*, 108(48):18535–18546, December 2004.

[220] G. Coudurier and J. C. Védrine. Catalytic and Acidic Properties of Boron Pentasil Zeolites. In Y. Murakami, A. Iijima, and J. W. Ward, editors, *Studies in Surface Science and Catalysis*, volume 28 of *New Developments in Zeolite Science and Technology*, pages 643–652. Elsevier, January 1986.

[221] Moein B. Sayed, Aline Auroux, and Jacques C. Védrine. The effect of boron on ZSM-5 zeolite shape selectivity and activity: II. Coincorporation of aluminium and boron in the zeolite lattice. *Journal of Catalysis*, 116(1):1–10, March 1989.

[222] K. F. M. G. J. Scholle, A. P. M. Kentgens, W. S. Veeman, P. Frenken, and G. P. M. Van der Velden. Proton magic angle spinning nuclear magnetic resonance and temperature programmed desorption studies of ammonia on the acidity of the framework hydroxyl groups in the zeolite H-ZSM-5 and in H-boralite. *J. Phys. Chem.*, 88(1):5–8, January 1984.

[223] Xu, W. Q., Suib, S. L., and O'Young, C. L. Studies of Acidic Sites on Boralites by Temperature-Programmed Desorption (TPD) of NH3, C2h4, and 1-C4h8. *Journal of Catalysis*, 144(1):285–295, November 1993.

[224] Raymond J. Gorte. Design parameters for temperature programmed desorption from porous catalysts. *Journal of Catalysis*, 75(1):164–174, May 1982.

[225] R. A. Demmin and R. J. Gorte. Design parameters for temperature-programmed desorption from a packed bed. *Journal of Catalysis*, 90(1):32–39, November 1984.

[226] T. J. Gricus Kofke, R. J. Gorte, and G. T. Kokotailo. Stoichiometric adsorption complexes in [B]- and [Fe]-ZSM-5 zeolites. *Journal of Catalysis*, 116(1):252–262, March 1989.

[227] D. J. Parrillo, A. T. Adamo, G. T. Kokotailo, and R. J. Gorte. Amine adsorption in H-ZSM-5. *Applied Catalysis*, 67(1):107–118, January 1990.

[228] G. L. Woolery, G. H. Kuehl, H. C. Timken, A. W. Chester, and J. C. Vartuli. On the nature of framework Brønsted and Lewis acid sites in ZSM-5. *Zeolites*, 19(4):288–296, October 1997.

[229] W. S. Borghard, P. T. Reischman, and E. W. Sheppard. Argon Sorption in ZSM-5. *Journal of Catalysis*, 139(1):19–23, January 1993.

[230] W. S. Borghard, E. W. Sheppard, and H. J. Schoennagel. An automated, high precision unit for low-pressure physisorption. *Review of Scientific Instruments*, 62(11):2801–2809, November 1991.

[231] Andrzej Cichocki, Jadwiga Parasiewicz-Kaczmarska, Marek Michalik, and Malgorzata Buś. Synthesis and characterization of boralites with the MFI structure. *Zeolites*, 10(6):577–582, July 1990.

[232] G. Scott, R. W. Thompson, A. G. Dixon, and A. Sacco. The role of triethanolamine in zeolite crystallization. *Zeolites*, 10(1):44–50, January 1990.

[233] M. Morris, A. Sacco, A. G. Dixon, and R. W. Thompson. The role of an aluminum-tertiary alkanolamine chelate in the synthesis of large crytal zeolite NaA. *Zeolites*, 11(2):178–183, February 1991.

[234] M. Morris, A. G. Dixon, A. Sacco, and R. W. Thompson. Investigations on the relative effectiveness of some tertiary alkanolamines in the synthesis of large-crystal zeolite NaA. *Zeolites*, 13(2):113–121, February 1993.

[235] H. Gies and R. P. Gunawardane. One-step synthesis, properties and crystal structure of aluminium-free ferrierite. *Zeolites*, 7(5):442–445, September 1987.

[236] Giovanni Perego, Giuseppe Bellussi, Roberto Millini, Alberto Alberti, and Stefano Zanardi. B-containing molecular sieves crystallized in the presence of ethylenediamine. Part I: crystal structure of as-synthesized B-FER. *Microporous and Mesoporous Materials*, 56(2):193–202, November 2002.

[237] Reza Karimi, Behruz Bayati, Nanzanin Charchi Aghdam, Mahbobeh Ejtemaee, and Ali Akbar Babaluo. Studies of the effect of synthesis parameters on ZSM-5 nanocrystalline material during template-hydrothermal synthesis in the presence of chelating agent. *Powder Technology*, 229(Supplement C):229–236, October 2012.

[238] Andrew J. Jones and Enrique Iglesia. Kinetic, Spectroscopic, and Theoretical Assessment of Associative and Dissociative Methanol Dehydration Routes in Zeolites. *Angew. Chem.*, 126(45):12373–12377, November 2014.

[239] Arian Ghorbanpour, Jeffrey D. Rimer, and Lars C. Grabow. Computational Assessment of the Dominant Factors Governing the Mechanism of Methanol Dehydration over H-ZSM-5 with Heterogeneous Aluminum Distribution. *ACS Catal.*, 6(4):2287–2298, April 2016.

[240] Andrew J. Jones, Stacey I. Zones, and Enrique Iglesia. Implications of Transition State Confinement within Small Voids for Acid Catalysis. *J. Phys. Chem. C*, 118(31):17787–17800, August 2014.

[241] P. B. Weisz and C. D. Prater. Interpretation of Measurements in Experimental Catalysis. In W. G. Frankenburg, V. I. Komarewsky, and E. K. Rideal, editors, *Advances in Catalysis*, volume 6, pages 143–196. Academic Press, January 1954.

[242] Michel Guisnet, Luís Costa, and Fernando Ramôa Ribeiro. Prevention of zeolite deactivation by coking. *Journal of Molecular Catalysis A: Chemical*, 305(1):69–83, June 2009.

[243] C. S. Cundy, B. M. Lowe, and D. M. Sinclair. Crystallisation of zeolitic molecular sieves: direct measurements of the growth behaviour of single crystals as a function of synthesis conditions. *Faraday Discussions*, 95(0):235–252, 1993.

[244] A. E. Persson, B. J. Schoeman, J. Sterte, and J. E. Otterstedt. Synthesis of stable suspensions of discrete colloidal zeolite (Na, TPA)ZSM-5 crystals. *Zeolites*, 15(7):611–619, October 1995.

[245] R. de Ruiter, J. C. Jansen, and H. van Bekkum. On the incorporation mechanism of B and AI in MFI-type zeolite frameworks. *Zeolites*, 12(1):56–62, January 1992.

[246] R. P. Gunawardane, H. Gies, and B. Marler. Long-chain polyamines and amine—boric acid pairs as templates for the synthesis of porous tectosilicates. *Zeolites*, 8(2):127–131, March 1988.

[247] Philip M. Kester, Jeffrey T. Miller, and Rajamani Gounder. Ammonia Titration Methods To Quantify Brønsted Acid Sites in Zeolites Substituted with Aluminum and Boron Heteroatoms. *Ind. Eng. Chem. Res.*, 57(19):6673–6683, May 2018.

[248] Qiwei Qiao, Rijie Wang, Minglei Gou, and Xiaoxia Yang. Catalytic performance of boron and aluminium incorporated ZSM-5 zeolites for isomerization of styrene oxide to phenylacetaldehyde. *Microporous and Mesoporous Materials*, 195:250–257, September 2014.

[249] K. F. M. G. J. Scholle and W. S. Veeman. The influence of hydration on the coordination state of boron in H-Boralite studied by 11b magic angle spinning n.m.r. *Zeolites*, 5(2):118–122, March 1985.

[250] Hubert Koller, Christian Fild, and Raul F. Lobo. Variable anchoring of boron in zeolite beta. *Microporous and Mesoporous Materials*, 79(1):215–224, April 2005.

[251] Jiří Dědeček, Dalibor Kaucký, Blanka Wichterlová, and Olga Gonsiorová. Co 2+ ions as probes of Al distribution in the framework of zeolites . ZSM-5 study. *Physical Chemistry Chemical Physics*, 4(21):5406–5413, 2002.

[252] Chengeng Li, Alejandro Vidal-Moya, Pablo J. Miguel, Jiri Dedecek, Mercedes Boronat, and Avelino Corma. Selective Introduction of Acid Sites in Different Confined Positions in ZSM-5 and Its Catalytic Implications. *ACS Catal.*, 8(8):7688–7697, August 2018.

[253] János B. Nagy, Zélimir Gabelica, and Eric G. Derouane. Position and configuration of the guest organic molecules within the framework of the ZSM-5 and ZSM-11 zeolites. *Zeolites*, 3(1):43–49, January 1983.

[254] U. Cornaro and B. W. Wojciechowski. The catalytic effect of boron substitution in ZSM-5 type zeolites. *Journal of Catalysis*, 120(1):182–191, November 1989.

[255] Sen Wang, Pengfei Wang, Zhangfeng Qin, Yanyan Chen, Mei Dong, Junfen Li, Kan Zhang, Ping Liu, Jianguo Wang, and Weibin Fan. Relation of Catalytic Performance to the Aluminum Siting of Acidic Zeolites in the Conversion of Methanol to Olefins, Viewed via a Comparison between ZSM-5 and ZSM-11. *ACS Catal.*, 8(6):5485–5505, June 2018.

[256] Martyn C. R. Symons. Water structure and reactivity. *Acc. Chem. Res.*, 14(6):179–187, June 1981.

[257] R. de Ruiter, K. Famine, A. P. M. Kentgens, J. C. Jansen, and H. van Bekkum. Synthesis of molecular sieve [B]-BEA and modification of the boron site. *Zeolites*, 13(8):611–621, November 1993.

[258] Aseem Chawla, Rui Li, Rishabh Jain, R. John Clark, James G. Sutjianto, Jeremy C. Palmer, and Jeffrey D. Rimer. Cooperative effects of inorganic and organic structure-directing agents in ZSM-5 crystallization. *Mol. Syst. Des. Eng.*, 3(1):159–170, February 2018.

[259] Flaviano Testa, Rosaria Chiappetta, Fortunato Crea, Rosario Aiello, Antonio Fonseca, and Janos B. Nagy. Synthesis of borosilicalite-1 with high boron content from fluoride-containing media. *Colloids and Surfaces A: Physicochemical and Engineering Aspects*, 115:223–227, August 1996.

[260] J. L. Casci and B. M. Lowe. Use of pH-measurements to monitor zeolite crystallization. *Zeolites*, 3(3):186–187, July 1983.

[261] Young Gul Hur, Philip M. Kester, Claire T. Nimlos, YoonRae Cho, Jeffrey T. Miller, and Rajamani Gounder. Influence of Tetrapropylammonium and Ethylenediamine Structure-Directing Agents on the Framework Al Distribution in B–Al–MFI Zeolites. *Industrial & Engineering Chemistry Research*, 58(27):11849–11860, July 2019.

[262] Joseph E. Sarneski, Henry L. Surprenant, Frederick K. Molen, and Charles N. Reilley. Chemical shifts and protonation shifts in carbon-13 nuclear magnetic resonance studies of aqueous amines. *Analytical Chemistry*, 47(13):2116–2124, November 1975.

[263] Barrie M. Lowe. An equilibrium model for the crystallization of high silica zeolites. *Zeolites*, 3(4):300–305, October 1983.

[264] Edwin N. Givens, Charles J. Plank, and Edward J. Rosinski. Converting low molecular weight olefins over zeolites, June 1976.

[265] Richard J. Quann, Larry A. Green, Samuel A. Tabak, and Frederick J. Krambeck. Chemistry of olefin oligomerization over ZSM-5 catalyst. *Industrial & Engineering Chemistry Research*, 27(4):565–570, April 1988.

A. EFFECTS OF HETEROATOMS AND ORGANIC STRUCTURE DIRECTING AGENTS ON ACTIVE SITE AND CRYSTALLITE PROPERTIES OF B-AL-MFI ZEOLITES

A.1 Introduction

In Chapter 4, B-Al-MFI zeolites were crystallized with tetra-*n*-propylammonium (TPA^+) and ethylenediamine (EDA) as cooperative organic structure directing agents (SDAs). MFI zeolite crystallite size (0.3-10 μm) and bulk Al composition (Si/Al = 74-153) were independently varied via the quantity of B heteroatoms added to synthesis solutions (Si/B = 2.6-13), circumventing heuristic trends that smaller MFI crystallites form in more Al-dense synthesis solutions [90–92], although the total amount of B incorporated into crystalline products was similar from these solutions (Si/B = 30-35). Selective titration methods with NH_3 were developed to distinguish between Brønsted acidic protons originating from B and Al heteroatoms, because the former are weaker acids (~70 kJ mol^{-1} higher deprotonation energies [33]), rendering them catalytically inconsequential in the presence of protons originating from the latter [213]. Validation of these site-counting methods was provided by zero-order methanol dehydration rate constants (415 K, per H^+_{Al}) on B-Al-MFI zeolites that were similar to those measured on Al-MFI zeolites under the same conditions [33,79]. First-order methanol dehydration rate constants (415 K, per H^+_{Al}) were lower than those typically measured on Al-MFI zeolites, suggesting that Al heteroatoms were preferentially sited in larger channel intersections (~0.7 nm) over channel voids (~0.55 nm), providing evidence that TPA^+/EDA mixtures and/or the presence of B heteroatoms influenced the siting of Al heteroatoms in crystallographically-distinct T-sites.

Chapter 5 used similar synthetic methods to those in Chapter 4, while also crystallizing MFI zeolites using only TPA^+ as the organic SDA. The resulting suite of

B-Al-MFI zeolites contained similar bulk Al densities (Si/Al $\sim$ 50) and varying B contents (Si/B = 26-∞) when made with only TPA$^+$ or from TPA$^+$/EDA mixtures. Co^{2+} ion-exchange procedures that were not uniform among independent reports in the literature [100, 115, 251, 252] were validated with ion-exchange isotherm measurements, site titration protocols were used to confirm the 2:1 removal of monovalent cations for each Co^{2+} site, and UV-visible spectroscopy to show the absence of CoO$_x$ features. B-Al-MFI zeolites crystallized with only TPA$^+$ contained a non-zero percentage of Al in paired configurations (20-40% Al in pairs), consistent with MFI zeolites with similar composition made with TPA$^+$ [77], while those made with TPA$^+$/EDA mixtures contained predominantly isolated Al (<5% Al in pairs). These results were independent of B content in synthesis solutions or crystalline solids, suggesting that EDA was responsible for isolating Al heteroatoms in MFI frameworks. Elemental analysis of crystalline products showed that B-Al-MFI zeolites crystallized with only TPA$^+$ contained four TPA$^+$ molecules per unit cell (96 T-atoms), corresponding to one per channel intersection and consistent with its maximum occlusion in MFI void spaces [60]. However, synthesis mixtures for B-Al-MFI zeolites with TPA$^+$/EDA mixtures had TPA$^+$/Si ratios of 0.02, therefore only supplying half of the TPA$^+$ molecules (per Si) required for maximum packing density within MFI void spaces. Only two TPA$^+$ molecules per unit cell were occluded in crystalline products, consistent with the limited amount of TPA$^+$ supplied to synthesis solutions. Two EDA molecules were occluded per unit cell in the absence of B, and increased to five per unit cell in a 1:2 stoichiometry with the addition of B heteroatoms, consistent with a boron-EDA complex previously observed in MFI syntheses with B and EDA [109, 246]. These results are reminiscent of those for MWW synthesis reported by Zones and co-workers, where structure-specific adamantyl SDAs were preferentially incorporated over non-specific amines when insufficient quantities of the adamantyl cations were supplied for complete filling of extracrystalline space [81, 82]. In case of B-Al-MFI zeolites, the quantity of the pore-filling SDA is varied by the amount of B present in synthesis, providing more evidence for a B-EDA complex forming during synthesis. Collectively, these methods provide synthetic routes to crystallize MFI zeolites with similar bulk properties (e.g., size, morphology, composition) and different distributions of Al heteroatoms in distinct locations and proximal ensembles, or with similar siting of Al heteroatoms and different diffusion pathlengths that guest molecules must traverse to access active sites and egress to extracrystalline spaces.

Independent influence over active site and crystallite properties in B-Al-MFI zeolite compositions provides new questions about the role of synthesis parameters on B-Al-MFI nucleation and growth, and on heteroatom incorporation in distinct T-sites and configurations. The structural isolation of Al heteroatoms in MFI zeolites observed in Chapter 5 may result from decreases in cationic charge density supplied by TPA$^+$ to MFI zeolites when diluted with EDA, biasing of Al to crystallogrphically-distinct locations when SDAs adopt particular intracrystalline configurations, or from different relative rates of nucleation, growth, and dissolution during crystallization when synthesis solutions are buffered by weak base amines. Here, we probe each of these possibilities, first by synthesizing B-Al-MFI zeolites with a variety of TPA$^+$/Si ratios in synthesis solutions (0.01-0.13) to crystallize zeolites with different amounts of occluded TPA$^+$ but similar bulk Al densities. ^{1}H-^{13}C cross-polarized magic angle spinning nuclear magnetic resonance (CP MAS NMR) spectroscopy is used to determine the conformations of TPA$^+$ and ethylenediamine occluded in B-Al-MFI zeolites, and time-resolved synthesis studies provide evidence that the pH of solutions containing EDA are constant during crystallization, unlike typical conditions where pH increases during crystallization as hydroxide ions are liberated into solution as silicates condense [260]. Preliminary results presented here suggest that a number of these phenomena are responsible for Al isolation in MFI zeolites crystallized with EDA and proposes additional experiments to further clarify how active site and crystallite properties depend on individual synthetic variables.

A.2 Experimental Methods

A.2.1 Synthesis of B-Al-MFI zeolites

Synthetic methods to crystallize B-Al-MFI zeolites were adapted from those reported in Chapters 4 and 5, as performed by Kester and co-workers [247,261]. TPAOH (40 wt%, Alfa Aesar) was diluted in deionized water (18.2 MΩ), followed by the addition of $Al(OH)_3$ (98 wt%, SPI Pharma) in a perfluoroalkoxy alkane (PFA) jar. In a separate PFA jar, ethylenediamine (99.5 wt%, Sigma-Aldrich) was diluted in deionized water (18.2 MΩ), followed by the addition of H_3BO_3 (99.5 wt%, Sigma-Aldrich), and each solution was stirred for 15 min under ambient conditions. These mixtures were then combined and stirred for an additional 15 min under ambient conditions, followed by addition of colloidal silica (Ludox AS-40, 40 wt%, Sigma) and stirring for 2 h under ambient conditions. The final solution compositions were 1 SiO_2/ x TPAOH/ 0.312-x EDA/ a H_3BO/ b Al_2O_3/ H_2O. Values of x, a, and b ranged from 0.01-0.13, 0-0.4, and 0.007-0.021, respectively. Solutions were then added to Teflon-lined stainless-steel autoclaves (Parr) and placed in a forced convection oven (Yamato DKN-402C) at 448 K under rotation at 40 rpm for 24-120 h. Samples in this work are denoted B-Al-MFI (a, b), where a is the Si/B molar ratio and b is the Si/Al molar ratio in synthesis solutions.

Samples were removed from convection ovens and washed in deionized water (18.2 MΩ) or 50/50 mixtures (by mass) of deionized water and acetone (>99.5 wt%, Sigma-Aldrich) in alternating washes (30 cm^3 (g solid)$^{-1}$ per wash) until the pH of the supernatant solution was constant. Solids were separated by centrifugation, dried in stagnant air at 373 K for 24, then treated in flowing dry air (1.67 cm^3 s^{-1} (g solid)$^{-1}$, UHP, 99.999%, Indiana Oxygen) to 854 K (0.0167 K s^{-1}) and held for 10 h in a muffle furnace (Naberther L/E 611 with a P300 controller) to remove organic structure directing agents from zeolite pores. NH_4^+, Na^+, and Co^{2+} ion-exchange procedures and additional thermal treatments were performed as reported in Chapter 5.

A.2.2 Physiochemical characterization of B-Al-MFI zeolites

Powder X-ray diffraction (XRD), micropore volume calculations from N_2 adsorption isotherms, and NH_3 titration methods of H^+_{Al} sites were performed as reported in Chapters 4 and 5. Elemental analysis was performed with inductively coupled plasma-optical emission spectrometry (ICP-OES) using a Thermo Scientific iCAP 7000 Plus Series. Zeolite samples (∼0.02g) were dissolved in hydrofluoric (HF) acid (∼2 g; 48 wt%, Alfa Aesar) for 3 days at 293 K. Deionized water (∼50 g, 18.2 MΩ) was then added, followed by ∼1.4 g of a 70 wt% HNO_3 solution (Sigma-Aldrich). Samples were then analyzed, and elemental compositions were calculated from calibration data collected from known standards. ^{1}H-^{13}C cross-polarized magic angle spinning nuclear magnetic resonance (CP MAS NMR) experiments were performed on a Chemagnetics CMX400 (Purdue Interdepartmental NMR Facility).

A.3 Results and Discussion

A.3.1 Summary of B-Al-MFI zeolite compositions

A series of B-Al-MFI zeolites were synthesized with different Si/Al (24-72), Si/B (2.5-∞), and TPA^+/Si ratios (0.01-0.13), and with different EDA compositions such that the SDA/Si ratio was 0.31. Tables A.1-A.3 show physiochemical properties of B-Al-MFI zeolites synthesized from solutions with Si/Al ratios of 50, 24, and 72, respectively, and XRD patterns and N_2 adsorption isotherms are shown in Figures A.1-A.3, respectively.

In all cases, crystalline B-Al-MFI products had similar Si/Al ratios to those found in synthesis solutions, consistent with previous findings for B-Al-MFI zeolites in Chapters 4 and 5. B-Al-MFI (2.5, 50) zeolites synthesized with TPA^+/Si ratios of 0.01 contained <5% of Al in paired configurations (Table A.1), consistent with previous findings for samples made with TPA^+/Si ratios of 0.02 (Chapter 5). However, B-Al-MFI (2.5, 50) synthesized with TPA^+/Si ratios of 0.08 contained 14% of Al in pairs, higher than MFI zeolites synthesized with TPA^+/EDA mixtures in Chapter 5 with similar Si/Al ratios. This observation is consistent with the hypothesis that Al isolation is related to the dilution of cationic charges from TPA^+, because MFI crystallized from more TPA^+-dense solutions likely contain more occluded TPA^+ cations (Chapter 5). Additional elemental analysis of Co^{2+} ion-exchange capacities and occluded organics are required to further support this hypothesis and show systematic trends in the fraction of Al pairs among MFI zeolites of similar bulk composition.

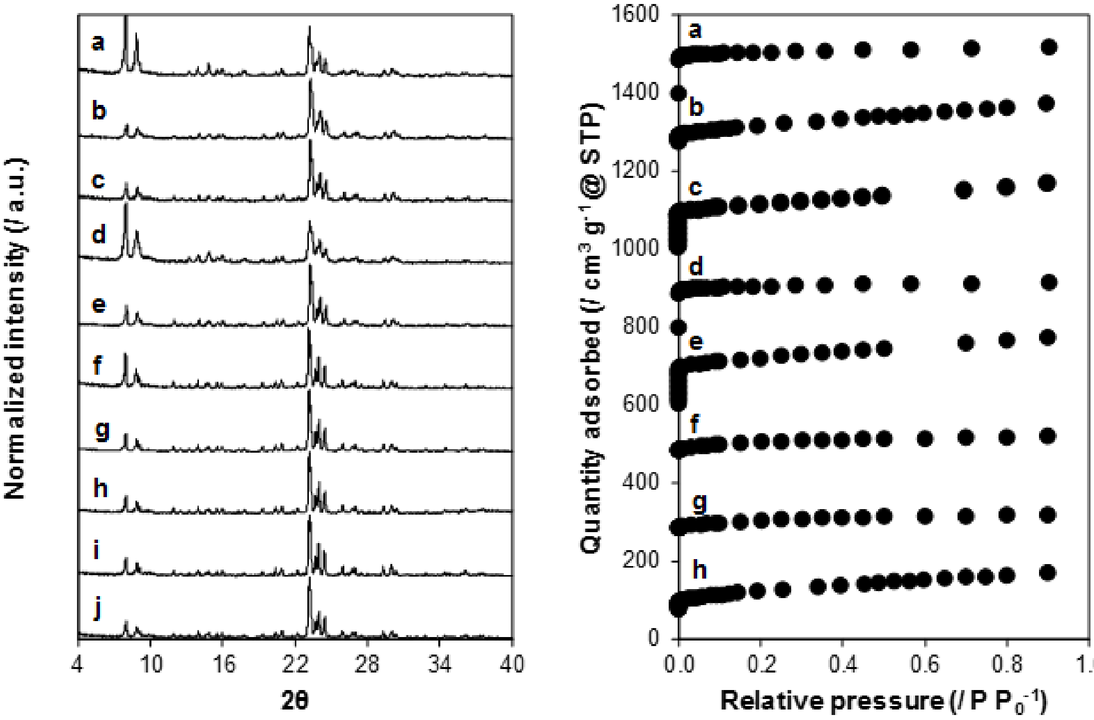

Figure A.1.: (left) XRD patterns and (right) N_2 adsorption isotherms (77 K, offset by 200 $cm^3\ g^{-1}$ for clarity) for (a) B-Al-MFI (2.5, 50)-0.01, (b) B-Al-MFI (2.5, 50)-0.04, (c) B-Al-MFI (2.5, 50)-0.06, (d) B-Al-MFI (2.5, 50)-0.08, (e) B-Al-MFI (2.5, 50)-0.13, (f) B-Al-MFI (50, 50)-0.01, (g) B-Al-MFI (50, 50)-0.08, (h) B-Al-MFI (100, 50)-0.04, (i) Al-MFI (50)-0.06, and (j) Al-MFI (50)-0.13.

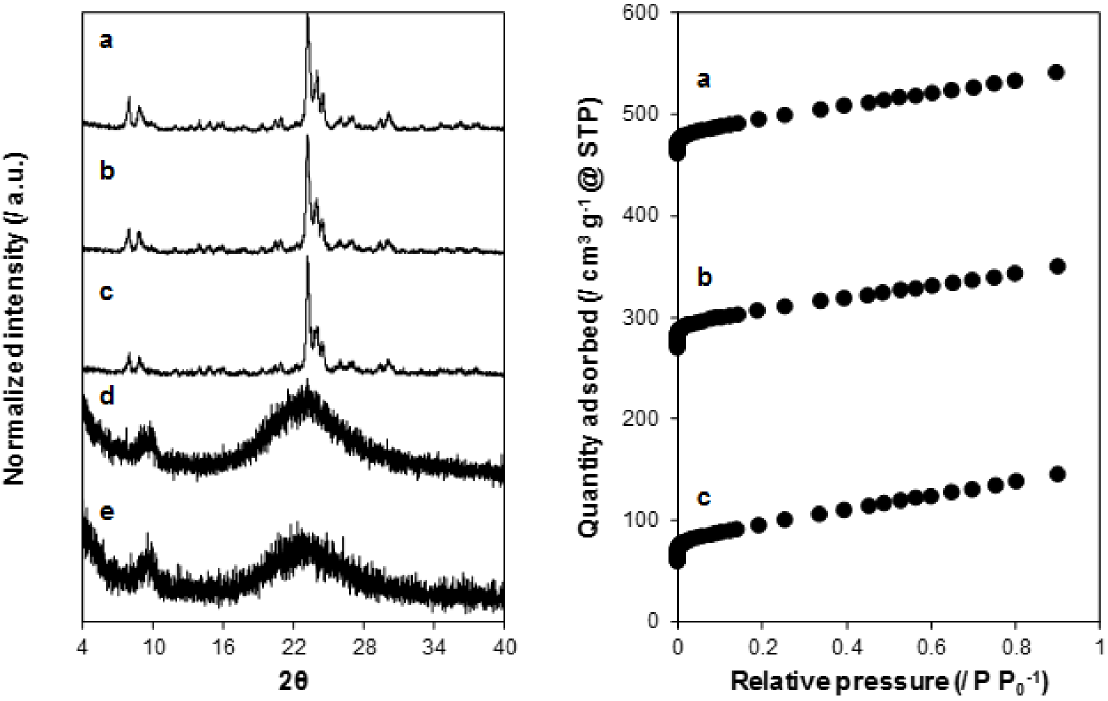

Figure A.2.: (left) XRD patterns and (right) N_2 adsorption isotherms (77 K, offset by 200 cm^3 g^{-1} for clarity) for (a) B-Al-MFI (2.5, 24)-0.02, (b) B-Al-MFI (2.5, 24)-0.04, (c) B-Al-MFI (2.5, 24)-0.08, (d) B-Al-MFI (50, 24)-0.02, and (e) B-Al-MFI (2.5, 24)-0.08.

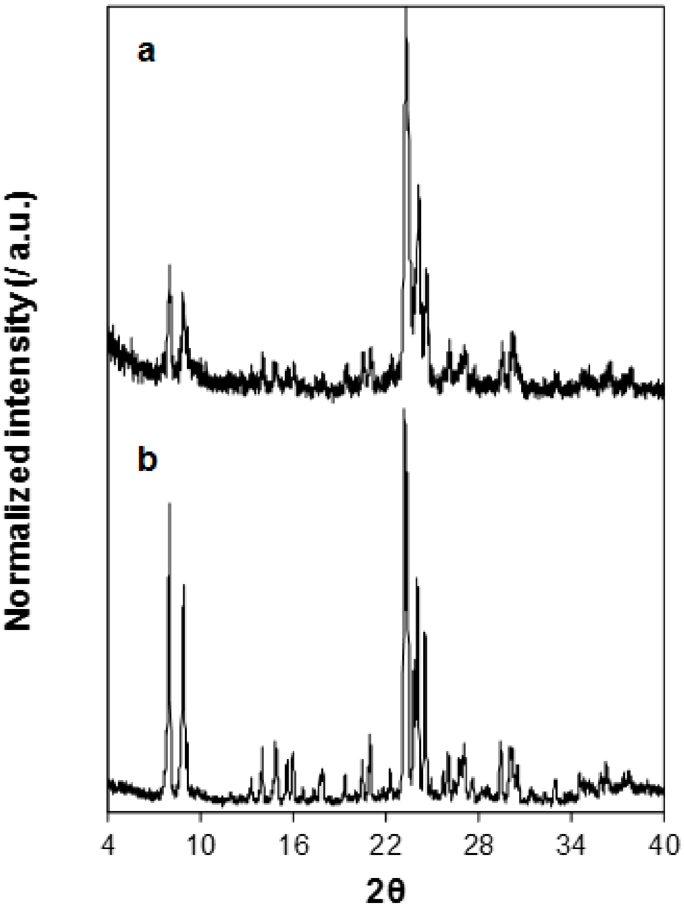

Figure A.3.: XRD patterns of (a) B-Al-MFI (2.5, 72)-0.02 and (b) B-Al-MFI (50, 72)-0.02.

Table A.1.: Physiochemical properties of B-Al-MFI (x, 50) zeolites synthesized with different TPA$^+$/Si ratios.

Sample^a	TPA$^+$/Si^b	EDA/Si^b	Phase	Si/Al$^c_{solid}$	Micropore volume^d	Co^{2+}/Al
B-Al-MFI (2.5, 50)	0.01	0.30	MFI	62	0.15	0.02
B-Al-MFI (2.5, 50)	0.04	0.27	MFI	n.m.*	0.15	n.m.*
B-Al-MFI (2.5, 50)	0.06	0.25	MFI	n.m.*	0.15	n.m.*
B-Al-MFI (2.5, 50)	0.08	0.23	MFI	60	0.15	0.07
B-Al-MFI (2.5, 50)	0.13	0.18	MFI	n.m.*	0.16	n.m.*
B-Al-MFI (50, 50)	0.01	0.30	MFI	51	0.14	0.03
B-Al-MFI (50, 50)	0.08	0.23	MFI	57	0.14	0.00
B-Al-MFI (100, 50)	0.04	0.27	MFI	n.m.*	0.16	n.m.*
Al-MFI (50)	0.06	0.25	MFI	n.m.*	n.m.*	n.m.*
Al-MFI (50)	0.13	0.18	MFI	n.m.*	n.m.*	n.m.*

[a] Samples are denoted B-Al-MFI (x, y), where x and y are the Si/B and Si/Al ratios in synthesis solutions.

[b] Composition in synthesis solution.

[c] Determined by ICP-OES. Errors are ±20%.

[d] Units are cm^3 g^{-1}. Errors are ±0.01 cm^3 g^{-1}.

*n.m.; not measured.

Table A.2.: Physiochemical properties of B-Al-MFI (x, 24) zeolites synthesized with different TPA^+/Si ratios.

Sample[a]	TPA^+/Si[b]	EDA/Si[b]	Phase	Si/Al^c_{solid}	Micropore volume[d]	Co^{2+}/Al
B-Al-MFI (2.5, 24)	0.02	0.29	MFI	29	0.12	0.07
B-Al-MFI (2.5, 24)	0.04	0.27	MFI	28	0.14	0.05
B-Al-MFI (2.5, 24)	0.08	0.23	MFI	31	0.12	0.07
B-Al-MFI (50, 24)	0.02	0.29	Amorphous	n.m.*	n.m.*	n.m.*
Al-MFI (24)	0.04	0.27	Amorphous	n.m.*	n.m.*	n.m.*
Al-MFI (24)	0.08	0.23	Amorphous	n.m.*	n.m.*	n.m.*

[a] Samples are denoted B-Al-MFI (x, y), where x and y are the Si/B and Si/Al ratios in synthesis solutions.

[b] Composition in synthesis solution.

[c] Determined by ICP-OES. Errors are ±20%.

[d] Units are $cm^3 g^{-1}$. Errors are ± 0.01 $cm^3 g^{-1}$.

*n.m.; not measured.

Table A.3.: Physiochemical properties of B-Al-MFI (x, 72) zeolites synthesized with different TPA^+/Si ratios.

Sample[a]	TPA^+/Si[b]	EDA/Si[b]	Phase	Si/Al^{c}_{solid}	Micropore volume[d]	Co^{2+}/Al
B-Al-MFI (2.5, 72)	0.02	0.29	MFI	76	n.m.*	0.05
B-Al-MFI (50, 72)	0.02	0.29	MFI	77	n.m.*	0.01

[a] Samples are denoted B-Al-MFI (x, y), where x and y are the Si/B and Si/Al ratios in synthesis solutions.

[b] Composition in synthesis solution.

[c] Determined by ICP-OES. Errors are ±20%.

[d] Units are $cm^3\ g^{-1}$. Errors are $\pm 0.01\ cm^3\ g^{-1}$.

*n.m.; not measured.

Crystallization barriers arise in more Al-dense synthesis solutions (Si/Al = 24, Table A.2) with lower B contents (Si/B >50). This Si/Al ratio corresponds to one Al per channel intersection, equal to the maximum occlusion of TPA^+ cations in MFI zeolites [60]. MFI zeolites synthesized using TPA^+ as the only organic SDA typically have Si/Al ratios greater than 24, while higher Al contents (Si/Al < 24) are attainable when other monovalent cations (e.g., Na^+) are provided to synthesis solutions [77]. Here, MFI zeolites crystallize from mixtures containing TPA^+/Al ratios less than unity, although they do not have enough cationic charge to compensate all Al atoms in solution. This may reflect lower yields (per Si) of MFI zeolites crystallized with these methods such that TPA^+/Al ratios in crystalline products are close to unity, or charge compensation provided by protonated EDA that are more prevalent at lower pH values. Figure A.4 shows the equilibrium fraction of protonated amine groups in EDA in aqueous media (298 K), which has pKa values of 10.7 and 7.6. The pH of B-Al-MFI (2.5, 24) synthesis solutions was ∼10.5, close to the pKa_1 of EDA. However, B-Al-MFI (50, 24) and Al-MFI (24) synthesis solutions had pH values of 12 and 14, respectively, suggesting that <10% were protonated in these syntheses. Therefore, protonated EDA molecules may provide cationic charge to Al heteroatoms in MFI frameworks when insufficient TPA^+ cations are available to compensate these framework anions. Additional elemental analysis and spectroscopic evidence is required to quantify the number and charge of occluded SDAs in these sample, and the implications on Al siting in distinct ensembles.

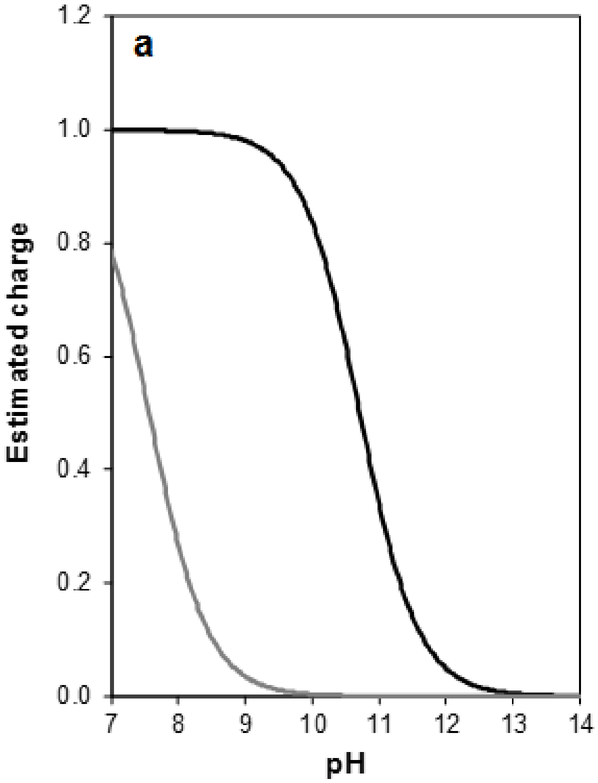

Figure A.4.: Predicted fraction of charged amine groups at first (black) and second (gray) nitrogen atom in ethylenediamine at 298 K.

A.3.2 ^{1}H-^{13}C MAS NMR of SDAs occluded during crystallization

^{1}H-^{13}C MAS NMR spectroscopy provides information about the structure of organics occluded in MFI zeolites during hydrothermal synthesis [61, 253]. Figures A.5 and A.6 show these NMR spectra for four MFI zeolites crystallized either with or without B (Si/B = 2.5, ∞) and from TPA$^+$ only or TPA$^+$/EDA mixtures at fixed total SDA concentration (TPA$^+$/Si = 0.312 or 0.02; SDA/Si = 0.312). ^{1}H-^{13}C MAS NMR spectra for all four zeolites show single features for -CH$_2$- carbons at $\sim$63 ppm and $\sim$16 ppm, consistent with previous reports of MFI zeolites synthesized from TPA$^+$/Na$^+$ mixtures [253]. Two features of similar magnitude are observed between 10-12 ppm for -CH$_3$ carbons are also consistent with previous reports [253], which were attributed to differences in the local environment around methyl groups in straight and sinusoidal channels. Similar magnitudes of these features corroborate this interpretation, because two straight and sinusoidal channels are each accessible from MFI intersections that house the central nitrogen atom. The feature for -CH$_3$ groups in sinusoidal channels ($|sim$10.5 ppm) is larger relative to those in straight channels ($\sim$11.5 ppm) in B-Al-MFI zeolites crystallized with EDA, which may be related to changes in the conformations of -CH$_3$ groups when EDA is occluded in channel environments [109].

^{1}H-^{13}C CP MAS NMR may also be used to determine the charge of amine groups in occluded EDA molecules, because ^{13}C NMR chemical shifts are sensitive to the charge of the adjacent amine [262]. However, features for ^{13}C atoms in EDA ($\sim$44.9 ppm) are not clearly observed in B-Al-MFI zeolites crystallized with EDA, although they contain 2.4-5.2 EDA molecules per unit cell (Chapter 5). Therefore, additional NMR experiments are required to identify and quantify the number of charge-neutral and cationic amine groups in B-Al-MFI zeolites crystallized with EDA.

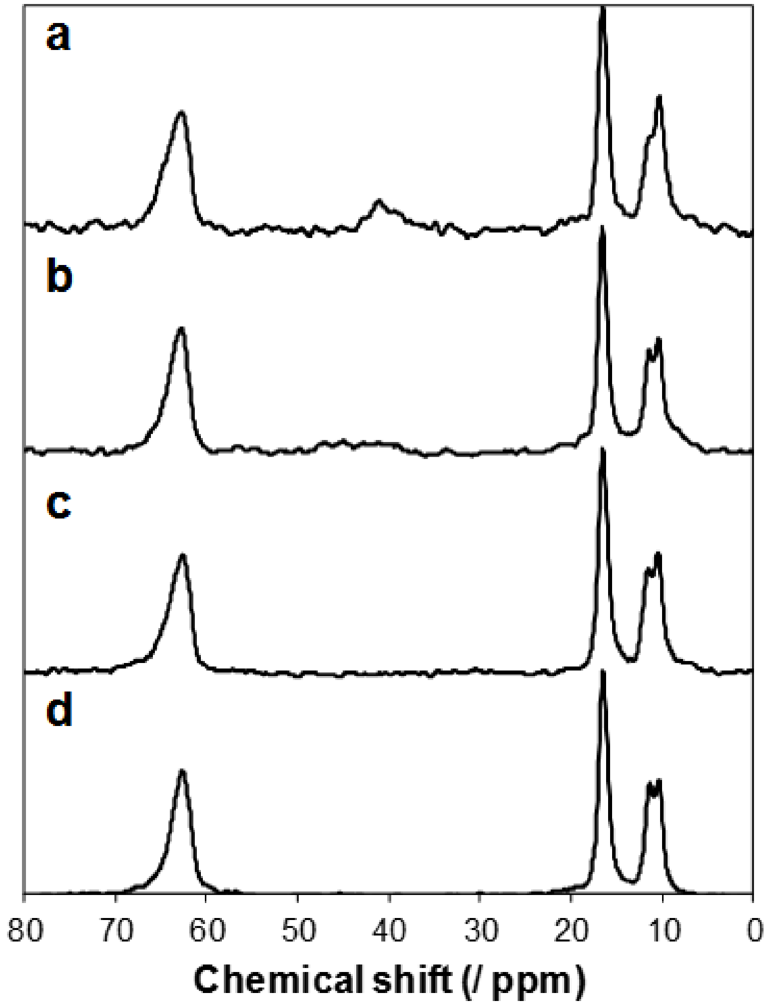

Figure A.5.: ^{1}H-^{13}C CP MAS NMR spectra of (a) B-Al-MFI-EDA (2.5, 50), (b) Al-MFI-EDA (50), (c) B-Al-MFI-TPA (2.5, 50), and (d) Al-MFI-TPA (50).

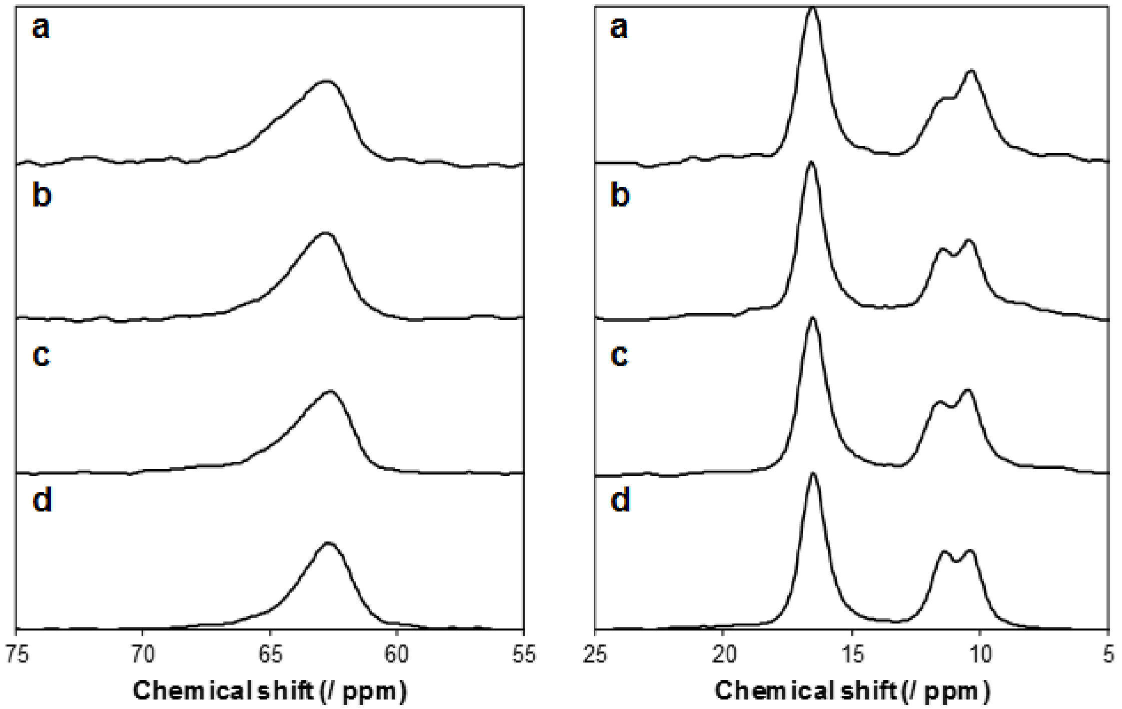

Figure A.6.: ^{1}H-^{13}C CP MAS NMR spectra of (a) B-Al-MFI-EDA (2.5, 50), (b) Al-MFI-EDA (50), (c) B-Al-MFI-TPA (2.5, 50), and (d) Al-MFI-TPA (50). Same data as Figure A.5 with different aspect ratios.

A.3.3 Time-resolved crystallization studies of B-Al-MFI synthesis

A B-Al-MFI synthesis solution with molar composition 1 SiO_2/ 0.02 TPAOH/ 0.29 EDA/ 0.01 Al_2O_3/ 0.4 H_3BO_3/ 10.2 H_2O was prepared and placed in four separate Teflon-lined stainless-steel autoclaves in a forced convection oven at 448 K under rotation at 40 rpm for 20-92 h. Samples are denoted B-Al-MFI (2.5, 50)-X, where X is the synthesis time (in h). XRD patterns and N_2 adsorption isotherms for these four samples are shown in Figure A.7. Solids were amorphous after 20 h and showed no discernable XRD peaks, while those crystallized for 46, 68, or 92 had XRD patterns (Figure A.7) and micropore volumes, calculated from N_2 adsorption isotherms (Figure A.7), typical of the MFI topology ($\sim$0.14 cm^3 g^{-1}). Si/Al ratios were between 60-65 and Si/B ratios were between 62-69 in all crystalline samples (Table A.4).

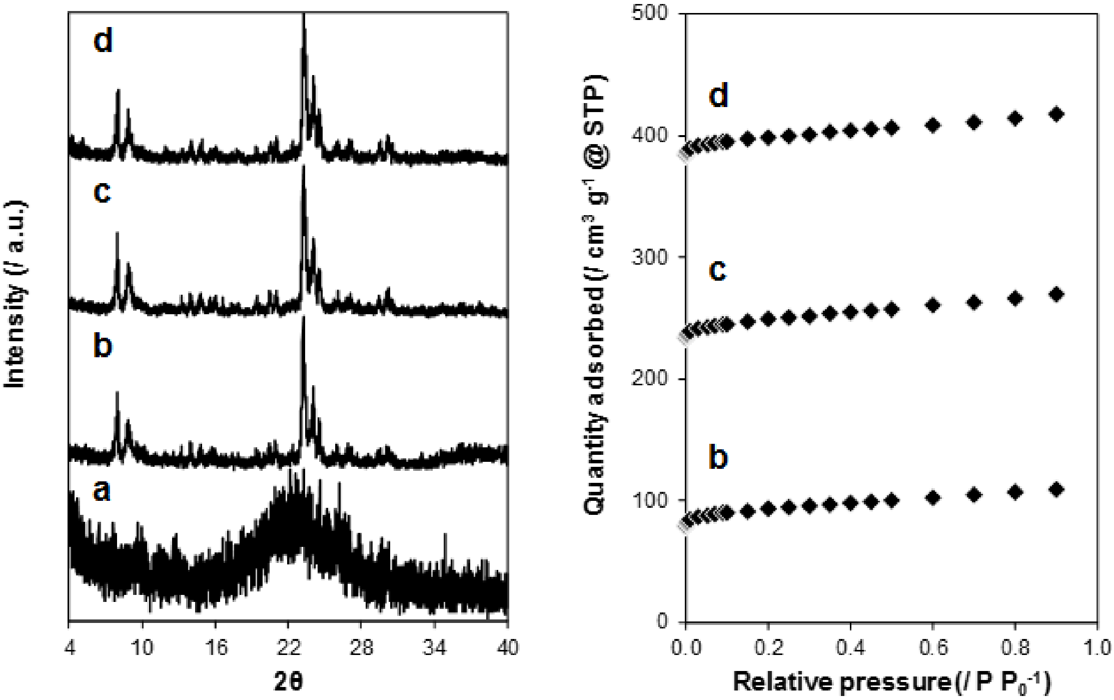

Figure A.7.: XRD patterns (left) and N_2 adsorption isotherms (77 K; right) on (a) B-Al-MFI (2.5, 50)-20, (b) B-Al-MFI (2.5, 50)-46 (c) B-Al-MFI (2.5, 50)-68, and (d) B-Al-MFI (2.5, 50)-92. N_2 adsorption isotherms are offset by 150 cm^3 g^{-1} for clarity and were not collected on B-Al-MFI (2.5, 50)-20.

Table A.4.: Physiochemical properties of B-Al-MFI (2.5, 50) zeolites crystallized with different hydrothermal synthesis times.

Sample[a]	Phase	$\mathrm{Si/Al}^{b}_{solid}$	$\mathrm{Si/B}^{b}_{solid}$	Micropore volume[c]
B-Al-MFI (2.5, 50)-20	Amorphous	n.m.*	n.m.*	n.m.*
B-Al-MFI (2.5, 50)-46	MFI	61	69	0.13
B-Al-MFI (2.5, 50)-68	MFI	64	65	0.14
B-Al-MFI (2.5, 50)-92	MFI	61	62	0.14

[a] Samples are denoted B-Al-MFI (x, y)-z, where x and y are the Si/B and Si/Al ratios in synthesis solutions and z is the synthesis time (in h).
[b] Determined by ICP-OES. Errors are ±20%.
[c] Units are $\mathrm{cm}^3\ \mathrm{g}^{-1}$. Errors are $\pm 0.02\ \mathrm{cm}^3\ \mathrm{g}^{-1}$.
*n.m.; not measured.

The pH of the synthesis solutions prior to heating was 10.3, which is below the pKa_1 of EDA (10.7). Therefore, approximately 60% of EDA molecules have one protonated amine group under these conditions, while the second is predominantly neutral (Figure A.4). The pH of the synthesis solution was constant over the 92 h period used for synthesis (Figure A.8), which contradicts typical observations of pH increases during crystallization as hydroxide molecules are liberated to solution as silicates condense [260]. This suggests that EDA buffers synthesis solutions during crystallization, because the pKa_1 of EDA is similar to the pH of these synthesis solutions. In a seminal work, Lowe proposed an equilibrium model for zeolite crystallization in the presence of buffering amines and predicted smaller changes in pH during synthesis as compared to syntheses with only alkylammonium cations (e.g., TPA^+) [263]. Here, the pH of the synthesis solution is influenced by the TPA^+, Al, and B contents in synthesis solution, and the fixed SDA/Si ratio imposed on these syntheses influences the quantity of EDA available to buffer solutions. Additional time-resolved crystallization studies that vary the quantity of TPA^+, EDA, boron, and aluminum in synthesis solutions are required to determine the role of each on the physiochemical properties of B-Al-MFI zeolites.

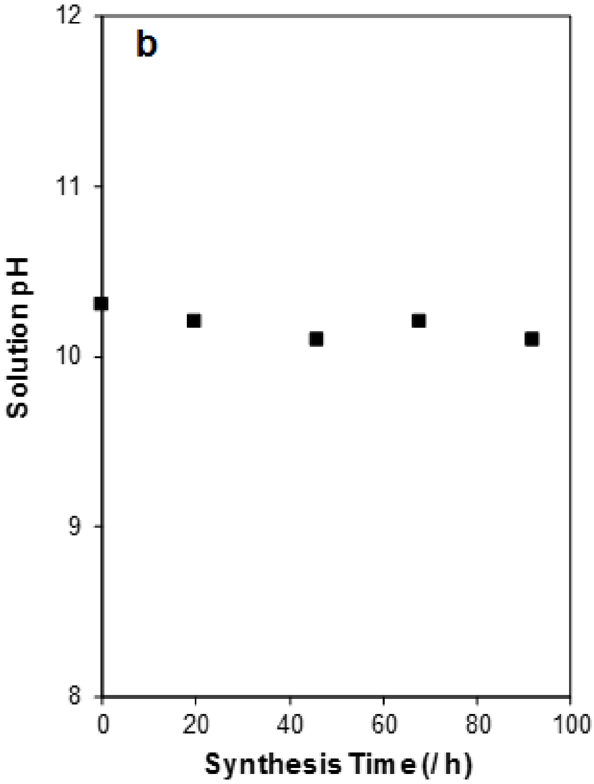

Figure A.8.: B-Al-MFI (2.5, 50) synthesis solution pH as a function of hydrothermal synthesis time.

A.4 Conclusions

B-Al-MFI zeolites crystallized with TPA^+ and EDA structure directing agents were synthesized over a variety of compositions (Si/Al = 24-72) from solutions containing TPA^+/EDA ratios of 2-30. MFI zeolites with Si/Al $\sim$ 50 have higher fractions of Al atoms in paired configurations when synthesized from solutions with higher TPA^+/EDA ratios when TPA^+/Si ratios are similar to the maximum value that MFI can accommodate (TPA^+/Si = 0.04). This is consistent with the hypothesis presented in Chapter 5 that the isolation of framework Al is related to decreases in cationic charge density supplied by TPA^+ cations in MFI frameworks. Crystallization barriers arise when Al/TPA^+ ratios approach unity in synthesis solutions, but are overcome in the presence of B heteroatoms that decrease solution pH and increase the fraction of cationic EDA molecules that may also charge-compensate anionic Al heteroatoms. Finally, we note that EDA buffers MFI synthesis solutions during crystallization, unlike conventional syntheses where solution pH increases as hydroxide anions are released into solution as silicates condense. This may influence the dynamics of MFI nucleation, growth, and dissolution in ways that are currently unclear and require additional time-resolved synthesis studies, and elemental analysis and spectroscopic evidence for the number and charge of organic SDAs occluded in MFI with these methods.

A.5 Acknowledgements

We would like to thank Sopuru Ezenwa (Purdue University) and Kaela Evans (Washington University St. Louis) for assistance in the synthesis and characterization of B-Al-MFI zeolites discussed in this work.

B. PROPENE OLIGOMERIZATION KINETICS ON B-AL-MFI ZEOLITES

B.1 Introduction

MFI zeolites are commonly used in hydrocarbon upgrading processes because their three-dimensional pore connectivity attenuates deactivation by pore blockage relative to one-dimensional zeolites (e.g., MOR), and because their pore-limiting and largest cavity diameters are of similar dimensions and thus allows for egress of bulky molecules formed within microporous voids unlike other zeolite frameworks with larger voids and smaller diffusion-limiting apertures (e.g., ERI) [242]. MFI zeolites have been used as solid acids for alkene oligomerization catalysis since the introduction of the Mobil Olefins to Gasoline and Distillate (MOGD) process [25, 264, 265], which proceeds through oligomerization, β-scission, isomerization, and hydride transfer reactions to form a distribution of hydrocarbon products from light alkenes [87].

Fundamental studies of oligomerization reactions on MFI zeolites have suggested that different active site arrangements and crystallite properties influence rate, product selectivity, and deactivation. Corma and co-workers used MFI zeolites of varying crystallite size and Al content to show that shorter diffusion path lengths attenuate deactivation during propene oligomerization [205] because bulky polyaromatics form at longer intracrystalline residence times, influenced by the number of acid sites that reactant molecules encounter per unit length in microporous domains [87]. These arguments have been used by Sarazen and co-workers to explain differences in propene oligomerization product distributions on MFI zeolites at low conversion ($\sim$1%) that more closely resemble binomial distributions expected from more prevalent secondary reactions with increasing diffusion path lengths [87]. However, initial propene dimerization rates in these experiments were similar among MFI zeolites of different composition [51], suggesting that protons in MFI zeolites are equally reactive for primary reaction events. Other studies by Mlinar et al. [71] and Bernauer et al. [72] have suggested that proximal active sites either decrease or increase propene oligomerization rates in MFI zeolites, respectively, by crowding of active sites by nearby adsorbates that decrease barriers for product desorption [71] or through repulsion of adsorbates by adjacent protons that more quickly removes oligomeric products [72]. These rate measurements, however, were performed at steady state under conditions where the number of active sites after partial deactivation is unknown. The placement of active sites in distinct voids can influence deactivation during these reactions, because protons in larger voids are more susceptible to deactivation by polyaromatics and coke precursors that cannot access smaller pore environments [209]. Additionally, no evidence was provided that product desorption was kinetically-relevant under the conditions used to measure propene oligomerization rates [71, 72], therefore differences in product desorption rates may not influence measured reaction rates. Other mechanistic interpretations showed that C-C bond formation was kinetically-relevant during propene oligomerization on MFI zeolites, evidenced by density functional theory and apparent kinetics that were first-order in propene pressure [51]. Therefore, kinetic measurements at initial time-on-stream on MFI zeolites with different active site and crystallite properties are required to quantify the role of these parameters on rate, product selectivity, and deactivation during alkene oligomerization catalysis.

Here, we measure propene oligomerization rates on B-Al-MFI zeolites synthesized and characterized in Chapter 4. Initial time-on-stream rate measurements reflect C_3-covered surfaces that become covered by products and carbonaceous intermediates at non-zero time-on-stream, resulting in deactivation that depends on active site and crystallite properties. Additional experiments are proposed to further probe the role of these properties in alkene oligomerization catalysis on MFI zeolites.

B.2 Experimental Methods

B.2.1 Synthesis of B-Al-MFI zeolites

B-Al-MFI zeolites were synthesized, treated, and characterized according to protocols reported in Chapter 4 [247].

B.2.2 Kinetic measurements of propene oligomerization on B-Al-MFI zeolites

H-B-Al-MFI zeolites were physically mixed with silica (Sigma-Aldrich, high-purity grade, 180-250 μm) in silica/MFI ratios of 5-20 (by mass), and pelletized and sieve together to retain 180-250 μm particles. The mixture was then loaded into a stainless-steel reactor (9.5 mm inner diameter) and a concentric thermowell (stainless-steel, 1/8 in. diameter) with a K-type thermocouple was placed at the axial center of the reactor to measure temperature. Samples were treated in flowing air (zero air, THC < 1 ppm, Indiana Oxygen) at 823 K for 5 h (0.023 K s^{-1}) before cooling to reaction temperature (503 K). Reactant mixtures were comprised of C_3H_6 (75 kPa), Ar (20 kPa), and CH_4 (5 kPa) as an internal standard. Reactant mixtures were further diluted in He to the desired C_3H_6 pressure and flow rate. Reaction products were transferred via heated lines (390 K) to a gas chromatograph (Agilent 7898A) equipped with a flame ionization detector and a GS GasPro column (0.320 mm i.d. 60 m, Agilent). Rates were normalized the number of Brønsted acid protons counted in *ex situ* NH_3 titrations (Chapter 4) [247]. Calculations for true oligomer selectivities were performed according to Sarazen et al [87].

B.3 Results and Discussion

B.3.1 Propene oligomerization rates and product selectivities on B-Al-MFI zeolites

Physiochemical properties of B-Al-MFI zeolites used here were taken from Chapter 4 and are shown in Table B.1. The number of Brønsted acid protons originating from Al heteroatoms (H^+_{Al}) in boroaluminosilicate compositions was quantified with NH_3 titration protocols that were developed in Chapter 4 and used to normalize propene oligomerization rates, because protons associated with B heteroatoms are much weaker acids (by ~70 kJ mol^{-1} [33]) than those at Al and thus catalytically inconsequential in the presence of Al heteroatoms [213]. Propene oligomerization rates (503 K, per H^+_{Al}) on B-Al-MFI zeolites are shown in Figure B.1 as a function of time-on-stream for these three samples at conversions below 1%. Initial rates were highest on H-B-Al-MFI (2.6, 176), which has the smallest diffusion parameter, and initial rates decreased systematically with diffusion parameter (Figure B.2). This suggests that active sites within B-Al-MFI zeolites with different diffusion parameters differ in their intrinsic reactivity, or that intracrystalline diffusion limits initial propene oligomerization rates measured under these conditions. We note that these B-Al-MFI zeolites contain predominantly isolated Al heteroatoms in channel intersections of MFI, and therefore similar Al distributions. These results differ from those reported by Sarazen and co-workers that initial propene dimerization rates were similar among H-form zeolites of different compositions and diffusion parameters [51]. However, the commercially-sourced samples used by Sarazen and co-workers contain different Al distributions and contain a higher fraction of Al pairs at lower Si/Al ratios, as shown by Song and co-workers on the same commercially-available samples with Co^{2+} ion-exchange methods [73]. Additional propene oligomerization experiments with B-Al-MFI zeolites with different fractions of isolated and paired Al (Chapter 5) and diffusion parameters, and under different experimental conditions that change the relative rates of reaction and diffusion, are required to determine propene oligomerization rates at distinct active sites in MFI zeolites.

Propene oligomerization rates decreased by ~2× from initial time-on-stream to steady-state on all samples (Figure B.1), consistent with deactivation commonly reported during alkene oligomerization on zeolites [205]. However, the population of active sites that turnover at non-zero time-on-stream is not known, precluding rigorous analysis of these rates normalized by *ex situ* active site counts. Future *in situ* site titrations may provide additional insight into the fraction of available active sites during steady-state propene oligomerization by introducing base titrants to reactant mixtures at nonzero time-on-stream.

Table B.1.: Physiochemical properties of B-Al-MFI zeolites.

Sample^a	Si/Al$^b_{solid}$	Si/B$^c_{solid}$	Micropore volume^d	Characteristic length^e	Diffusion parameter^f
B-Al-MFI (2.6, 176)	142	32	0.13	0.3	0.02
B-Al-MFI (2.6, 88)	88	30	0.13	0.4	0.07
B-Al-MFI (13, 176)	153	30	0.13	8.9	15

[a] Samples are denoted B-Al-MFI (x, y), where x and y are the Si/B and Si/Al ratios in synthesis mixtures.
[b] Determined by atomic absorption spectroscopy. Errors are ±10%.
[c] Determined by ICP-OES. Errors are ±10%.
[d] Units are $\mathrm{cm^3\ g^{-1}}$. Errors are $\pm 0.01\ \mathrm{cm^3\ g^{-1}}$.
[e] Determined from scanning electron microscopy images.
[f] Units are mol H^+_{Al} $\mathrm{nm^{-1}}$.

Sarazen and Iglesia have previously shown that the product selectivity toward primary C_6 products decreases relative to products of secondary oligomerization and β-scission reactions in zeolites with increasing diffusion parameters [87]. They defined the "true oligomer selectivity" as the fraction of C_6 products formed from primary reaction steps relative to all other products formed through multiple reaction events. Figure B.3 shows the true oligomer selectivity as a function of the diffusion parameter for these B-Al-MFI samples, and for a commercially-available MFI zeolite (CBV2314, Si/Al = 13, Zeolyst International). The selectivity to true oligomer products decreased with increasing conversion on CBV2314, consistent with increasing

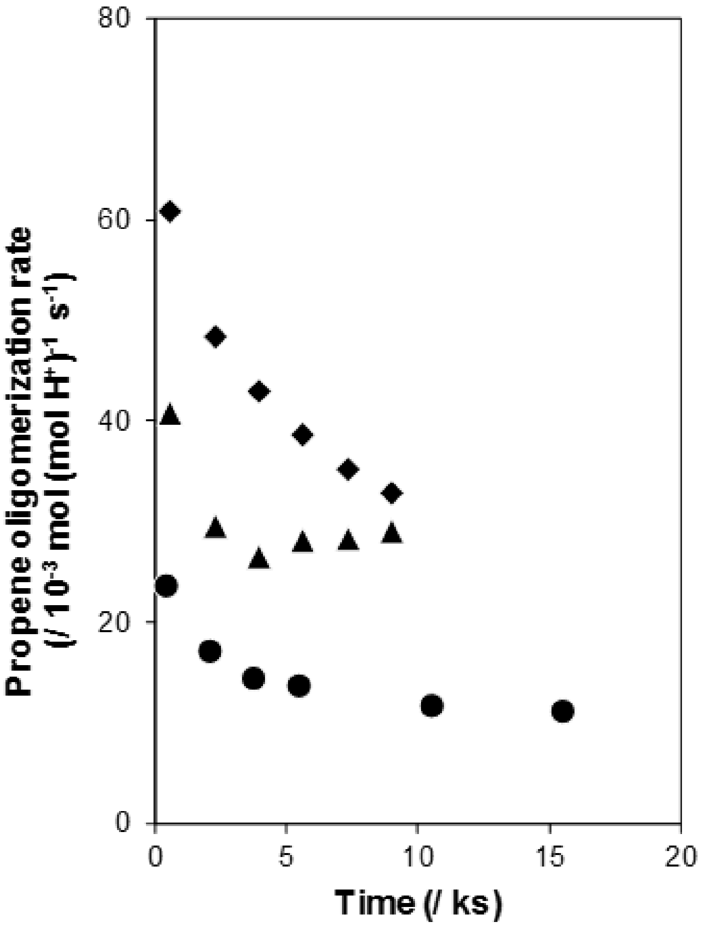

Figure B.1.: Propene oligomerization rates (503 K, per H^+_{Al}, 169 kPa C_3H_6) as a function of time-on-stream on H-B-Al-MFI (2.6, 176) (◆), H-B-Al-MFI (2.6, 88) (▲), and H-B-Al-MFI (13, 176) (●).

numbers of secondary reactions at longer residence times. True oligomer selectivities increased with conversion among B-Al-MFI zeolites, and higher true oligomer selectivities were observed on samples with higher initial propene oligomerization rates and lower diffusion parameters (Figure B.2). Initial rate measurements collected at different conversions are required to further comment on the role of active site and crystallite properties on propene oligomerization kinetics, and this suite of B-Al-MFI zeolites provides model materials to decouple the roles of material properties at these different length scales on catalysis.

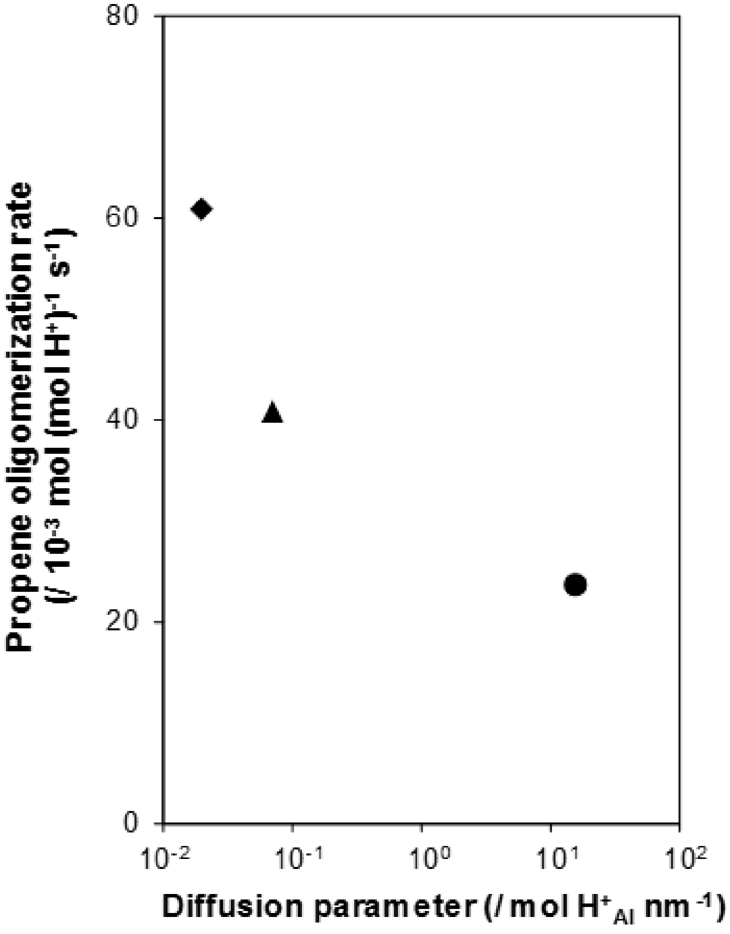

Figure B.2.: Initial propene oligomerization rates (503 K, per H^+_{Al}, 169 kPa C_3H_6) on B-Al-MFI zeolites as a function of the characteristic diffusion parameter. H-B-Al-MFI (2.6, 176) (◆), H-B-Al-MFI (2.6, 88) (▲), and H-B-Al-MFI (13, 176) (●).

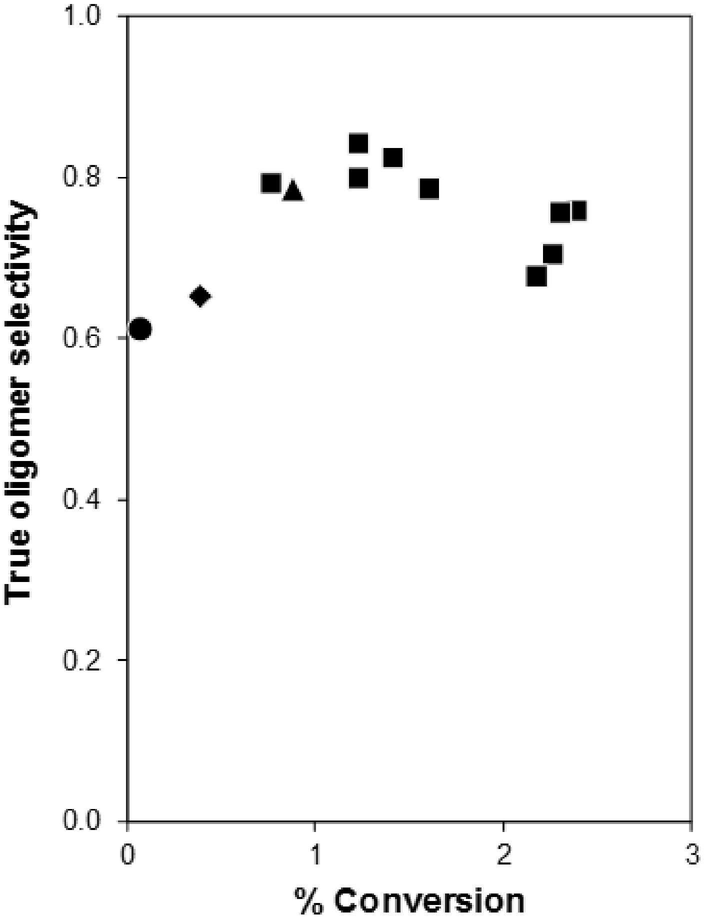

Figure B.3.: True oligomer selectivity (503 K, 169 kPa C_3H_6) as a function of initial conversion on H-B-Al-MFI (2.6, 176) (◆), H-B-Al-MFI (2.6, 88) (▲), H-B-Al-MFI (13, 176) (●), and H-MFI (CBV2314) (■).

B.4 Conclusions

Mechanistic interpretations of alkene oligomerization reactions in microporous solid acids require knowledge active site distributions in distinct locations and local ensembles, active site coverage by surface intermediates, and the relative rates of reaction and diffusion as bulkier product molecules are formed within microporous voids. Prior studies have generally used either steady-state kinetic analysis on zeolites made with different distributions of active sites [71, 72], or initial rate analysis on commercially-sourced samples with systematic trends in bulk and active site properties [51, 87]. Here, we present preliminary data on propene oligomerization kinetics measured on B-Al-MFI zeolites, whose active site and crystallite properties were independently influenced through synthetic methods. Initial rate analysis on this diverse suite of zeolites will be used in future work to quantify the role of active site and crystallite properties on initial and steady-state alkene oligomerization catalysis, informing synthetic protocols to influence reactivity and deactivation in these chemistries.

B.5 Acknowledgements

We would like to thank Elizabeth Bickel for performing propene oligomerization kinetic experiments and helpful technical discussions in preparing this document.

VITA

Philip “Phil” Kester was born in Cincinnati, Ohio and raised in Mason, Ohio. Growing up, Phil enjoyed playing golf and hockey, cycling, and playing saxophone. He was also an active member of Boy Scout Troop 43 and attained the rank of Eagle Scout in 2010. Upon graduating from William Mason High School, Phil attended The Ohio State University where he majored in chemical engineering with a minor in physics. While an undergraduate, Phil continued his musical endeavors in the athletic band and organized the annual Beat Michigan 5K with Tau Beta Pi, benefiting local food pantries. Phil had internships at the Wright Brothers Institute through Wright Patterson Air Force Base, Battelle Memorial Institute in their Process Systems Engineering Group, and undergraduate research experience in Prof. Umit Ozkan’s research group at Ohio State where he became interested in heterogeneous catalysis.

This motivated Phil to pursue a Ph.D. at Purdue University, where he joined Prof. Raj Gounder’s research group in 2014. Phil served as the Outreach Coordinator for the Purdue Catalysis Center, teaching K-12 students about science, engineering, and catalysis, and was the first chair of the Student Leadership Council for the Center for the Innovative and Strategic Transformation of Alkane Resources. Outside of the lab, Phil was a founding member of the Wabash Mountain Boyz, a band dedicated to leaving talent at the door and playing as many open mic nights as possible. He also honed his golf skills in the Purdue Staff Golf League and carded a career-best 69 on the Ackerman-Allen course. Phil spent many weekends traveling to and from Columbus, Ohio to visit his girlfriend Amy, whom he married in August 2018. Upon graduation from Purdue, Phil will join Dow in Midland, Michigan in their Chemical Sciences group where he will continue to apply fundamental principles of catalytic science and technology to complex kinetic and reaction engineering problems.